McKelvey School of Engineering Theses & Dissertations

McKelvey School of Engineering

Winter 12-15-2018

Nanopower Analog Frontends for Cyber-Physical Systems

Kenji Aono

Washington University in St. Louis

Recommended Citation

Aono, Kenji, "Nanopower Analog Frontends for Cyber-Physical Systems" (2018). *McKelvey School of Engineering Theses & Dissertations*. 390.
https://openscholarship.wustl.edu/eng_etds/390

WASHINGTON UNIVERSITY IN ST. LOUIS

School of Engineering and Applied Science
Department of Computer Science and Engineering

Dissertation Examination Committee:
Shantanu Chakrabartty, Chair
Roger D. Chamberlain
Baranidharan Raman
William D. Richard
Xuan Zhang

Nanopower Analog Frontends for Cyber-Physical Systems
by
Kenji Aono

A dissertation presented to the
The Graduate School
of Washington University in
partial fulfillment of the
requirements for the degree
of Doctor of Philosophy

December 2018
St. Louis, Missouri

Table of Contents

List of Figures

List of Tables

Acknowledgments

Major funding came from the National Science Foundation's Graduate Research Fellowships Program (GRFP) and Graduate Research Opportunities Worldwide (GROW) under grant numbers DGE-0802267 and DGE-1143954. Additional support came from the Japan Society for the Promotion of Science (GR14001), administered through The University of Tokyo, and from the National Aeronautics and Space Administration (NASA) administered by Michigan Space Grant Consortium (2012–2015) and The University of Michigan. Support from Semiconductor Research Corporation (SRC) and Metal Oxide Semiconductor Implementation Services (MOSIS) were vital in fabricating chips for this dissertation.

In addition to the Ph.D. committee listed from Washington University in St. Louis, portions of this dissertation were undertaken while the author was at Michigan State University under the guidance of the Ph.D. committee of professors: Shantanu Chakrabartty, Fathi Salem, Selin Aviyente, Wen Li, and Richard J. Enbody. Special thanks to Professor Nizar Lajnef and his research team for the extensive collaborative work done on the Piezoelectric-Floating-Gate sensors. Thanks are also given to Professor Toshihiko Yamasaki and Professor Arun Ross for their guidance in developing software for recognition tasks.

Kenji Aono

Washington University in Saint Louis

December 2018

Research is 50% risk — as long as it works

Shantanu Chakrabartty

ABSTRACT OF THE DISSERTATION

Nanopower Analog Frontends for Cyber-Physical Systems

by

Kenji Aono

Doctor of Philosophy in Computer Engineering

Washington University in St. Louis, 2018

Professor Shantanu Chakrabartty, Chair

In a world that is increasingly dominated by advances made in digital systems, this work will explore the exploiting of naturally occurring physical phenomena to pave the way towards a self-powered sensor for Cyber-Physical Systems (CPS). In general, a sensor frontend can be broken up into a handful of basic stages: transduction, filtering, energy conversion, measurement, and interfacing. One analog artifact that was investigated for filtering was the physical phenomenon of hysteresis induced in current-mode biquads driven near or at their saturation limit. Known as jump resonance, this analog construct facilitates a higher quality factor to be brought about without resorting to the addition of multiple stages and poles in the filter. Exploiting this allows a filter that mimics mammalian cochlea using nW of power, and the viability of such a filter was demonstrated in the application of speaker recognition. Features were extracted using a silicon cochlea analog frontend, which outperformed features from traditional linear filters when classification was done with a Gini-SVM.

To realize the measurement stage of the frontend, a previously reported technology, the Piezoelectric-Floating-Gate (PFG) was employed. The PFG matches physics of Impact-Ionized Hot-Electron Injection (IIHEI) in silicon metal-oxide field effect transistors with a piezoelectric transducer to drive nonvolatile data-logging measurements. The PFG implementation is self-powered in the sense that the energy required for sensing comes from the signal being observed, which allows for continuous, zero-downtime measurements of signals that exceed the IIHEI threshold and can drive nW loads. Moreover, since it directly matches the transduction stage to measurement, it obviates the need for an explicit energy conversion stage in the frontend. Multiple interfacing technologies were evaluated, including: wired, self-powered radio-frequency (RF) backscatter, periodic 915 MHz active RF, and a hybrid model that uses energy scavenging to determine if an interrogator is within range before transmitting. A multi-year deployment of this sensor frontend for structural health monitoring is currently active on the Mackinac Bridge in northern Michigan and demonstrates successful transition from laboratory to practice for a CPS.

Finally, a modification to the PFG topology to include filtering aspects borrowed from earlier study was proposed and fabricated on a standard 0.5 µm CMOS process. Measurements show that the PFG sensor can be endowed with frequency discriminating capabilities to better focus on signals of interest. The modifications also give rise to a means for higher sensitivity (input stimuli below IIHEI threshold) data-logging that would vastly expand the potential application space.

Chapter 1

Research Theme

1.1 Analog Sensing in a Digital World

Since I signed up for college some 12 years ago, many things have changed in the world of technology. The first iPhone was introduced, ushering in an age of ever-connected people through their smartphones. YouTube was bought out by Google, streaming services such as Netflix and Hulu emerged to keep audiences entertained through the Internet. Facebook and Twitter invaded the social media landscape, making it common place for people to share all sorts of information previously kept private. Meanwhile, cloud services like Amazon Web Services and Microsoft Azure took advantage of big data. IBM released custom chips to mimic the synapses found in brains. NVIDIA enabled a revolution in machine learning called deep learning. And there are seemingly daily advances on a litany of topics such as robotics, self-driving cars, and wireless communication. Throughout this period, Moore's Law has marched on, and silicon transistors are now reaching single atom. Our daily interactions now rely on a digital world.

Yet, the crux of the matter is that this world we live in is driven by analog processes. While the APIs and block diagrams of modern computers appear digital, inside are hidden application-specific integrated analog circuits that accelerate the processing of data. When pursuing the limits of energy efficiency, many solutions have exploited physical phenomenon that are inherently analog. To interface with the natural world also requires translating between analog and digital domains. It is in this particular domain of translating, or analog sensing, that this work is focused on. The underlying motivation has been to take hints from biological systems and incorporate similar capabilities in-silico. An eye towards keeping the power requirements of the silicon implementation is maintained, with the goal of realizing a monolithic self-powered sensing unit. In Table 1.1, some common sources of energy utilized in energy harvesting are outlined. One of the most well-known is solar. If it is available, a single square centimeter could drive 15 mW; however, solar is not omnipresent, and when relying on other sources of power, the expected power is in the µW scale.

Table 1.1: Comparison of Sensors with Different Power Sources

Type	**Transducer**	**Power Density**
Solar	Photovoltaic	$15\,000\,\mu W/cm^2$ [1]
RF	LC coupling, antenna	$40\,\mu W/cm^2$ at 10m [2]
Mechanical	Electromagnetic, piezoelectric	$3.89\,\mu W/cm^3$ to $830\,\mu W/cm^3$ [3, 4]
Thermal	Pyroelectric, thermoelectric	$2000\,\mu W/cm^2$ with 12°C gradient [5]
Chemical	Glucose, fructose	$2\,mW/cm^2$ to $4\,mW/cm^2$ [6]

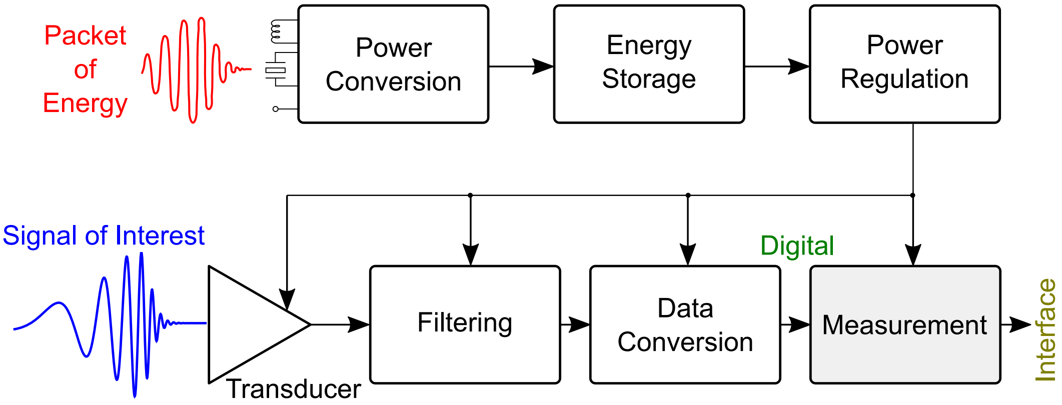

Figure 1.1: A block diagram showing commonly encountered components of a sensor for Cyber-Physical-Systems (CPS). The packet of energy (in red) has to undergo several stages of power management before it can supply the filter, interface, and measurement components. In this architecture, the signal of interest is only periodically measured.

1.2 A Sensor

In Figure 1.1, the block diagram depicts a typical sensor used in a Cyber-Physical System (CPS). Oftentimes in CPS, the sensor will be power-constrained. This is due to the impracticability of deploying power cables to every single node that needs to be monitored by sensors. Therefore, it is common to have three types of sensor powering methods. Figure 1.2a shows the case of a battery-powered sensor, which will periodically wakeup the sensor to measure the environment. Since the batter has a finite amount of energy stored, one method to extend the operational lifespan is to add trickle-charging to harvest spare energy from the environment (typically solar energy) and store it on a rechargeable battery or super capacitor. In the second type, of Figure 1.2b, the sensor is only interrogated when an external signal is present. The external signal might be a acoustic, optical, radio-frequency (RF), or magnetic. The actual sensing of the environment will only occur when the external signal provides sufficient energy. In both of the aforementioned types, the sensor is only periodically sampling the environment, and is liable to miss rare events. A more ideal solution would be that of Figure 1.2c, in this case the environmental signal to be measured is providing sufficient energy to complete a sensing task. Although this would be a relatively simple task if the signal of interest were solar (an intense light source), it becomes exceedingly non-trivial when attempting to sense smaller signals like mechanical power across piezoelectrics, RF coupled to an antenna, or even photovoltaics being activated with a weak light source. Note that in this solution of using the input stimuli as the energy source, the top row of blocks in Figure 1.1 are eliminated from consideration, simplifying the design requirements and minimizing the wasted energy that would have been lost in the energy conversion, storage, and regulation stages.

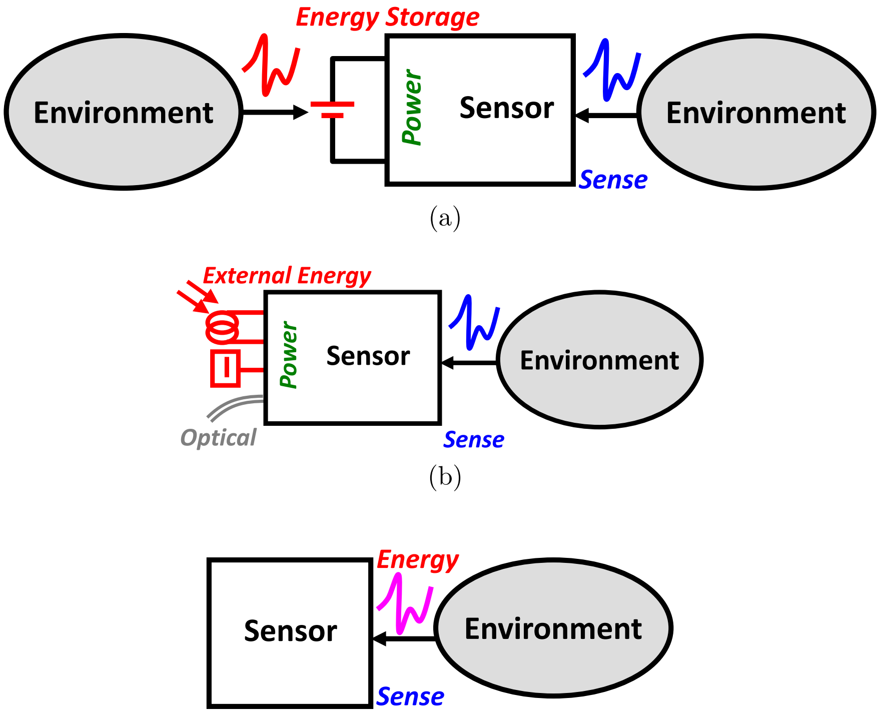

(a)

(b)

(c)

Figure 1.2: Showing three types of sensors, (a) passive that will periodically wake up to make measurements, (b) energy harvesting that needs to scavenge enough energy from the environment before making periodic measurements, (c) self-powered, continuous sensor in which the stimuli to measure is sufficient energy.

1.2.1 Transduction

The first stage of a sensor that is making a measurement of its environment is to couple the signal of interest with a transducer. There may be some confusion between the differences of a sensor and transducer, luckily The American National Standards Institute (ANSI) has given the following definition for a transducer.

> A device which provides a usable output in response to a specific measurand.

It seems then, that many devices would thus be eligible as transducers. In the context of this work, a transducer is assumed to be a device that merely converts any observable energy into an electrical signal. Thus, when discussing a "sensor" in this work, it can be assumed that everything beyond the transduction stage takes place in the electrical domain. For example, if the signal of interest is optical, a photovoltaic cell could be used to convert photons into electrons. Similarly, when sensing strain, a piezoelectric might be sufficient to generate an electric field to couple to the sensor. In Table 1.2.1, four common sources are listed with their respective operating frequency, open circuit voltage, and source impedance. The electrical characteristics of each source, when coupled to a typical transducer for that source, will need to be considered for the downstream blocks after transduction.

1.2.2 Filter

After getting the signal from the transducer in the form of an electrical signal, a typical step is to have protection circuitry. This could come in the form of resistors to limit inrush current, capacitors to smooth out ripples, or diodes to prevent overvoltage. Resistors and capacitors (and less commonly on older CMOS processes, inductors) could also be used to

Table 1.2: Electrical Properties of Transducers for Different Power Sources

Source	**Typical Open-Circuit Voltage V_{OC}**	**Operating Frequency f_{S}**	**Typical Source Impedance Z_{S}**
Optical	$0.5 - 5\,\text{V}$	DC	Variable Impedance Low $\text{k}\Omega - 10\text{s of k}\Omega$
Thermal	$10\,\text{mV} - 10\,\text{V}$	DC	Resistive Impedance $1 - 100s$ of Ω
Vibration	$10 - 50\,\text{V}$	$0.1\,\text{Hz} - 1\,\text{kHz}$	Capacitive impedance $10s$ of $\text{k}\Omega - 100\,\text{k}\Omega$
RF & Inductive	$100\,\text{mV} - 5\,\text{V}$	$100\,\text{kHz} - 5\,\text{GHz}$	Inductive Impedance Low $\text{k}\Omega$

do filtering of the signal in the frequency domain. Perhaps the environment generate many spurious high-frequency signals that are not of particular interest for a given application. A good sensor would be able to filter out the noise and leave the observer with a measurement that has a high signal-to-noise ratio.

1.2.3 Data Conversion

In the analog world, the data conversion step is not necessary before measurement. For certain types of interfacing, a data conversion block may appear between the measurement and interface components of Figure 1.1.

1.2.4 Measurement

Perhaps the key component in the sensor system of Figure 1.1 after the transducer. This stage will store the transduced (i.e. converted to electrical) and filtered signal-of-interest for an observer to collect through the interface stage. Depending on the sensor, this measurement block might be a simple capacitor that loses its memory almost as quickly as it stores it. In applications demanding rapid interfacing, this is not an issue. Recognizing that many CPS applications would have slower consumption of their data than in high-throughput, mains driven sensors, this block might be better served by a non-volatile memory that retains the information for later retrieval by an observer. For most commercial sensors, this measurement memory would be implemented using NAND flash memory or other digital storage, either within the sensor or on an external memory chip.

1.2.5 Interface

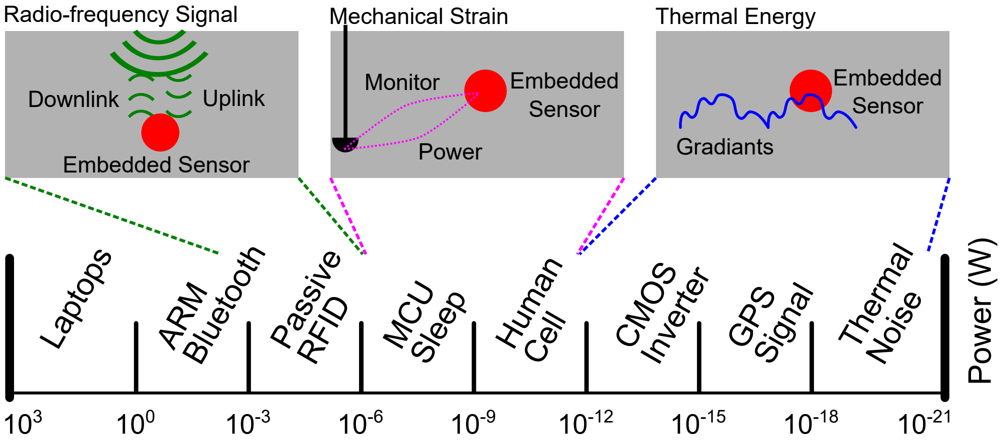

Figure 1.3: Illustrating approximate energy requirements for certain processes. In the top half of the figure, three methods of energy-harvesting are shown with typical target driving power.

When an observer wishes to retrieve the information that was measured by a sensor, they do so through an interface. This could be any modality such as wires, RF transmissions, a buffered voltage, or even acoustic [7]. When considering the interface method, it is important to keep in mind the required energy level for various processes. From Figure 1.3, the lower end of digital interface appears to be in the µW range.

1.3 Objectives and Contributions

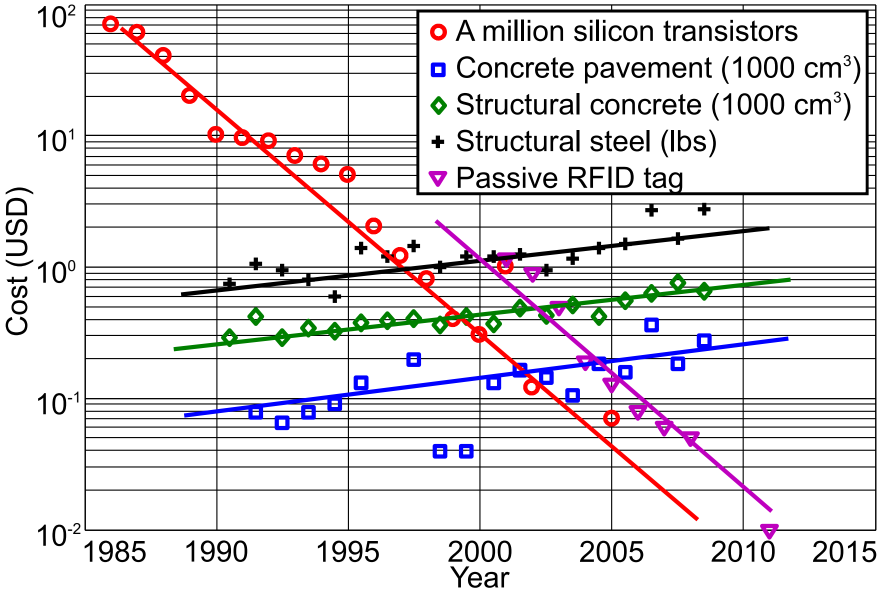

Figure 1.4: A plot that shows an increase in construction material cost versus a decrease in cost to implement silicon. In recent times, the cost of adding a million transistors to a pound of construction material appears to be a small fraction.

One of the consequences of the celebrated Moore's law [8] is that the cost of fabricating silicon integrated circuits (ICs) has reduced exponentially over the last several decades, as shown in Fig. 1.4. Nowhere has this trend manifested more profoundly than in the area of radio-frequency identification (RFID) tagging technology where the volume production cost of a single tag is less than ten cents [9]. If compared against the price trend of typical construction and structural materials (e.g. concrete or steel) during the same period, it can be seen from Fig. 1.4 that it is now economically viable to embed an RFID tag within every pound of concrete brick or inside every square foot of a large structure such as pavement highway, buildings, or multi-span bridges. In the past decade since the data points on the figure were last updated, Intel has claimed to maintain the same rate of reduction in cost per

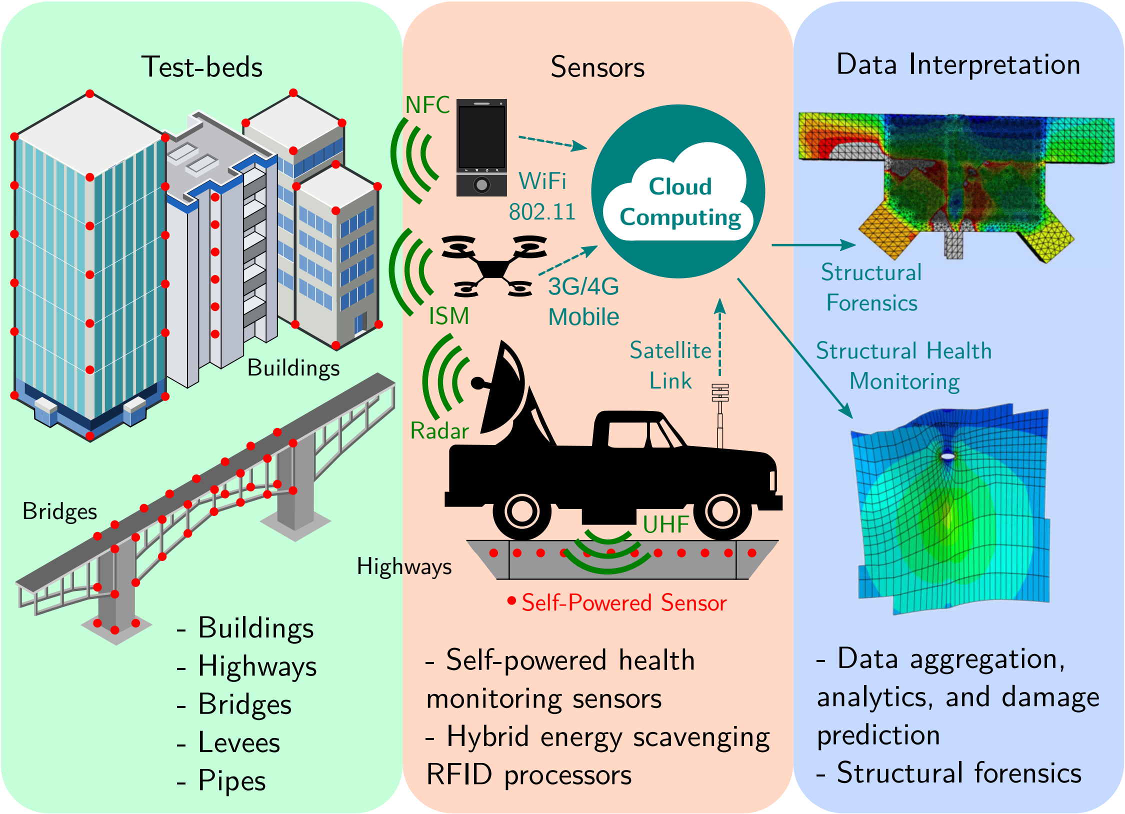

Figure 1.5: Overview of the infrastructural Internet of Things framework, green background shows potential CPS applications, the red background is for the enabling technology, and blue is for data interpretation by domain experts. The self-powered sensors are mocked up as red dots.

transistor, and steel prices have continued to trend up leading to another order of magnitude in price difference. If these tags are endowed with sensing capabilities, these sensors could form a part of the infrastructural Internet-of-Things (i-IoT) vision for monitoring health of civil infrastructure (as shown in Fig. 1.5) where millions of embedded sensors continuously monitor the mechanical usage of the structure and the usage data could then be used for condition-based maintenance of the structure. An i-IoT deployment could potentially lead to significant savings and prevention of hazards and catastrophic failures. For instance in the US, each state highway agency currently spends several million dollars per year to inspect highway structures and bridges for damage. These inspection methods are reactive in nature and require significant personnel time or use of costly capital equipment. Also, an infrastructure monitoring network as envisioned in Fig. 1.5 could be used to quickly assess damage to infrastructure after a seismic event such that maintenance procedure could be directed to the areas that need immediate attention. By being proactive with maintenance, society could reduce the chances of a catastrophic failure.

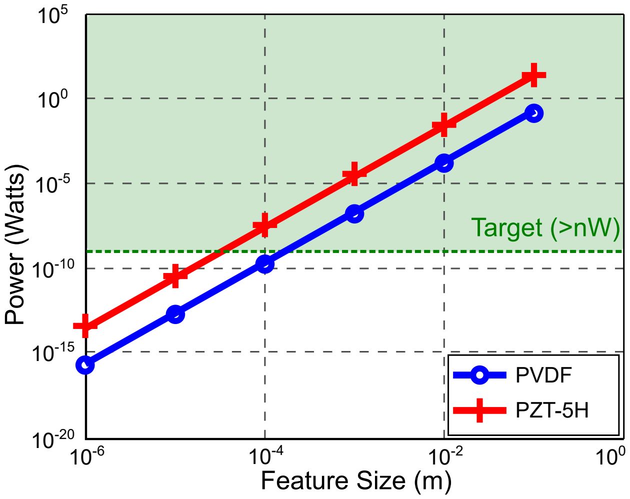

Figure 1.6: Showing the amount of power that PVDF or PZT transducers would generate for a given size.

The grand-vision is practical only if the sensor itself does not require any maintenance, implying that the sensors do not experience down-time, i.e. they operate without the need for replacing batteries and the operational life of the sensor matches or exceeds the useful life of the host structure. Additionally, for practical reasons, the sensors need to be low-cost and should be easy to install and deploy. Therefore, an end-to-end sensor System-on-Chip (SoC) is investigated starting from the filtering stage, data conversion, measurement, and interface. The transducer component is left out of consideration since the energy conversion from a target stimuli to an electrical signal is beyond the scope of a computer engineering degree. Moreover, there exist a litany of commercial transducers such as microphones or piezoelectrics made of polyvinylidene difluoride (PVDF) and lead zirconate titanate (PZT) that could provide sufficient energy to have a self-powered sensor as outlined in Figure 1.2c. From readily available data, the power levels of PVDF and PZT for a given area are shown in Figure 1.6 and verify that as long as the sensor can operate in the nW range a minimally sized piezoelectric would suffice.

1.3.1 Filter: Speaker Recognition

The problem of developing a filter is considered in isolation to the other components. A general overview of filter analysis is presented in Chapter 2, followed by a current-mode biquad filter implemented in hardware and verified on a speaker recognition task presented in Chapter 3. The lessons learned in this endeavor are folded into the other sensor components that were developed in parallel.

1.3.2 Data Conversion & Measurement: Piezolectric-Floating-Gate

Table 1.3: Comparison for Piezoelectric Harvesting Circuit Efficiency.

Ref.	**Method**	**Resonant f**	**Efficiency (%)**	**Max Power**
[10]	DSSH	105.3 Hz	40	5.5 mW
[11]	SSHI	1 kHz	20.2	<400 µW
[12]	Bias flip	225 Hz	87.5	<70 µW
[13]	Synchronous bridge rectifier	125 Hz	50–70	8 µW
[14]	Rectifier	301 Hz	64	25 µW
[15]	Switched-inductor	100 Hz	41.7	30 µW
[16]	Adaptive feedback	250 Hz	60	300 µW

For the target application of CPS for Structural-Health Monitoring (SHM), monitoring strain levels through piezoelectrics is one of the most impactful. Table 1.3 shows the maximum power and efficiency of several methods for harvesting energy from piezoelectrics. These results demonstrate the potential for implementing a Figure 1.2c style sensor since there in an abundance of energy. The data conversion and measurement components are implemented using a piezoelectric-floating-gate (PFG) circuit that allows the direct coupling of the analog electrical energy from a piezoelectric to a data-logging floating-gate [17, 18]. The core technology was previously reported under laboratory testing conditions [19, 20]. A SoC version of the core technology was developed and testing under rigorous conditions as reported in Chapter 4, and several trials were conducted in harsh, real-world conditions. The lessons learned during the filtering component testing are merged with the PFG in Chapter 5.

1.3.3 Interface: Wireless Interrogation Techniques

Taking the core technology out of the laboratory and test it in the real world required the removal of any wired dependencies (external voltage references, input commands, and output data). To this end, several wireless technologies from self-powered backscattering to active RF transmission are explored in Chapter 6.

Chapter 2

Analysis of Filters

2.1 Linear

When dealing with filters, it is often assumed that one may operate in the "linear" region of the filter. From a mathematical perspective, one may state that a filter is linear as long as it can satisfy the following conditions:

Additive for any two inputs $x_1(t)$ and $x_2(t)$,

$$F\left[x_1(t) + x_2(t)\right] = F\left[x_1(t)\right] + F\left[x_2(t)\right] \tag{2.1}$$

Homogeneous for any input $x(t)$ and constant α,

$$F\left[\alpha x(t)\right] = \alpha F\left[x(t)\right]. \tag{2.2}$$

If both conditions are met, the filter F is "linear"; under such an assumption, one may simplify the small signal analysis to make first-order approximations of a filter's behavior. To demonstrate a linear and nonlinear function, consider first this function $y(t) = t^2 x(t)$.

Is it additive?

$$F\left[x_1+x_2\right]=t^2\left(x_1(t)+x_2(t)\right) \tag{2.3}$$

$$=t^2x_1(t)+t^2x_2(t) \tag{2.4}$$

$$=F\left[x_1(t)\right]+F\left[x_2(t)\right], \quad \text{Yes} \tag{2.5}$$

Is it homogeneous?

$$F\left[\alpha x(t)\right]=t^2\alpha x(t)=\alpha t^2x(t) \tag{2.6}$$

$$=\alpha F\left[x(t)\right], \quad \text{Yes} \tag{2.7}$$

Thus, one may conclude that the function $y(t) = t^2x(t)$ is linear. On the other hand, a function such as $y(t) = x^2(t)$ would be nonlinear since

It is not additive,

$$\left(x_1(t)+x_2(t)\right)^2=x_1^2(t)+2x_1(t)x_2(t)=x_2^2(t)\neq x_1^2(t)+x_2^2(t) \tag{2.8}$$

nor homogeneous (unless $\alpha \in \{0, 1\}$)

$$\left(\alpha x(t)\right)^2=\alpha^2x^2(t)\neq \alpha x^2(t) \tag{2.9}$$

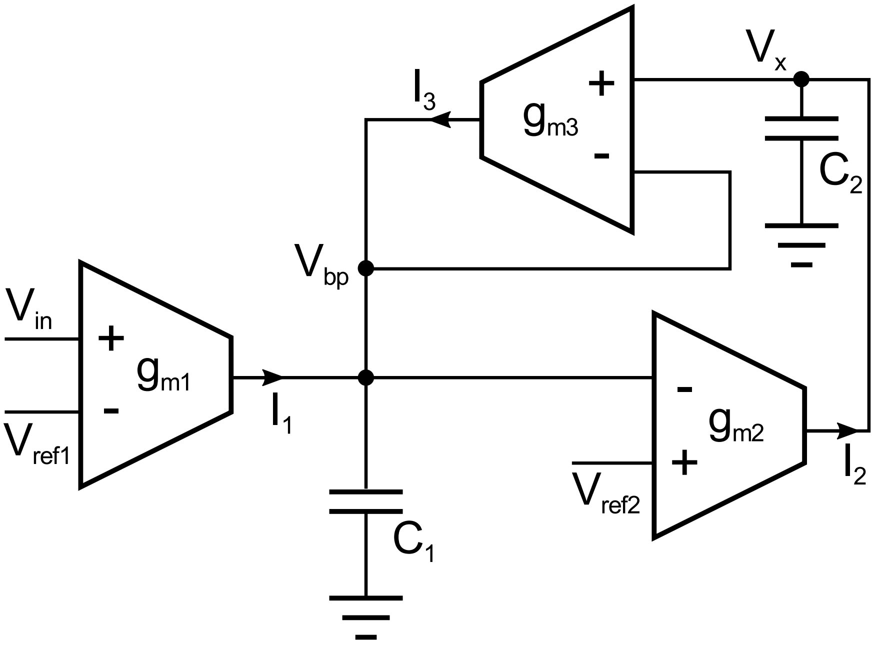

Figure 2.1: A schematic representation of a biquad filter implementation using transconductance amplifiers.

2.1.1 Derivation of $\mathrm{G_m}$-Ciquad Filter Transfer Function

Given a filter architecture as in Fig. 2.1, the linear transfer function can be approximated using the knowledge that the transfer function of each transconductance amplifier is

$$I_{\mathrm{out}} = g_{\mathrm{m}} * \left(V_{+} - V_{-}\right). \tag{2.10}$$

For a small signal analysis, we treat the DC references V_{ref1} and V_{ref2} as virtual ground, then the three output currents from the transconductance amplifiers is:

$$I_1 = g_{\mathrm{m1}} V_{\mathrm{in}}, \tag{2.11}$$

$$I_2 = g_{\mathrm{m2}} \left(V_{\mathrm{x}} - V_{\mathrm{bp}}\right), \tag{2.12}$$

$$I_3 = g_{\mathrm{m3}} \left(0 - V_{\mathrm{bp}}\right). \tag{2.13}$$

The voltage V_{x} is determined by the capacitance at the node being charged by the output current from g_{m2} since the inputs of the transconductance draw essentially no current. That is,

$$V_{\mathrm{x}} = \left(\frac{1}{sC_2}\right) g_{\mathrm{m3}} \left(-V_{\mathrm{bp}}\right), \tag{2.14}$$

where $\frac{1}{sC_2}$ is the Laplace transform for the node V_{x}. Similarly, the node V_{bp} is described as

$$\begin{aligned} V_{\mathrm{bp}} &= Z_{\mathrm{C_1}} \left(I_1 + I_2\right) && (2.15) \\ &= \left(\frac{1}{sC_1}\right)\left(g_{\mathrm{m1}}V_{\mathrm{in}} + g_{\mathrm{m2}}\left(-V_{\mathrm{bp}}\right)\left(1 + \frac{g_{\mathrm{m3}}}{sC_2}\right)\right) && (2.16) \\ &= V_{\mathrm{in}}\left(\frac{g_{\mathrm{m1}}}{sC_1}\right)\left[1 + \frac{g_{\mathrm{m2}}}{sC_1} + \frac{g_{\mathrm{m2}}g_{\mathrm{m3}}}{s^2C_1C_2}\right]^{-1}. && (2.17) \end{aligned}$$

This leads to a transfer function of

$$\begin{aligned} H(s) = \frac{V_{\mathrm{bp}}}{V_{\mathrm{in}}} &= \left(\frac{g_{\mathrm{m1}}}{sC_1}\right)\left[1 + \frac{g_{\mathrm{m2}}}{sC_1} + \frac{g_{\mathrm{m2}}g_{\mathrm{m3}}}{s^2C_1C_2}\right]^{-1} && (2.18) \\ &= \frac{s\left(\frac{g_{\mathrm{m1}}C_2}{g_{\mathrm{m2}}g_{\mathrm{m3}}}\right)}{s^2\left(\frac{C_1C_2}{g_{\mathrm{m2}}g_{\mathrm{m3}}}\right) + s\left(\frac{C_2}{g_{\mathrm{m3}}}\right) + 1} && (2.19) \end{aligned}$$

2.2 Nonlinear

In the real world, one would be hard-pressed to find a linear filter, especially if an active filter is being considered. In a simple sense, nonlinearity is experienced when the output of a system does not vary in direct proportion to its input, e.g. a diode. More strictly, one need only to check if the system is linear using the criterion from the previous section, if it is not linear then one may state that it is nonlinear. When dealing with active filters, the nonlinearity of the core amplifiers can dictate the performance of the filter system. There are a multitude of nonlinearities that can come into play based on magnitude or frequency of the system as outlined in the Table 2.1.

Table 2.1: Types of Nonlinearity

Magnitude	**Frequency**
Saturation	Jump resonance
Dead zone	Limit cycle
Friction	Harmonics
Backlash	Chaotic behavior
Relay	Self excitation

For the purposes of this dissertation, the consideration of saturation nonlinearity is sufficient.

2.2.1 Saturating Nonlinearity

A common method for approximating the nonlinearity in a system is to use a describing function, in this subsection, the derivation of a describing function for saturation is presented. Given the characteristic curve in Fig. 2.2, with an input excitation of

$$X(t) = X\sin(\omega t), \tag{2.20}$$

the output is thusly defined as:

$$Y(t) = AX\sin(\omega t), \qquad \text{for } 0 \leq \omega t \leq \beta \tag{2.21}$$

$$Y(t) = As, \qquad \text{for } \beta \leq \omega t \leq \pi - \beta \tag{2.22}$$

$$Y(t) = AX\sin(\omega t), \qquad \text{for } (\pi - \beta) \leq \omega t \leq \pi. \tag{2.23}$$

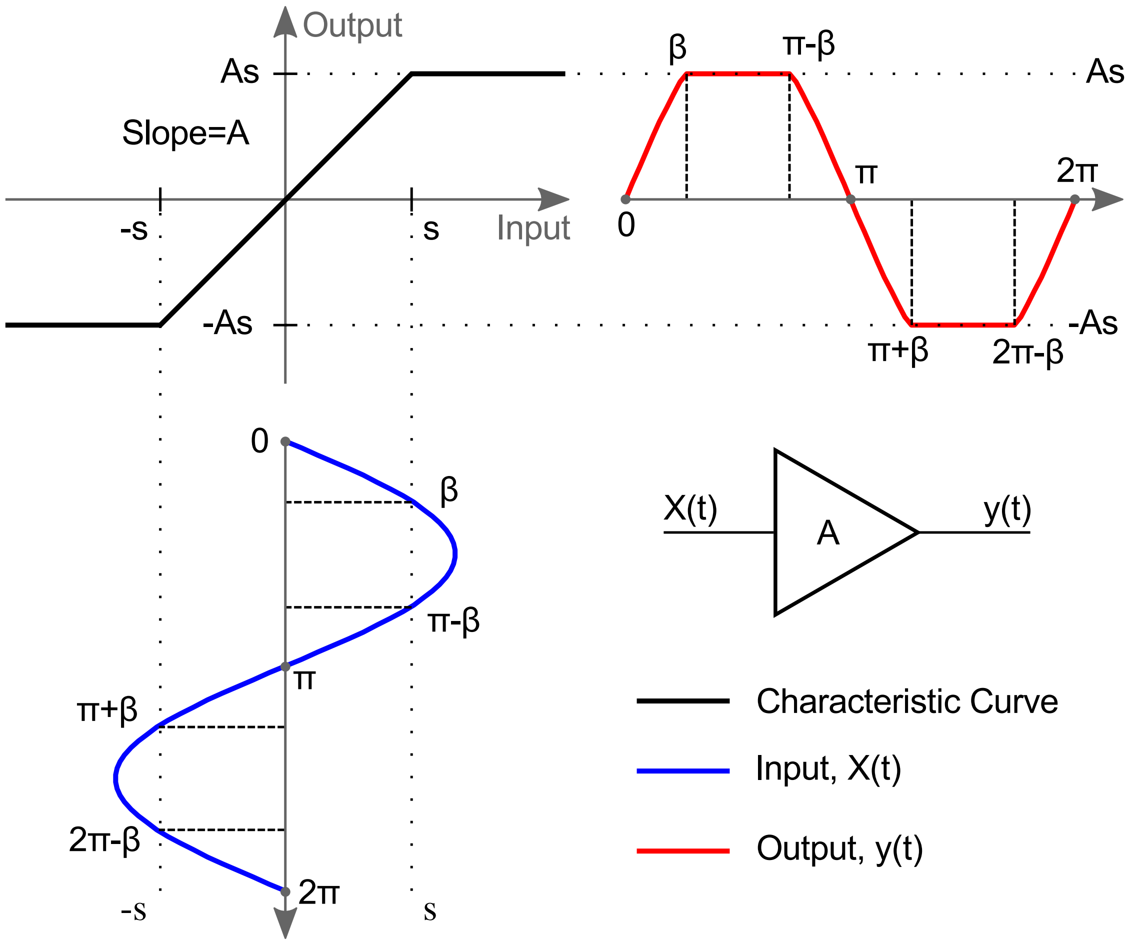

Figure 2.2: The characteristic curve of a saturating nonlinearity and the approximate output for a sinusoidal input.

When considering the Fourier series,

$$f(x) \approx \frac{a_0}{2} + \sum_{n=1}^{\infty} a_{\mathrm{n}} \cos\left(\frac{2\pi}{L}nx\right) + b_{\mathrm{n}} \sin\left(\frac{2\pi}{L}nx\right), \tag{2.24}$$

the coefficients can be calculated as

$$\begin{aligned} a_1 &= \frac{1}{\pi}\int_0^{2\pi} y(t)\cos(\omega t)\, d(\omega t) && (2.25) \\ &= 0 && (2.26) \end{aligned}$$

$$
\begin{aligned}
b_1 &= \frac{1}{\pi}\int_0^{2\pi} y(t)\sin(\omega t)\ d(\omega t) && (2.27)\\
&= \frac{4}{\pi}\int_0^{\pi/2} y(t)\sin(\omega t)\ d(\omega t) && (2.28)\\
&= \frac{1}{\pi}\left[\int_0^{\beta} AX\sin^2(\omega t)\ d(\omega t) + \int_{\beta}^{\pi/2} As\sin(\omega t)\ d(\omega t)\right] && (2.29)\\
&= \frac{4A}{\pi}\left[\frac{X\beta}{2} - \frac{X}{4}\sin(2\beta) + s\cos(\beta)\right] && (2.30)\\
&= \frac{2AX}{\pi}\left[\beta + 2\frac{S}{X}\cos(\beta) - \sin(\beta)\cos(\beta)\right]. && (2.31)
\end{aligned}
$$

With the further knowledge that

$$
\begin{aligned}
AX\sin(\omega t) &= As,\ \text{if } \omega t = \beta && (2.32)\\
\Rightarrow \sin &= \frac{As}{AX} && (2.33)\\
\Rightarrow \beta &= \sin^{-1}\left(\frac{s}{X}\right), && (2.34)
\end{aligned}
$$

The coefficient b_1 is further simplified to

$$
b_1 = \frac{2AX}{\pi}\left[\sin^{-1}\left(\frac{s}{X}\right) + 2\frac{S}{X}\cos\left(\sin^{-1}\left(\frac{s}{X}\right)\right) - \sin\left(\sin^{-1}\left(\frac{s}{X}\right)\right)\cos\left(\sin^{-1}\left(\frac{x}{X}\right)\right)\right] \tag{2.35}
$$

$$
= \frac{2AX}{\pi}\left[\sin^{-1}\left(\frac{s}{X}\right) + \left(\frac{s}{X}\right)\sqrt{1 - \left(\frac{s}{X}\right)^2}\right]. \tag{2.36}
$$

Further, the phase angle of the describing function is $\angle \tan^{-1}\left(\frac{a_1}{b_1}\right) = \angle 0°$. Thus, the final describing function, $N = \frac{b_1}{X}\angle 0°$ is

$$\frac{2A}{\pi}\left[\sin^{-1}\left(\frac{s}{X}\right) + \left(\frac{s}{X}\right)\sqrt{1-\left(\frac{s}{X}\right)^2}\right]\angle 0°. \tag{2.37}$$

2.3 Boundary Curves

For a simple filter system that is comprised of a linear filter block and a nonlinear saturating element that depends on the input magnitude and frequency, as depicted in Fig. 2.3, we can gain an insight into how the saturating nonlinearity will affect a filter system's response.

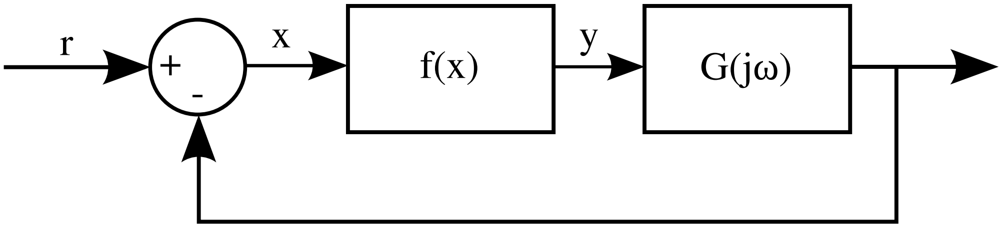

Figure 2.3: A block diagram of a simple nonlinear filter feedback system, with linear filter $G(j\omega)$ and nonlinearity $f(x)$.

To begin the analysis, we must make some assumptions, namely: (a) the system shown in Fig. 2.3 is stable; (b) the linear block G($j\omega$) is frequency dependent and amplitude independent; (c) the nonlinearity f(x) is single-valued, odd, continuously differentiable, and frequency independent; (d) higher harmonics are suppressed by G($j\omega$) and f(x) creates negligible harmonics [21, 22, 23]. We assume that the input signal is sinusoidal, as before (2.20).

Based on the aforementioned assumptions, the resulting output at x should be periodic and of the form:

$$x(t) = Xsin(\omega t + \phi). \tag{2.38}$$

To evaluate the nonlinear feedback system that is driven by a periodic input, without resorting to complicated nonlinear analysis, the describing function (2.37) is written in the general form [24, 25, 26]

$$N(X) = \xi(X) + j\eta(X) \tag{2.39}$$

Also without delving into the specific transfer function, $H(j\omega)$, of the linear filter block, the general form is used.

$$H(j\omega) = \frac{1}{G(j\omega)} = h_r(j\omega) + jh_i(j\omega) \tag{2.40}$$

Equations (2.41-2.43) show the analysis in the Laplace domain for finding the output at x, as it relates to the input r.

$$X(s) = \quad R(s) - G(s)Y(s) \tag{2.41}$$

$$Y(s) = \quad N(s)X(s) \tag{2.42}$$

$$X(s) = \quad R(s) - N(s)G(s)X(s) \tag{2.43}$$

Using the result from (2.43) and plugging in (2.39) and (2.40) to find the closed-loop transfer function gives:

$$\frac{Xe^{j\theta}}{Re^{j\theta}} = \frac{1}{1+N(X)G(j\omega)} \tag{2.44}$$

$$= \frac{1}{1+N(X)H^{-1}(j\omega)} \tag{2.45}$$

$$= \left(\frac{H(j\omega)+N(X)}{H(j\omega)}\right)^{-1}. \tag{2.46}$$

Squaring (2.46) will remove the dependence on complex terms and will result in the amplitude of the transfer function; i.e.,

$$\left(\frac{R}{X}\right)^2 = \frac{(h_r(\omega)+\xi(X))^2 + (h_i(\omega)+\eta(X))^2}{h^2{}_r(\omega)+h^2{}_i(\omega)}. \tag{2.47}$$

Since we have assumed that f(x) will be single-valued, the condition for nonlinear behavior to occur is dependent on the input signal. For a constant input frequency ($d\omega = 0$), the input amplitude of r will correspond to the amplitude at x when the describing function (2.39) is continuously differentiable, and the point of the first jump will occur at $\partial R/\partial E|_{d\omega=0} = 0$, since a change in output does not require a change of the input. Previous research [27, 28, 29, 30] has shown that a sufficient condition for the sudden change in output amplitude and phase is as follows:

$$\left.\frac{\partial R}{\partial X}\right|_{d\omega=0} \leq 0. \tag{2.48}$$

Evaluating the partial derivative of (2.47) requires solving the following expression:

$$2(h^2{}_r + h^2{}_i)R\frac{\partial R}{\partial X} = X^2((h_r+\xi(X))^2 + (h_i+\eta(X))^2). \tag{2.49}$$

The partial derivative of $X^2(h_r + \xi(X))^2$ can be solved independently as:

$$\begin{aligned}\frac{\partial X^2(h_r+\xi(X))^2}{\partial X} &= X^2\left(\frac{\partial}{\partial X}(h_r+\xi(X))^2\right) \\ &\quad +(h_r+\xi(X))^2\left(\frac{\partial}{\partial X}(X^2)\right) \qquad (2.50)\\ &= X^2\left[2(h_r+\xi(X))\left(\frac{\partial}{\partial X}h_r+\xi(X)\right)\right] \\ &\quad +2X(h_r+\xi(X))^2 \qquad (2.51)\\ &= 2X^2(h_r+\xi(X))\frac{\partial \xi}{\partial X} \\ &\quad +2X(h_r+\xi(X))^2. \qquad (2.52)\end{aligned}$$

A result similar to (2.52) can be found for the h_i and $\eta(X)$ terms, both of which can be applied to (2.49) to write the partial derivative as:

$$\begin{aligned}2({h^2}_r+{h^2}_i)R\frac{\partial R}{\partial X} &= 2X\left[(h_r+\xi(X))X\frac{\partial \xi}{\partial X}\right. \\ &\quad +(h_i+\eta(X))X\frac{\partial \eta}{\partial X}+(h_r+\xi(X))^2 \\ &\quad \left.+(h_i+\eta(X))^2\right] \qquad (2.53)\end{aligned}$$

Furthermore, by using the algebraic manipulation (2.54), the equation in (2.53) can be rewritten as (2.55).

$$\begin{gathered}(h_r+\xi(X))X\frac{\partial \xi}{\partial X}+(h_r+\xi(X))^2 = \\ \left(h_r+\xi(X)+\frac{X}{2}\frac{\partial \xi}{\partial X}\right)-\left(\frac{X}{2}\frac{\partial \xi}{\partial X}\right)^2\end{gathered} \qquad (2.54)$$

$$
\begin{aligned}
({h^2}_r + {h^2}_i)R\frac{\partial R}{\partial X} = \quad & X\left[-\left(\frac{X}{2}\frac{\partial \xi}{\partial X}\right)^2 - \left(\frac{X}{2}\frac{\partial \eta}{\partial X}\right)^2\right. \\
& + \left(h_r + \xi(X) + \frac{X}{2}\frac{\partial \xi}{\partial X}\right) \\
& \left. + \left(h_i + \eta(X) + \frac{X}{2}\frac{\partial \eta}{\partial X}\right)\right] \qquad (2.55) \\
= \quad & X\left[-\frac{(\xi - \gamma_1)^2 + (\eta - \gamma_2)^2}{4}\right. \\
& + \left(h_r + \frac{\xi + \gamma_1}{2}\right)^2 \\
& \left. + \left(h_i + \frac{\eta + \gamma_2}{2}\right)^2\right] \qquad (2.56) \\
& \qquad (2.57)
\end{aligned}
$$

To simplify the equation (2.55) to (2.56), the terms from (2.58) and (2.59) were used.

$$\gamma_1 = \xi + X\frac{\partial \xi}{\partial X} \tag{2.58}$$

$$\gamma_2 = \eta + X\frac{\partial \eta}{\partial X} \tag{2.59}$$

Taking care to define variables ρ, p_1, and p_2, such that ρ relates to a radius, while p_1 and p_2 define a center point of the form $p_1 + jp_2$, one will find that,

$$\rho = \frac{1}{2}\sqrt{(\xi - \gamma_1)^2 + (\eta - \gamma_2)^2} \tag{2.60}$$

$$p_1 = \frac{-1}{2}(\xi + \gamma_1)\ ,\ p_2 = \frac{-1}{2}(\eta + \gamma_2). \tag{2.61}$$

The final expression that guarantees the presence of a nonlinearity, according to the condition set forth in (2.48), is thus,

$$(h_1 - p_1)^2 + (h_i - p_2)^2 \leq \rho^2. \tag{2.62}$$

From which we can conclude that the point where the left-hand side of (2.62) is equal to the right-hand side is when an abrupt change in output amplitude and phase will occur for, virtually, no change in input signal. Graphically, this is the point, on the complex plane, for which any H($j\omega$) loci intersects the boundary circle defined by p_1, p_2, and ρ. In terms of the frequency of the jump, it is at frequency ω_j when the following equation is satisfied,

$$\partial R/\partial X|_{\omega=\omega_j} = \rho \tag{2.63}$$

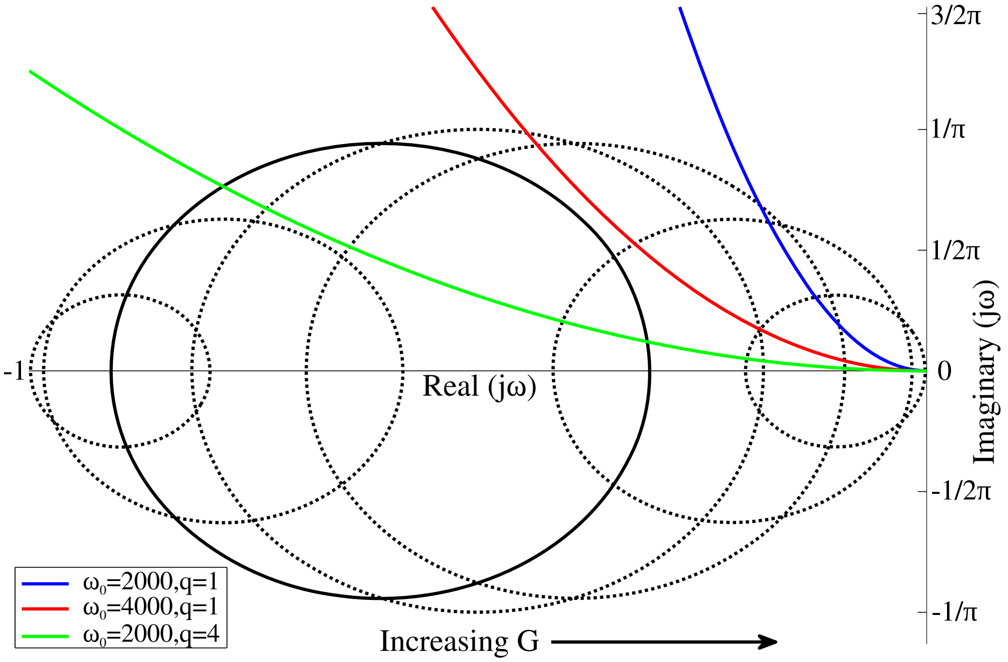

Figure 2.4: A set of typical boundary curves using saturation as the nonlinear function $f(x)$ plotted against the s-domain filter response $H(j\omega)$.

It should be noted that each p_1, p_2 pair will have a corresponding ρ value; when evaluating the intersection points graphically, there will be several circles that could intersect H($j\omega$). Because f(x) is assumed to be single-ended, these boundary circles will be symmetric with respect to the real axis. A saturating nonlinearity, which has ordinates equal to zero for all points of interest, will create boundary curves of the type shown in Fig. 2.4, using the linear filter responses shown in Fig. 2.5. An estimated nonlinear filter response using the linear filters from Fig. 2.5 and the boundary curve shown in solid black in Fig. 2.4 is given in Fig. 2.6.

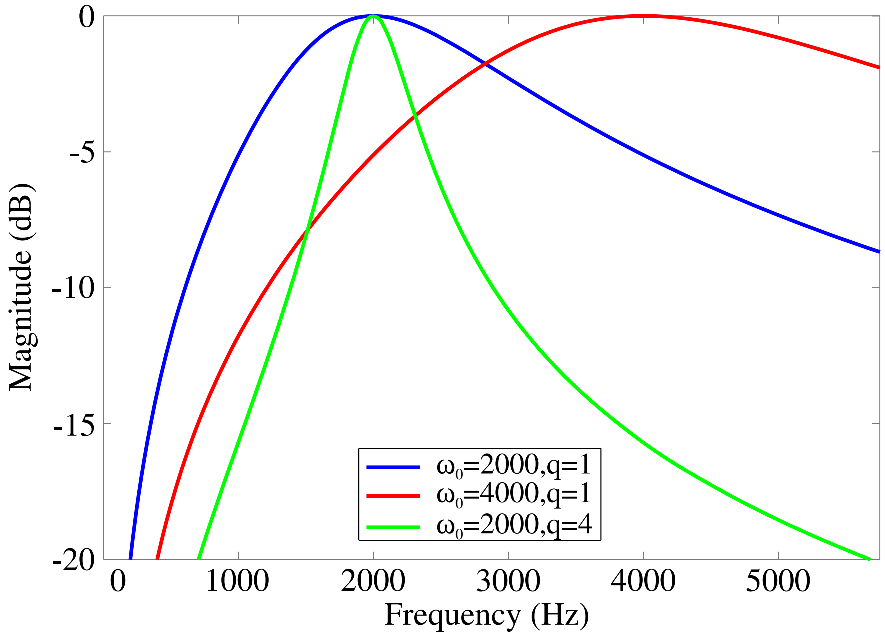

Figure 2.5: The linear filter component ($G(j\omega)$ of Fig. 2.3) response from the analysis presented in Fig. 2.4.

Since the condition (2.62) is $\leq$, jumps may also occur when the H($j\omega$) trace is within the boundary of a circle. Considering a transfer function of a bandpass filter, a higher quality factor will require a smaller input amplitude to drive a system to become nonlinear, as is shown in Fig. 2.4 [31]. The filter tuned to a higher center frequency of 4,000 rad/s was close

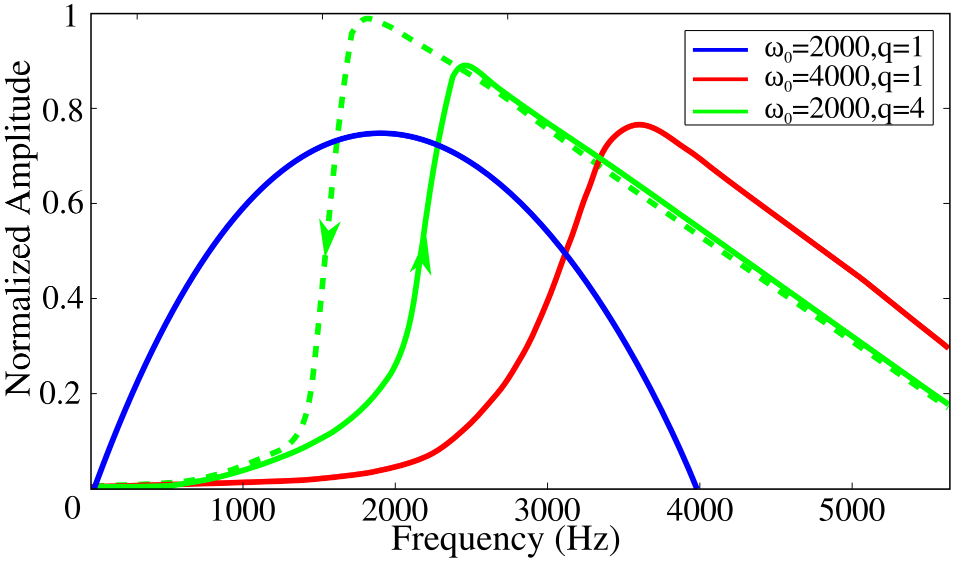

Figure 2.6: The estimated nonlinear filter response of Fig. 2.3 when considering a saturation nonlinearity as $f(x)$ and the linear filter $G(j\omega)$ as given in Fig. 2.5.

to the boundary curve, but did not pass through it, therefore it begins to present a shark-fin-like response, but does not exhibit the nonlinearity of jump resonance. The conditions set forth in the preceeding analysis do not guarantee the existence of jump resonance (or other nonlinearities), rather the conditions must be met if the nonlinearity is to exist.

Chapter 3

Jump Resonance

3.1 Motivation

Jump resonance is a phenomenon observed in nonlinear circuits where the output can exhibit abrupt variations for a continuous, well-behaved, periodic input signal [27, 32]. The phenomenon has been observed and studied extensively in nonlinear control systems and in analog filters [31] where jump-resonance leads to a hysteresis behavior when the frequency of the input signal is varied. This is illustrated in Fig. 3.1 where the output signal magnitude is not only a function of the input signal frequency, but also a function of the direction of the frequency sweep. Thus, for frequencies within the hysteresis band defined by $\omega_1 < \omega < \omega_2$, the magnitude of the output signal could have two possible magnitudes depending on the frequency trajectory. Current-mode analog-filters that are biased in weak-inversion are typically susceptible to artifacts due to jump-resonance. This is due to the fact that sub-threshold biasing hinders the filter's inherent inability to respond rapidly to the given input signal [33]. This may be because the magnitude of the input signal exceeds the filter's linear range, or that the frequency of the input signal varies more quickly than the slewing ability of the filter's active circuit elements.

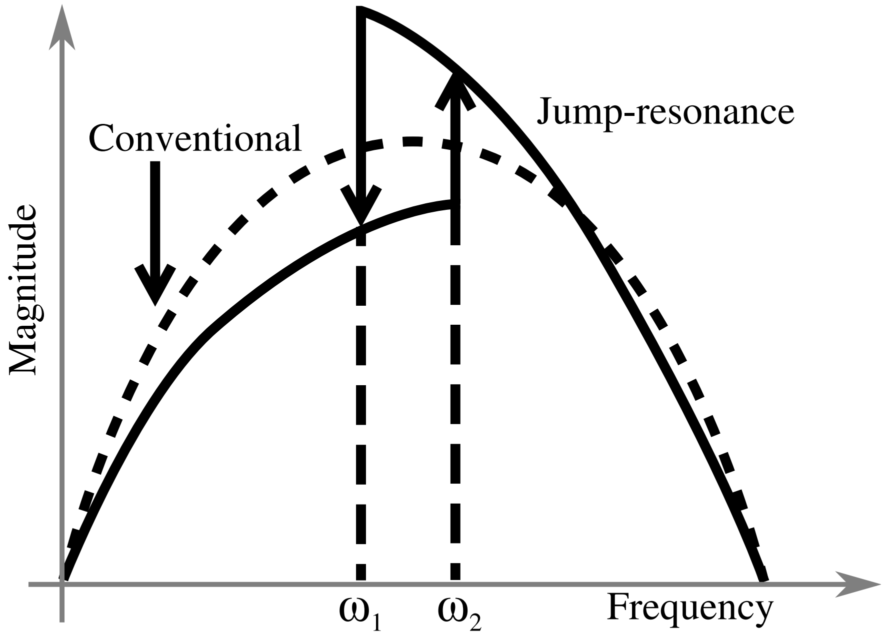

Figure 3.1: Illustration of a band-pass response exhibiting jump-resonance and its comparison with a conventional band-pass response.

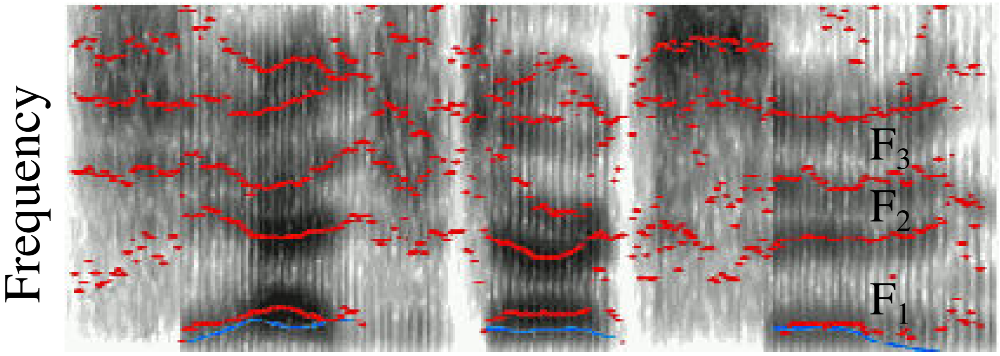

Figure 3.2: Spectrogram of a sample speech utterance showing frequency or formant trajectories.

In the design of auditory front-ends (AFEs) like the silicon cochlea, such a filter response has been considered undesirable and several methods have been proposed to predict and remedy jump-resonance artifacts [33, 27]. However, the hysteretic response with respect to the direction of the frequency sweep could be used as a computational tool for encoding formant trajectory in speech signal. Formants in speech signal correspond to the resonant frequencies of the vocal tract, in particular, when vowels are pronounced. Fig. 3.3(b) shows

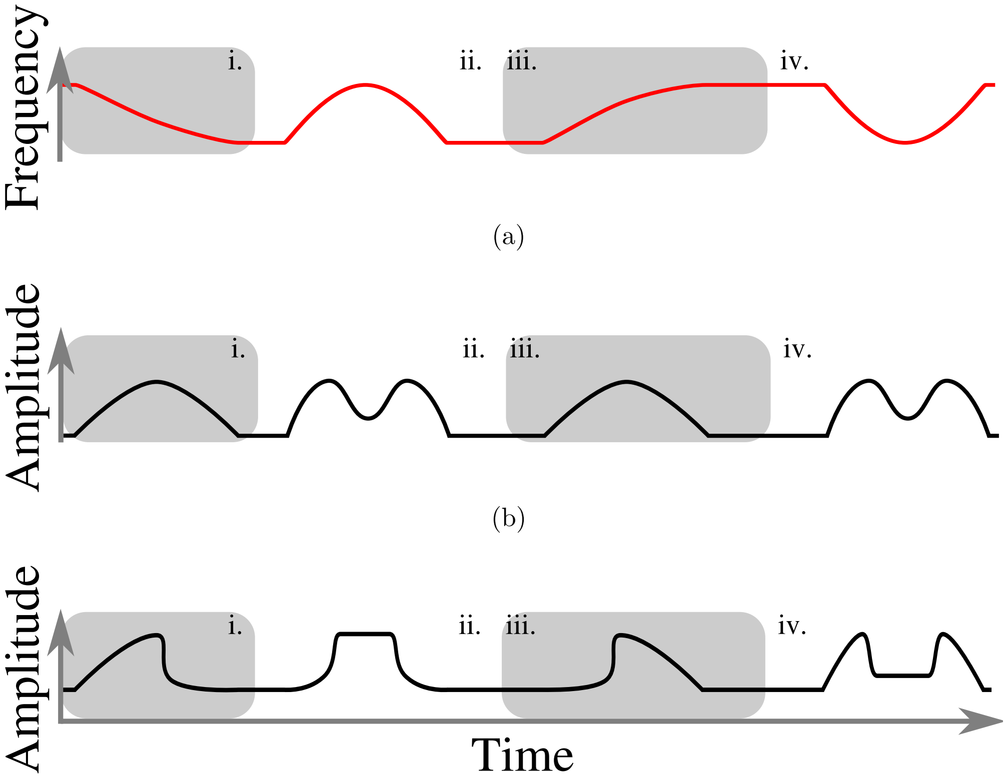

(a)

(b)

(c)

Figure 3.3: (a) Sample format trajectories during a phonetic utterance in English language. For the sample trajectory: (b) response expected from a conventional band-pass filter; and (c) response expected from the filter exhibiting jump-resonance for the sample trajectories.

the location of three formant frequencies (F1, F2 and F3) on a spectrogram. Trajectory of formants over time (as shown in Fig. 3.3(b)) are particularly relevant for speaker recognition because they are indicator of the mechanical dynamics of the vocal tract and that these signatures are robust to corruption by ambient noise [35]. For example, Fig. 3.4 and Fig. 3.5 show example trajectories of the formants F1 and F2 corresponding to different English vowels and corresponding to male and female speakers. Conventional auditory front-ends for speaker recognition extract formant trajectories by complementing the output of the filter-banks by Δ, or velocity features, and by $\Delta\Delta$, or acceleration features, which have been hypothesized as being capable of capturing infrasonic signatures [36]. Using digital signal processing, the process of extracting Δ and $\Delta\Delta$ features entails a linear and a quadratic

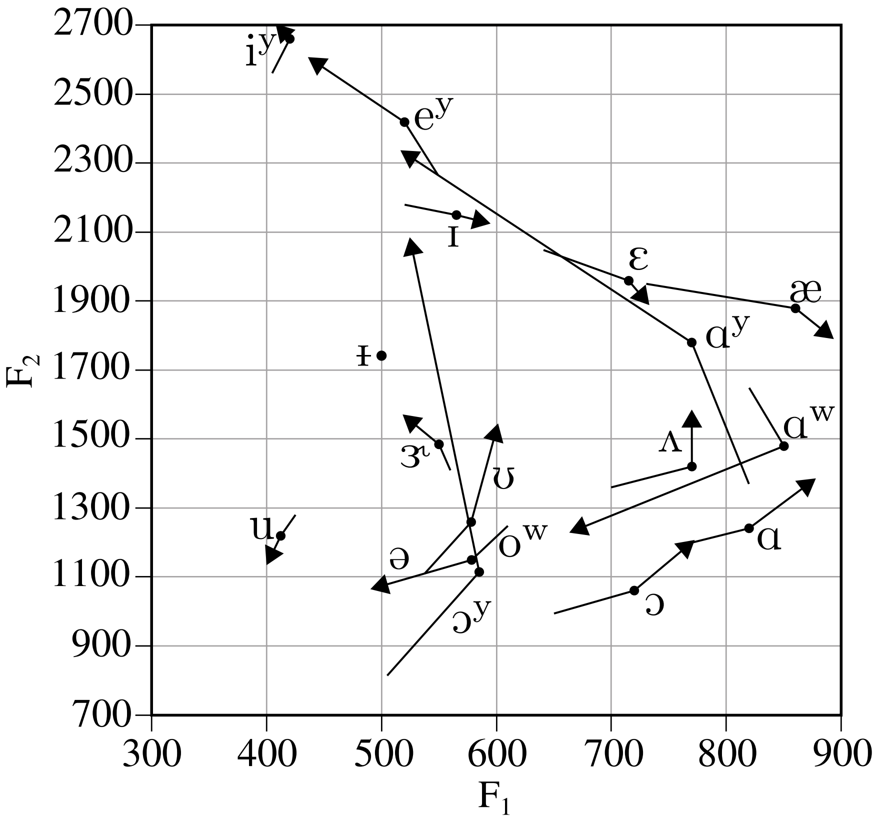

Figure 3.4: Vowel formant trajectories for female speakers, recreated from data in [34].

regression over the filter-bank output. However, for analog signal processors like the ones used in silicon cochlea [37, 38], computing Δ and ΔΔ features is prohibitively complex and inaccurate. In this regard, exploiting jump-resonance based hysteresis in analog filters could be an attractive method in augmenting the output of a conventional silicon cochlea with formant trajectory information. Fig. 3.3(b) illustrates an example of this principle using different formant trajectories in a spectrogram of a typical speech utterance; and Fig. 3.3(c) shows a stylization of some of these trajectories. Also shown in Fig. 3.3(d)–(e) are the comparisons of expected outputs that will be produced by a conventional auditory filter that does not exhibit jump-resonance versus the output produced by similar filter exhibiting jump-resonance. For instance the output produced by the conventional filter in regions ii and iv (see Fig. 3.3(d)) are identical even though the frequency trajectories in these regions

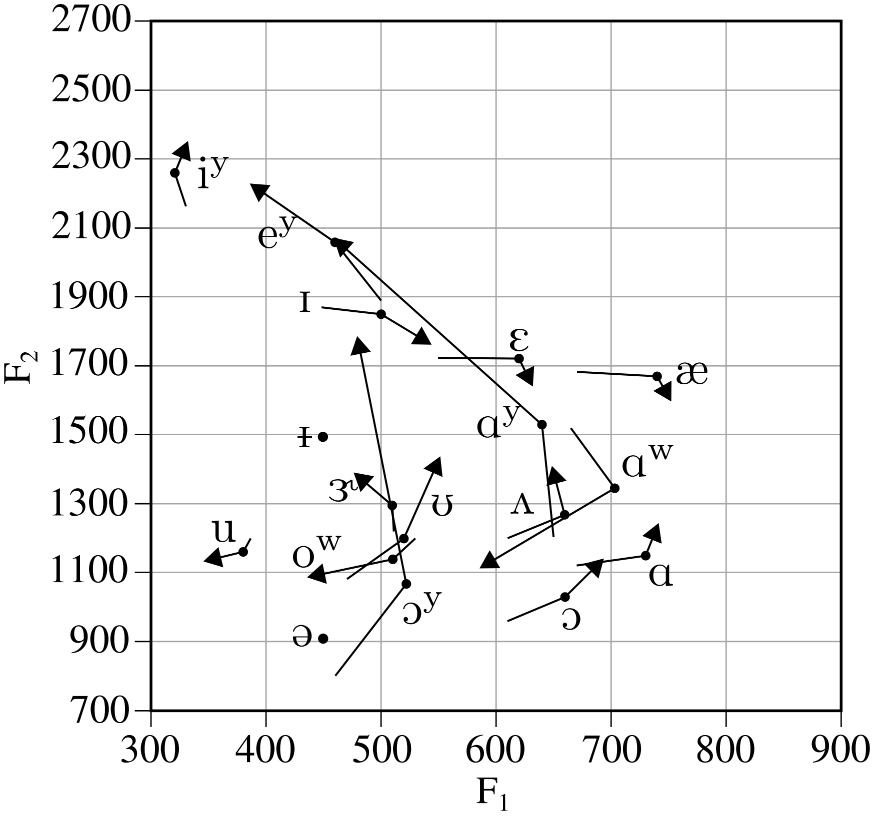

Figure 3.5: Vowel formant trajectories for male speakers, recreated from data in [34].

(see Fig. 3.3(c)) is different. However, this is not the case for the output produced by the jump-resonance filters (see Fig. 3.3(e)). Thus, the illustration shows that jump-resonance could lead to output signatures that are unique to the frequency trajectory and hence could be useful in providing more discriminatory information to a back-end speech or speaker recognition system.

The hysteresis in the filter response caused by the jump-resonance may improve the performance of speaker recognition, as small variations of spectral content caused by a hoarse voice or other voice modulations don't have to result in large changes in the output [39]. It is theorized that by varying the width of the hysteresis region, one may also control how large of a variation in spectral content is required before there is a significant change in the output signal. The use of hysteresis in silicon auditory front-ends is also of interest, due to this similarity to the mechanical hysteresis phenomenon observed in animal cochlea. Research conducted on gerbils has revealed that the cochlea exhibits a nonlinear transducer function that exhibits a sigmoid-shaped hysteresis loop with counterclockwise traversal [40]. Further research has also suggested that the transducer nonlinearity in humans would be similar or possibly more pronounced than the results obtained from gerbils [41]. There are many studies that indicate biological systems have jump resonance hysteresis, and they serve as an inspiration to employed similar tactics in silicon filters, with the goal of improving speaker recognition system performance.

3.2 Jump Resonance Criteria for $G_\mathrm{m}C$ilter

A general criteria that must be satisfied for the existence of a jump resonance nonlinearity considering an amplifier with a saturating nonlinearity was presented earlier in Section 2.3, based on the simple filter of Fig. 2.3. Here, we present a derivation of the jump resonance criteria in a G$_m$-C filter of Fig. 3.6.

In this configuration, the biquad filter consists of linear transconductors with transconductances g_{m1}, g_{m2} and g_{m3} and a transfer function, as dereived earlier in 2.1.1, of

$$G(j\omega) = \frac{V_o(s)}{V_i(s)} = \frac{G\frac{\omega_0}{Q}s}{s^2 + \frac{\omega_0}{Q}s + {\omega_0}^2}. \tag{3.1}$$

The center-frequency (ω_0), quality-factor (Q) and filter-gain G can be expressed in terms of g_{m1},g_{m2} and g_{m3} as

$$Q = \sqrt{\frac{g_{m2}}{g_{m3}}} \tag{3.2}$$

$$\omega_0 = \frac{\sqrt{g_{m2} \times g_{m3}}}{C} \tag{3.3}$$

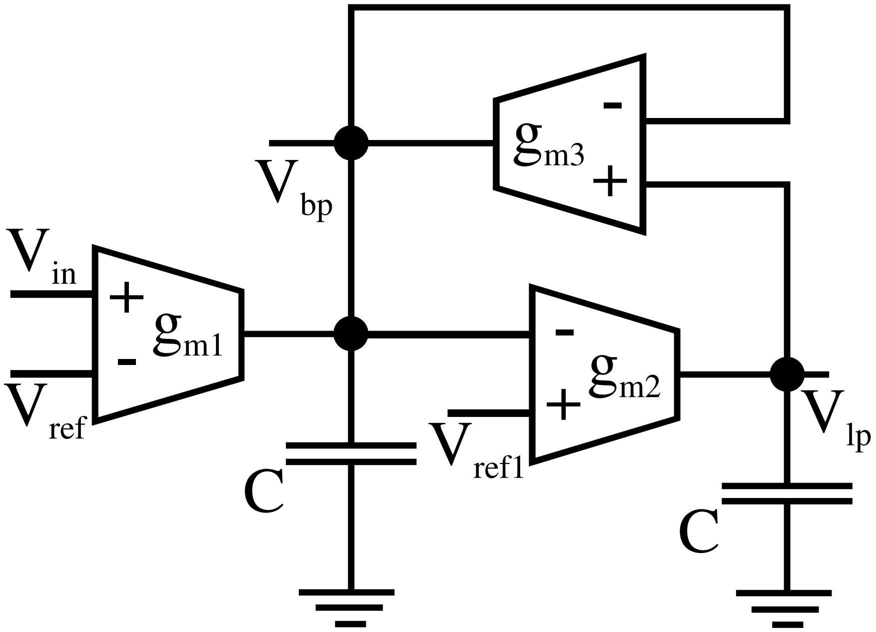

Figure 3.6: A schematic representation of a biquad filter implementation using transconductance amplifiers.

$$G = \frac{g_{m1}}{g_{m3}}. \tag{3.4}$$

As we explained in the previous chapter, any practical amplifier, i.e. transconductors, will exhibit a nonlinear saturating response due to their finite input-output dynamic range. Therefore, a closed-form analysis of the circuit presented in Fig. 3.6 becomes troublesome and an approximation using graphical techniques is preferred; here we use the describing function approach from literature [24, 25, 26]. The assumption that only g_{m2} exhibits a saturating nonlinearity is made to simplify the analysis, and the second-order system transfer function of (3.1) is decomposed into the feedback architecture of Fig. 3.7. Thus, Fig. 3.6 is modeled as a linear filter combined with a nonlinear element g_{m2}, which conforms to a classical topology encountered in non-linear control systems. The linear portion of the architecture is a low-pass filter that attenuates higher-order harmonics generated by the non-linear element. Note that when g_{m2} is assumed to be linear, the system transfer function reduces exactly to (3.1).

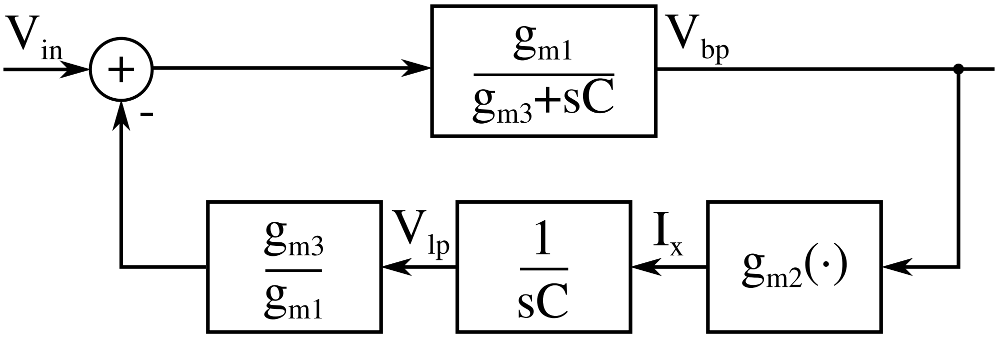

Figure 3.7: Signal-flow diagram for Fig. 3.6 to analyze nonlinear artifacts in the biquad filter.

The describing function method linearizes the operation of g_{m2} in the frequency domain, where the dynamics of the system can be analyzed at a specific frequency ω. Let the signal at the input of the transconductor g_{m2} be denoted by $V_{bp}\sin(\omega t)$; the output current be denoted by $I_x \sin \omega t$; and the signal at the input of the system be denoted by $V_{in}\sin(\omega t+\beta)$. Here we have assumed that the non-linearity in g_{m2} is frequency independent and hence does not introduce any phase-shifts. Therefore, I_x and V_{bp} are related through the non-linearity as:

$$\frac{I_x}{V_{in}} = N(V_{bp})\frac{V_{bp}}{V_{in}}, \tag{3.5}$$

where $N(V_{bp})$ is the frequency independent describing function and is only a function of signal amplitude V_{bp}.

Also, I_x, V_{bp} and V_{in} are related to each other through the linear portion of the system as

$$\begin{aligned}\frac{V_{bp}}{V_{in}} =& \left|\frac{g_{m1}}{g_{m3}+j\omega C}\right|\sqrt{1-\left(\frac{I_x g_{m3}}{V_{in}\omega C g_{m1}}\sin\left(\theta_1-\frac{\pi}{2}\right)\right)^2} \\ &-\left|\frac{g_{m1}}{g_{m3}+j\omega C}\right|\frac{I_x g_{m3}}{V_{in}\omega C g_{m1}}\cos\left(\theta_1-\frac{\pi}{2}\right)\end{aligned} \tag{3.6}$$

A more detailed look into the derivation of this relationship is in the subsequent subsection.

To get an insight on how jump-resonance is introduced by the non-linearity due to g_{m2}, we will assume a simplistic saturation non-linear model shown in Fig. 2.2. The describing function for the model is well known [42, 43, 44] and can be expressed as:

$$N(V_{bp}) = \begin{cases} g_{m2} & , V_{bp} \leq \delta \\ \left(\frac{g_{m2}}{\pi}\right)(2\alpha + \sin(2\alpha)) & , V_{bp} > \delta \end{cases} \tag{3.7}$$

$$\text{where} \quad \alpha = \sin^{-1}\left(\frac{\delta}{V_{bp}}\right). \tag{3.8}$$

The loci corresponding to (3.6) is plotted in Fig. 3.8 as the frequency ω is varied. Also plotted are the curves corresponding to (2.37), for the case when g_{m2} is linear and for the case when g_{m2} exhibits a saturating non-linearity corresponding to Fig. 2.2. The intersection between the two curves represents the solution (I_x, V_{bp}) obtained at a frequency ω. For instance, the point P_1 is the system solution at frequency ω_1. As the frequency is increased the intersection point traverses P_2 and P_3. For the linear system, as the frequency is increased the magnitude of the output reaches a maximum at P_4 (frequency ω_4) and then decreases as the frequency is increased. This response is illustrated in the magnitude plot shown in Fig. 3.9. The response is typical of a band-pass biquad filter with center-frequency ω_4. For the non-linear system, the initial system trajectory is similar to that of the linear system but deviates from P_3 as equations (3.6) and (2.37) become tangential to each other. At this point, the system exhibits a jump to the solution Q_3 after which the magnitude reduces as the frequency is increased further. This is the jump-resonance phenomenon and can be clearly seen in the filter magnitude response in Fig. 3.9. The hysteresis due to jump-resonance can be understood by following the trajectory of the solution for the non-linear case in Fig. 3.8. As the frequency is reduced, the solution moves to S_4, after which the curves given by equations (3.6) and (3.7) become tangential to each other. As a result the solution exhibits another jump which is larger than the previous. This is illustrated in the filter magnitude response, which shows the hysteresis introduced by jump-resonance.

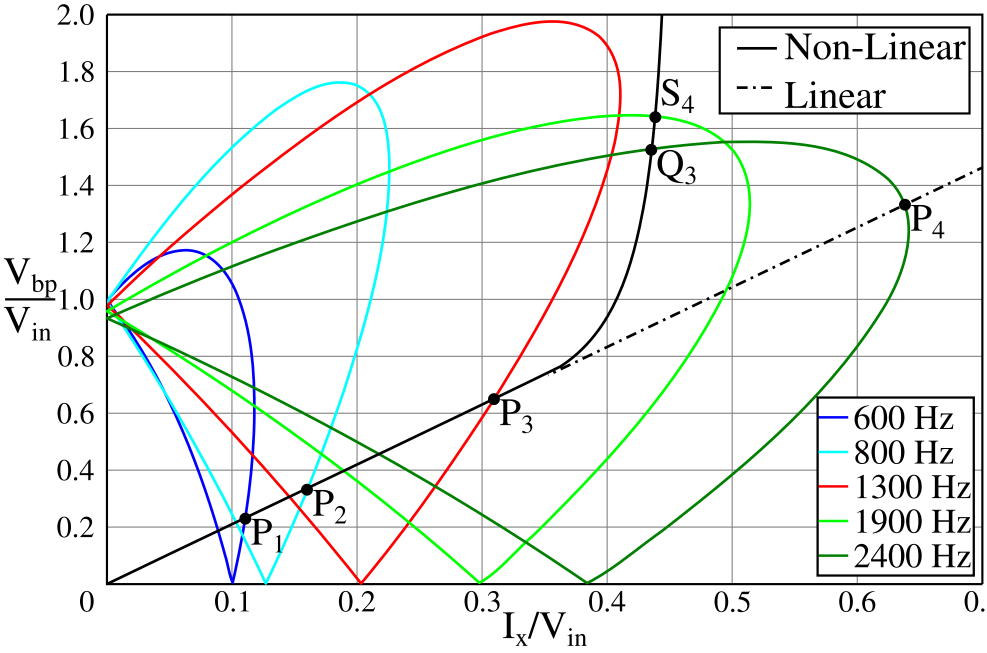

Figure 3.8: Plot showing the loci of a describing function based solution, as frequency of operation is varied.

3.2.1 I_x, V_{bp} and V_{in} Relationship

From the system given in Fig. 2.3, one can write V_{bp} as:

$$V_{bp}\sin(\omega t) = V_{in}\left|\frac{g_{m1}}{g_{m3}+j\omega C}\right|\sin(\omega t+\theta_1+\beta) - \\ I_x\left|\frac{g_{m1}}{g_{m3}+j\omega C}\right|\frac{g_{m3}}{\omega C g_{m1}}\sin(\omega t+\theta_1-\frac{\pi}{2}). \quad (3.9)$$

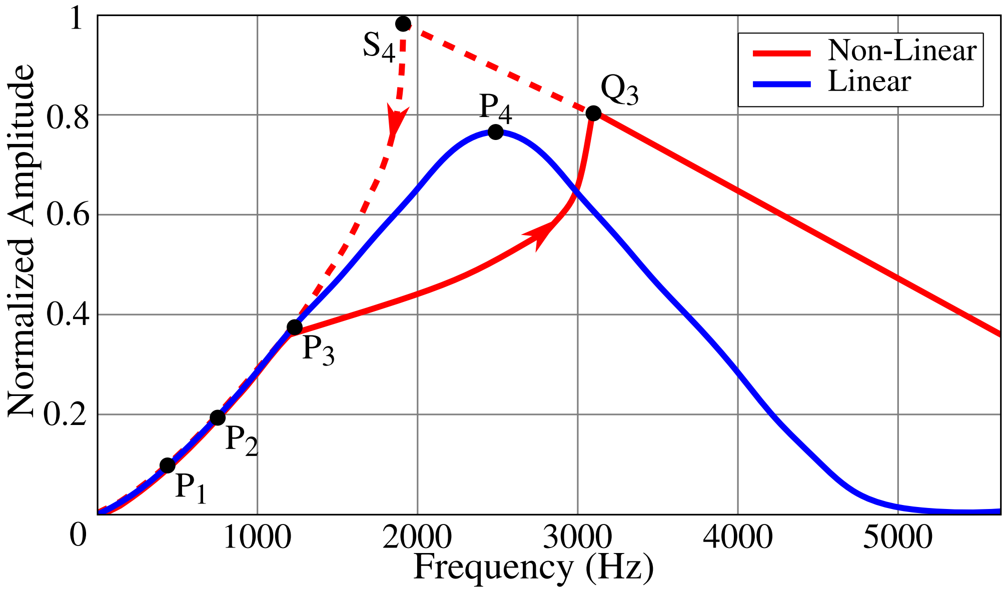

Figure 3.9: From the loci in Fig. 3.8, a magnitude response plot is generated for a linear and nonlinear biquad filter

This statement assumes that the system is stable, the linear response is frequency dependent and amplitude independent, and that the higher harmonics are relatively suppressed in the linear filter [21, 22, 23]. The term β is due to the phase offset in the input, $V_{in}\sin(\omega t+\beta)$. θ_1 is the phase of the filter $\frac{g_{m1}}{g_{m3}+j\omega C}$.

By multiplying both sides of (3.9) with $\sin(\omega t)$ and integrating with respect to $t \in [0\ ,\ \frac{2\pi}{\omega}]$, we find that

$$\begin{aligned} V_{bp} = V_{in}\left|\frac{g_{m1}}{g_{m3}+j\omega C}\right|\cos(\theta_1+\beta) - \\ I_x\left|\frac{g_{m1}}{g_{m3}+j\omega C}\right|\frac{g_{m3}}{\omega C g_{m1}}\cos(\theta_1-\frac{\pi}{2}). \end{aligned} \tag{3.10}$$

Similarly, by multiplying both sides of (3.9) with $\cos(\omega t)$ and integrating, we get

$$\begin{aligned} 0 = V_{in} &\left|\frac{g_{m1}}{g_{m3}+j\omega C}\right| \sin(\theta_1+\beta) - \\ I_x &\left|\frac{g_{m1}}{g_{m3}+j\omega C}\right| \frac{g_{m3}}{\omega C g_{m1}} \sin(\theta_1 - \frac{\pi}{2}). \end{aligned} \tag{3.11}$$

From (3.10) and (3.11), one can eliminate the variable β to simplify the relationship as:

$$\begin{aligned} \frac{V_{bp}}{V_{in}} = &\left|\frac{g_{m1}}{g_{m3}+sC}\right| \left(\frac{I_x g_{m3}}{V_{in} g_{m1} \omega C}\right) \cdot \\ &\left(\sqrt{\left(\frac{V_{in} g_{m1} \omega C}{I_x g_{m3}}\right)^2 - \cos^2(\theta_1)} - \sin(\theta_1)\right). \end{aligned} \tag{3.12}$$

Alternatively, (3.13) can be expressed as:

$$\begin{aligned} \frac{V_{bp}}{V_{in}} = &\left|\frac{g_{m1}}{g_{m3}+j\omega C}\right| \left(\left(\frac{-g_{m3} I_x}{\omega C g_{m1} V_{in}}\right) \cos(\theta_1 - \frac{\pi}{2}) + \right. \\ &\left. \sqrt{1 - \left(\frac{g_{m3}}{\omega C g_{m1}} \left(\frac{I_x}{V_{in}}\right) \sin\left(\theta_1 - \frac{\pi}{2}\right)\right)^2}\right). \end{aligned} \tag{3.13}$$

The nonlinearity of g_{m2} can be analyzed using the describing function shown in Fig. 2.2, and is defined as (3.5). Using these approximations, one can express $\frac{I_x}{V_{in}}$ as $\frac{V_{bp}}{V_{in}} N(V_{bp})$, which takes into account the first order approximation of a saturation nonlinearity. More general methods for analyzing jump criterion of circuits with various types of nonlinearities are presented by other authors [27, 28, 29, 30].

3.3 Architecture of Silicon Implementation

We have designed and prototyped an 11 channel silicon AFE; the architecture and circuit level schematic of a single channel is shown in Fig 3.10, which consists of a band-pass biquad filter. A half-wave rectifier, as shown in Fig. 3.10, computes the energy within the frequency band (determined by the center-frequency and the quality-factor of the biquad filter). The rectifier is implemented using a pMOS diode which based on the polarity of the biquad filter output, steers the current towards a pulse-encoder (first-order continuous-time $\Sigma\Delta$ modulator). The output of the rectifier is maintained at a virtual ground by the feedback amplifier in the pulse-encoder and this reduces the artifacts due to finite output impedance of the transconductor g_{m4}. The pulse-encoder integrates the rectified current to compute a measure of the instantaneous energy of the biquad output. It then encodes the energy signal using pulse-width modulated (PWM) digital spike-trains. The pulses are generated by comparing the integrator output against a reference voltage V_{ref} which is then used to turn ON or OFF the reference current I_{ref} that discharges the integrator. It can be shown that the average of the comparator output tracks the average of the input current, which in this case is the instantaneous energy of the biquad signal. The transconductance g_{m1}, g_{m2} and g_{m3} are tuned by adjusting the bias current of the transcondutors using on-chip current-mode digital-to-analog converters (shown in Fig. 3.10). The micrograph of the prototyped silicon AFE is presented in Fig. 3.11a.

All of the transconductors in the biquad are biased in the weak-inversion region, which easily allows us to observe the jump-resonance phenomenon. In general, transconductors are more susceptible to nonlinear operation than their switched-capacitor or MOSFET-C counterparts, which have larger dynamic ranges, and the current-mode biasing can be used to control the slew-rate of the transconductors. In the mathematical analysis presented in subsection 3.2,

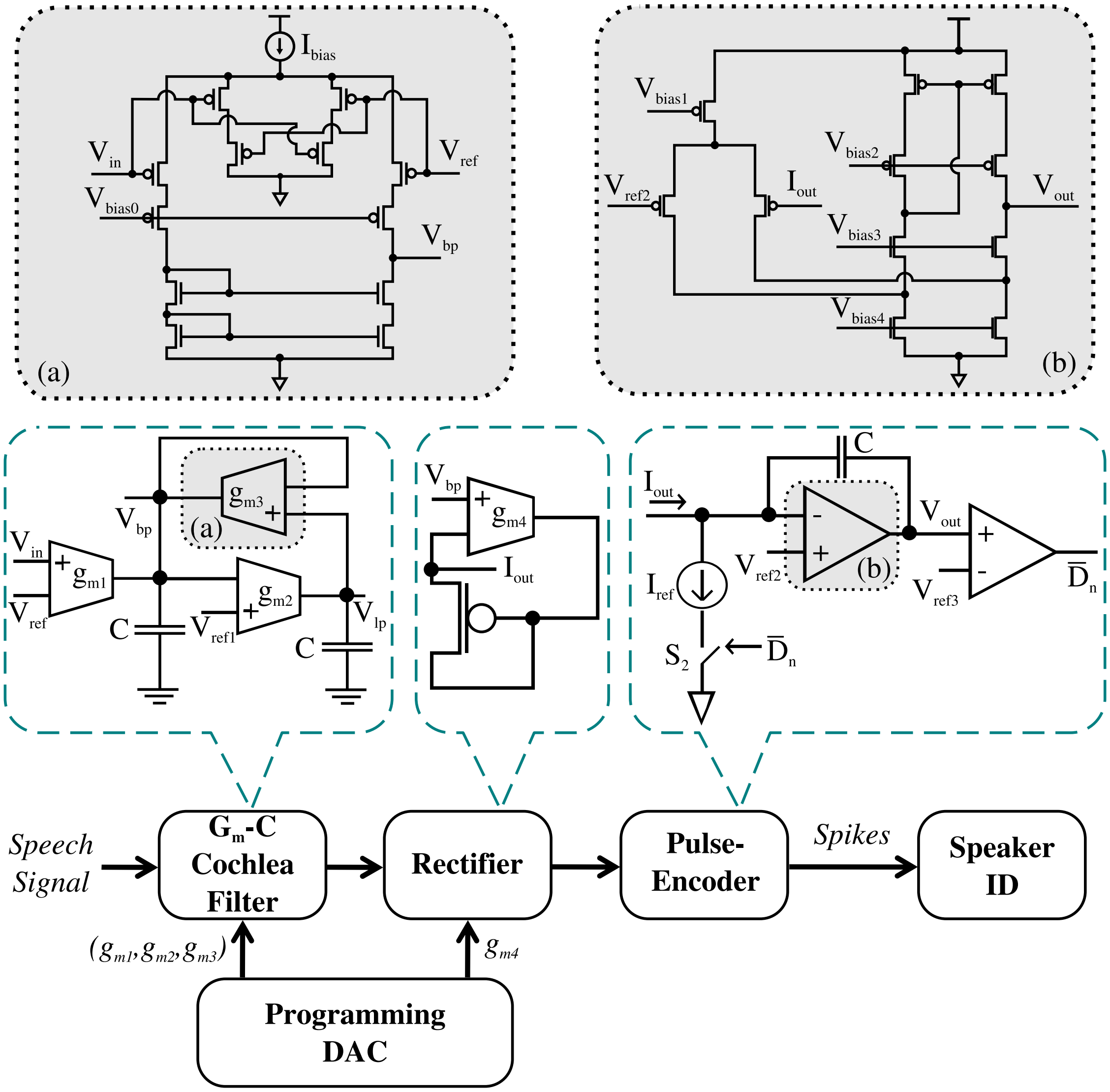

Figure 3.10: System and schematic level architecture of one channel in the silicon auditory front-end. Transistor-level schematics are shown for: (a) transconductor and (b) operational amplifier.

the saturating parameter α of the transconductance g_{m2} was used to introduce non-linearity into the feed-back architecture and hence introduce jump-resonance in the filter-response. The parameter δ could be tuned to change the hysteretic behavior. This is a stable and reliable way of tuning the hysteretic behavior of the filter. However, for the biquad filter topology used for this work (as shown in Fig. 3.10), modulating δ also affects the value of g_{m2},

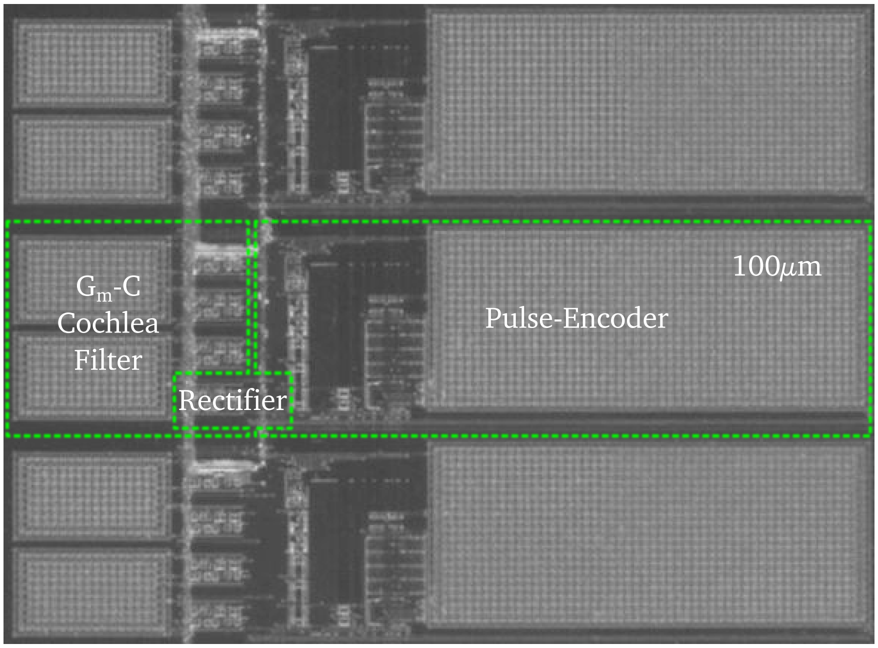

(a)

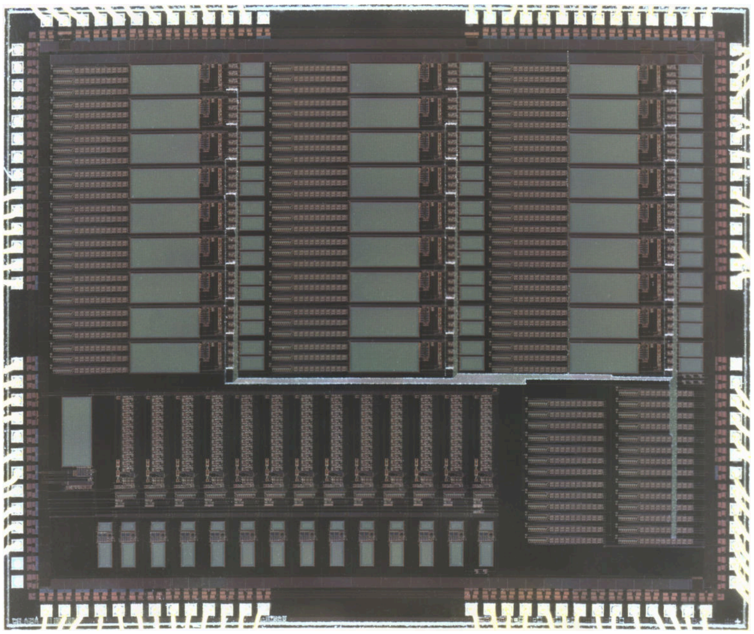

(b)

Figure 3.11: (a) Partial micrograph showing a single channel of the silicon analog front end and (b) the full micrograph of a 27 channel implementation, the first 11 channels are used for this AFE.

which in-turn affects the center frequency and the Quality factor of the filter. Therefore, for this paper we resort to modulating the value of $|V_{bp}|$ to adjust the parameter α. This implies either adjusting the magnitude of the external stimuli V_{in} or adjusting the transconductance g_{m1} to increase the gain of the filter. Since pushing a filter beyond its slew rate enhances the jump-resonance (increases the width of the hysteresis and has sharper transitions), one may also modulate the behavior of jump-resonance through g_{m1}. Therefore, the tuning algorithm for each AFE channel involved the following steps:

1. Set g_{m1} to a low-value using the programming DAC such that all transconductors operate in the linear-region.
2. Adjust g_{m2} and g_{m3} (using DACs) such that the frequency response of the AFE channel has the desired center-frequency and Quality factor. The frequency response of a single channel is measured by applying a chirp signal (magnitude 100mV) with forward and reverse frequency sweeps lasting three seconds. The pulse-encoded output produced by the AFE channel (see Fig. 3.10) is filtered and decimated to obtain the frequency response during the forward and reverse frequency sweeps.
3. For the fixed value of g_{m2} and g_{m3}, increase the value of g_{m1} such that the measured frequency response exhibits jump-resonance hysteresis with a specific hysteretic width.

Note that the accuracy of the calibration procedure is determined by the accuracy of the programming DACs. However, the main motivation of this paper is to investigate the effect of jump-resonance on the performance of a speaker recognition system and future work will investigate filter topologies that can be used to independently tune the hysteretic behavior.

3.4 Measurement Results

Fig. 3.12 shows the measured response obtained from a single channel of the silicon AFE when the frequency of the input sinusoidal signal is first increased (forward-sweep) and when the frequency of the input signal is decreased (reverse-sweep). For this result, we have ensured that all the transconductors operate within the linear range. Therefore, as shown in Fig. 3.12, the responses of both the forward and reverse sweep match, which is expected from an linear biquad filter. Table 3.1 summarizes the measured specification of a single-channel of the fabricated auditory front-end. Note that the filters consume only 3 nW to 30 nW of power depending on the center-frequency and quality-factor of the biquad.

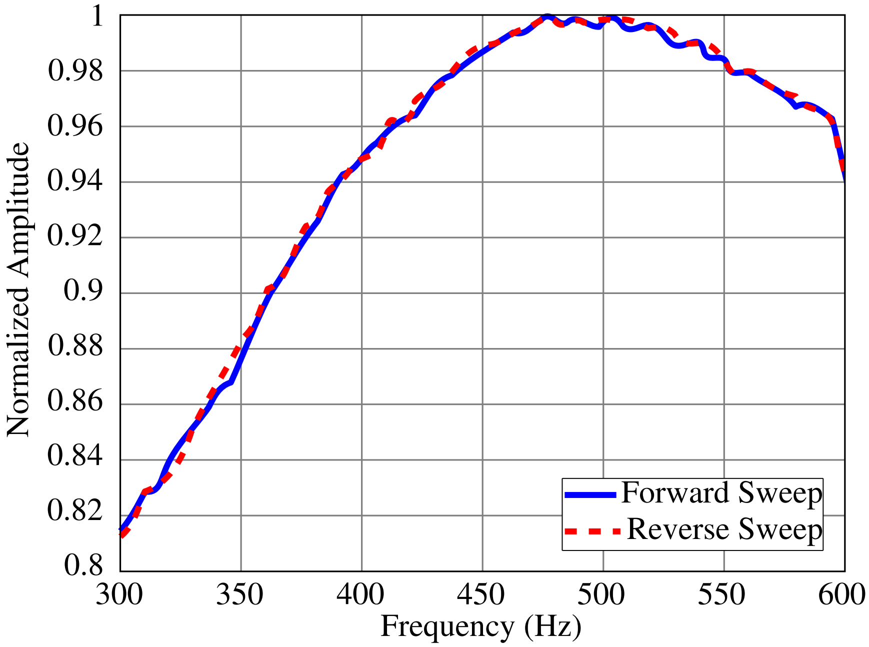

Figure 3.12: Measured response from the biquad filter when biased in the linear region. The frequency of the input signal is swept (i.e. chirp) in the forward (increasing) and reverse (decreasing) direction.

Table 3.1: Design and Measured Specification of Fabricated G$_m$-C Filter

Parameters	**Value**
Technology	0.5 µm CMOS
Supply Voltage	3.3 V
Center-frequency Range	100 Hz – 4 kHz
Input Voltage Range	100 mV
Power Dissipation	3 nW – 30 nW
Capacitance	1.28 pF
Transconductance (design)	0.8 nS – 32 nS
DAC resolution (design)	10 bits
Effective DAC resolution	7 bits

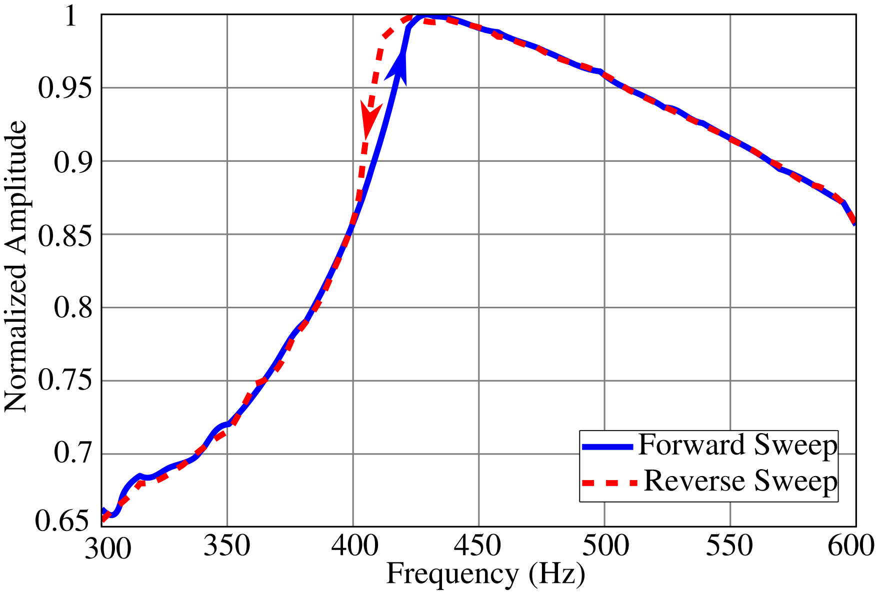

Figure 3.13: Jump resonance obtained when the value of $g_{m1} > g_{m2}$.

Figure 3.13 and Figure 3.14 are the jump-resonances observed in the fabricated front-end for two settings of g_{m1}. Note that the values of the transconductances are adjusted using an on-chip DAC, so in the measured results we can only report the DAC settings or the relative values of g_{m1}. For a lower-value of g_{m1}, the width of the hysteresis region reduces and is shown in Figure 3.13 to be approximately 10Hz. For a larger-value of g_{m1} the width increases to 50Hz demonstrating that the jump-resonance can be effectively controlled. We have verified

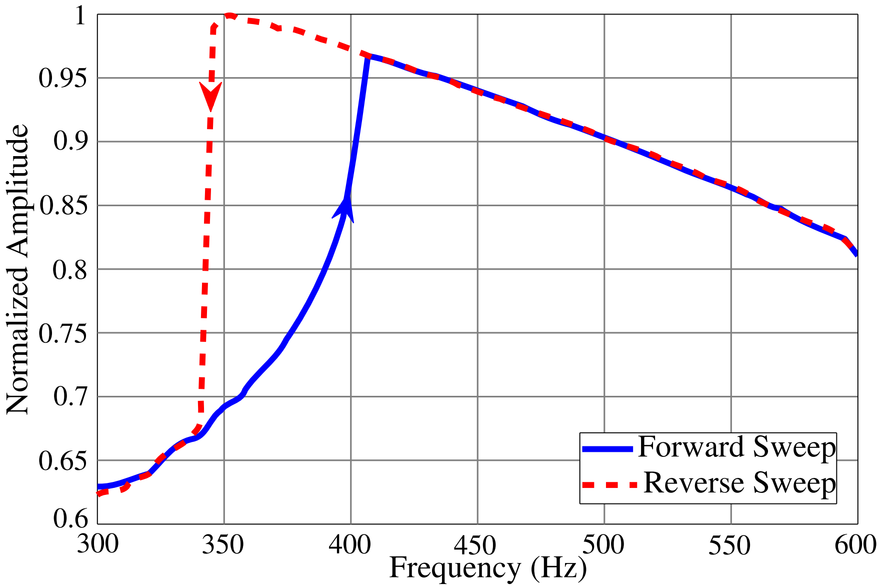

Figure 3.14: Jump resonance obtained when the value of $g_{m1} \gg g_{m2}$.

that the effect is reproducible across multiple experimental runs (for the same channel) and hence does not involve any chaotic phenomena. To obtain these results, we employed an iterative tuning process which increased g_{m1} (using the DACs) from its original value of $g_{m1} = g_{m2}$ (G = 1, according to (3.4)), until the increased gain pushes the biquad filter beyond its linear range of operation. As depicted earlier, by varying the value of g_{m1}, it is possible to effectively control the width of the jump-resonance. However, we would like to point out that the response is sensitive to temperature, implying proper compensation techniques are required to ensure stable operation. Also, when operating in the nonlinear region, where jump-resonance occurs, the filter response is both signal and frequency dependent, and the previously introduced transfer function (3.1) no longer sufficiently describes the filter response. One key difference is that as the input signal amplitude increases, the quality factor of the filter will increase, while the center frequency decreases, which leads to complications in the filter calibration.

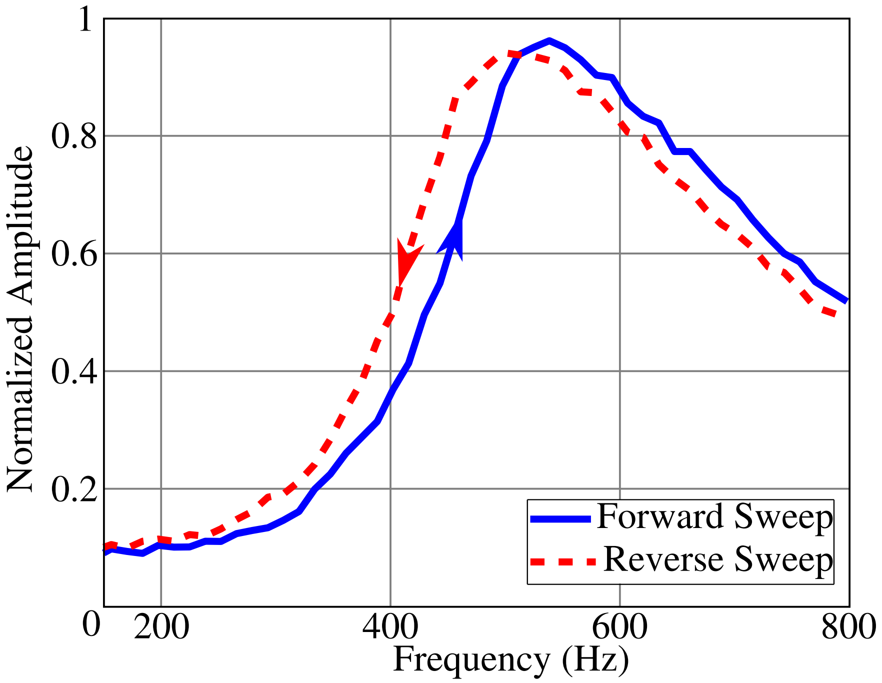

Figure 3.15: Response obtained when jump resonance hysteresis tuned to 15% of the filter center frequency.

Further investigation was conducted to test the amount of mismatch between different channels of the filter bank; channels 1, 2, and 11 were calibrated to a center frequency of 640 Hz, with a hysteresis width of approximately 10%. The tuning response curves are presented in Figure 3.19, with the resulting center frequencies as: 634.02 Hz, 641.55 Hz, and 638.26 Hz for channels 1, 2, and 11, respectively. Due to the resolution and the non-linearity of the programming DACs, the mismatch between the channels is mainly determined by the accuracy of the calibration algorithm, which allows for (± 5%) error. Note that the outputs of the AFE are used for training a back-end recognizer, so certain degree of mismatch is compensated for during the supervised training phase of the speaker recognition system.

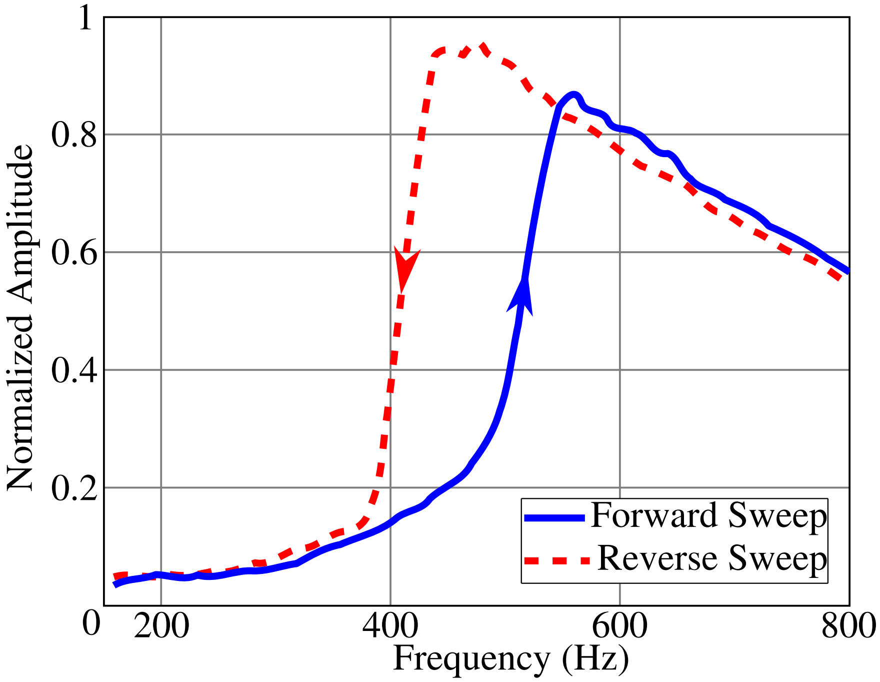

Figure 3.16: Response obtained when jump resonance hysteresis tuned to 30% of the filter center frequency.

3.5 Application to Speaker Recognition

To verify that encoding formant trajectories using jump-resonant hysteresis is beneficial for recognition, we used the output generated by the fabricated silicon AFE to train a speaker recognition system. A YOHO speaker verification database, which consists of sets of four combination lock phrases spoken by 168 speakers, was chosen for training and testing [45, 46]. The experimental set up is shown in Figure 3.20 consisted of a PC based audio system which was used to play each of the YOHO utterances through an audio interface to the silicon AFE. The real-time 11 channel pulse-encoded output from the silicon AFE was recorded using an FPGA and is retrieved back to the PC through a USB interface. The pulse-encoded output were then post-filtered using a moving average window, after which the output was subsampled at a lower-rate to generate a vector of features specific to the utterance [47].

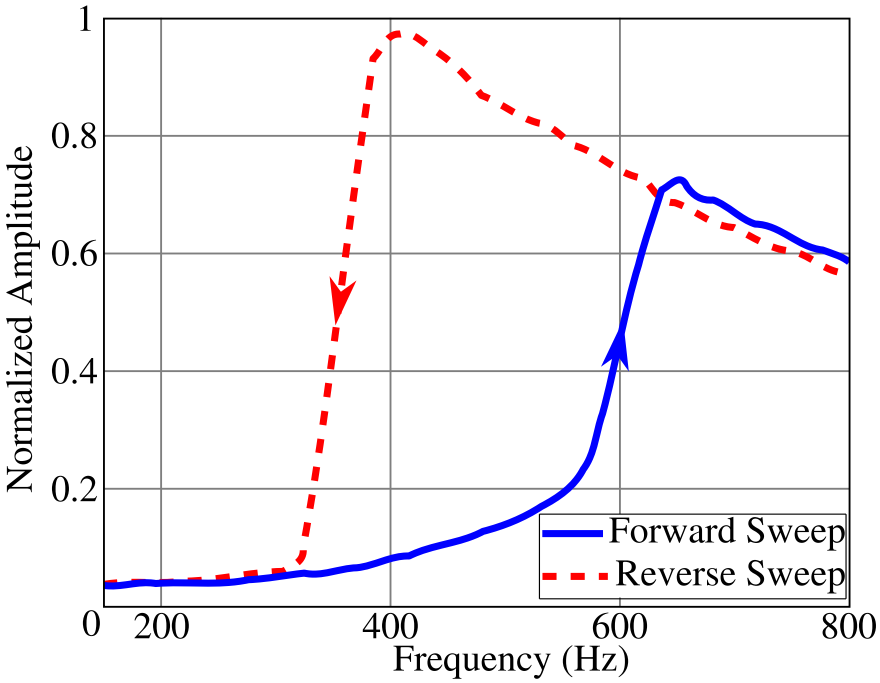

Figure 3.17: Response obtained when jump resonance hysteresis tuned to 60% of the filter center frequency.

Figure 3.21 visually compares the output of the AFE with linear-filters and jump-resonance filters for the utterance "26 · 81 · 57". To demonstrate that jump-resonance can produce features that are markedly different from that of a conventional filter-bank based AFE, we inspect the output of a single filter channel as shown in the Figure 3.22 corresponding to the same speech utterance "26 · 81 · 57". The filters of the channel were tuned to a center frequency of 1.138 kHz. The solid-blue trace is the output of a conventional linear filter, and the red trace is the output of a jump-resonance filter with a 30% hysteresis. The dashed-green trace in Figure 3.22 is obtained after scaling and translating the linear-filter features. While some correlation exists between the two features, the results indicate that the output of the jump-resonance filters are different. As shown in the top-left portion of Figure 3.21, between index 10 and 20 of filter channels two and three, the peak responses are aligned vertically. Observe that the response for the bottom-left portion of Figure 3.21, corresponding to the jump features, does not have peak responses that are aligned vertically.

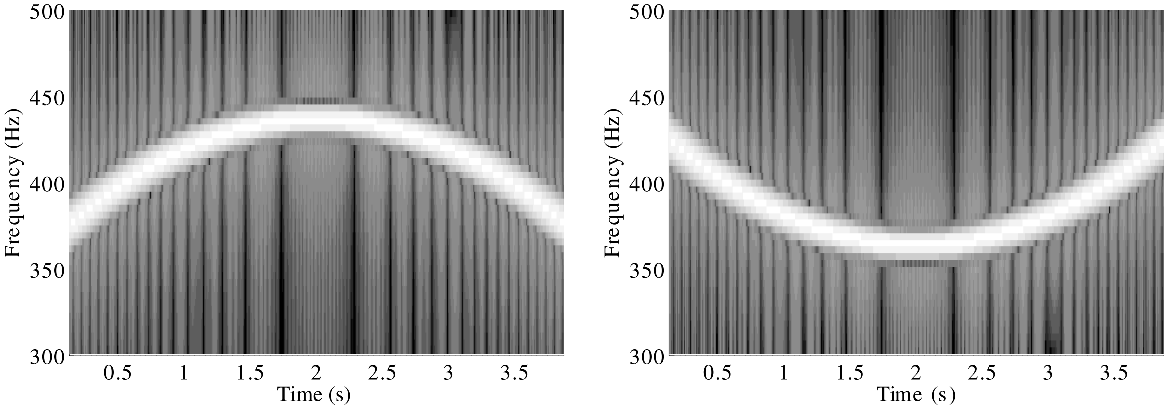

(a) 435 Hz → 365 Hz → 435 Hz

(b) 365 Hz → 435 Hz → 365 Hz

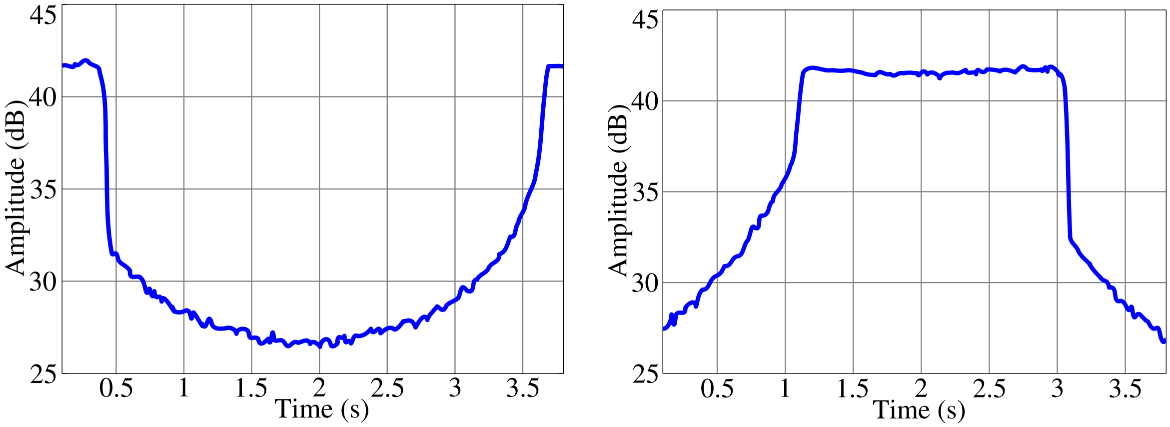

(c) Filter output for Figure 3.18a.

(d) Filter output for Figure 3.18b.

Figure 3.18: Measured responses (c) and (d) from the jump-resonance AFE when signals with different frequency trajectories, shown in (a) and (b) are applied.

Inspecting the original speech signal (in the middle-left of Figure 3.21) between 200 ms and 300 ms at frequencies 200 Hz to 500 Hz, which is roughly the region that would produce the features previously described, shows that there is a high energy speech pattern that spreads in frequency. A similar effect is observed between the index points 70–90 in Figure 3.21, which again shows the local maxima of each filter channel being aligned in time for a linear filter, while there are shifts in the jump-resonance filter. The region in the original signal that would have created these features is approximately between 1.3s and 1.4s, which as shown in Figure 3.21 has a large sweep in frequency content. As theorized earlier, it is possible

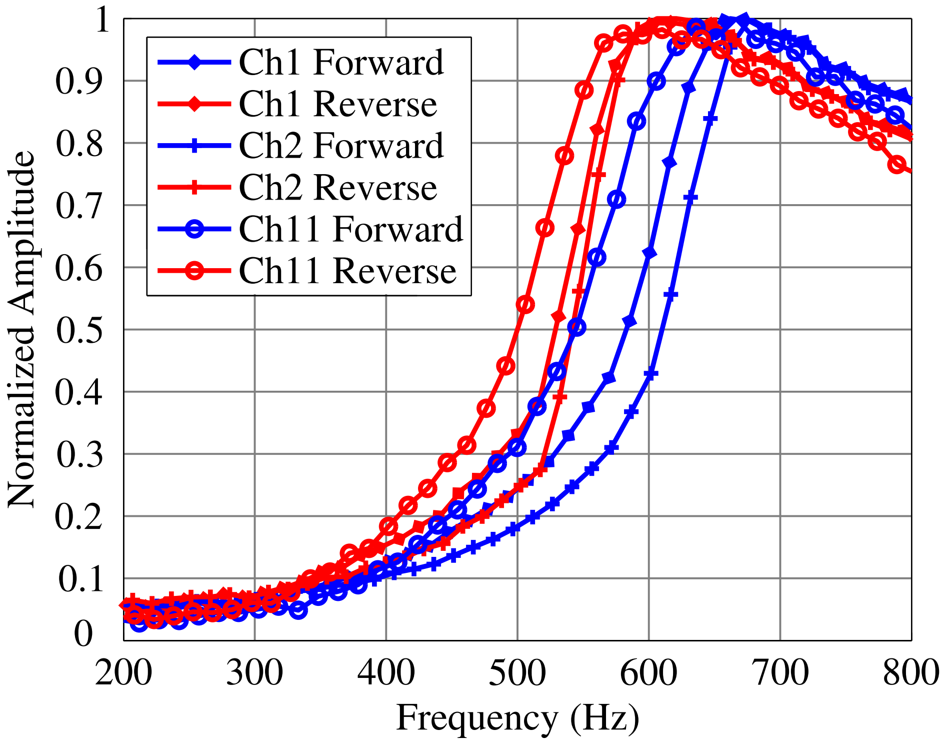

Figure 3.19: Measured jump-resonance responses for different AFE channels tuned to a common center frequency and quality factor.

that using the jump-resonance filtering method does lead to additional information about the frequency trajectory of a signal; it appears that this information is not only apparent through filter responses that favor speech, as shown in Figure 3.18, but it also manifests as a phase offset between the multiple filter channels.

In the next set of experiments, the output of the AFE was used to train an SVM based speaker recognition system, similar tests were done on non-SVM systems [48]. The AFE filters were calibrated to center frequencies that were spaced according the Mel-scale [35, 49]. For training, 10 speakers (speaker ID: 101-110) were chosen from the YOHO database and the AFE features were extracted for all utterances corresponding to each speaker. To reduce the total number of training points, a K-means clustering was performed (starting with a random set of initial points) for each speaker to obtain 1000 cluster points for the

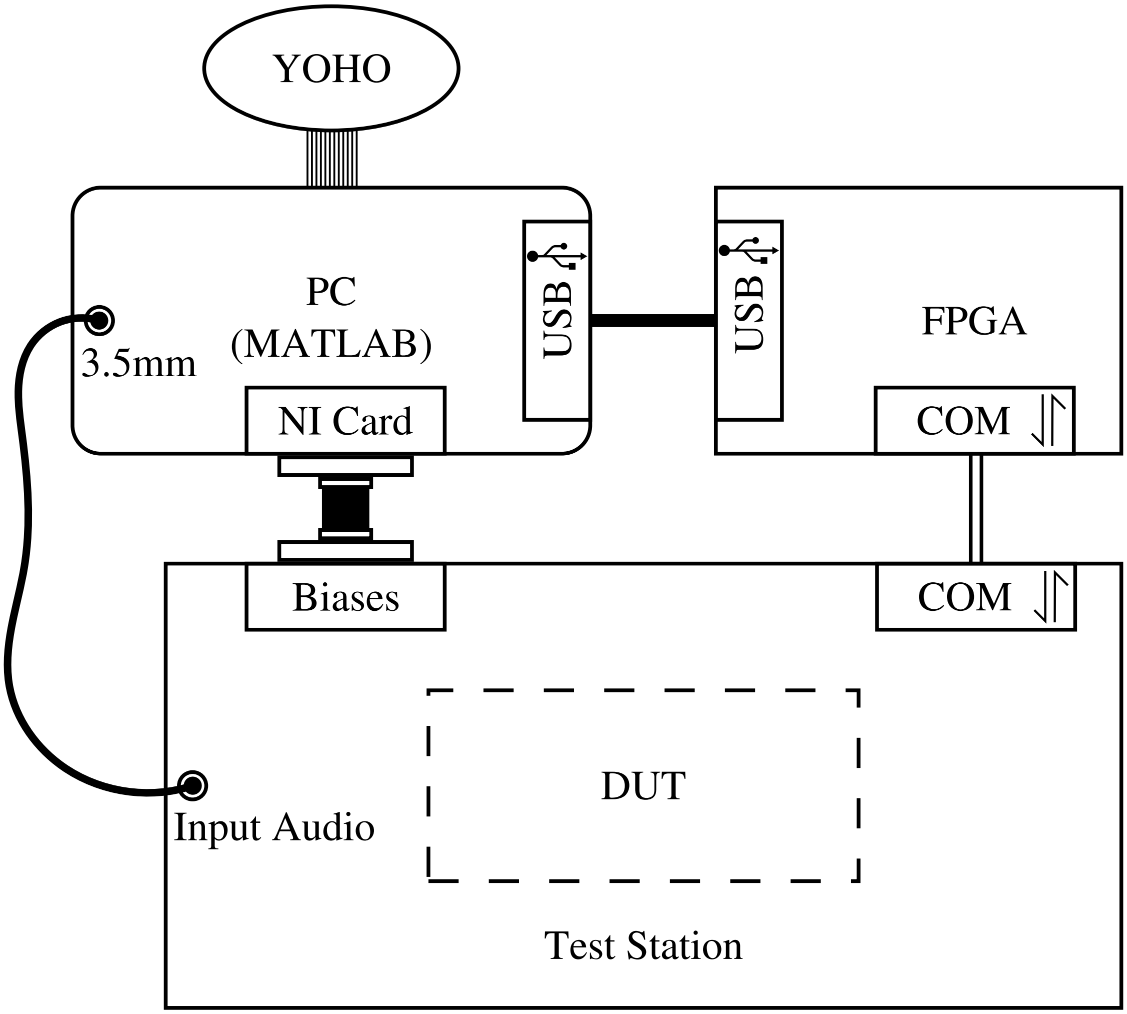

Figure 3.20: The experimental setup used for measurements.

correct speaker, and 100 cluster points for each imposter speaker. For each speaker (101-110), this procedure was repeated to obtain a training set of 10 × 900 AFE feature vectors. A *Gini*-support vector machine (SVM) classifier was trained specific to each speaker using the GiniSVM toolkit (http://www.egr.msu.edu/aimlab/ginisvm). Compared to conventional large-margin SVM, *Gini*-SVM is a multi-class classifier that directly produces an estimate of class conditional probabilities given the speech feature vector. These normalized probability scores can be integrated over several speech frames in an utterance [50] to arrive at global

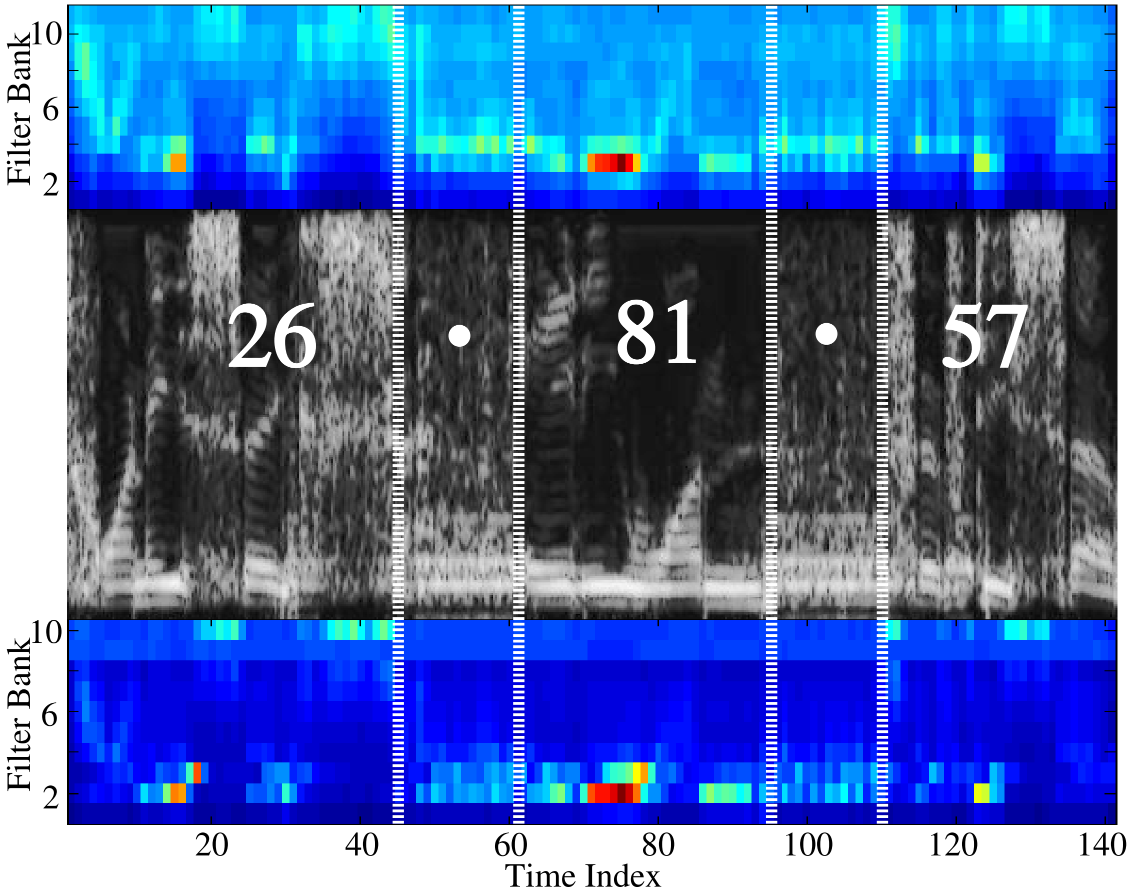

Figure 3.21: Spectrograms from (top) conventional filter bank, (middle) input, and (bottom) jump resonance filters.

acceptance/rejection scores. Even though conventional large-margin SVMs have been successfully applied for the task of speaker verification [51], the cumulative scores generated by SVMs are susceptible to corruption by impulse noise, which increases false acceptance rate. The underlying theory of *Gini*-SVM has been described elsewhere and interested readers are referred to [52] for additional details. 25% of the training data was used for a cross-validation procedure during which the parameters of the *Gini*-SVM classifier were optimized to achieve a pre-determined probability-of-detection (PD) on the cross-validation set.

To evaluate the recognition performance of the trained speaker identification system, utterances corresponding to 10 speakers were chosen from the YOHO test set. These utterances

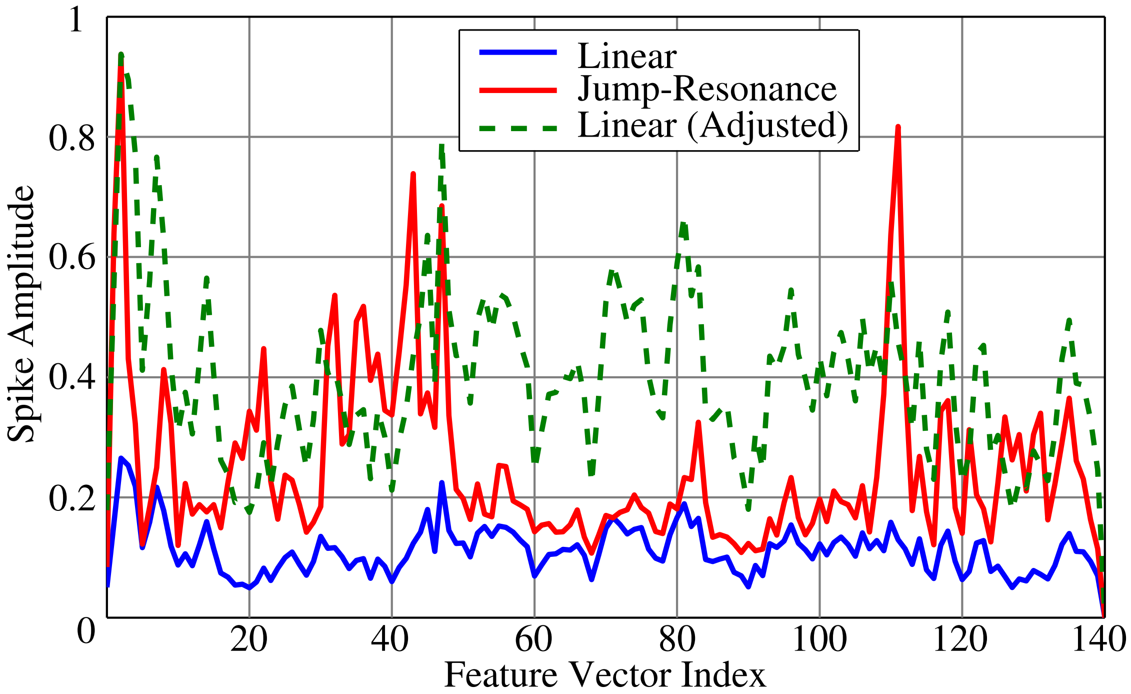

Figure 3.22: The comparison between linear filter and nonlinear (jump resonance) filter output with center frequency 1.138 kHz.

were then played back to the silicon AFE using the set up shown in Figure 3.20 and the post-processed features were then presented as input to the software-based *Gini*-SVM classifiers. Confidence scores generated by *Gini*-SVM for each speech frame were integrated over the duration of the utterance to obtain the final cumulative score. For each receiver-operating-curve (one per speaker) an equal error rate (EER) parameter was computed. The EER metric is widely used for quantifying performance of a biometric system and is defined as the error rate at which total false positive rate is equal to false rejection rate. Thus, the lower the EER, the more robust is the performance of a biometric system. For this experiment, EERs corresponding to each speaker verification system (101-110) were averaged to obtain an equivalent system EER. Another metric which is important for evaluating the performance of the speaker recognition system is the probability of detection (PD) or the rate at which the true speaker is correctly identified.

Table 3.2 summarizes the EER and PD of the speaker identification system corresponding to different durations of the moving average window and window step-size. The table compares the recognition metrics obtained using the jump-resonance based AFE, the recognition metrics obtained using the linear-filter AFE and the recognition metrics obtained using a MFCC-based AFE implemented in software. To ensure a fair comparison between the different features, the recognition results have been reported for a system using 11-dimensional MFCC features and using 22-dimensional MFCC features (which includes 11 velocity or Δ coefficients). The recognition results show that the jump-resonance based AFE demonstrates better performance than the linear filter-bank based AFE and under some conditions even outperforms its MFCC counterpart.

The linear filter setup achieved the best performance for a step size of 12 ms and a window size of 16 ms, resulting in a probability of detection (PD) of 95.63% and an equal error rate (EER) of 2.01%, as outlined in Table 3.2. The jump features (Jump_b) were able to outperform the linear hardware features with a PD of 100% for all step sizes, and achieved a minimal EER of 0.14% when the overlap was 0 ms. For this jump configuration, the hardware features were able to outperform the simulated Mel-frequency cepstral coefficients (MFCC) with no additive noise, which had a minimum EER of 2.01% and corresponding PD of 98.75%. In fact, the performance is at par with the 22-dimensional MFCC features. This attribute verifies our hypothesis that jump-resonance based features can encode information corresponding to Δ features which are difficult to compute in analog AFEs. We would like to point out that jump-resonance with smaller hysteresis widths (Jump_a) yielded results that were worse compared to that of the linear features, with a maximum PD of 95.63% and EER of 2.88%.

The results presented in Table 3.3 are from testing with speaker IDs 101-110 and 201-210, for a total of 20 speakers. In this case, the linear filter was only able to achieve a 90.94%

PD maximum, and 5.39% EER minimum for step sizes of 8 ms and 12 ms, respectively. The jump features (Jump_b) also had a deterioration in performance with a maximum PD of 98.75% for an 8 ms step size and a minimum EER of 1.50% for step sizes 12ms and 16ms respectively. Both features suffered an increase of the EER in excess of 1%, however, the smaller jump features' (Jump_a) minimum EER only rose by 0.29%. It's maximum PD also increased to 95.94%, instead of decreasing, which suggests that for speakers 201-210 the optimal jump width may be closer to 15% of the center frequency compared to the 30% used in Jump_b. Although the Jump_b features may not have the optimal parameters, it is still able to outperform the traditional linear features and the software MFCC (11-dimension) speaker recognition results for the 20 speakers tested. The experimental results show that it may be possible to improve the performance of speaker detection algorithms by carefully optimizing the hysteretic properties of jump-resonance [53]. Additional studies have demonstrated the potential for using jump-resonance in filtering of electromyography to extract speech induced muscle activity of individuals [54, 55, 56, 57].

Table 3.2: Comparison of EER and PD obtained using an 11 filter AFE for a linear and jump resonance filter bank with an MFCC-based system

	Experimental settings: window size = 16ms, number of speakers = 10									
	Linear		Jump_a [Figure 3.15]		Jump_b [Figure 3.16]		MFCC (11 filters)		MFCC (22 filters)	
Step Size	EER	PD	EER	PD	EER	PD	EER	PD	EER	PD
4ms	0.0288	0.9563	0.0441	0.9313	0.0063	1.0000	0.0187	0.9812	0.0035	1.0000
8ms	0.0253	0.9563	0.0431	0.9250	0.0104	1.0000	0.0247	0.9688	0.0017	1.0000
12ms	**0.0201**	**0.9563**	0.0340	0.9437	0.0066	1.0000	0.0201	0.9875	0.0076	0.9938
16ms	0.0260	0.9375	0.0288	0.9563	**0.0014**	**1.0000**	0.0201	0.9688	0.0017	1.0000

Table 3.3: Comparison of EER and PD obtained using an 11 filter AFE for a linear and jump resonance filter bank with an MFCC-based system

	Experimental settings: window size = 16ms, number of speakers = 20									
	Linear		Jump_a [Figure 3.15]*		Jump_b [Figure 3.16]		MFCC (11 filters)		MFCC (22 filters)	
Step Size	EER	PD	EER	PD	EER	PD	EER	PD	EER	PD
4ms	0.0576	0.8875	0.0376	0.9500	0.0166	0.9781	0.0213	0.9812	0.0040	1.0000
8ms	0.0569	**0.9094**	0.0360	0.9406	0.0163	**0.9875**	0.0247	0.9781	0.0043	1.0000
12ms	**0.0539**	0.9031	0.0341	0.9594	**0.0150**	0.9781	0.0216	0.9812	0.0089	1.0000
16ms	0.0586	0.8812	0.0317	0.9594	**0.0150**	0.9719	0.0260	0.9750	0.0079	0.9969

Chapter 4

Linearized Floating-Gate Injection

With respect to portable or embedded sensors, one of the biggest design considerations is energy. Can we harvest the required energy from the deployed environment? Does the sensor require a battery or other energy storage solution? How long can we expect sensor to function on a given amount of energy? Under such stringent power constraints, we aim to eliminate the overhead and losses from power regulators, data converters, digital signal processors and conventional memory structures. In this section, a method for data-logging that is powered by the input stimuli itself will be detailed.

4.1 Floating-Gate Implementation

4.1.1 Principle of Operation

In pursuit of realizing a "sense-now, analyze-later" sensor, the Adaptive Integrated Microsystems Laboratory has been studying the floating-gate (FG) transistor. Floating-gate transistors are a nonvolatile programmable circuit that has been used in digital EEPROM and flash memory applications [58]. The FG transistor is a metal oxide semiconductor field effect transistor (MOSFET) with a polysilicon gate that is DC-insulated by a surrounding layer of silicon dioxide. Since the gate is surrounded by a good electrical insulator, any charge that is on the gate will, with high probability, remain there. Taking advantage of the lossless property of a FG MOSFET, structures can be designed to use lossless charge sharing to improve input range, lower circuit complexity, and build independently and simultaneously trimmable circuits [59, 60].

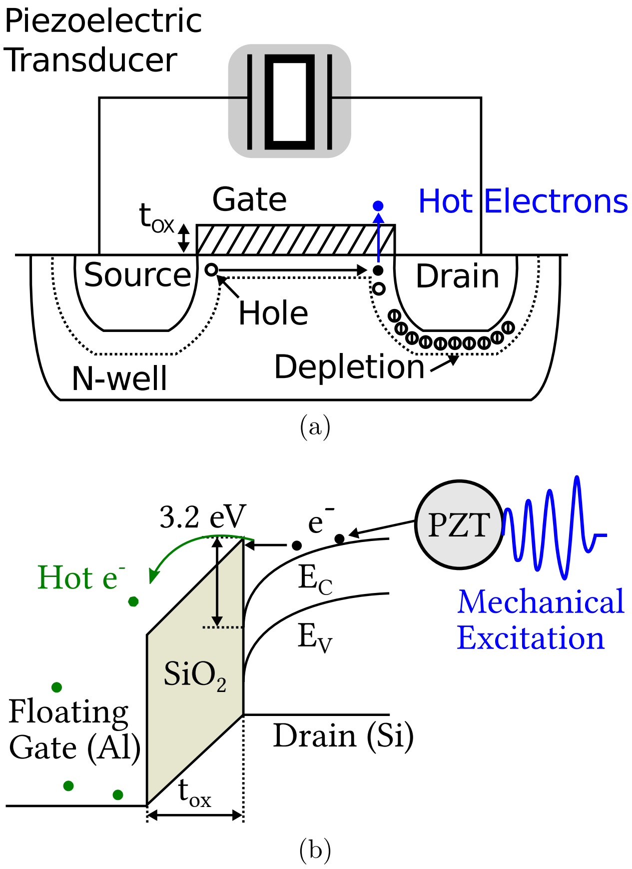

Figure 4.1: Impact ionized hot-electron injection illustrations (a) energy band diagram and (b) a cross-sectional view of P-MOSFET FG transistor.

A common method for programming FG transistors is through Fowler-Nordheim (FN) tunneling and impact ionized hot-electron injection (IIHEI) [61, 62]. IIHEI for a p-channel MOSFET is induced with the introduction of a strong electric field being formed between the drain-to-channel depletion region. When subjected to a strong electric field, the primary carriers in a p-channel, the holes, can gain sufficient energy to dislodge electrons via impact ionization with high probability, see Figure 4.1 for an energy band diagram and cross-sectional view to aid in the illustration of this process. In this illustration, the strong electric field is supplied by an external piezoelectric transducer. Any electron that has been dislodged is a “hot electron” that can accelerate towards the channel region, gaining kinetic energy in the process. If the total kinetic energy exceeds 3.2 eV, the momentum of the electron can be sufficient to overcome the Si-SiO$_2$ barrier, thus allowing the hot electron to get injected into the oxide. For the 0.5 µm CMOS process available through the MOSIS educational program, IIHEI will require a voltage of approximately 4.2 V to generate a sufficient electric field to add electrons onto the FG (and thus reducing the voltage potential). To remove electrons from the FG the FN tunneling process is used, whereby a high voltage potential (>14 V in the 0.5 µm process) is applied across a parasitic capacitor that is coupled to the FG. This will draw away any charge on the FG and leave it in an empty state.

Because FN tunneling requires high voltages, it is treated as a global erasure mechanism for the FG memory, and IIHEI is used for programming specific analog memory values. IIHEI current I_{inj}, in a p-channel MOSFET, has been shown to be dependent on the transistor source current I_{s}, the source-to-drain voltage V_{sd}, and the gate-to-drain voltage V_{gd} across the transistor. To date, this dependence has only been described using empirical models, such as this one:

$$I_{\mathrm{inj}} = \alpha I_{\mathrm{S}} \exp\left(\frac{\lambda V_{\mathrm{sd}}}{V_{\mathrm{inj}}}\right) \exp\left[\frac{-\beta}{(V_{\mathrm{gd}} + \delta)^2}\right], \tag{4.1}$$

which is assumed to be valid for most of the transistor’s operating region (weak, moderate, and strong inversion). The parameters $\alpha, \lambda, \beta, \delta$, and V_{inj} are estimated from measured data. With a circuit architecture as in Figure 4.2, all other factors that affect the injection current ($I_{\mathrm{S}}, V_{\mathrm{sd}}$, and V_{gd}) are held at constant potentials, thus the injection current I_{inj} as modeled

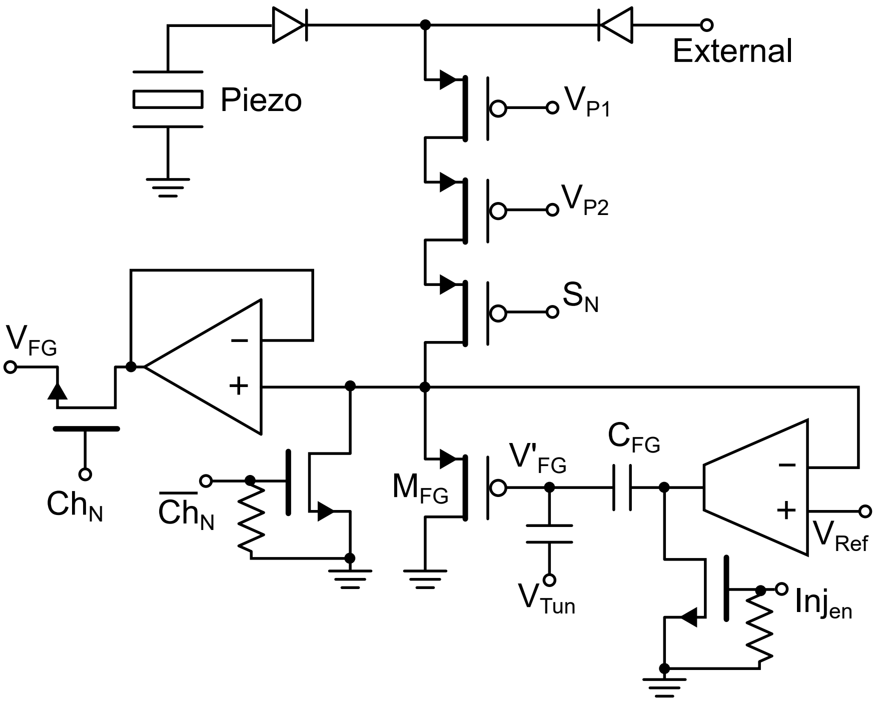

Figure 4.2: The core of the PFG's linear injector core has many configuration states, the transistor-level details are shown here.

in (4.1) is also constant.

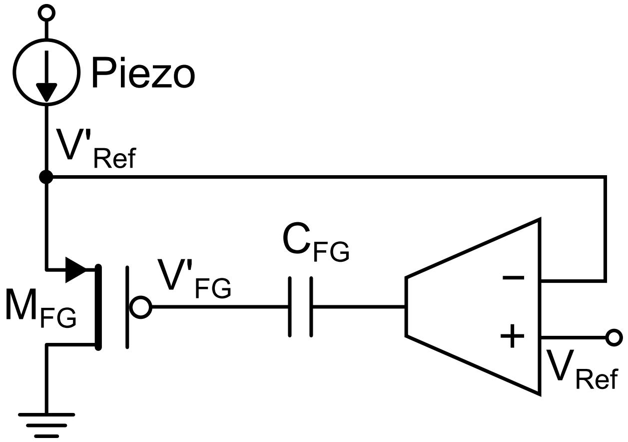

Figure 4.3: Equivalent circuity when configured for self-powered operation, with Vdd supplied by the input stimuli on the piezo through Figure 4.9.

During the sensing mode (Figure 4.3), the switch S_p is open, thus enabling the negative feedback of the operational amplifier to be formed in conjunction with the FG. With a constant I_{ref}, the source-to-gate voltage, V_{sg} will be kept constant during injection. The operational amplifier will continuously adjust the control-gate voltage V_{cg} to maintain a constant source-to-drain voltage V_{sd}, thereby ensuring a constant injection current. For reading out the stored value, the switch is closed (Figure 4.4c), connecting the control-gate to a ground reference, thus the floating-gate voltage V_{fg} is a function of the previously injected charge and the capacitor C_{fg}. Omitting the mathematical derivation, the injection current during sensing was shown to be:

$$I_{\mathrm{inj}} = I_{\mathrm{inj}}^{0} \exp\left[\frac{-\left(G_{\mathrm{s}} + G_{\mathrm{fg}}\right) t}{C_{\mathrm{T}}\left(1 + A_{\mathrm{V}}\right)}\right]. \tag{4.2}$$

Where G_{s} and G_{fg} are the injection transconductance parameters with respect to the source and floating-gate terminals, and can be estimated to be in the range 0.149 to 2.316 fS for reference currents between 45 and 90 nA. A_{V} is the gain of the operational amplifier, which only requires a small-signal gain of 40 dB. t is the injection time and C_{T} is the total capacitance at the floating-gate, including the parasitic and nonparasitic floating-gate, tunneling, source, drain, and bulk capacitors. Additional literature detailing applications of the FN tunneling and IIHEI process, including a method for recording the time-of-occurrence of injection are available [63, 64, 65, 66, 67, 68]. Many of these methods are dependent on a novel self-powered timer devices that was developed in the Adaptive Integrated Microsystems laboratory [69, 70].

4.1.2 Circuit Implementation

Taking the linear injector designed for self-powered sensing using piezoelectric transducers, as detailed in Section 4.1.1, a System-on-Chip (SoC) is designed following the block diagram

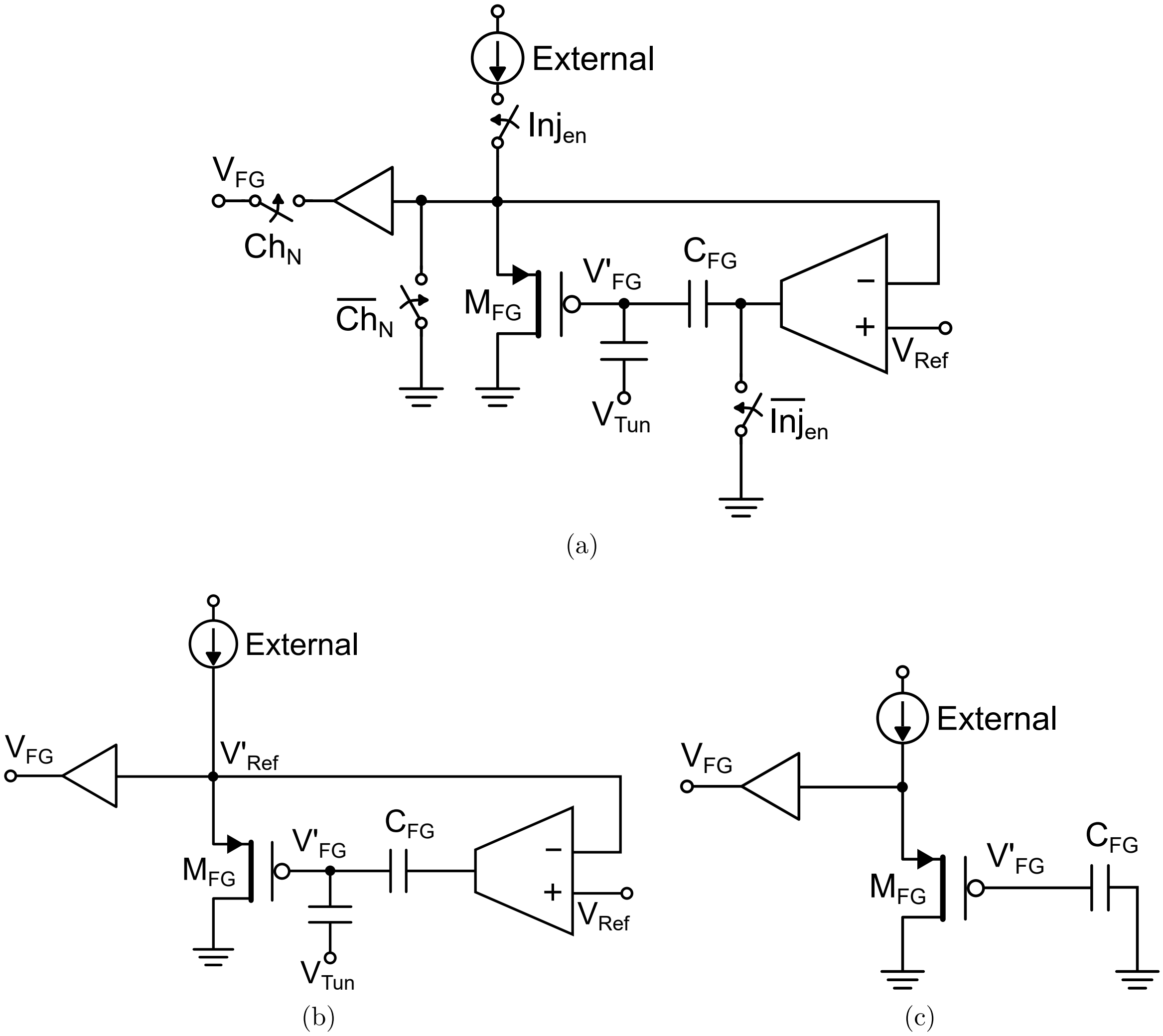

Figure 4.4: (a) The base configuration of the PFG when energy is supplied from an external DC source, bypassing the piezo input stage. (b) For initial programming of the PFG using IIHEI or FN tunneling. (c) Configured for reading V'_{FG}.

of Figure 4.5. The floating-gate core is highlighted in green, and is the portion of the SoC that will remain active whether it is powered from the energy in the input stimuli or from external DC sources (e.g. batteries, solar panel, rectified radio-frequency, etc.). If there is an external DC source available, the red portions of the diagram can be activated. These are primarily used to program the initial floating-gate charge before deployment as well as for powering an analog-to-digital (ADC) converter. The ADC is that of a pulse encoder variety, which generates an output waveform that consists of a train of square wave pulses,

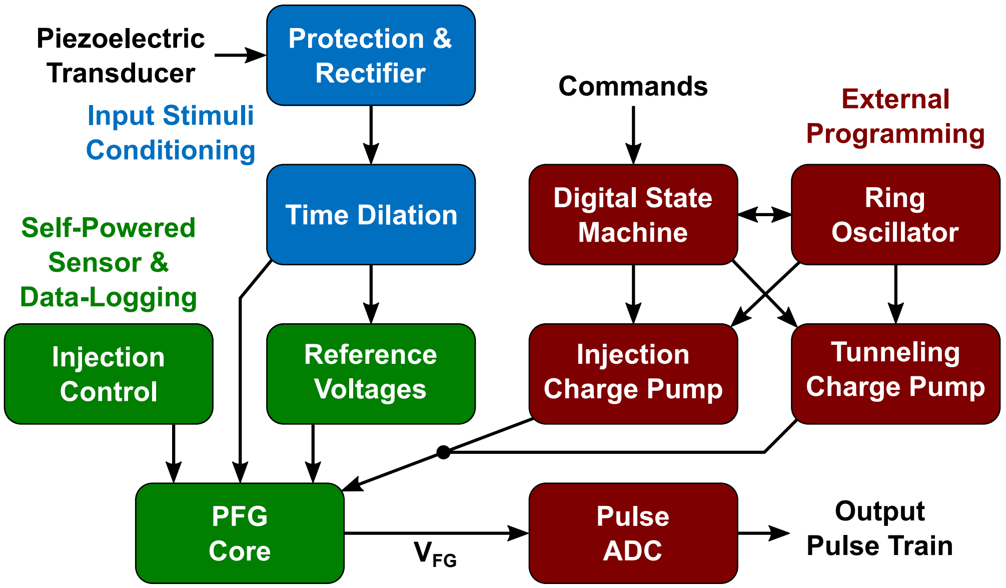

Figure 4.5: Block diagram of the major components included in the PFG SoC.

the analog input value is encoded as the frequency of the pulses. A schematic showing the circuit details of the pulse encoder ADC are shown in Figure 4.6.

The digital state machine, ring oscillator, injection and tunneling charge pump details are omitted in this dissertation as they do not materially affect the PFG core during self-powered operation, or during in-field interrogation of the floating-gate values. During self-powered sensing, besides the PFG core (detailed in the previous subsection), an injection control circuit will be active. For implementations detailed in this dissertation, the injection control is based on using varying lengths of diode chains to detect thresholds of input voltage from the piezoelectric. A single channel of the control circuit is presented in Figure 4.7 for the first channel of a bank of PFG cores, $N = 1$, which will activate $\mathrm{Level}_{\mathrm{N}}$ and subsequently S_{N} with a voltage of around 7 V. Note that by using $\mathrm{Inj}_{\mathrm{en}}$, the channel activation can be manually triggered.

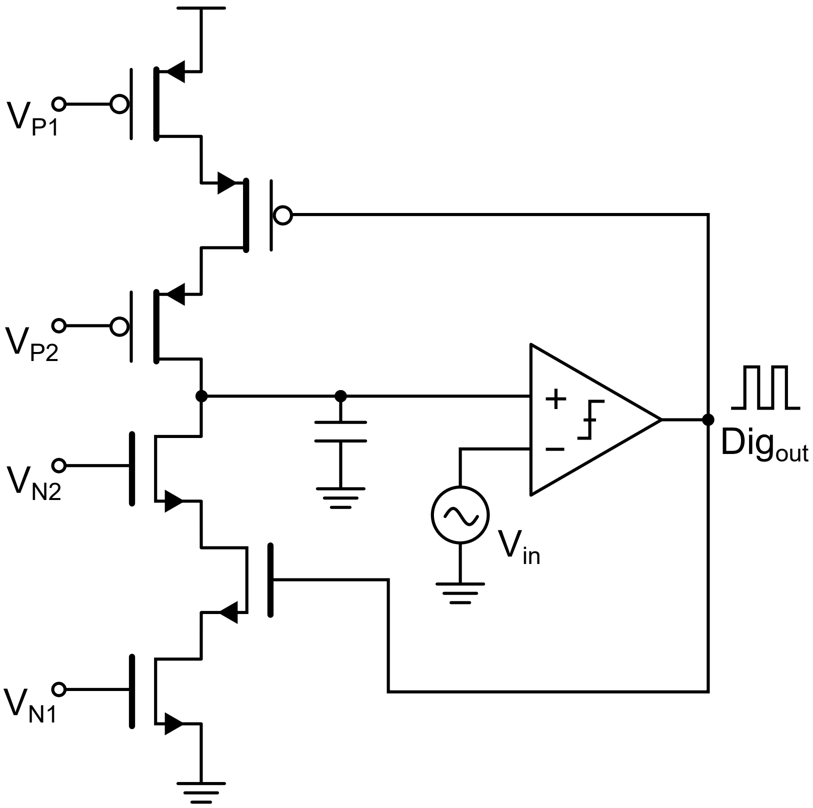

Figure 4.6: The analog-to-digital (ADC) circuit is implemented using a pulse encoder. The frequency of the output train correlates to the input analog value.

In the self-powered mode of Figure 4.5, the last key components are the voltage references. There are multiple voltage references built into the chip, and they mostly follow the architecture of Figure 4.8. It consists of cascaded current mirrors that are variably tunable by adding external resistances to R_{dec} or R_{inc}. Most references have been designed with an on board resistor such that keeping R_{dec} floating and R_{inc} tied to ground will set the PMOS and NMOS voltage biases to their desired points. The two capacitors and NMOS transistors on the left-hand side of the circuit operate as a startup circuit to ensure that the current mirrors are in a valid operating region.

The blue regions of the Figure 4.5 denote circuitry that is used as for input stimuli conditioning. For the purposes of this dissertation the input stimuli is typically assumed to be that

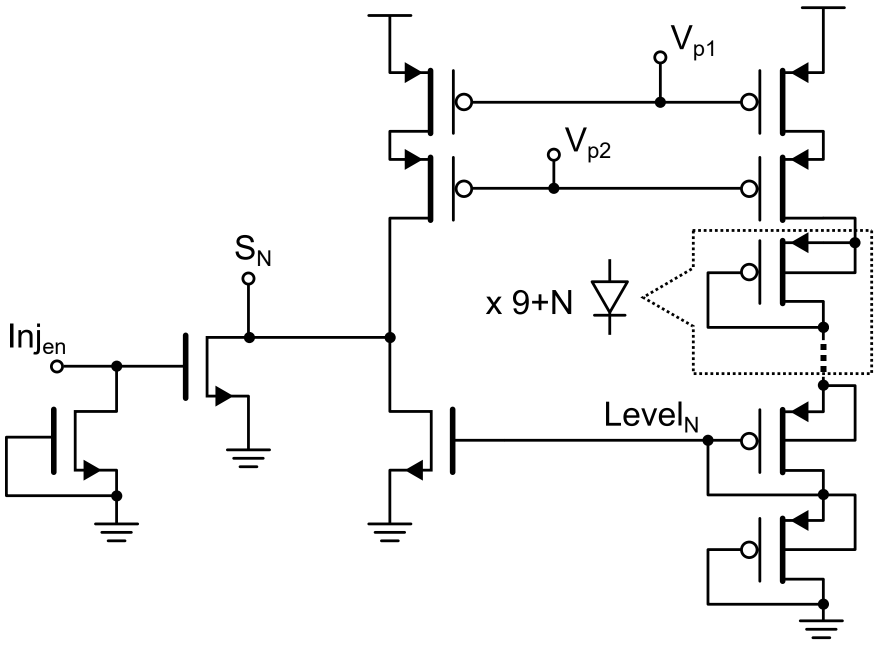

Figure 4.7: During self-powered mode, the injection is controlled by diode threshold detection, each channel (N) will have a varying activation threshold.

of a piezoelectric transducer generating voltages between 7 V and 12 V. Since many desired target applications tend to generate voltages larger than that range, we utilize a time-dilation circuit and overvoltage protection diodes as shown in Figure 4.9 [71, 72, 73, 74]. The left portion of the figure is an equivalent model of a piezoelectric transducer. As the figure illustrates, the input conditioning consists of a parallel capacitor to filter some high frequency content and smooth out minor ripples, series resistors to limit inrush current, diode chains that will short the piezoelectric when exceedingly large voltages are present, and a full bridge rectifier to generate the on-chip supply rails. The portion of the figure on the right, highlighted in purple, is the time-dilation circuitry.

For the sake of completeness, the transistor-level schematics for some of the components presented in previous figures are included here. Namely: the comparator (Figure 4.10), which is used in the pulse encoder ADC; the transconductance amplifier (Figure 4.11) that comprises the feedback amplifier of the PFG core; and an operational amplifier (Figure 4.12)

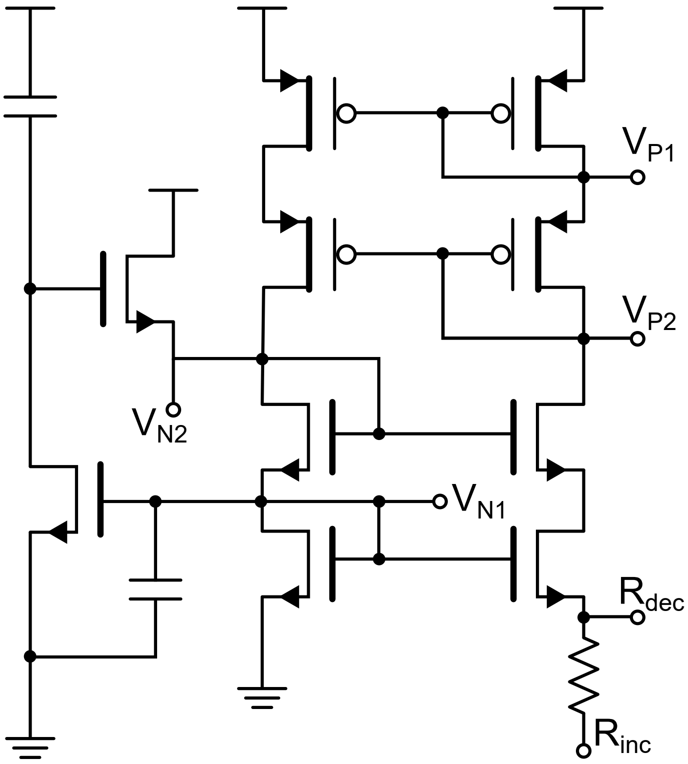

Figure 4.8: Schematic showing the transistor-level implementation for voltage references. This circuit is implemented multiple times to generate the necessary onboard voltages, and can be tuned via external resistance.

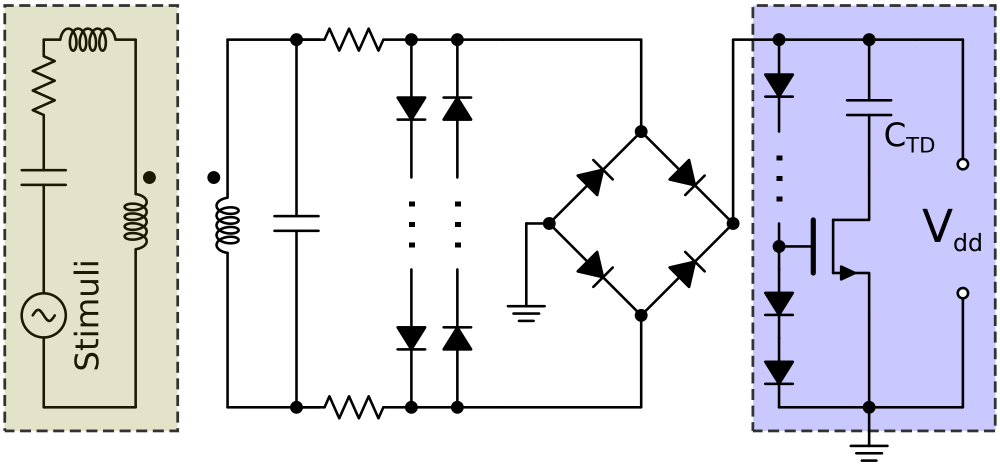

Figure 4.9: On the left a piezoelectric transducer is modeled. The center portion includes series resistance to limit inrush current, diode chains to prevent overvoltage, and a full bridge rectifier. The output of the full bridge rectifier is attached to a time-dilation component before serving the chip as Vdd.

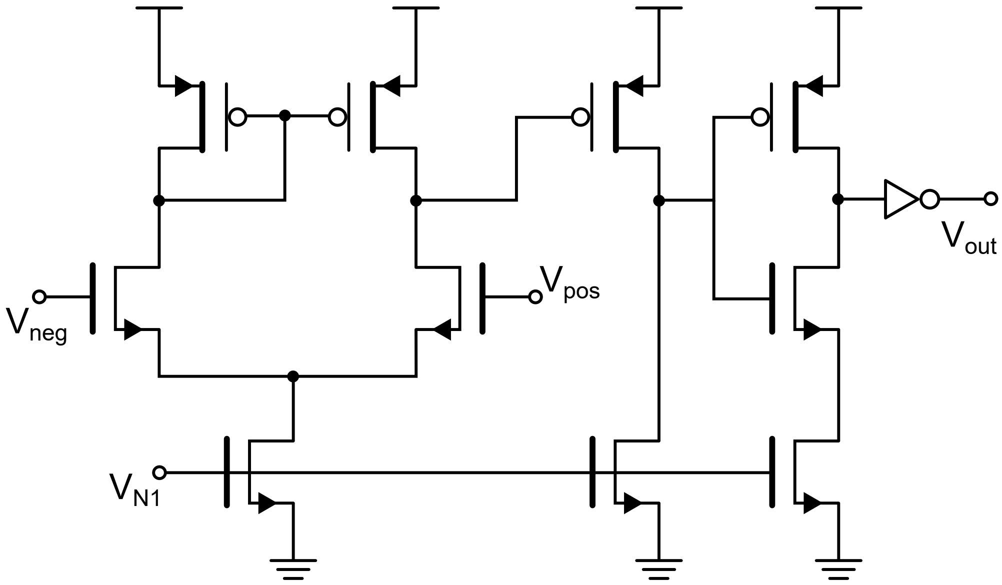

Figure 4.10: The transistor-level implementation of the comparator used in the pulse encoder ADC.

that is used whenever an analog signal needs buffering before being sent off-chip. The operational amplifier also serves as an isolation buffer between multiple PFG channels and the single ADC that is on-board. Note that the transconductance amplifier has been designed and biased to operate in a current-starved sub-threshold region, thus shorting its output to ground will not result in significant damage.

This circuit architecture has been reported first by [75, 76] as having a linearity greater than 13-bits, with other circuit parameters listed in Table 4.1 [77]. The same circuit architecture, or sensor core, has been integrated with piezoelectric sensing and successfully deployed in numerous field applications, including those that operate within RF energy harvesting power envelopes [78, 79, 80, 81]. Details of some of the deployments undertaken as part of this dissertation research follows in Chapter 6, with additional applications reported in the Appendices. A micrograph showing one implementation of a fabricated linear injector System-on-Chip (SoC) is presented as Figure 4.13.

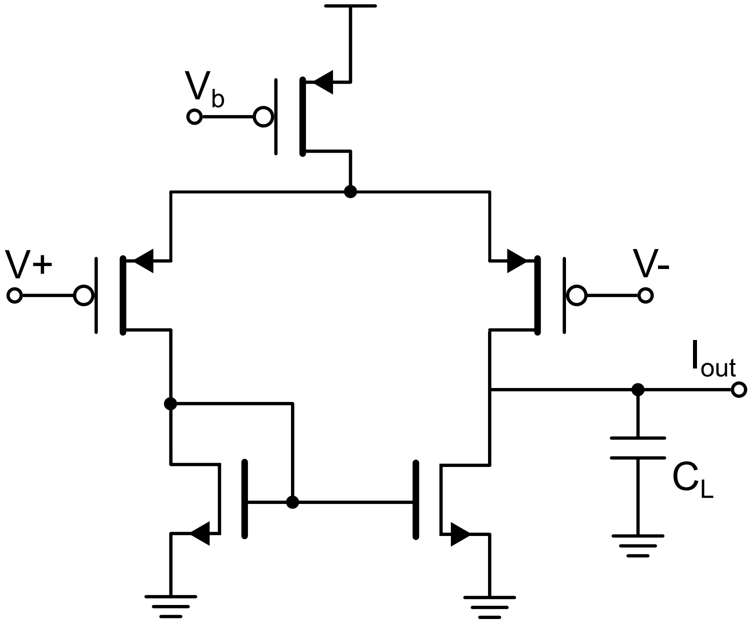

Figure 4.11: This transconductance amplifier is current-starved and utilized as the feedback amplifier of the PFG core.

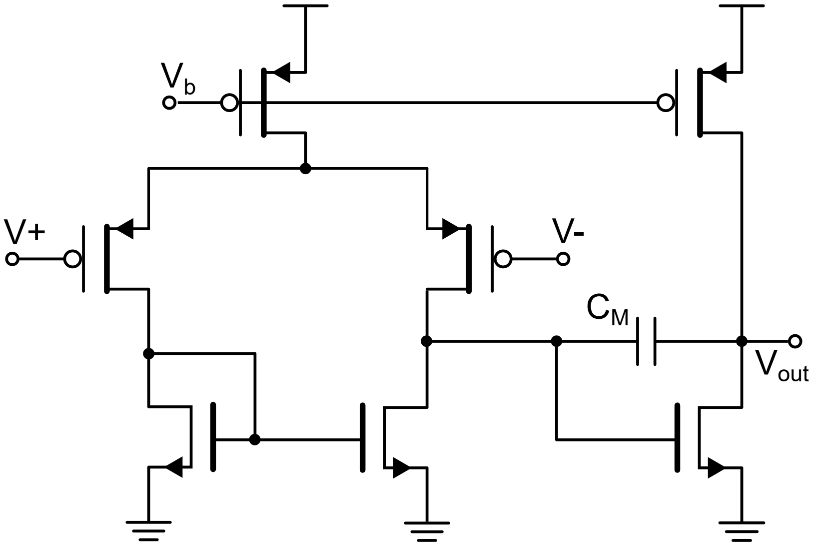

Figure 4.12: When buffering analog signals before connecting to the pads of the chip, this op-amp is used.

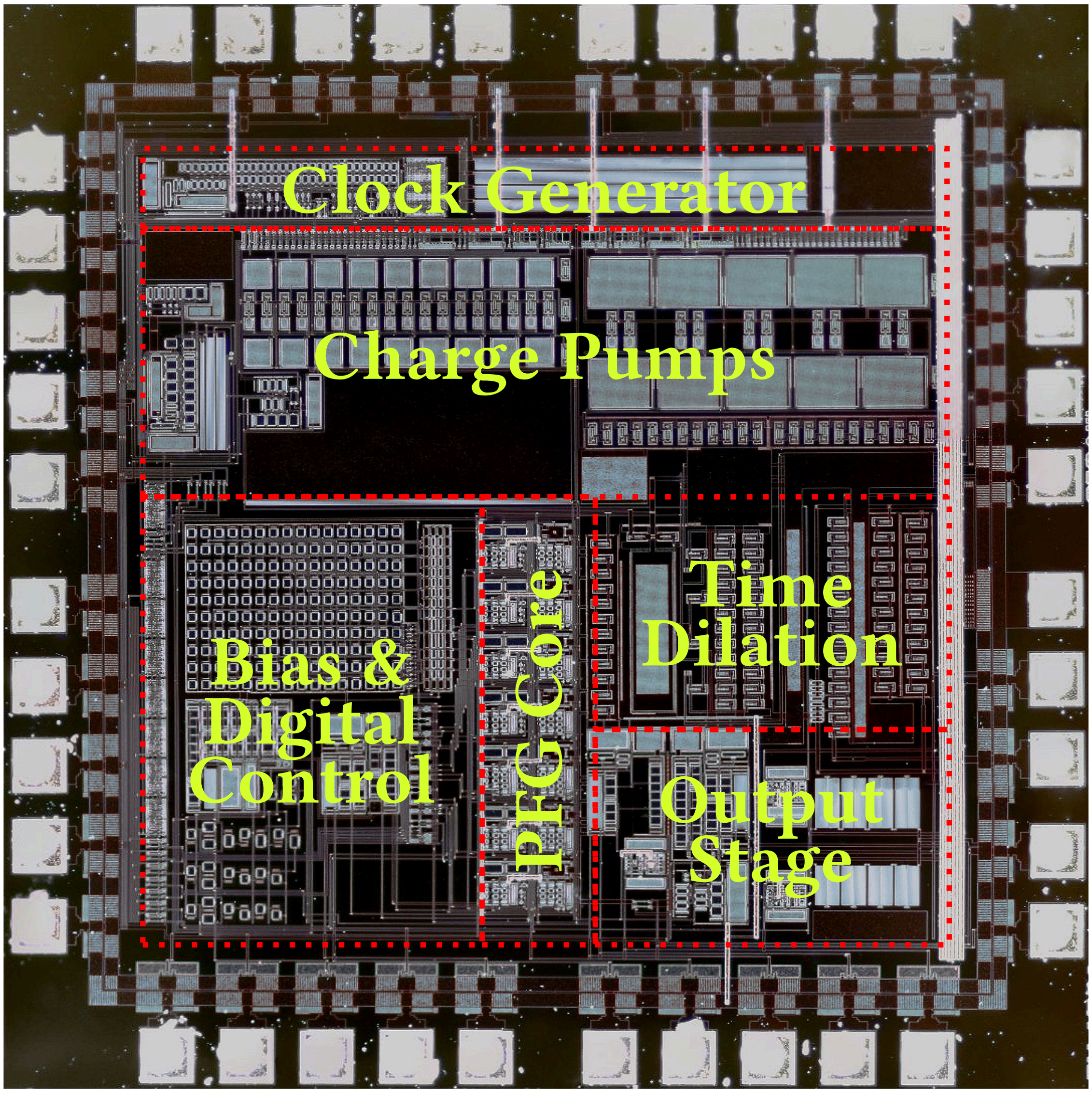

Figure 4.13: Micrograph of an integrated solution with floating-gate linear injector core and necessary supporting circuitry. The die is $1.5 \times 1.5\,\mathrm{mm}^2$, and fabricated through MOSIS.

4.2 Laboratory Characterization Results

4.2.1 Linearity

Starting with an "empty", or fully tunneled floating-gate, we apply a one second injection pulse from a function generator and record the stored floating-gate voltage after each injection. Supply voltage to the chip was 1.8 V and the injector's reference voltage was 5 V. The

Table 4.1: Specification of Linear Injector Circuit

Parameters	**Value**
Technology	0.5 µm CMOS
Supply Voltage	1.8 V
Floating-Gate Capacitance	100 fF
Power Dissipation (Programming)	500 nW
Power Dissipation (Biasing)	250 nW
Minimum Energy (Sensing)	100 nJ
Maximum Accuracy	13.4 bits
Programming Range	0.1 V to 4.1 V

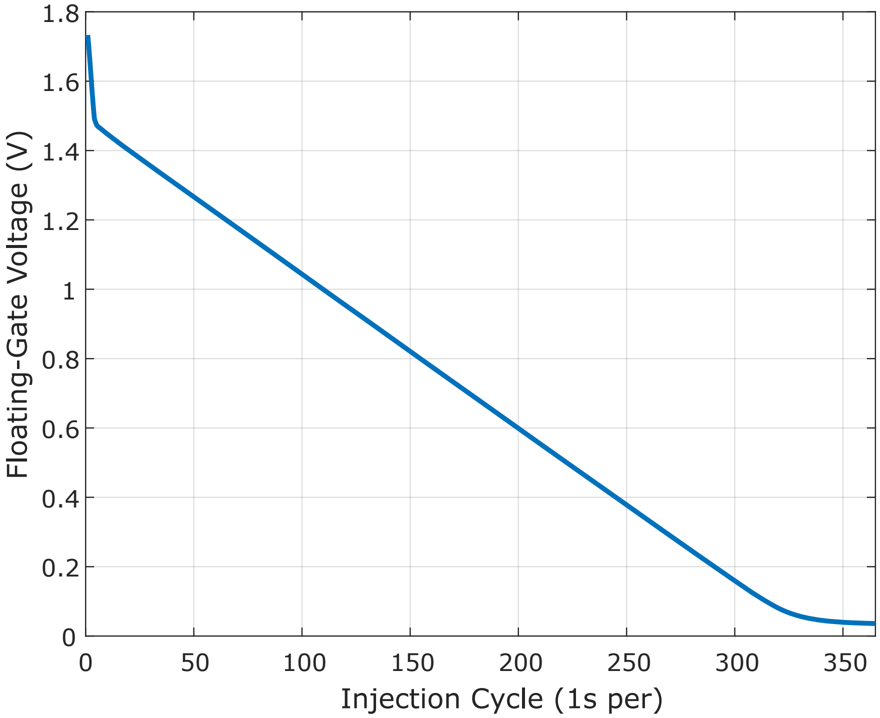

Figure 4.14: A complete data logging analysis of the linear injector for a 1.8 V supply.

resulting data is given as Figure 4.14, and the change in stored voltage (i.e. derivative) is presented in Figure 4.15, which illustrates that the usable linear region is between injection cycles 15 and 304 (arbitrarily defined as within 5% of the median change). In this linear region, each injection cycle predictably changes the voltage on the floating-gate by 4.5 mV. For the first few cycles, the stored charge on the floating-gate causes the voltage to exceed

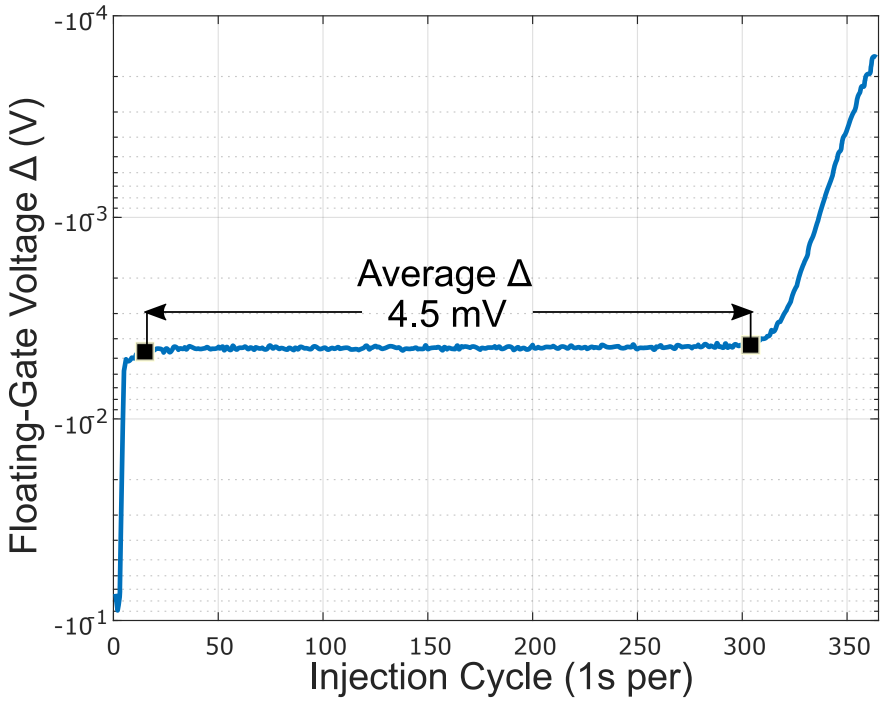

Figure 4.15: Plot showing the change in floating-gate voltage per injection cycle of Figure 4.14.

the maximum output swing of the on-chip buffer and similarly near the tail end of the linear region the buffer has trouble faithfully tracking the change as it is not designed to be rail-to-rail.

From the data of the linear region in Figure 4.14, an analysis into the Integral Nonlinearity (INL) and Differential Nonlinearity (DNL) are calculated and shown as Figure 4.16. The resulting effective number of bits, 12.9, compares favorably to the earlier published results considering this version of the chip has been compacted to a $1.5 \times 1.5\,\mathrm{mm}^2$ die on a QFN package and includes supporting circuitry such as: charge pumps, digital state machines, multiple channels, buffers, and an analog-to-digital converter. A slight decrease from the reported 13.5 bits can also be attributed to the lower supply voltage utilized (1.8 V versus 4 V), which exacerbates the impact of having non-ideal buffers. Other researchers have reported data retention of over eight years for at least eight bits of precision [82].

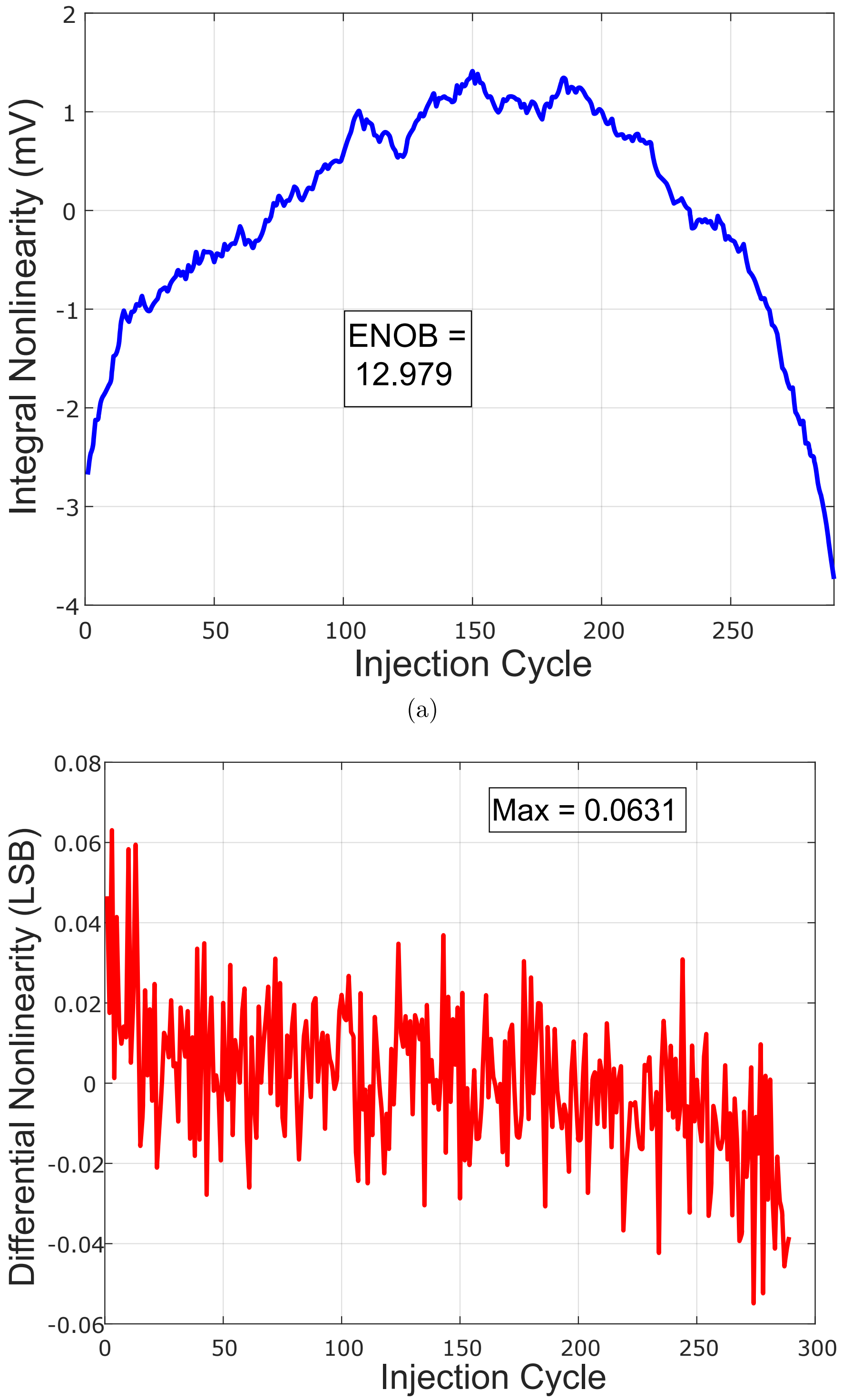

(a)

(b)

Figure 4.16: (a) INL and (b) DNL for the linear region, showing an effective number of bits around 12.9.

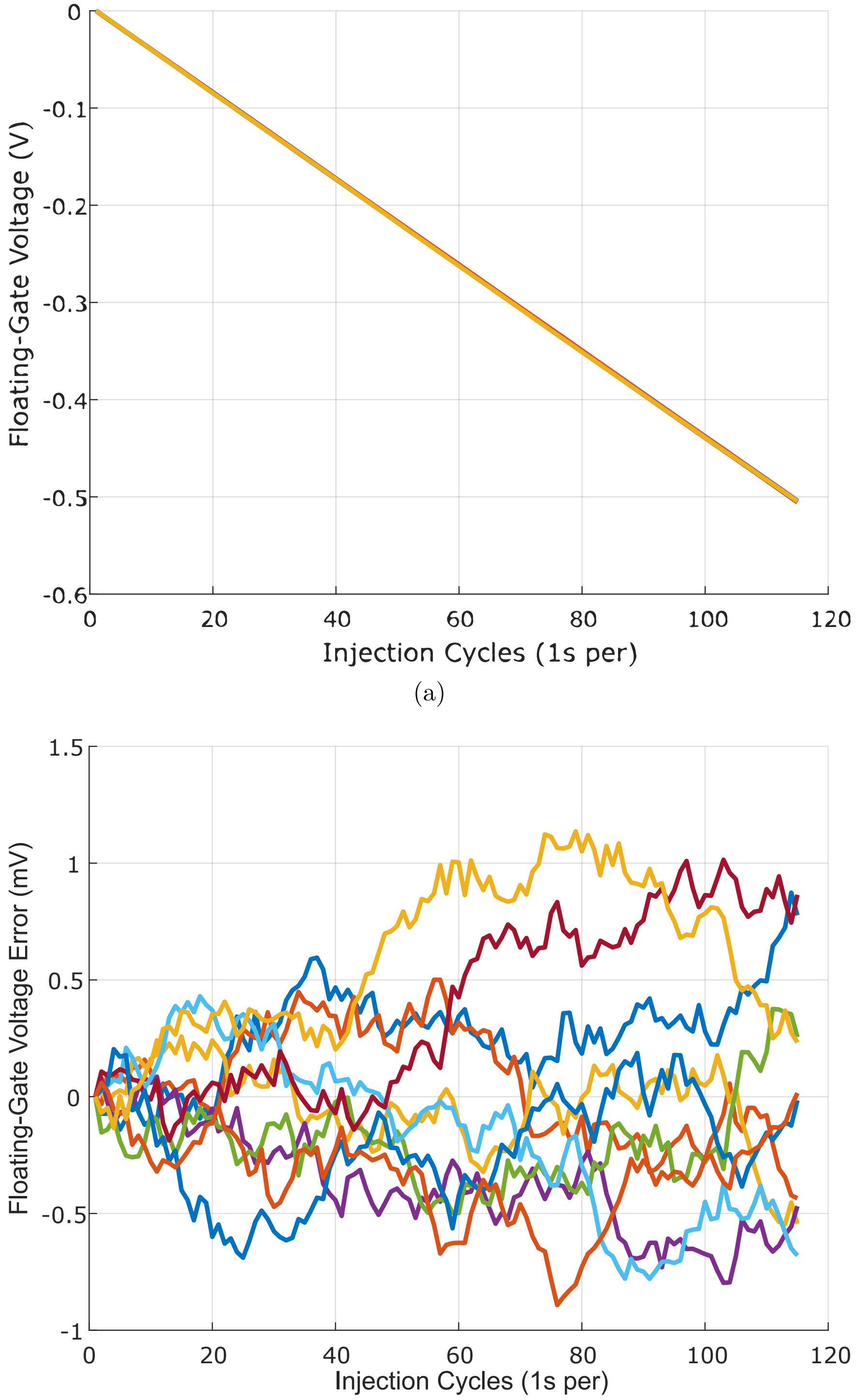

(a)

(b)

Figure 4.17: Multiple test iterations of programming 500 mV onto the floating-gate using the linear injector architecture. (a) shows the injection cycles versus stored charge and (b) is the deviation from ideal.

4.2.2 Repeatability and Stability

A floating-gate was initially tunneled to the linear region, and repeatedly injected over 100 cycles with a reference voltage of 5 V and supply voltage of 1.8 V. The result of running this test for 10 runs is plotted as Figure 4.17a, and the deviation from ideally linear is given in Figure 4.17b. This testing shows that across a large range of the floating-gate, and over multiple iterations, the expected systematic error is below 0.1 percent. The main cause of the error is the non-ideal voltage references implemented within the SoC, as even in a stable thermal environment small deviations and drift can be observed as in Figure 4.18.

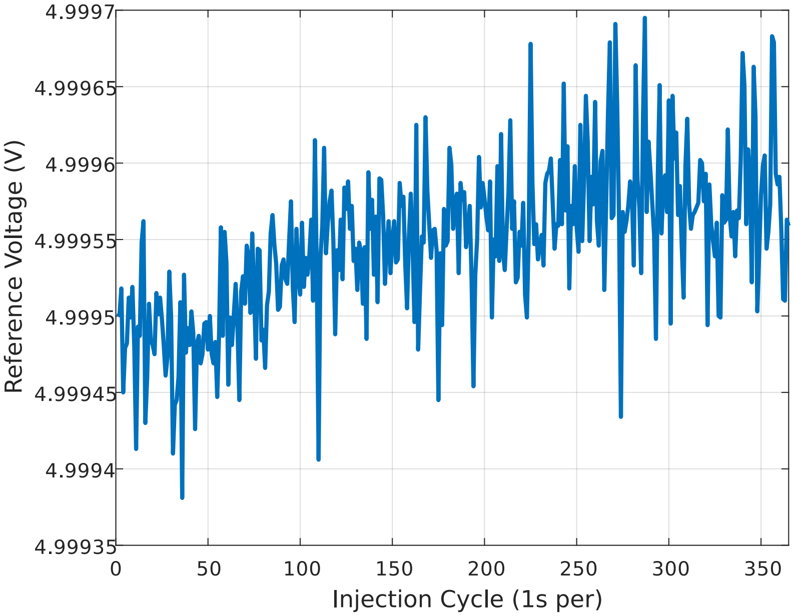

Figure 4.18: The on-board reference voltage is not ideal and exhibits some deviation even in a temperature-stable environment.

The sensitivity, or precision, of how much charge is “recorded” onto the floating gate per injection cycle is tunable via an external resistor to the onboard voltage references. Figure 4.19 shows the variability in sensitivity using reference voltages from 4.5 V to 5.3 V, 4.19a presents

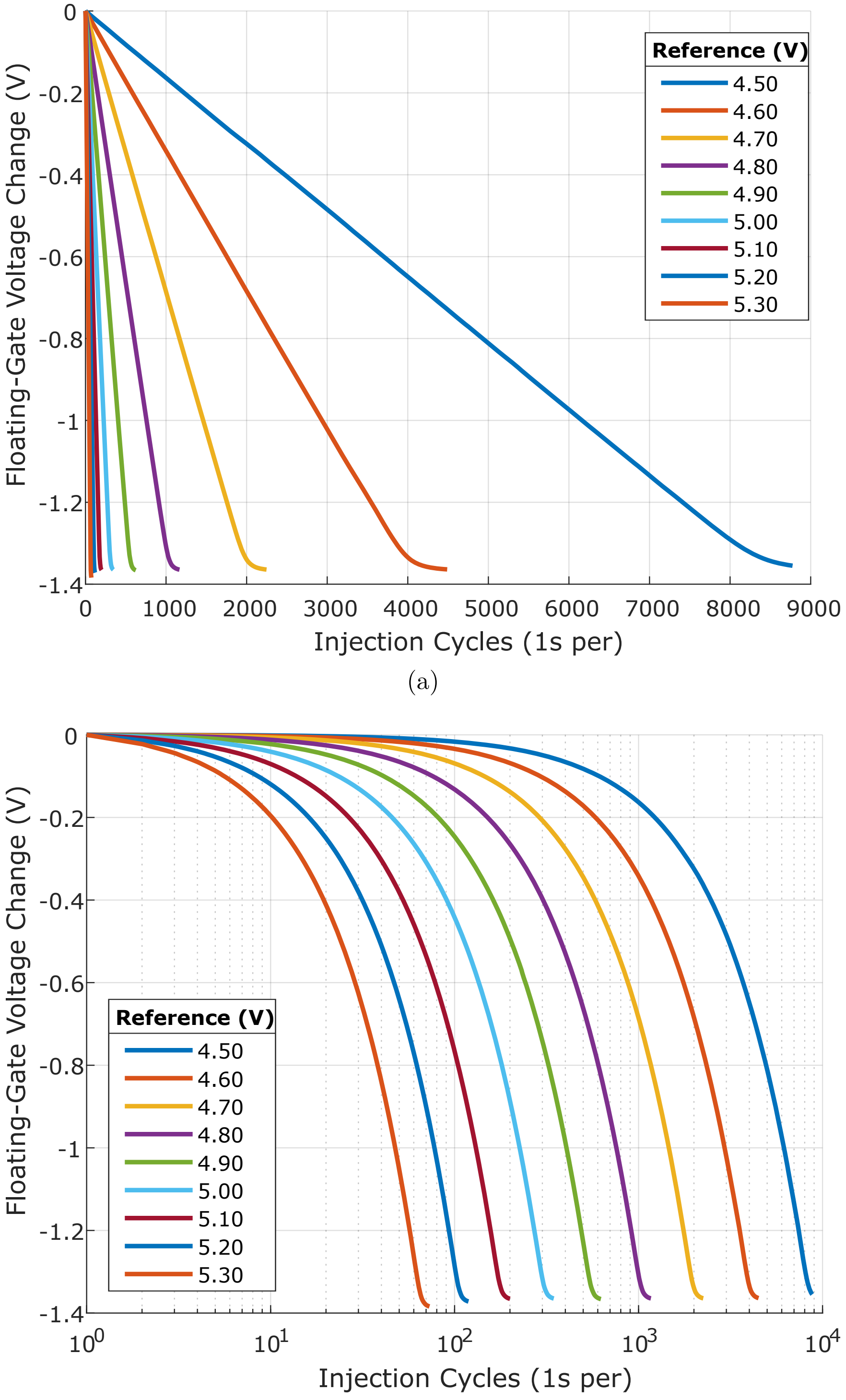

Figure 4.19: Varying the reference voltage allows tuning of the sensitivity of the precision, x-axis in (a) linear and (b) logarithmic scale.

the data with a linear scale for the x-axis to reinforce that the data logging is linear while 4.19b is plotted on a logarithmic x-axis to give some insight into how a linear change in reference voltage gives rise to a logarithmic relation for maximum number of recordable injection cycles. It should be noted that with a sufficiently large reference voltage, the system would act equivalently to a single level cell NAND flash memory in that the stored value is binary. On the other hand, as discussed earlier, the minimum voltage for reliable injection in this process is approximately 4.2 V — with a reference voltage near this threshold the maximum number of stored cycles would be exponentially larger. However, our earlier analysis leads us to assume a maximum usable linearity of about 12 to 13 bits, which would be just under 8,192 unique points. Hence, the minimum reference voltage we show in Figure 4.19 is 4.5 V, which already exceeds that number in this particular test configuration.

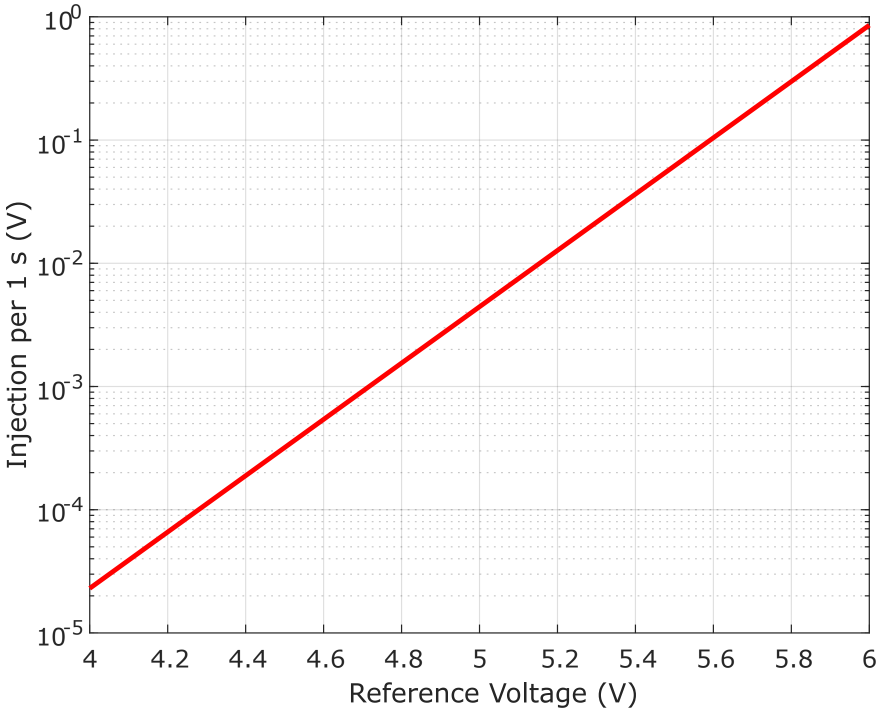

Figure 4.20: A linear change in reference voltage leads to an exponential change in the amount of charge injected per cycle.

Longer duration testing has been verified with reference voltages near the threshold; however, the change in stored voltage is on the order of mVs for 24 hours of injection and thus not productive to include in the previous figure. It will, however, allow the PFG to log millions of injection cycles, albeit at the expense of only being able to detect injection cycles in groups of several hundred. A plot showing the relationship between the externally-tunable reference voltage, and the size of a one second injection pulse is shown in Figure 4.20, and demonstrates that with just 2 V of range in the voltage reference, the number of detectable injection cycles spans almost five orders of magnitude.

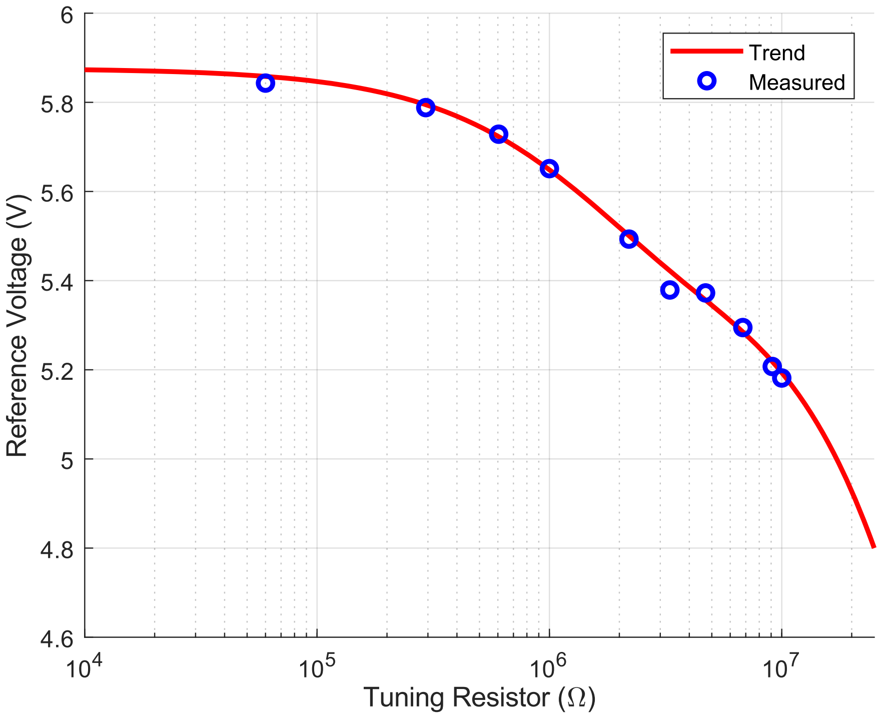

Figure 4.21: Tuning one of the reference voltages by changing the external resistor.

As previously mentioned, the reference voltage is tuned using an external resistor, and in Figure 4.21, precision resistors ranging from 500 kΩ to 1 GΩ were used along with less precise potentiometer resistors to visualize the trend between tuning resistor value and resulting

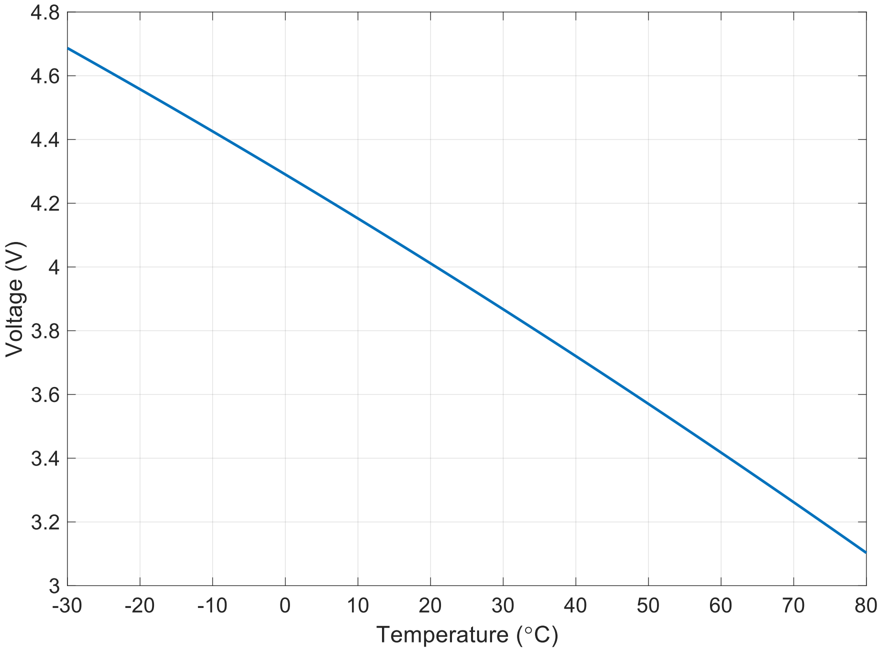

Figure 4.22: A reference voltage that was tuned to approximately 4 V at 20 °C varies as the ambient temperature is changed.

reference voltage. Note that the PFG SoC has four taps of the reference voltage that are offset by a diode drop (about 700 mV), which allows for easily generating reference voltages 3.4 V and 6.2 V without resorting to resistors in excess of 1 MΩ. The on-chip voltage reference did not utilize bandgap technology, and is quite susceptible to temperate effects, as verified in the testing for Figure 4.22, which shows more than 1 V variation between −20 °C and 60 °C. This variation is directly observed in the temperature effects of a one second injection pulse at differing ambient temperatures, which is given in Figure 4.23.

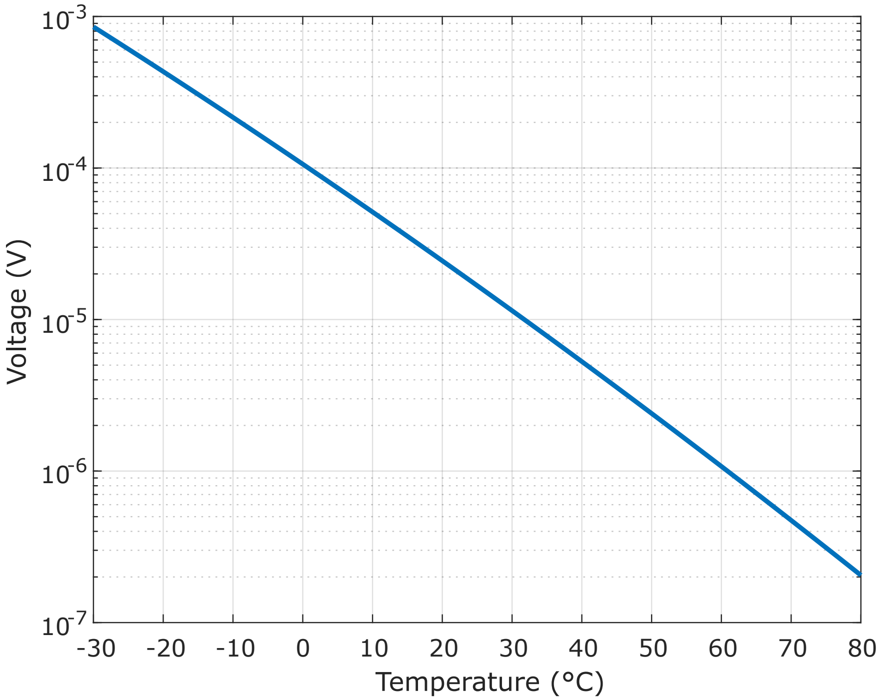

Figure 4.23: Primarily due to the reference voltage having a temperature dependence as shown in Figure 4.22, the rate of injection will vary similarly to having changed an ideal voltage reference as in Figure 4.20.

4.2.3 Digital Output

In simulating the transfer function of the pulse encoder ADC from Figure 4.6, two points of concern were noted: the input-output relationship was not monotonic nor linear. With respect to the linearity, the simulation model showed two exponential relationships with differing parameters depending on if the input voltage was above or below the NMOS activation level for a sub-threshold circuit on the 0.5 µm CMOS process from On Semi. A graph showing the model simulation versus the measured results from one fabricated chip is given in Figure 4.24. For inputs below approximately 500 mV, there is a rapid increase in the output pulse train frequency as the input voltage increases; however, for input voltages larger than 500 mV, there is a more gradual decay of the pulse encoder's output frequency as the input voltage increases.

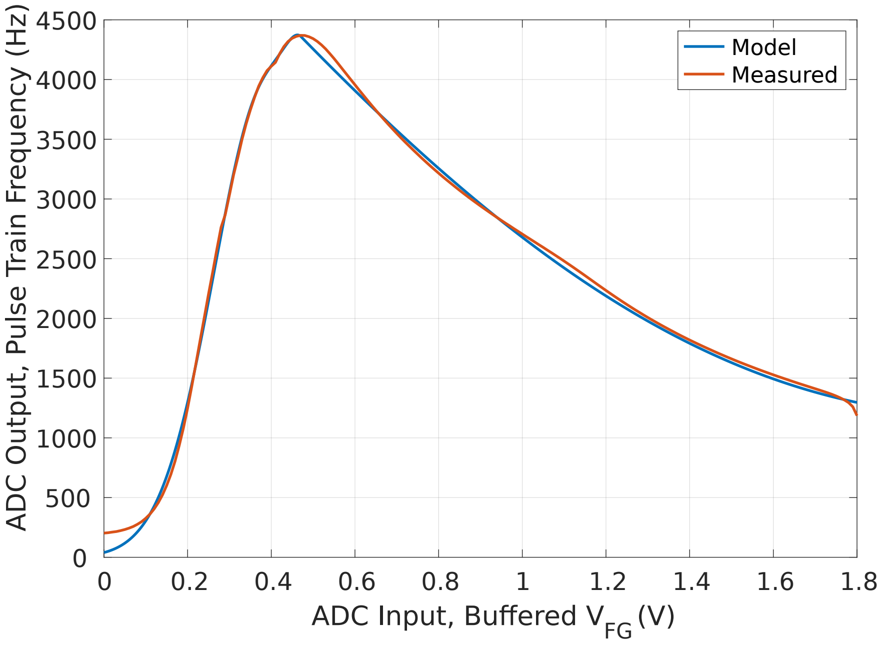

Figure 4.24: The PFG SoC has a pulse encoder analog-to-digital output stage, with a non-monotonic relation between floating-gate voltage and output pulse train frequency.

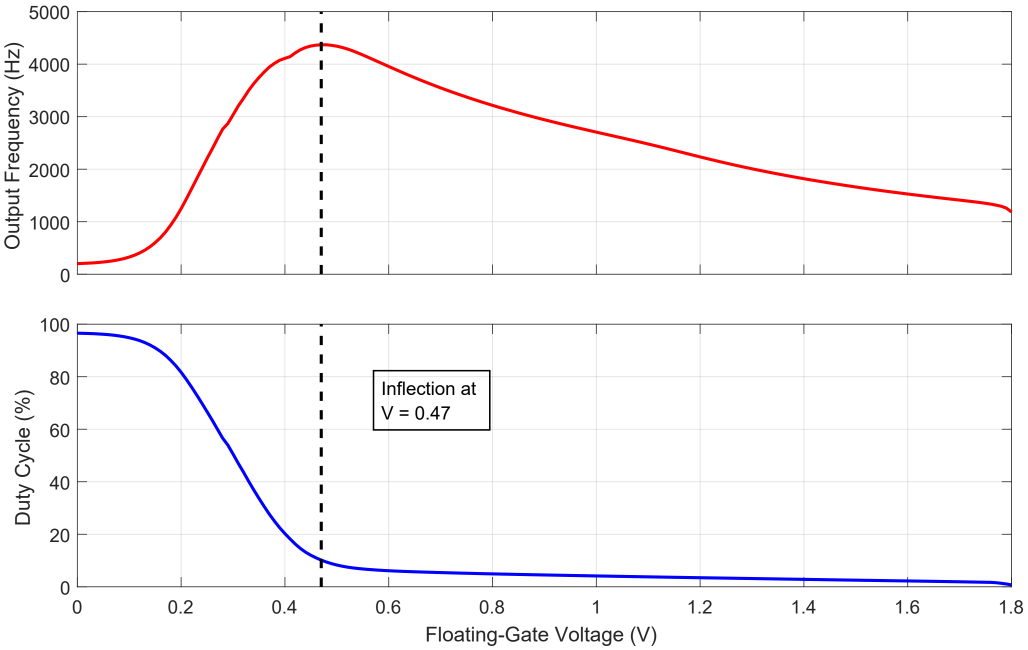

Figure 4.25: Although the frequency output of the pulse encoder is not monotonic, as demonstrated in Figure 4.24, the duty cycle of the output pulse train allows one to differentiate between same output frequencies.

The issue of having a non-linear transfer function was not a large concern for the prototype SoC. Since the measured response closely matched the model, a simple lookup table could translate the measured output frequency to its equivalent input voltage. The non-monotonic nature is also not of concern since one can discern whether or not the measured output frequency correlates to an input voltage that is above or below the inflection point. This is illustrated int the average measured results for five chips as shown in Figure 4.25. For larger input voltages, the pulse encoder maintains a very low duty cycle (around 3 to 5%). With smaller input voltages, the duty cycle will rapidly tend towards 100%.

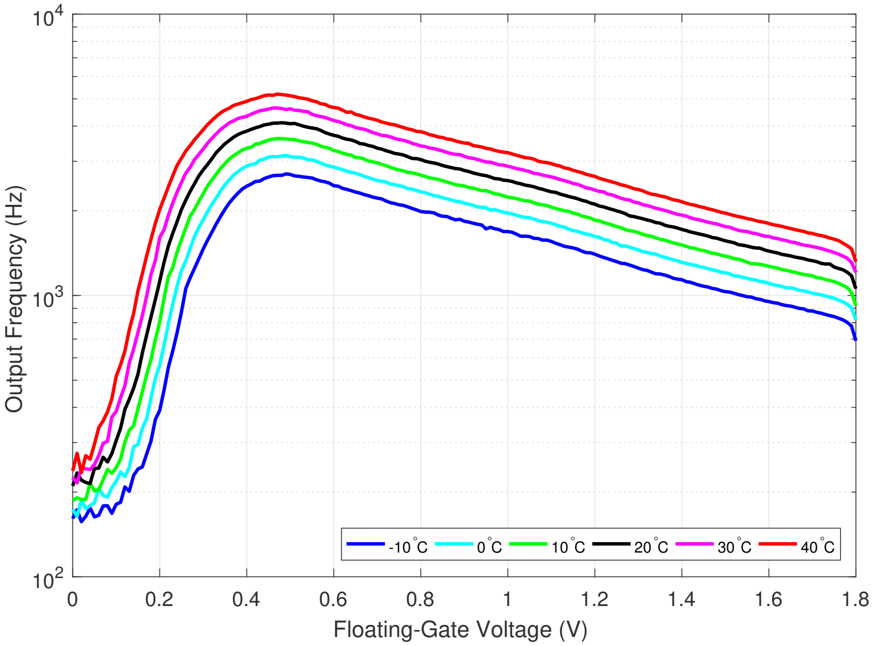

Figure 4.26: The ADC's charge rate is a function of the onboard reference voltages, and suffers from temperature effects.

Another limitation of the implemented pulse encoder is that the biasing voltages depend on the voltage reference of Figure 4.8. Because the 0.5 µm On Semi CMOS process did not have readily available bipolar transistors or other components for creating a bandgap or other high performance voltage reference. The Proportional To Absolute Temperature

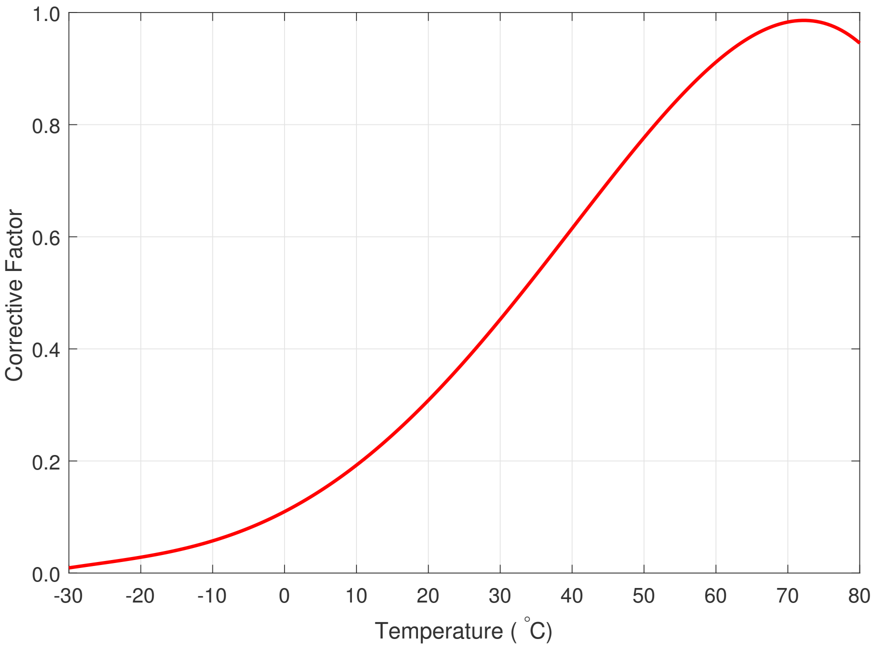

Figure 4.27: The necessary corrective scaling to apply to measurements taken at typical temperatures.

(PTAT) current source generated by the resistor (any combination of internal or external) of Figure 4.8 has a strong temperature dependence that causes the output bias voltages to change rather noticeably. In Figure 4.26, a fabricated PFG chip was tunneled to 1.8 V equivalent charge, and placed in a thermally controlled environment chamber. It was then injected in 1 s intervals with a reference voltage of 4.8 V, which decreased the floating-gate voltage until the pulse encoder output's duty cycle increased to 100%. The general trend that was simulated in Figure 4.24 remains in tact across the tested temperatures, and the general trend shows that higher ambient temperatures result in higher output pulse train frequencies. Also, the inflection point does not change significantly due to changes in temperature. This test procedure was repeated for a litany of temperatures to generate the corrective factor of Figure 4.27. To apply the corrective factor, the measured PFG pulse encoder output frequency shall be divided by the corrective factor corresponding to the ambient temperature during measurement. For example, if the ambient temperature was 10 °C, the measured frequency should be divided by 0.2, or multiplied by a factor of 5. For temperatures below −40 °C and above 90 °C, either the fabricated SoC failed to respond in time, or the laboratory equipment was not rated for testing in those extreme temperature conditions.

Chapter 5

Modified PFG Injector Core

5.1 Modifications from Linear Injector

5.1.1 Motivation

The Piezo-Floating-Gate (PFG) sensor based on the linear injector described in Chapter 4 showed great potential for logging strain levels in structures, as demonstrated in Chapter 6. The induced strain levels on the piezoelectric transducer are a function of the object being monitored. In Figure 5.1a, typical ranges of acceleration for different sensing domains is plotted; although there is some separation between the domains across various acceleration ranges, it remains an arduous task to develop a machine learning algorithm that could successfully detect the domain [84, 85]. One method for making such a task easier would be to add extra features of the input stimuli to the data-logging. In Figure 5.1b, the benefit of adding the frequency information of the input stimuli is demonstrated, as the clustering of domains becomes more readily visible. This improved clustering drives our requirement for adding frequency discriminatory data-logging to the existing PFG sensor.

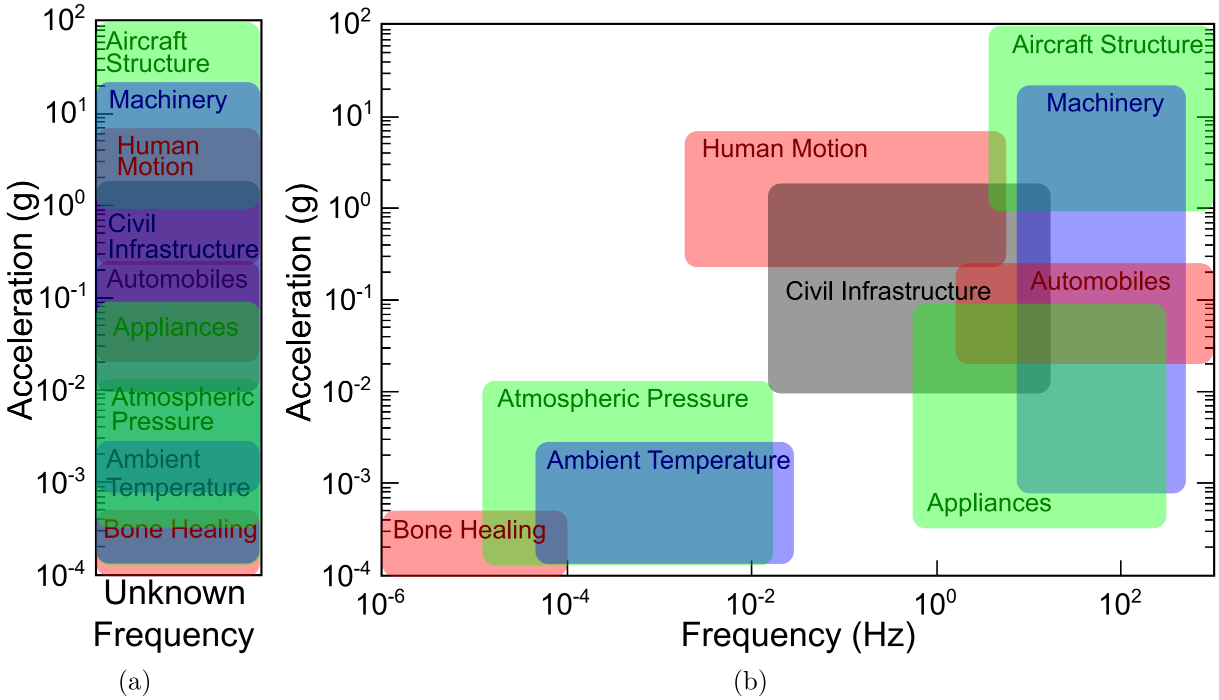

Figure 5.1: When given only the acceleration information (a), it is difficult to ascertain the source of the stimuli. (b) A plot showing some typical frequencies encountered when sensing in the natural world makes it easier (recreated from [83]).

5.1.2 Proposed Architecture

As illustrated in Figure 5.1, having a means to filter the input signal to the PFG could allow much greater capabilities in specificity of logged information. If ignoring the human motion and bone healing domains, it could be useful to have a low-pass filter that has a cutoff near 50 Hz for demarcating between civil infrastructure and automobiles. Another useful cutoff might be near 50 mHz to discern between civil infrastructure induced acceleration and those from atmospheric pressure or ambient temperature.

One of the simplest circuits for low-pass filtering is a passive RC as shown in Figure 5.2a, the equivalent Z-domain circuit is shown in Figure 5.2b. From basic circuit theory, one can

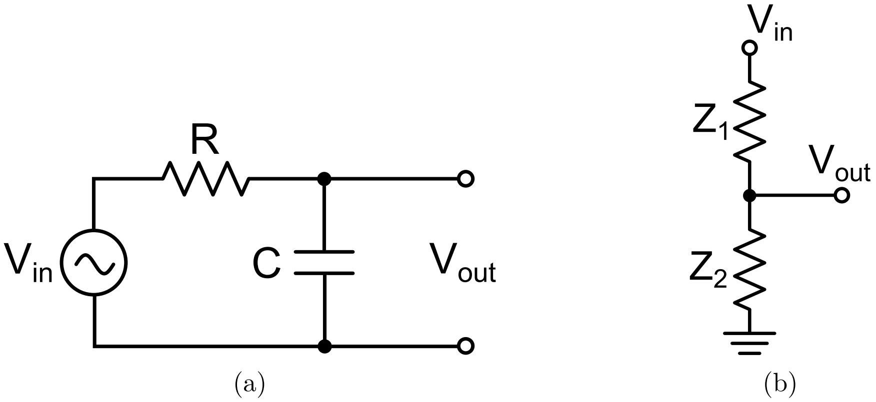

Figure 5.2: (a) A basic circuit to implement a passive low-pass filter (b) the equivalent circuit using impedances.

say that

$$V_{\text{out}} = V_{\text{in}}\frac{Z_2}{Z_1 + Z_2} = \frac{X_{\text{C}}}{\sqrt{R^2 + X_{\text{C}}^2}}, \quad X_{\text{C}} = \frac{1}{2\pi f C}. \tag{5.1}$$

When considering the $-3\,\text{dB}$ cutoff frequency, one can simply look at

$$f_{\text{c}} = \frac{1}{2\pi RC} = \frac{1}{2\pi\tau}. \tag{5.2}$$

For a relatively low frequency of 10 Hz, this would suggest the need for a time constant τ of around 1.59×10^{-2}. On the 0.5 µm process, integrated passive resistors are difficult to incorporate once they exceed 10 MΩ, similarly there is an upper bound to useful sized capacitors around 10 pF. Even with integrated resistance and capacitances near these limits, a time constant of 10^{-5} would be achieved — much too small for implementing the 10 Hz cutoff, let alone the sub-hertz target we have outlined in Section 5.1.1. To alleviate this constraint, an active resistor can be built using a transconductance amplifier in negative feedback. An active capacitive element could also be used, but to reduce the circuit complexity, the active low-pass filter topology of Figure 5.3 is settled upon.

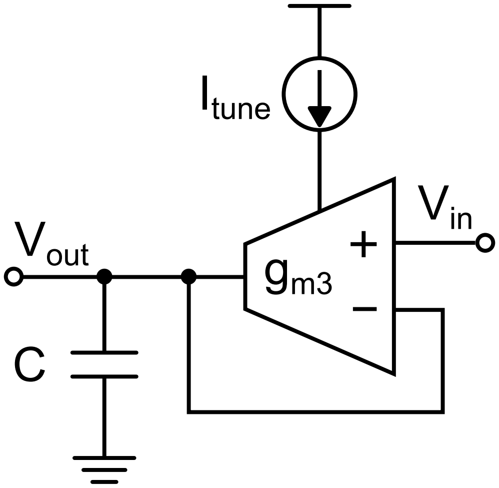

Figure 5.3: Implementing a low-pass filter using a current conveyor as an active element to realize a large resistance.

The input impedance of a transconductance amplifier in negative feedback is simply $\frac{1}{g_{\mathrm{m}}}$, which can be adjusted by tuning I_{Bias}. As reported in the jump resonance study, we have designed an amplifier that can tune between 0.8 nS to 32 nS of transconductance with I_{Bias} in the single digit nano amperes. Thus, with a simple negative feedback transconductance amplifier we can get resistance on the order of 1 GΩ, thus giving a time constant on the order of 10^{-2} when combined with a large passive capacitor. As an extension to this approach, it may be possible to replace the capacitor with an active capacitor as well, which could multiply the effective capacitance by as much as 10^5 [86]. With such an extension, the time constant τ would be on the order of 10^3, yielding a cutoff frequency less than 1 mHz. Using the equivalent noise model for a transconductor, where

$$\frac{\Delta \overline{v_{\mathrm{n}}}^2}{\Delta f} = E_{\mathrm{N}} \times 4kT\frac{1}{g_{\mathrm{m}}}, \tag{5.3}$$

and assuming that supply voltage excess (E_{V}) and supply current excess (E_{I}) factors are unity, then the following equations will detail the active low-pass filer of Figure 5.3. Of note is that the power dissipation of this filter when configured to have a signal-to-noise ratio of

30 dB is a mere $33\,\mathrm{aW\,kHz^{-1}}$, small enough to be negligible for our use case [87].

$$f_{\mathrm{c}} = \frac{g_{\mathrm{m}}}{2\pi C} \tag{5.4}$$

$$\mathrm{NoisePower} = \overline{v_{\mathrm{on}}{}^{2}} = E_{\mathrm{N}} \times \frac{kT}{C} \tag{5.5}$$

$$\mathrm{MinimumCapacitance} = C = E_{\mathrm{N}} \times 8kT\frac{\mathrm{SNR}}{V_{\mathrm{pp}}^{2}} \tag{5.6}$$

$$\mathrm{Power} = E_{\mathrm{V}}E_{\mathrm{I}}E_{\mathrm{N}} \times 8kTf_{\mathrm{C}}(\mathrm{SNR}) \tag{5.7}$$

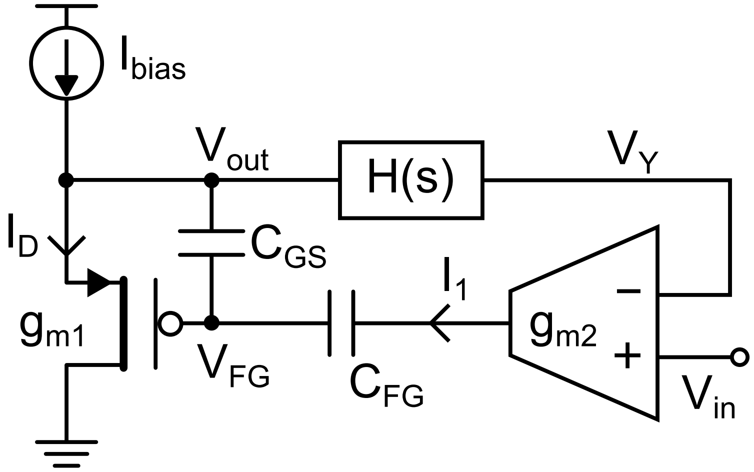

Figure 5.4: Proposed modification to the linear injector from Section 4 that adds an $H(s)$ to the feedback loop.

The low-pass filter block of Figure 5.3 is denoted as $H(s)$ and is added to the linear injector core's feedback path. Figure 5.4 shows the modified architecture of the linear injector with additional filtering capabilities endowed.

5.1.3 Analysis

To begin analyzing the circuit response of Figure 5.4, several transfer characteristics of the circuit need to be laid out before proceeding to combine them algebraically. In this analysis,

$H(s)$ is implemented using Figure 5.3, and its capacitance will be denoted by C_{Y}, the V_{out} as V_{Y} and the V_{in} is the same net as V_{out} of Figure 5.4.

$$V_{\mathrm{out}} = (I_{\mathrm{b}} - I_{\mathrm{gs}} - I_{\mathrm{D}})\frac{1}{sC_{\mathrm{FG}}} \tag{5.8}$$

$$V_{\mathrm{Y}} = I_{\mathrm{Y}}\frac{1}{sC_{\mathrm{y}}} \tag{5.9}$$

$$I_{\mathrm{FG}} = (V_{\mathrm{X}} - V_{\mathrm{FG}})\frac{1}{sC_{\mathrm{FG}}} \tag{5.10}$$

$$I_{\mathrm{gs}} = sC_{\mathrm{gs}}(V_{\mathrm{FG}} - V_{\mathrm{out}}) \tag{5.11}$$

$$I_{\mathrm{D}} = g_1 V_{\mathrm{FG}} \tag{5.12}$$

$$I_{\mathrm{Y}} = g_3(V_{\mathrm{out}} - V_{\mathrm{Y}}) \tag{5.13}$$

$$I_{\mathrm{X}} = (V_{\mathrm{in}} - V_{\mathrm{Y}})\, g_2 = g_2\left(V_{\mathrm{in}} - I_{\mathrm{Y}}/sC_{\mathrm{Y}}\right) = g_2 V_{\mathrm{in}} - \frac{g_2 g_3}{sC_{\mathrm{Y}}}\left(V_{\mathrm{out}} - V_{\mathrm{Y}}\right) \tag{5.14}$$

$$V_{\mathrm{X}} = I_{\mathrm{X}}\left(\frac{1}{sC_{\mathrm{FG}}}\right) = \frac{g_2}{sC_{\mathrm{FG}}}(V_{\mathrm{in}} - V_{\mathrm{out}}) \tag{5.15}$$

By merging these expressions, the following circuit response for the output voltage is derived:

$$V_{\mathrm{out}} = \left(I_{\mathrm{b}} - (V_{\mathrm{FG}} - V_{\mathrm{out}})\, sC_{\mathrm{gs}} - g_1 V_{\mathrm{FG}}\right)/sC_{\mathrm{L}}. \tag{5.16}$$

Assume g_1 is an ideal source-follower $\therefore V_{\mathrm{out}} \equiv V_{\mathrm{FG}} \rightarrow I_{\mathrm{b}} = I_{\mathrm{FG}}$. Combining several of the previous equations into a single expression:

$$V_{\mathrm{out}} = \frac{1}{sC_{\mathrm{L}}}\left(sC_{\mathrm{FG}}\left[\frac{g_2}{sC_{\mathrm{FG}}}\left(V_{\mathrm{in}} - \frac{V_{\mathrm{out}}}{1 + C_{\mathrm{Y}}/g_3}\right) - V_{\mathrm{out}}\right] - g_1 V_{\mathrm{out}}\right). \tag{5.17}$$

Expand the terms and consolidating the expression will result in the final transfer function detailed in (5.22). Keeping the denominator common, one can observe that there is a low-pass component ($g_2 g_3$) and a high-pass component ($s g_2 C_\mathrm{L} C_\mathrm{Y}$).

$$V_\mathrm{out} = \frac{s g_2 C_\mathrm{FG}}{s^2 C_\mathrm{L} C_\mathrm{FG}} V_\mathrm{in} - \left(\frac{s g_2 C_\mathrm{FG}}{s^2 C_\mathrm{L} C_\mathrm{FG}}\right)\left(\frac{V_\mathrm{out}}{1 + s C_\mathrm{Y}/g_3}\right) - \frac{s C_\mathrm{FG}}{s C_\mathrm{L}} V_\mathrm{out} - \frac{g_1}{s C_\mathrm{L}} V_\mathrm{out} \tag{5.18}$$

$$V_\mathrm{out}\left[1 + \frac{g_1}{s C_\mathrm{L}} + \frac{C_\mathrm{FG}}{C_\mathrm{L}} + \frac{g_2}{s C_\mathrm{L}}\left(\frac{1}{1 + s C_\mathrm{Y}/g_3}\right)\right] = \frac{g_2}{s C_\mathrm{L}} V_\mathrm{in} \tag{5.19}$$

$$\frac{V_\mathrm{out}}{V_\mathrm{in}} = \left(\frac{g_2}{s C_\mathrm{L}}\right) \div \left(1 + \frac{C_\mathrm{FG}}{C_\mathrm{L}} + \frac{g_2}{s C_\mathrm{L} + s^2 C_\mathrm{L} C_\mathrm{Y}/g_3}\right) \tag{5.20}$$

$$= \frac{g_2}{s C_\mathrm{FG} + s C_\mathrm{L} + \dfrac{g_2}{1 + s C_\mathrm{L} C_\mathrm{Y}/g_3}} \tag{5.21}$$

$$= \frac{g_2 g_3 + s g_2 C_\mathrm{L} C_\mathrm{Y}}{s^2\left(C_\mathrm{FG} C_\mathrm{L} C_\mathrm{Y} + C_\mathrm{L}^2 C_\mathrm{Y}\right) + s g_3\left(C_\mathrm{FG} + C_\mathrm{L}\right) + g_2 g_3} \tag{5.22}$$

Plugging in nominal values for the capacitance and transconductances as simulated on an extracted layout view of the circuit, the bode plot of Figure 5.5 is generated. The values of g_2 =1 n, g_3 =20 n, $\mathrm{C_{FG}}$ =1 pF, $\mathrm{C_L}$ =1 pF, and $\mathrm{C_Y}$ =1.28 pF results in exactly 500 mHz as the −3 dB cutoff frequency.

5.2 Measurement Results

5.2.1 Single Configuration

The chip was designed in using Cadence tools and sent to MOSIS for fabrication with ON Semiconductor's 0.5 µm process. A micrograph giving a chip-level view of the fabricated

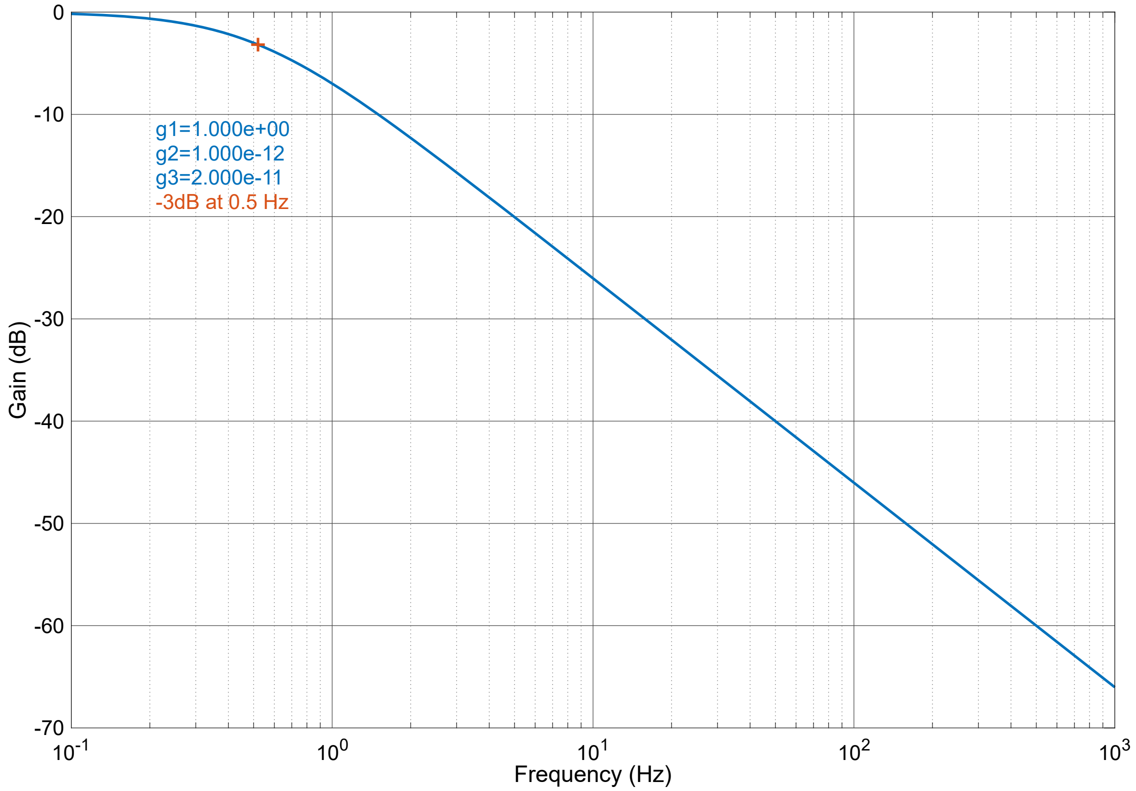

Figure 5.5: Bode plot for Figure 5.4 showing a low-pass response.

die is given as Figure 5.6. For testing, a computer was used to interface with a Rigol function generator, a Tektronix oscilloscope, a Keithley SMU, and a custom test station. In Figure 5.7, the input signal to the chip is shown in blue, and the buffered analog output of a single channel is plotted in orange. To get this response, the input was configured to have a 500 mV peak-to-peak amplitude and a sinusoidal shape with frequency 34.61 Hz. The active resistor element of Figure 5.4 is tuned by I_{tune}, which is controlled through a PMOS current source with a gate bias of 3.4 V. The entire chip was operating on a supply voltage of 4 V from the SMU. The output is measured on the 8 bit oscilloscope that was programmed to have a window size approximately equal to 10 periods of the input sin wave.

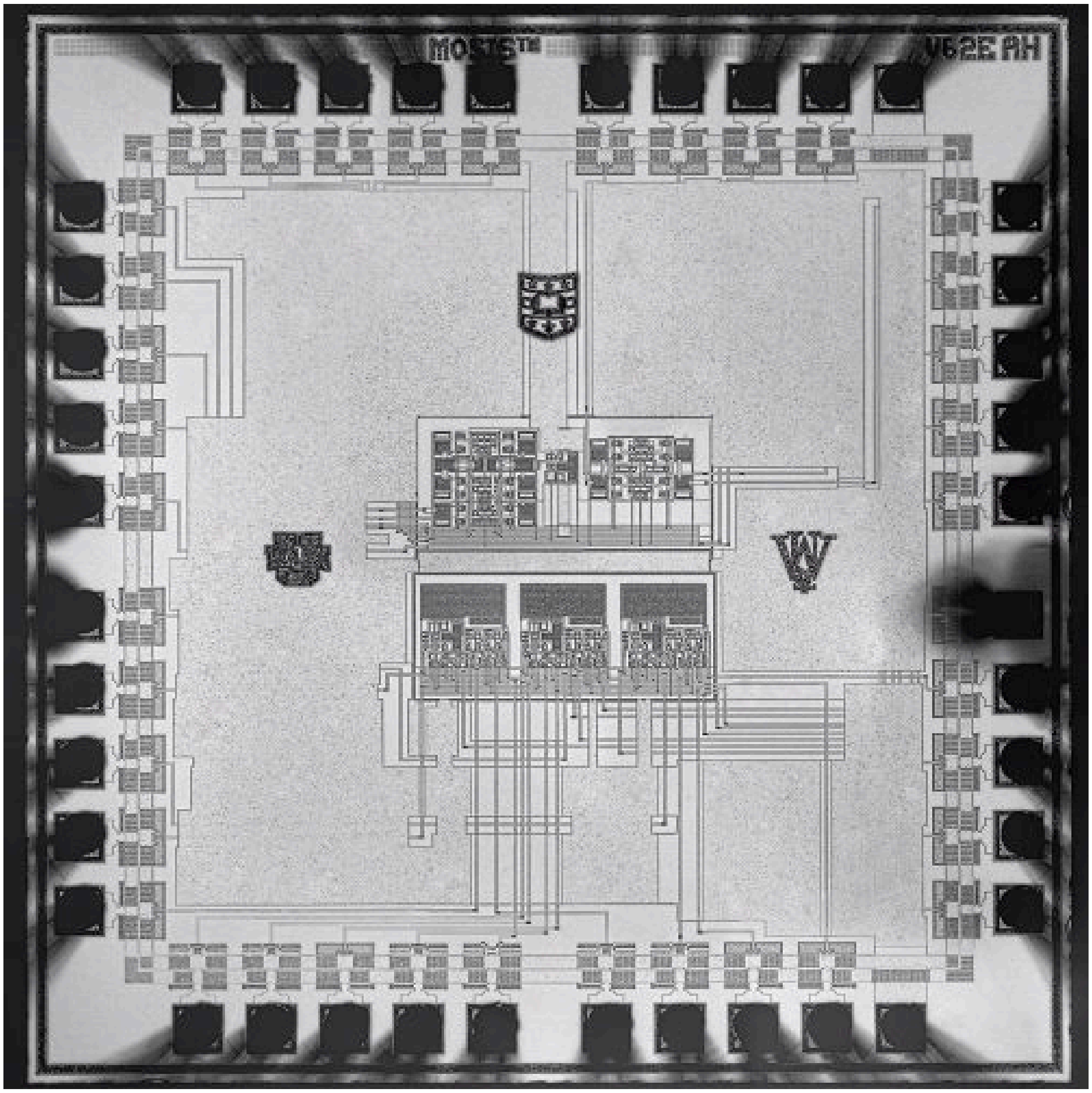

Figure 5.6: A micrograph of the fabricated chip on the 0.5 µm CMOS process by ON Semiconductor through MOSIS.

What Figure 5.7 shows is that there is some amount of gain present in the channel configuration, and that it is not a one-to-one transfer function. To better investigate the circuit behavior under these biasing conditions, the input frequency was modulated between 500 mHz and 100 kHz. In Figure 5.8, Figure 5.9, and Figure 5.10, the response at select frequencies (denoted by the text label near the top of each subplot) is presented. To save space, the y-axis has been fixed to 1 V to 2.2 V and the x-axis is selected to show approximately two

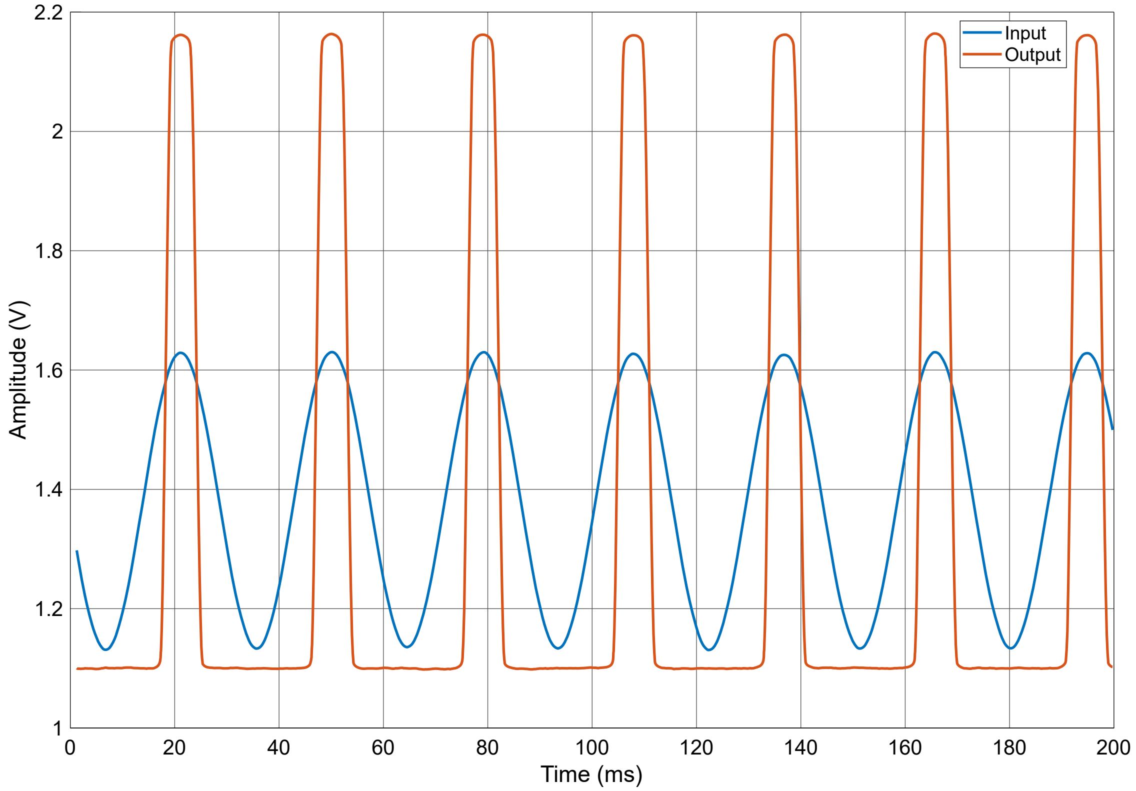

Figure 5.7: The measured input (500 mV peak-to-peak) and output voltages for the modified injector that is tuned to 34.61 Hz. I_{tune} of Figure 5.4 is set using 3.4 V on a PMOS gate supplied by 4 V.

and half periods of the input signal. The plots show that at a low input frequency the output is less than 1 V and for sub-10 kHz inputs there is some gain in the peaks, but not across the entire waveform. For signals above the 10 kHz range there appears to be some attenuation.

When considering the sensitivity of the modified linear injector core to select frequencies, it might be useful to look at the amount of time that the output signal exceeds the input signal. Because the Impact-Ionized Hot-Electron Injection (IIHEI) process is exponential, the input reference could be set with a DC offset near the threshold for noticeable injection. If the input stimuli's AC component is attenuated, then the input reference will never exceed the threshold, and there won't be any significant injection (i.e. data-logging). For times when the modified injector has larger outputs, the AC component could nudge the input reference

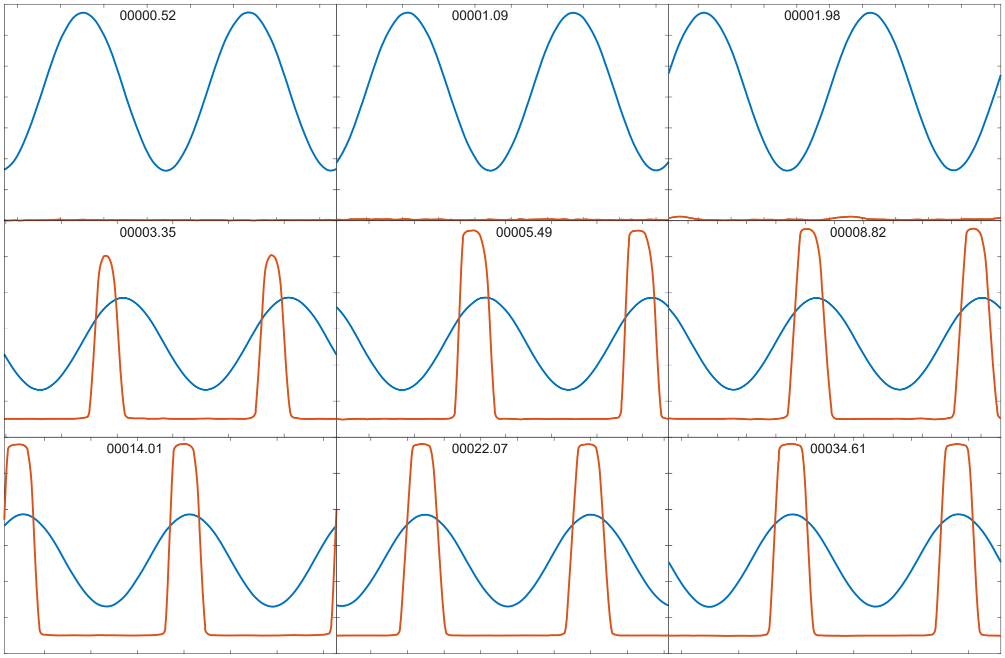

Figure 5.8: Raw input and output data collected for low input frequencies using configuration from Figure 5.7.

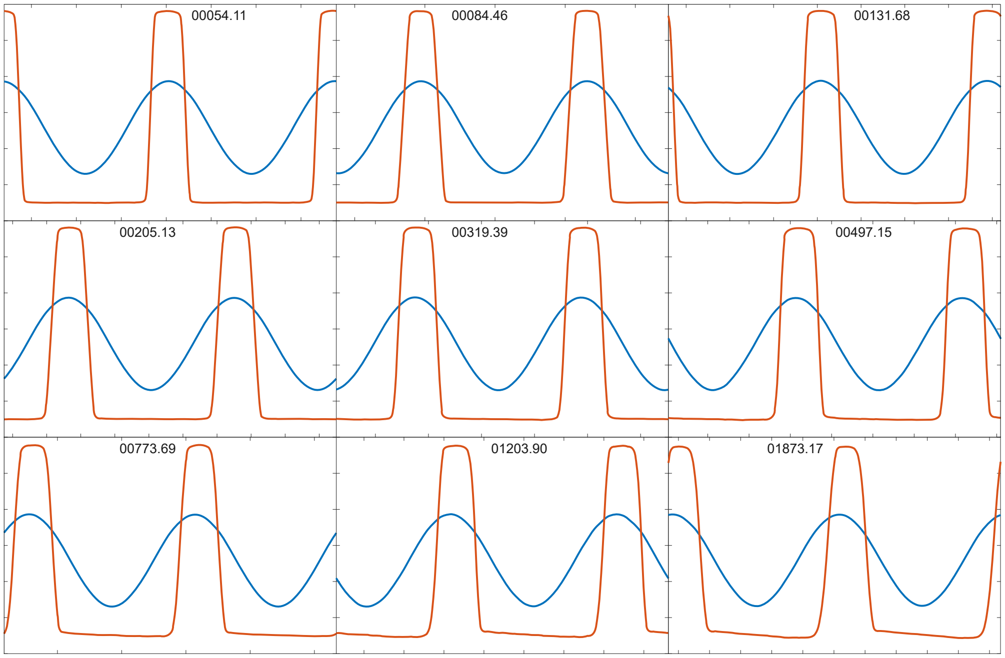

Figure 5.9: Raw input and output data collected for medium input frequencies using configuration from Figure 5.7.

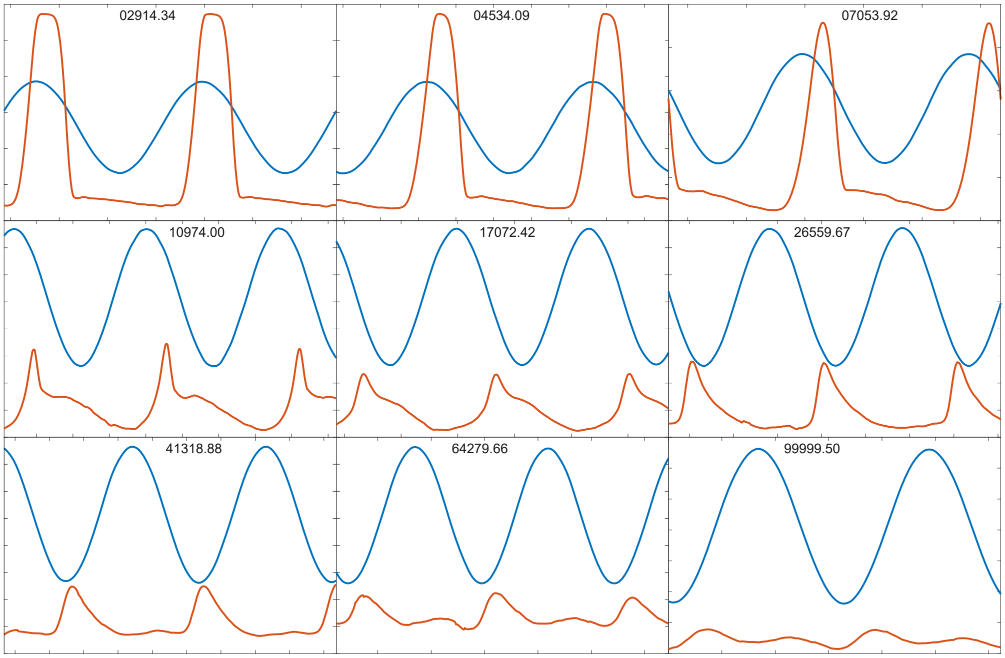

Figure 5.10: Raw input and output data collected for high input frequencies using configuration from Figure 5.7.

high enough that a recordable amount of injection occurs. Therefore, plots showing when the output exceeds the input amplitude are shown in Figure 5.11, Figure 5.12, and Figure 5.13. Similar to the previous figures, the input stimuli's frequency is shown near the top of each subplot in black text. The blue text indicates the ratio of time that the output exceeds the input.

5.2.2 Aggregate Plots

Several biasing conditions of the modified core were tested. Similar to the basic configuration of Figure 5.7, Figure 5.14 decreases the gate voltage that controls I_{tune} to 3.0 V, thereby increasing the supply current to the transconductance. Figure 5.15 further decreases the gate voltage to 2.6 V. Just showing the lower input frequencies in these two figures, it is apparent that the filtering characteristics have changed.

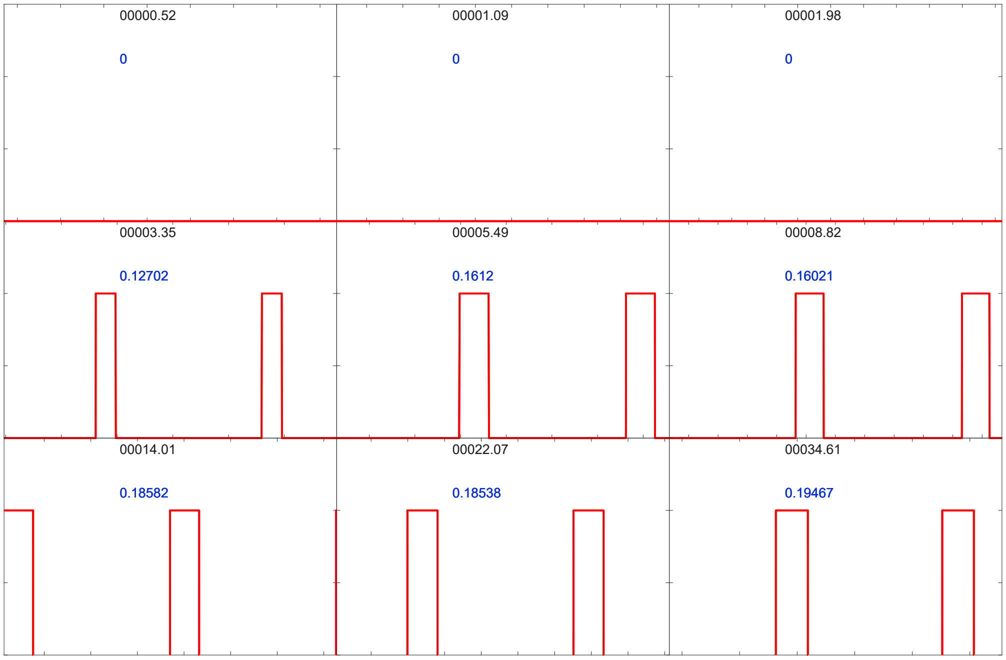

Figure 5.11: True or false plots showing when output exceeds input for low input frequencies using configuration from Figure 5.7.

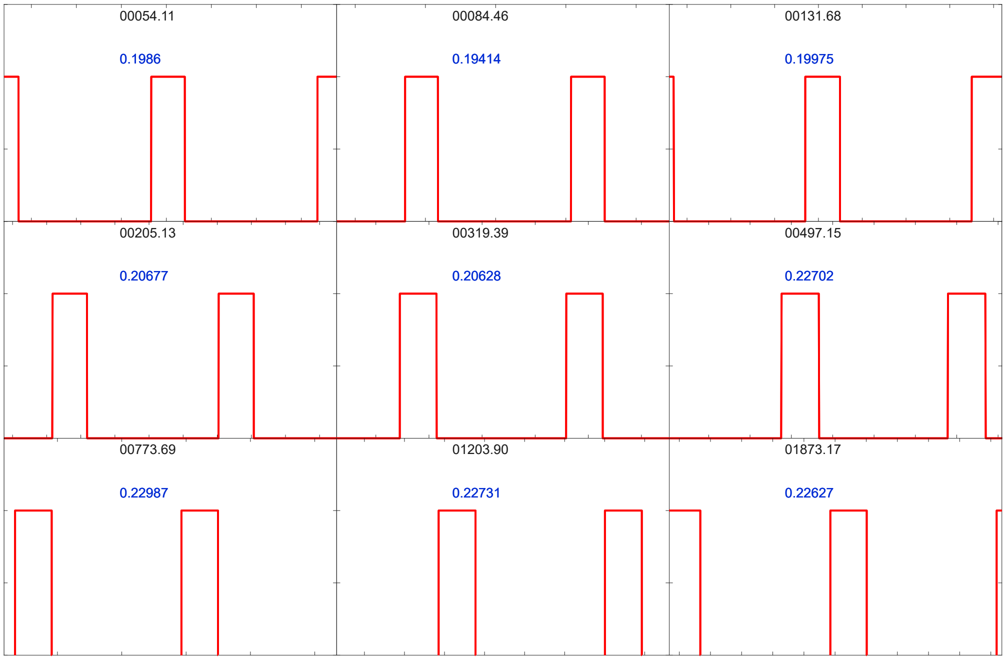

Figure 5.12: True or false plots showing when output exceeds input for medium input frequencies using configuration from Figure 5.7.

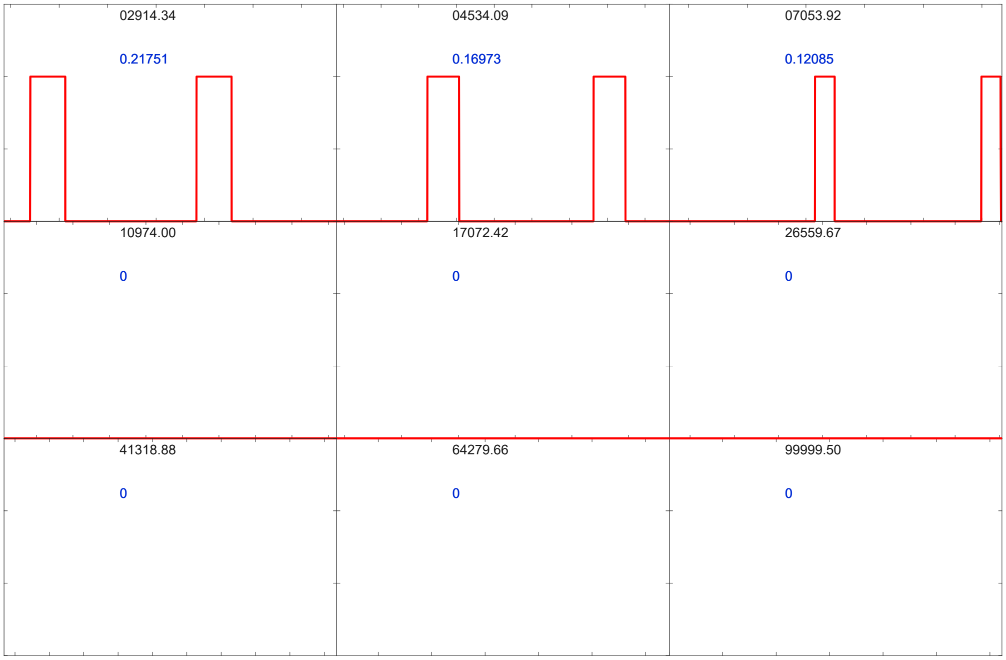

Figure 5.13: True or false plots showing when output exceeds input for high input frequencies using configuration from Figure 5.7.

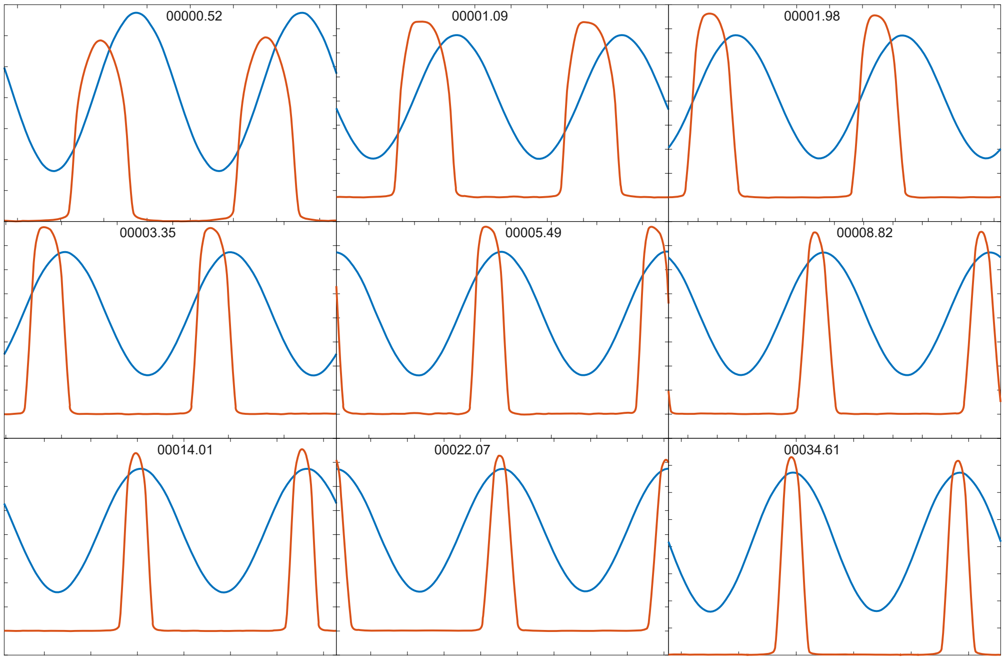

Figure 5.14: Similar to Figure 5.8, but with a larger $\mathrm{I}_{\mathrm{tune}}$.

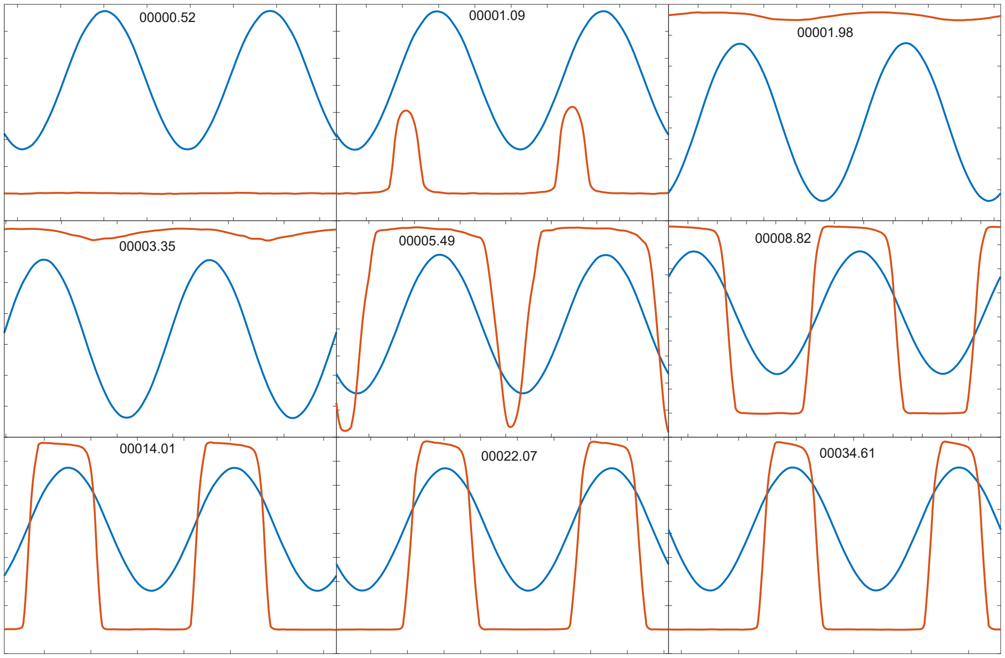

Figure 5.15: Similar to Figure 5.14, but with a larger I_{tune}.

To approximate the useful transfer characteristics of different configurations, Figure 5.16 plots the mean ratio of when the output exceeds the input (as collected from Figure 5.11, Figure 5.12, and Figure 5.13). One can observe that at low I_{tune} (plotted in yellow as 3.40) there is a flat bandpass like response. For a slightly higher current (orange, 3.0 in figure), the transfer function appears to be a low-pass, or perhaps a bandpass with the lower cutoff frequency below 500 mHz. Using even more current (blue, 2.60 in figure), the bandpass is no longer flat, and sharper trends are observed. Figure 5.17 repeats the test results for a smaller input amplitude of 100 mHz and Figure 5.18 considers the case of a larger input amplitude of 1 V. Note that some data points in Figure 5.17 may not have been recorded properly during the automated testing that iterated over thousands of test configurations across several days. It should also be noted that these plots are not the same as traditional transfer plots as in the bode plot of Figure 5.5, thus a direct comparison cannot be drawn.

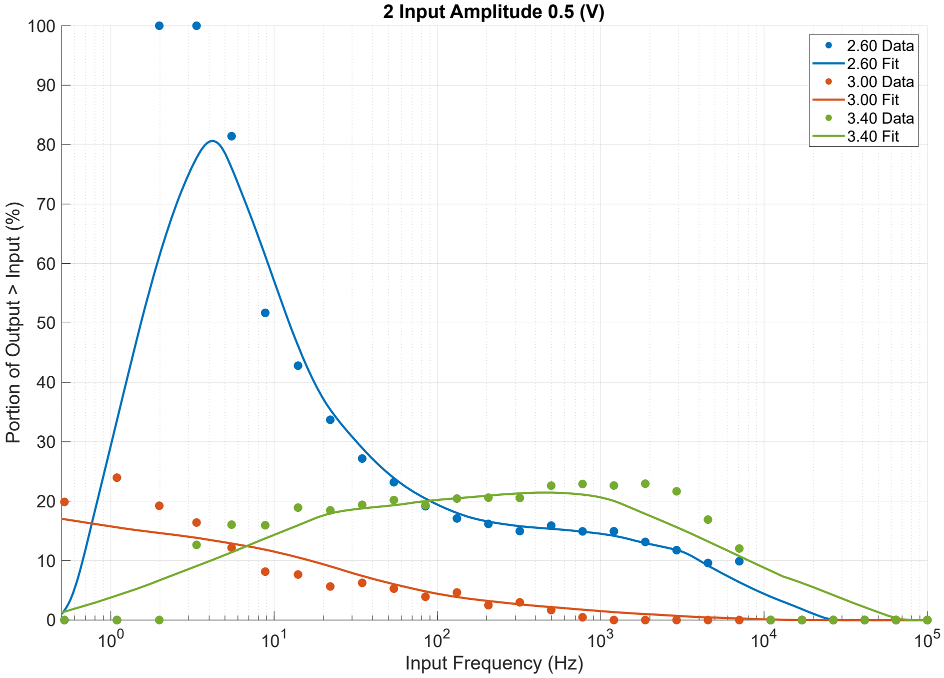

Figure 5.16: Plotting the aggregate response of Figure 5.11, Figure 5.12, and Figure 5.13 for three I_{tune} values.

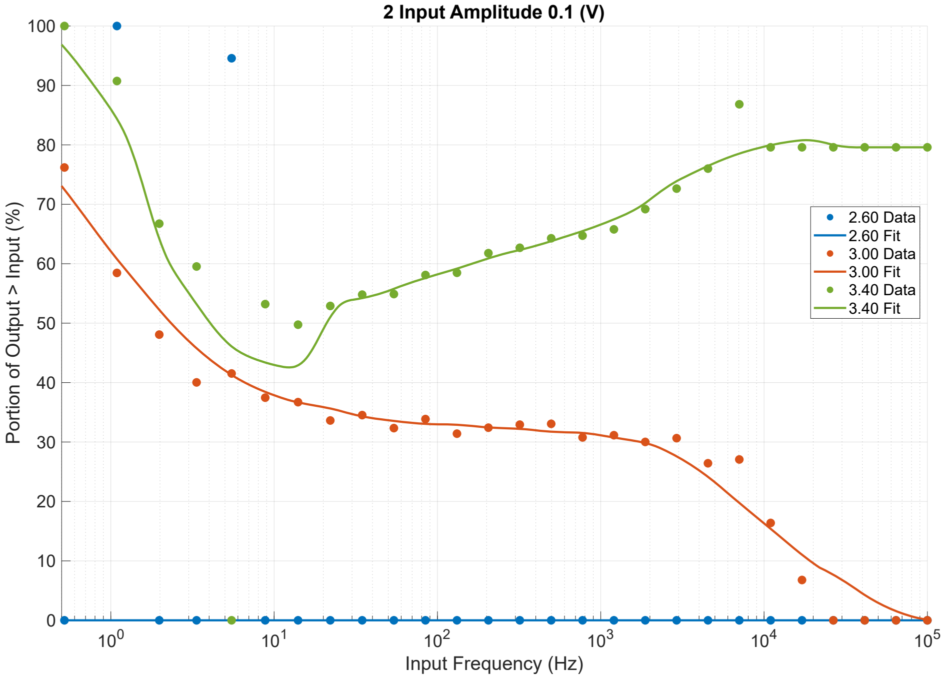

Figure 5.17: As in Figure 5.16, but now with input amplitudes of 100 mV.

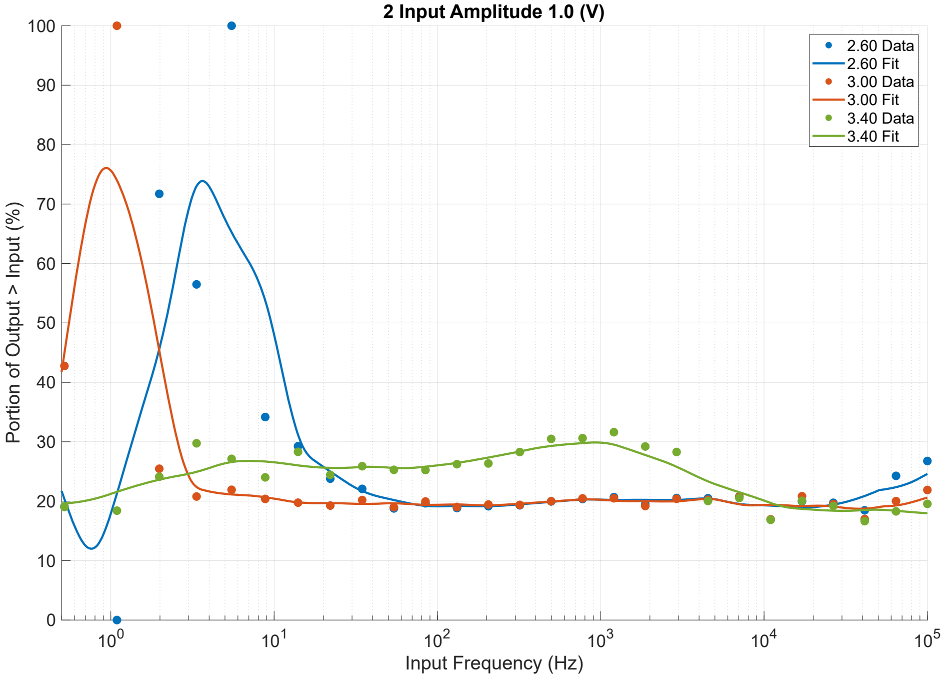

Figure 5.18: As in Figure 5.16, but now with input amplitudes of 1 V.

5.3 Post-Analyis

5.3.1 Restricted Injection Filter

Contrary to the approximations presented in Section 5.1.3, the measurement results of Section 5.2.2 displayed a more bandpass like response. To achieve a bandpass like response following similar analysis techniques, the circuit in Figure 5.19 could be used.

Applying Kirchoff's current law to the net at V_{FG},

$$(V_{\mathrm{in}} - V_{\mathrm{FG}}) \div \left(\frac{1}{sC_{\mathrm{in}}}\right) + (V_{\mathrm{X}} - V_{\mathrm{FG}}) \div \left(\frac{1}{sC_{\mathrm{FG}}}\right) = (V_{\mathrm{FG}} - V_{\mathrm{out}}) \div \left(\frac{1}{sC_{\mathrm{gs}}}\right). \tag{5.23}$$

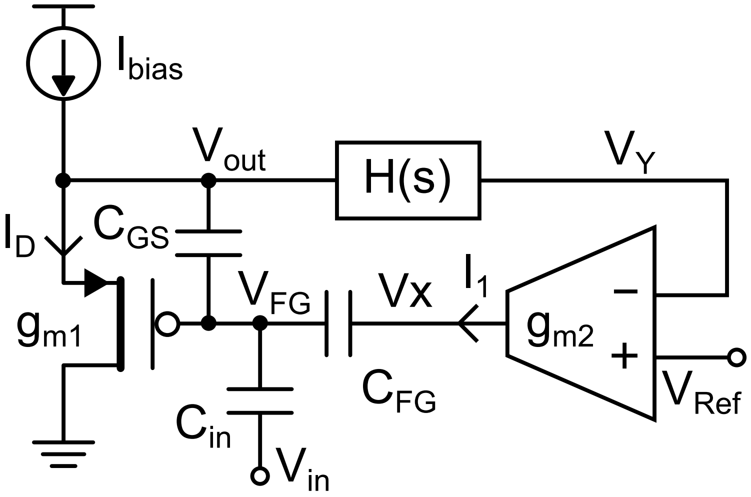

Figure 5.19: An alternative input as compared to that of Figure 5.4.

Again, assuming that g_1 is an ideal source-follower $\therefore V_{\mathrm{out}} \equiv V_{\mathrm{FG}}$, (5.23) simplifies to:

$$0 = sC_{\mathrm{in}}V_{\mathrm{in}} - V_{\mathrm{FG}}sC_{\mathrm{in}} + sC_{\mathrm{FG}}V_{\mathrm{X}} - V_{\mathrm{FG}}sC_{\mathrm{FG}}, \tag{5.24}$$

$$sC_{\mathrm{in}}V_{\mathrm{in}} + sC_{\mathrm{FG}}V_{\mathrm{X}} = V_{\mathrm{FG}}(sC_{\mathrm{in}} + sC_{\mathrm{FG}}). \tag{5.25}$$

Additionally, the voltage at the output of the transconductance g_2 is approximated as:

$$V_{\mathrm{X}} = \frac{g_2}{sC_{\mathrm{FG}}}\left(V_{\mathrm{Ref}} - H(s)V_{\mathrm{FG}}\right). \tag{5.26}$$

Using this approximation, (5.25) expands thusly

$$\begin{aligned}
sC_{\mathrm{in}}V_{\mathrm{in}} + g_2V_{\mathrm{Ref}} - g_2H(s)V_{\mathrm{FG}} &= V_{\mathrm{FG}}(sC_{\mathrm{in}} + sC_{\mathrm{FG}}) && (5.27)\\
g_2V_{\mathrm{Ref}} + sC_{\mathrm{in}}V_{\mathrm{in}} &= V_{\mathrm{FG}}\left[s\left(C_{\mathrm{in}} + C_{\mathrm{FG}}\right) + g_2H(s)\right] && (5.28)\\
g_2V_{\mathrm{Ref}} + sC_{\mathrm{in}}V_{\mathrm{in}} &= g_2V_{\mathrm{FG}}\left[\frac{s}{g_2}(C_{\mathrm{in}} + C_{\mathrm{FG}}) + H(s)\right] && (5.29)
\end{aligned}$$

Finally, the output expression for Figure 5.19 is given as:

$$V_{\text{out}} = \frac{V_{\text{Ref}}}{\frac{s}{g_2}(C_{\text{in}} + C_{\text{FG}} + H(s))} + \frac{sC_{\text{in}}V_{\text{in}}/g_2}{\frac{s}{g_2}(C_{\text{in}} + C_{\text{FG}} + H(s))}. \tag{5.30}$$

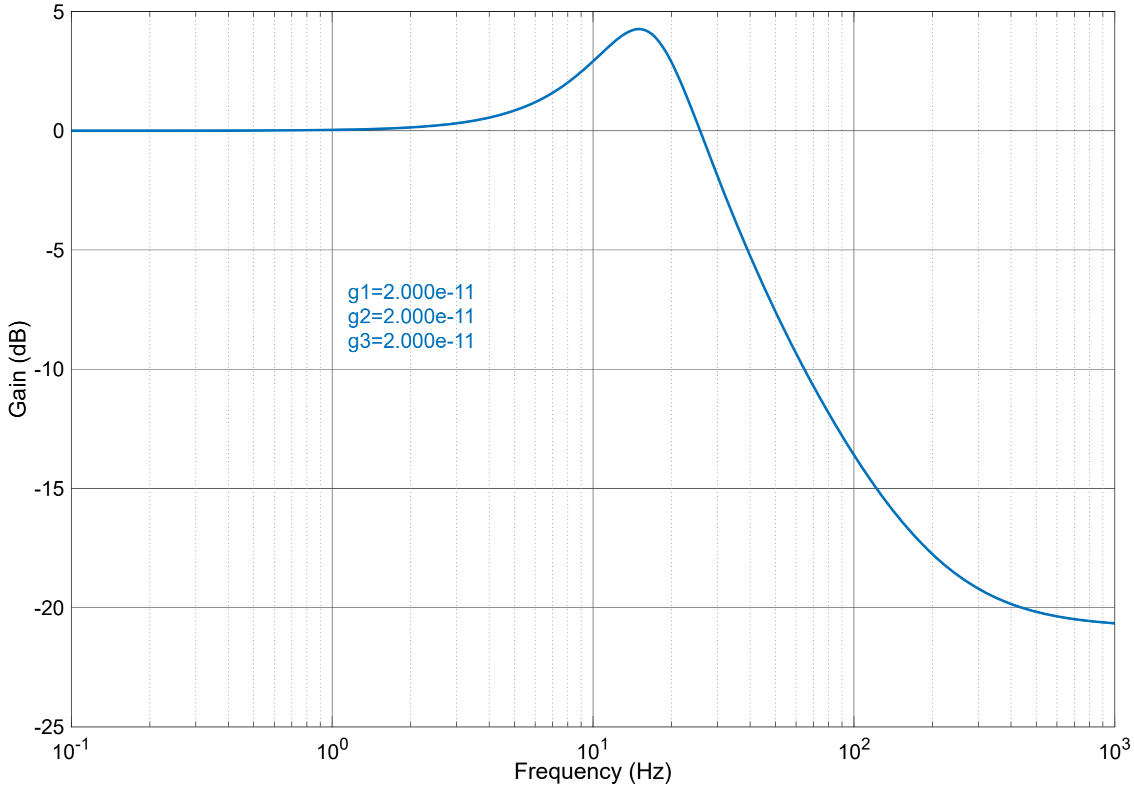

Figure 5.20: Bode plot showing the response for the conditions given in Figure 5.19.

The resulting bode plot is presented in Figure 5.20, and the simulated response appears to be a low-pass filtering, but could also be used as a bandpass filter near 15 Hz. It is likely that these approximations in the analysis are neglecting important capacitance or other feedback mechanisms that would cause the transfer functions to have a much stronger high-pass element as observed during measurement. These results may appear in future literature [88].

5.3.2 Improved Sensitivity

The alternative configuration of Figure 5.19 also introduces an interesting method for providing improved input stimuli sensitivity. When starting this dissertation, it was envisioned that the entire sensing platform, including wireless interrogation, would operate in a self-powered mode. Since that time, digital circuits have improved 33 fold with respect to the number of operations per watt (looking at GFLOPS/W of the top supercomputer on Green 500). Commercial entities have also vastly improved the energy efficiency of wireless communication as smartphones became common place and Moore's law marched on. Accordingly, in Chapter 6, the platform has moved from completely self-powered solution, to one that relies on battery-powered wireless communication. Leveraging the already present battery allows the PFG to power onboard references and even its feedback amplifier whilst sipping mere nano amperes. Even with an always-on reference and amplifier drawing current, most battery's operational lifespan would be dominated by the self-dischage leakage current. One of the best primary lithium-metal cells on the market (Tadiran LiSOCl2) has a shelf life of 40 years, thus a 100 mAh battery has a constant leakage current of approximately 300 nA. In the case of rechargeable Lithium-ion and other more common batteries, this leakage rate is several times larger.

With the PFG chip configured as constantly-on, an input stimuli can capacitively couple to the floating-gate to directly modulate the gate-source voltage. If the modulation increases the voltage, it will increase the chance of IIHEI occurring. This has been verified as shown in Figure 5.21, for three conditions for multiple injection cycles. For the null case, 1 V is applied to C_{in}, but the feedback of g_{m2} is disabled, the resulting green plot shows no data-logging. For the red plot, injection was enabled, but the input to the capacitor was tied to ground. It will inject since the reference voltage is 5.823 V, albiet at a reduced rate as tested in Chapter 4.

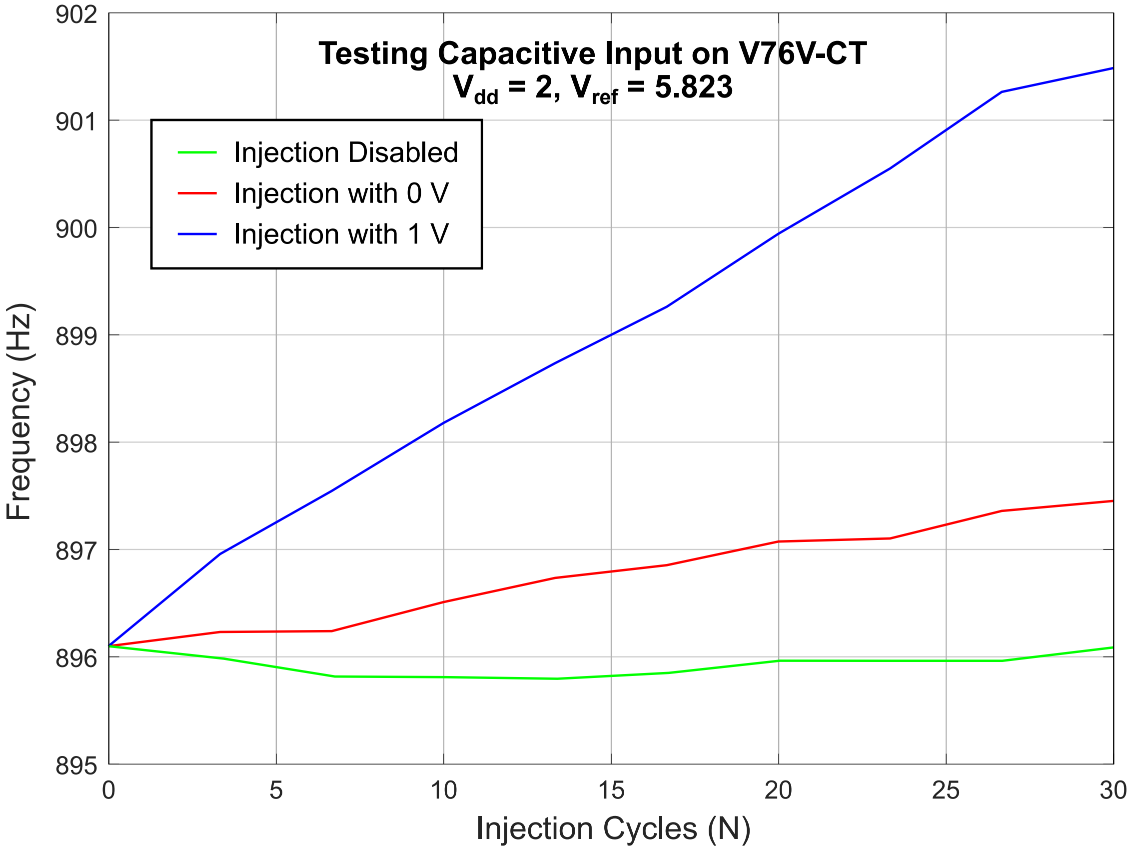

Figure 5.21: Modulating V_{in} of Figure 5.19 allows extended sensitivity of the PFG injector.

Finally, an input voltage of 1 V was applied during the injection cycles, with the injection pin also enabled. This plot shown in blue on Figure 5.21 logs data much more rapidly than when the input capacitor was tied to ground. This testing verifies that stimuli smaller than the reported minimum sensitive of the previous PFG design (6 V to 7 V) can lead to injection. A more comprehensive study of using this mechanism for detection and logging of mV level stimulation is left to future cohorts of the Adaptive Integrated Microsystems laboratory.

Chapter 6

Transfer To Practice

Deploying the Analog Frontend

6.1 Piezoelectric Transducer

Before the Piezoelectric-Floating-Gate (PFG) sensor can be deployed, it needs to be coupled with a suitable piezoelectric transducer [89]. In this section, testing done in conjunction with Professor Nizar Lajnef's research team at Michigan State University, on the characteristics of potential piezoelectrics, is presented. Specifically, this chapter will focus on the deployment of the analog frontends for Structural Health Monitoring (SHM) applications. Based on discussions with these domain experts, many target applications would require the detection of micro-strain energy from structural elements such as steel beams, or asphalt. The type of transducer that is coupled to the PFG sensor will affect the amount of information that is logged. In a controlled laboratory setting, the behavior of three different piezoelectric transducers is investigated. Primarily, we focus on piezoelectric ceramic discs (PZTs) that were sourced from STEMINC Incorporated, with properties as specified in Table 6.1. For the purpose of this section, the considered piezoelectric discs are labeled as PZT1, PZT2, and PZT3. PZT1 and PZT3 have the same diameter of 20 mm, and PZT2 is larger with a diameter of 25 mm. PZT2 and PZT3 have the same material thickness (height) of 700 µm, and PZT1 has a larger height of 800 µm. In Figure 6.1a, a diagram of the testing apparatus is illustrated, and Figure 6.1b shows how a test specimen is placed in an MTS device for precision loading. Figure 6.1c gives a close-up of the PZTs affixed to the an aluminum test specimen of dimensions 457.2 mm×50.8 mm×12.7 mm (18 in×2 in×1/2 in). The specimen will undergo a four-point bending test, with measurement results presented in the following subsections.

Table 6.1: Piezoelectric Specifications

Parameter	**Unit**	**Symbol**	**Value**
Electromechanical Coupling Coefficient	–	Kp	0.58
		Kt	0.45
		K31	0.34
Frequency Constant	Hz m	Np	2200
		Nt	2070
		N31	1680
Piezoelectric Constant	$10\,\mathrm{pm\,V^{-1}}$	d33	320
		d31	-140
	$10\,\mathrm{mm\,N^{-1}}$	g33	25
		g31	-11.0
Elastic Constant	$1010\,\mathrm{N\,m^{-2}}$	Y33	7.3
		Y11	8.6
Mechanical Quality Factor	–	Qm	1800
Dielectric Constant	at 1 kHz	e_{T33}/e_0	1400
Dissipation Factor	% at 1 kHz	$\tan\delta$	0.4
Curie Temperature	°C	Tc	320
Density	$\mathrm{g\,cm^{-3}}$	r	7.9

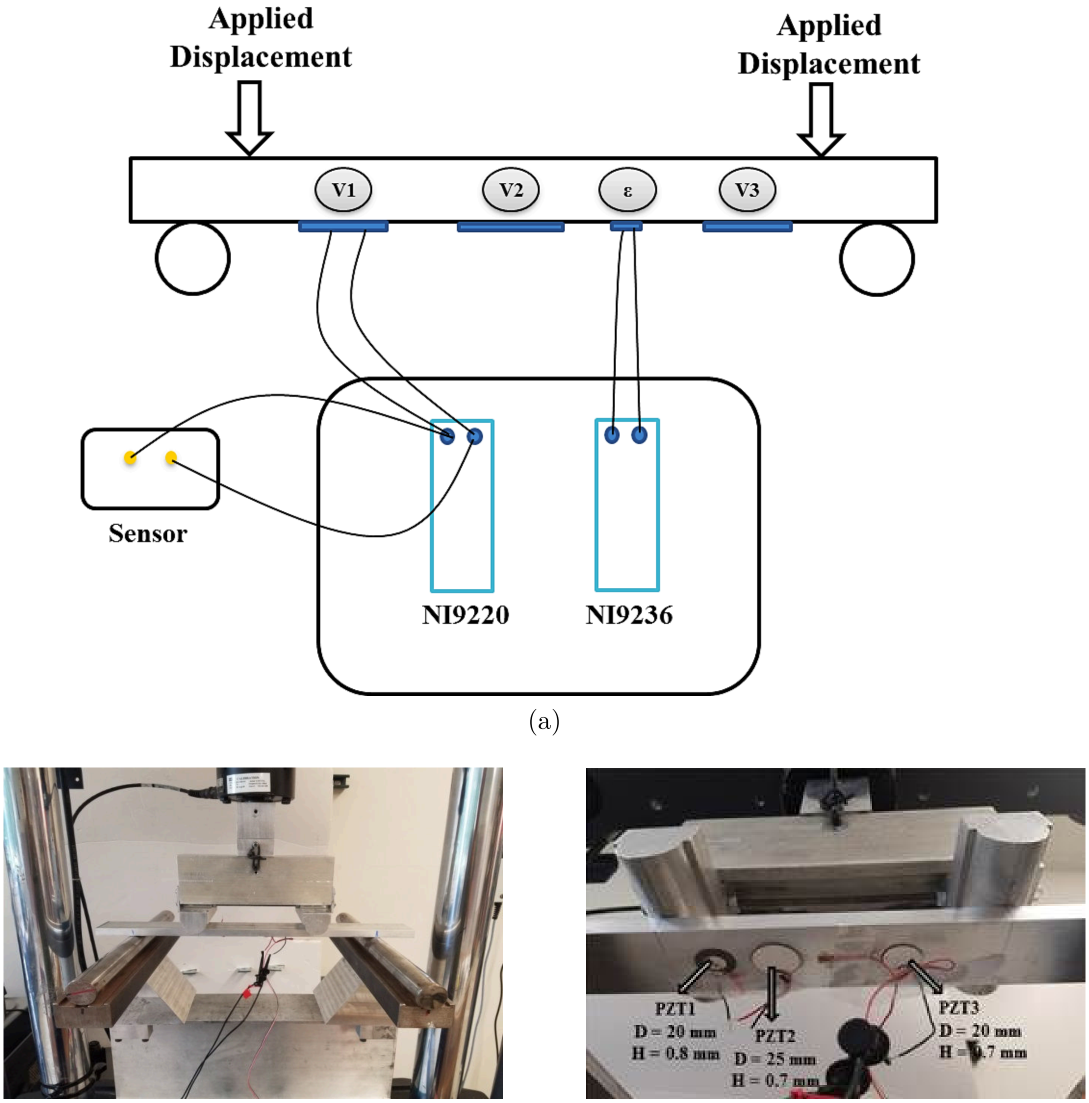

(a)

(b)

(c)

Figure 6.1: (a) A diagram of the testing apparatus, (b) an image of the actual MTS setup, and (c) closeup of the PZTs affixed to the sample under strain.

In this four-point bending test, the strain is assumed to be constant between the load application points, with strain amplitude given as:

$$\eta_{\text{surf}} = \frac{3FA}{Ebh^2}, \tag{6.1}$$

where F is the applied force, A is the coordinate of the first inner clamp with respect to the first outer clamp, b is the width of the specimen under test, h is the height, and E is the elastic modulus.

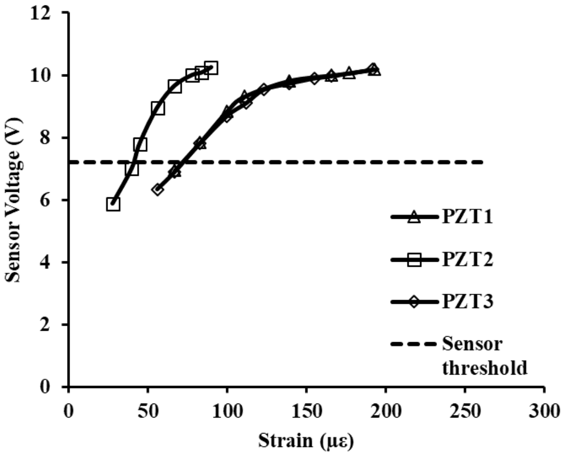

Figure 6.2: Plotting the voltage generated by the PZT samples (i.e. Sensor Voltage) as a function of the induced strain.

The voltages generated from the PZTs are logged using an NI9220, similarly the strain gage behavior is logged using an NI9236, both devices were purchased from National Instruments. Additionally, each PZT is connected to a PFG sensor (with an equivalent impedance of 50 MΩ) as depicted in the diagram of Figure 6.1a. The testing load is applied using an MTS servo-hydraulic machine in a displacement-controlled mode, with a cyclic displacement applied for each test iteration. The number of cycles for the input load was initially started at 50, with a cycle frequency of 2 Hz, and the number of cycles was gradually increased until the first channel of the PFG began to log data. This procedure of programmaticly increasing the number of cycles was repeated for each subsequent channel of the PFG until all seven channels would log some data due to the input stimuli. The actual strain levels are simultaneously recorded via the strain gage during these testing cycles, and a plot showing the strain levels with respect to the PZT voltage that is input into the PFG sensor is given in Figure 6.2. From these results, it is evident that PZT1 and PZT3 share a similar response as a function of the input strain levels, while PZT2 will generate a larger voltage potential at equivalent input strain levels. It is also shown that PZT1 and PZT3 will log data for strains in the range of 75 µϵ to 220 µϵ and PZT2 is effective at lower ranges of 50 µϵ to 100 µϵ. A combination of PZT2 and (PZT1 or PZT3) would allow the PFG sensor to record strains from 50 µϵ to more than 220 µϵ.

Low Frequency and Temperature

Table 6.2: Measured PZT Strain-Voltage and PFG Activation versus Frequency

Strain (µϵ)	400 mHz		500 mHz	
	Voltage (V)	PFG Channel	Voltage (V)	PFG Channel
50			5.00	0
60–62	6.67	0	6.73	0
73	7.38	0	7.68	1
80	7.83	1	8.64	3
87–89	8.31	2	9.33	4
99–101	8.84	3	9.67	5
119–121	9.60	4	9.89	5

Typical SHM applications will contain low frequency stimuli (as alluded to in Figure 5.1b), thus testing on PZT2 (the most sensitive from testing in Section 6.1) with load cycle frequencies of 400 mHz and 500 mHz was conducted. The measurement data are presented in Table 6.2, from which it is observed that the PZT generated higher voltages for faster cycling. For both cases, the threshold strain-level to begin logging data to the PFG was approximately 70 µϵ.

Table 6.3: Measured PZT Strain-Voltage and PFG Activation versus Temperature

Strain (μϵ)	20 °C		−20 °C	
	Voltage (V)	PFG Channel	Voltage (V)	PFG Channel
50–51	7.37	1	7.04	0
62	8.50	2	7.75	1
72–73	9.38	4	8.67	2
82–83	9.80	5	9.42	4
92–94	10.05	6	9.77	5
103			9.91	5

An additional consideration for deployment in real-world applications is the temperature effects on PZT performance. It is a well-known fact that typical piezoelectric materials will show output response sensitivity to temperature (typically being less responsive in the cold for PZT), and here it is verified that lower temperatures won't significantly hinder the data logging capabilities of the PFG sensor. Again, the testing apparatus follows that of Figure 6.1 and the preceding sections. The main difference being that the piezoelectric transducer element is protected from environmental conditions using "Flex Seal," a spray-on rubberized sealant. The coating provides protection against water, humidity, air, and other environmental factors that could cause damage such as corrosion to present itself on the PZT. We repeat the 500 mHz testing as before, but this time at 20 °C and −20 °C, with the resulting plots and data shown in Table 6.3. A shift in the channel activation to higher strains for lower temperature is observed, yet with the selected PZT, the PFG remains a viable sensor for the strain levels of interest at either temperature.

Cabling Effects

An important consideration is that the PFG will need to be wired to the piezoelectric transducer that was selected. The in-lab connections are not rated for the extreme conditions of the environment that will be experienced in deployment situations, be it the sub-zero temperatures of winters, or the greater than 100 °C during asphalt compaction. The type of wiring could have a noticeable affect on the sensor performance, as the capacitance and electrical resistance of the wires could vary depending on the gauge, shielding, or wire arrangement of a cable. Under consideration is the C0744A.41.10 multiconductor (eight wires) cable from General Cable, which uses 24 AWG stranded copper as the conducting wires with 0.0320 in of poly-vinyl chloride (PVC) insulation with a rated operational temperature range of 20 °C to 80 °C and inter-wire capacitance of 30 pF/ft and wire-to-shield capacitance of 55 pF/ft. This cable was chosen for its low-cost and high availability (it is similar to cables used for Ethernet) as well as the low capacitance offered by thin conductors. To test the effects of a more robust cable, the C8101.41.03, also from General Cable, was sampled. The cable only has two conductors of 18 AWG each and a much more robust 0.0160 in Fluorinated Ethylene Propylene (FEP) jacket insulation with operational ratings of −40 °C to 150 °C and inter-wire capacitance of 51 pF/ft and wire-to-shield capacitance of 91 pF/ft.

Testing was carried out in the low input frequency and room temperature configuration of the four-point bending test. From recorded threshold strain levels and voltage generated, it was found that for PZT2 the average difference in PFG channel thresholds between the two cables was about 0.86 µϵ or 15.7 mV, similarly for PZT3 the average differences were 1.85 µϵ and 10.0 mV — that is to say that the cables had negligible affect on the threshold performance of the PFG sensors. Although the performance was not degraded by the choice of cabling, it would be important to source cables that are rated for the expected deployment environment, which could exclude the PVC jacket insulation if freezing conditions are expected.

6.1.1 Piezoelectric-Floating-Gate Verification

Previously, in Chapter 4, Section 4.2, and [90], the Piezoelectric-Floating-Gate (PFG) sensor's characteristics were presented, when tested with ideal sources, such as function generators or other electrically-controlled systems. In this section, the PFG is connected to the piezoelectric as selected following the testing in Section 6.1, and the functionality is verified. The first result is presented in Table 6.4, which shows the approximate voltages generated by the PZT2 (henceforce, PZT) transducer that activated each PFG channel.

Table 6.4: Approximate Activation Thresholds for PFG Channels

Voltage (V)	PFG Channel
<7.75	0
7.75	1
8.22	1–2
8.69	1–3
9.15	1–4
9.62	1–5
10.09	1–6
10.56	1–7

Figure 6.3 shows example injection profiles for four different floating gates on a sensor prototype. Following the test procedure described in Section 6.1, in this sample data shown in Figure 6.3, the input loading is increased until the response strains hit a level sufficient to activate the first three memory cells (noted as Strain Level 1). Then, the loading is gradually increased until the fourth channel is activated. At each strain level, the input loading is cycled for fifty iterations to show the injection profile. The test results show good agreement between fabricated chips, and verifies the concept of the PFG sensor logging cumulative strain histories. As discussed in Section 4, the tuning resistance is lowered for this

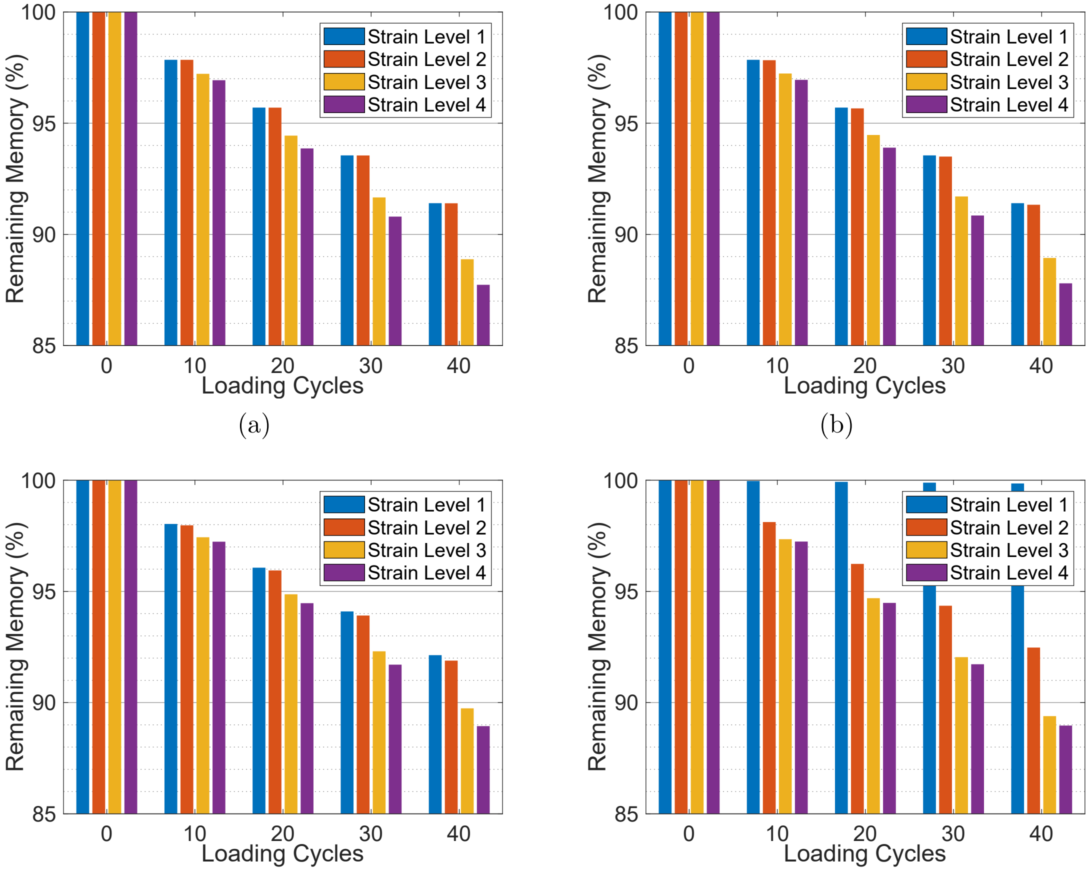

(a) (b) (c) (d)

Figure 6.3: Verifying the injection profile with four different fabricated chips, there is some variation between chips due to fabrication mismatch.

prototype to observe changes with tens of cycles. It should be noted that this dissertation focuses on the electrical design of the PFG sensor, and the task of data interpretation has been left to domain experts, primarily in civil engineering, with results widely reported in literature [91, 92, 93, 94, 95, 96, 97, 98, 99, 100].

6.1.2 Destructive Structural Testing

The selection of PZT, and verification of compatibility with the PFG sensor was conducted under the assumption of a structure that experiences gradual decay in the integrity of steel plates or cracking of asphalt. In this section, the catastrophic response of piezoelectrics was tested on an actual structure. This work was done in collaboration with Professor Gokhan Pekcan at the University of Nevada, Reno (UNR). Measurements from the structure provide an insight into the expected amplitudes that the PFG would need to record during structural failure in a concrete superstructure, and also gives the basis for analyzing the expected response of the cumulative data-logging analog frontend.

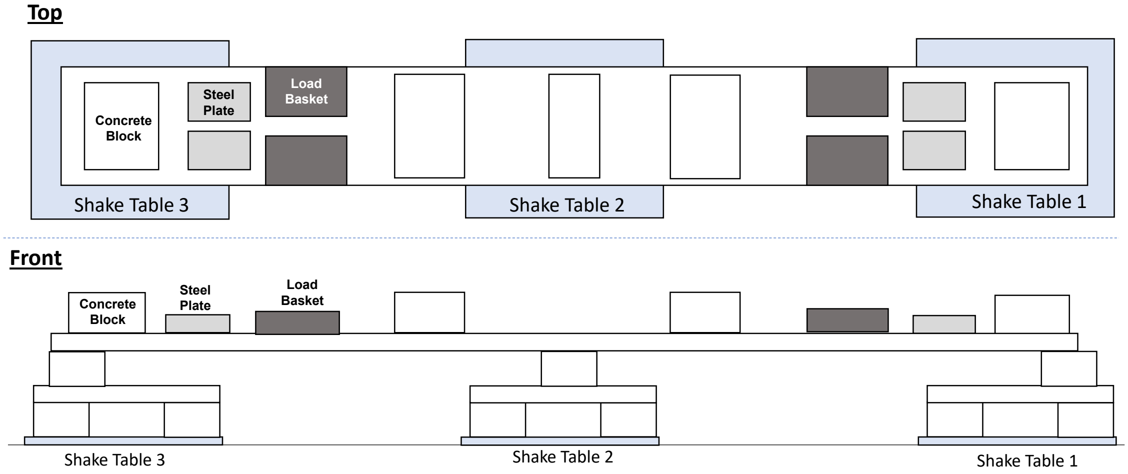

Figure 6.4: A sketch depicting the bridge structure.

Precast component and connections at the system level are used in accelerated bridge construction (ABC) to build a two-span 0.35-scale bridge that fits on shake tables that can simulate bidirectional earthquakes. Rough sketches showing the 100 ton, 70 ft bridge on three 14 ft square shake tables is presented in Figure 6.4, with an image of the site shown in Figure 6.5. A PZT on a cantilever was used to collect acceleration data, while a polyvinylidene difluoride (PVDF) piezoelectric was attached to rebar to collect strain measurements. In this application, the PVDF was selected due to the large strain levels expected during destructive testing, that would overload the PZT. Data were logged using UNR's data acquisition system of their earthquake laboratory. The construction of this bridge was done in collaboration with the United State Department of Transportation's Accelerated Bridge Construction University Transportation Center, with additional details on the UNR test facilities and procedures available online [101, 102].

Figure 6.5: An image showing the actual test site at University of Nevada, Reno.

The ABC prototype was designed for a site class D with VS30=270 $\mathrm{m\,s^{-1}}$ in the Los Angeles area. Acceleration history from the 1994 Northridge earthquake was recorded at the Sylamr Converter Station, and used as the basis earthquake for the destructive testing. Due to requirements of the collaborator's other testing, the time axis of acceleration was compressed by a factor of 0.592, and the amplitude was scaled by 0.535. Simulated ground motion was applied via three shake tables, with intensities varying from 20% to 200% (which would be 1.07 times larger in amplitude than the observed Northridge event). Before each test, low-level white noise tests were run for system identification purposes. Further testing parameters are available from the collaborator's site [102].

(a) (b)

Figure 6.6: (a) The PFG acceleration sensors were placed on top of the bridge deck, alongside commercial sensors, (b) the piezoelectric transducers are attached on longitudinal support rods to be encased in a concrete column.

Acceleration Data

Here, data collected from PZT discs attached to a cantilever to act as an accelerometer are presented. These sensors were placed on the surface of the deck bridge, and subject to transverse and longitudinal accelerations ranging from 0.07 g at 20% design excitation (0.107 scale factor) to 0.86 g at 175% excitation (0.936 scale). The peak full-scale (200% design excitation) acceleration data were not explicitly available in the measurements supplied to the author at the time of publishing, but based on the trend, a peak of 0.98 g is expected at 200% excitation. In Figure 6.7, the voltage outputs from a commercial accelerometer (blue) are compared to the PZT cantilever (red).

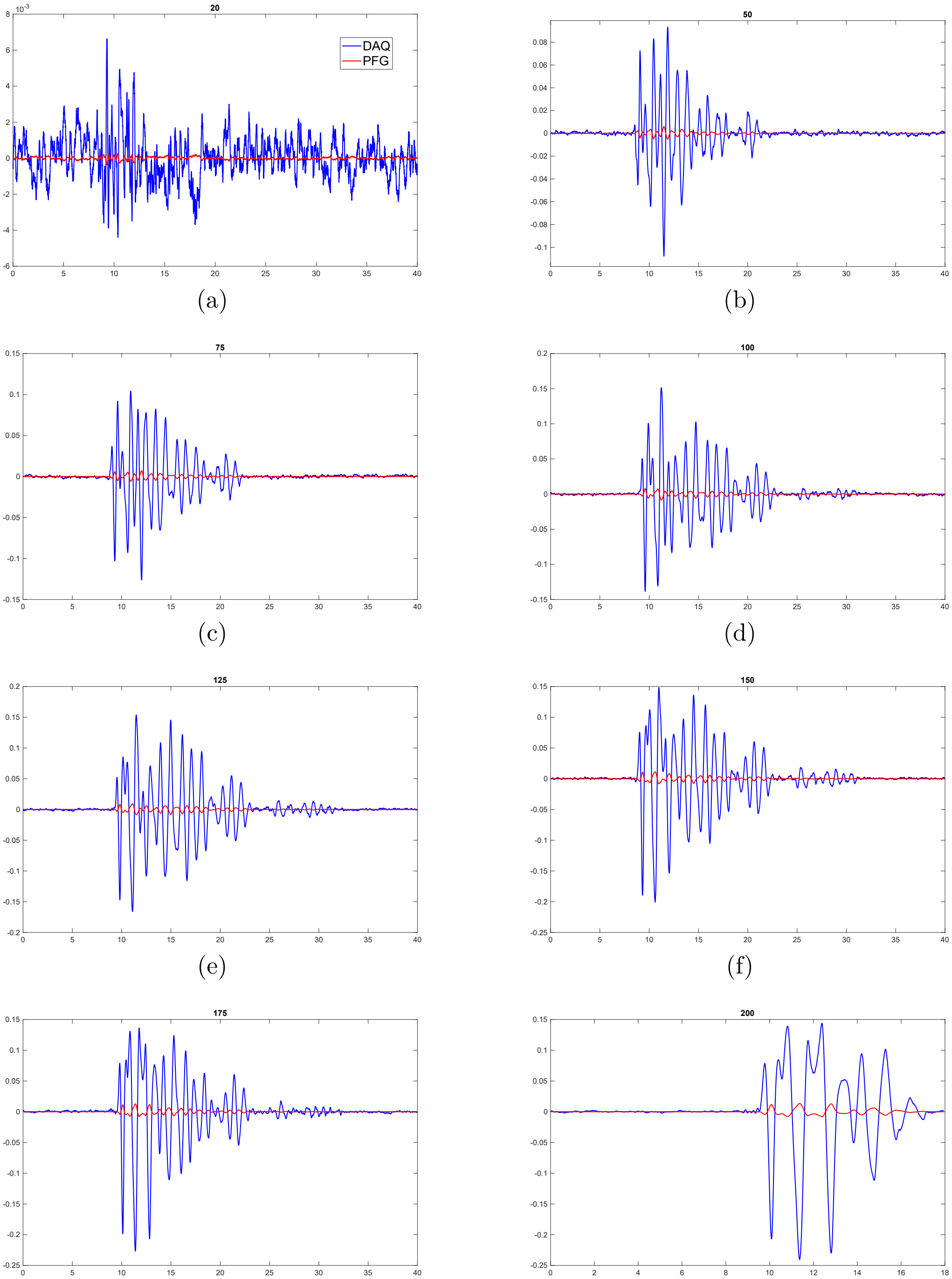

(a) (b) (c) (d) (e) (f) (g) (h)

Figure 6.7: Acceleration data from commercial sensors (blue) and the PZT accelerometer (red) for design excitations of (a) 20%, (b) 50%, (c) 75%, (d) 100%, (e) 125%, (f) 150%, (g) 175%, and (h) 200%.

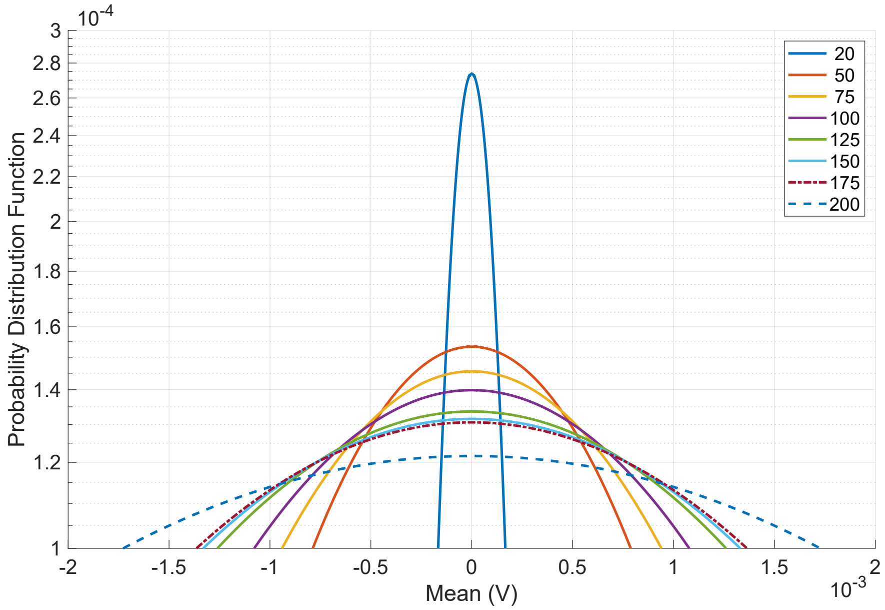

Figure 6.8: The PDF of data from Figure 6.7.

Since the PFG records the cumulative experienced history, the probability distribution function, fit to a normal distribution, of the measured data are best used for analysis. This is presented in Figure 6.8, and shows that for the 20% design excitation, the measured acceleration was more consistent and generated smaller voltages. As the excitation increases, the acceleration of the deck increased, thus generating larger voltages on the accelerometer sensors. Plotting the trend of the peak PDF in Figure 6.9 shows that the larger accelerations follow a roughly logarithmic pattern. It should be noted that the bridge was progressively subjected to the larger excitations, and the measured data from later shake scales will reflect a change in the behavior as the bridge is damaged to the point of failure. One point of note is that the small levels of excitation (<250 mV) would not be sufficient for data-logging on the PFG topology from Chapter 4, but the topology from Chapter 5 could be used in this case.

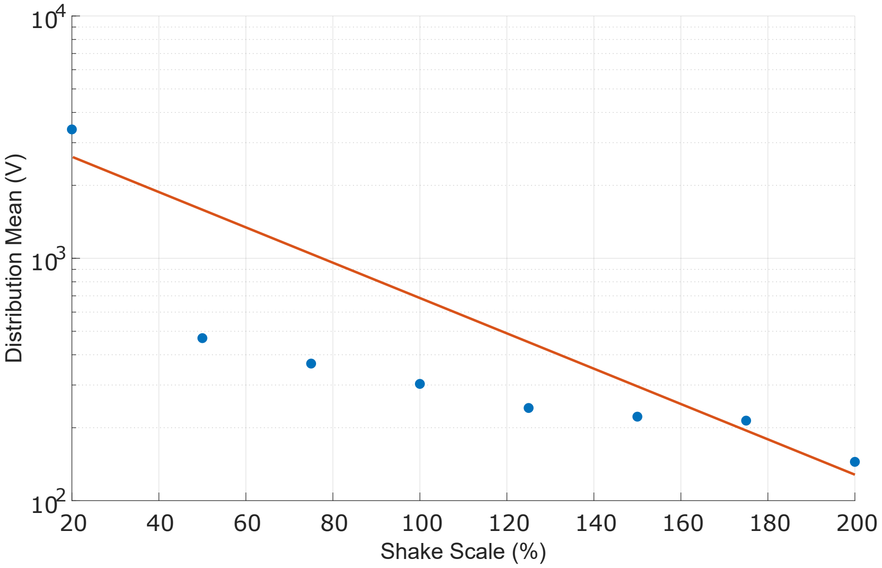

Figure 6.9: The trend of the PDF peak shows a shift in the distribution as the structure is damaged.

Strain Data

For the same test conditions, the measured strain from PVDF transducers embedded in the vertical support columns is presented in Figure 6.10, with the corresponding probability distribution function in Figure 6.11. In these strain measurements, the bridge column showed significant cracking and structural compromises that would affect the stiffness and response of the piezoelectrics to the displacements induced by the shake table. This is reflected in the probability distribution function trends plotted in Figure 6.12, which shows a more pronounced change in the distribution mean as the structure is damaged and the shake scale increased. The large voltages (>100 V) from these strain measurements would need to undergo a time-dilation correction to maximize the amount of energy that is utilized for data-logging as detailed in the circuit of Chapter 4, and has been reported in literature [72, 73].

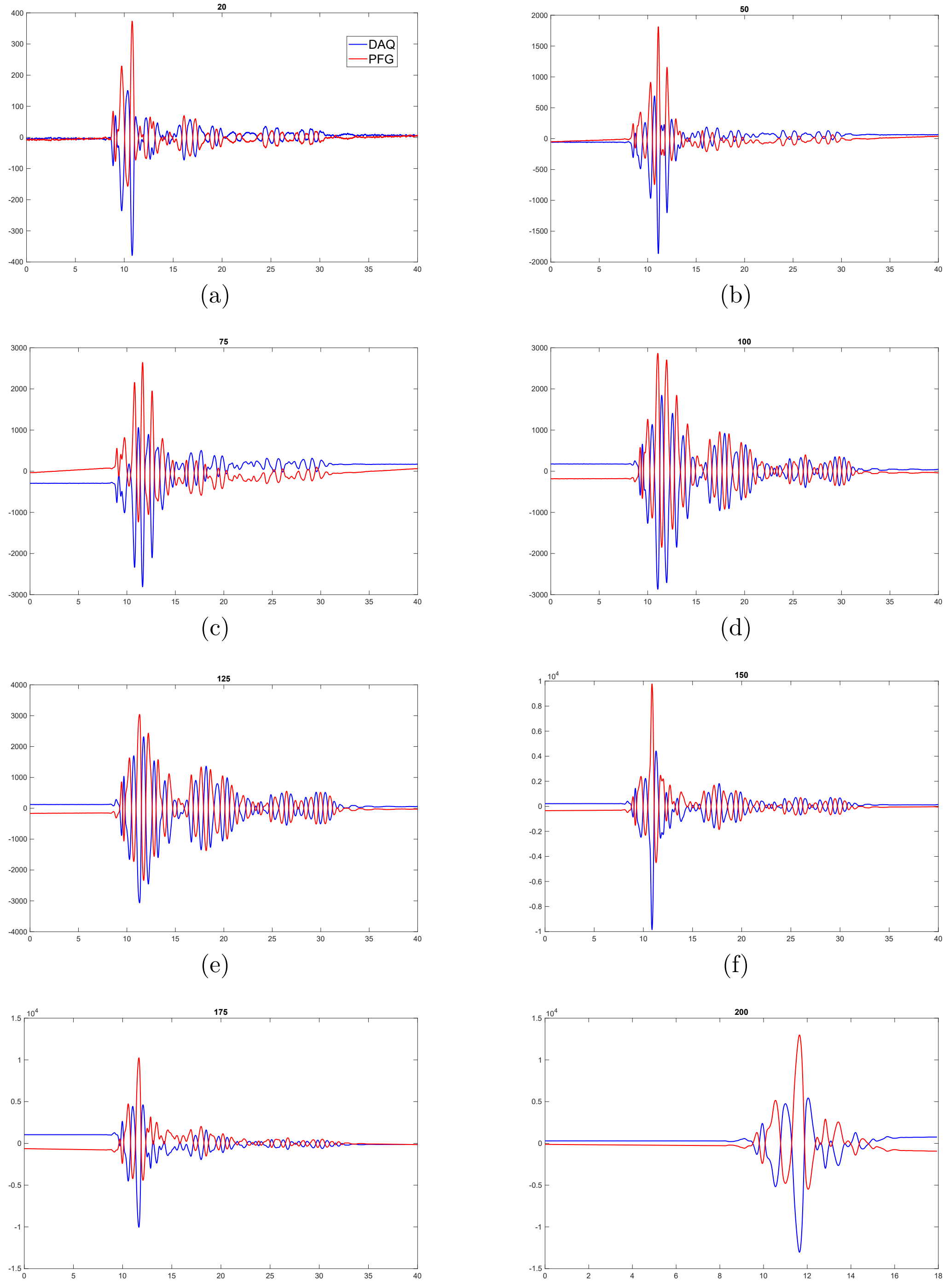

(a) (b) (c) (d) (e) (f) (g) (h)

Figure 6.10: Strain data from commercial sensors (blue) and the PZT accelerometer (red) for design excitations of (a) 20%, (b) 50%, (c) 75%, (d) 100%, (e) 125%, (f) 150%, (g) 175%, and (h) 200%..

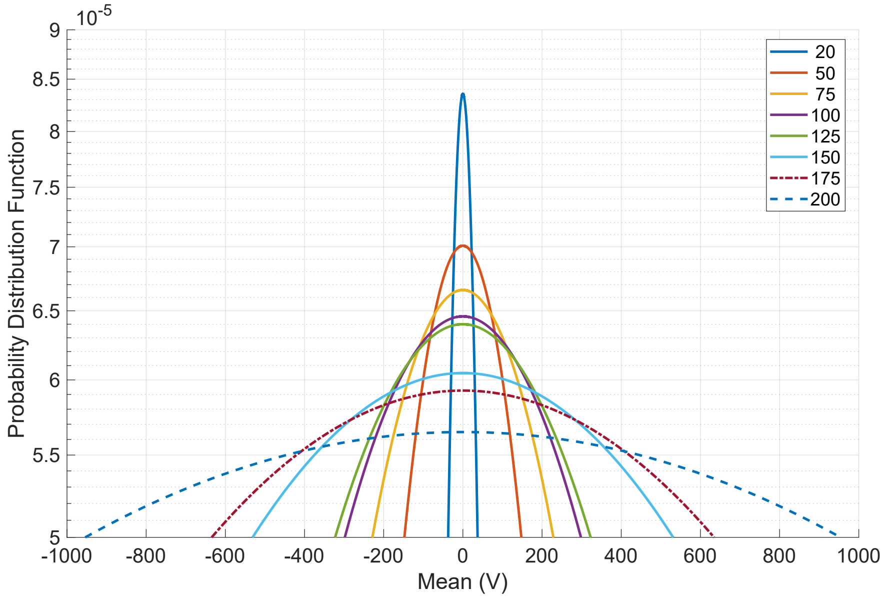

Figure 6.11: The PDF of data from Figure 6.10.

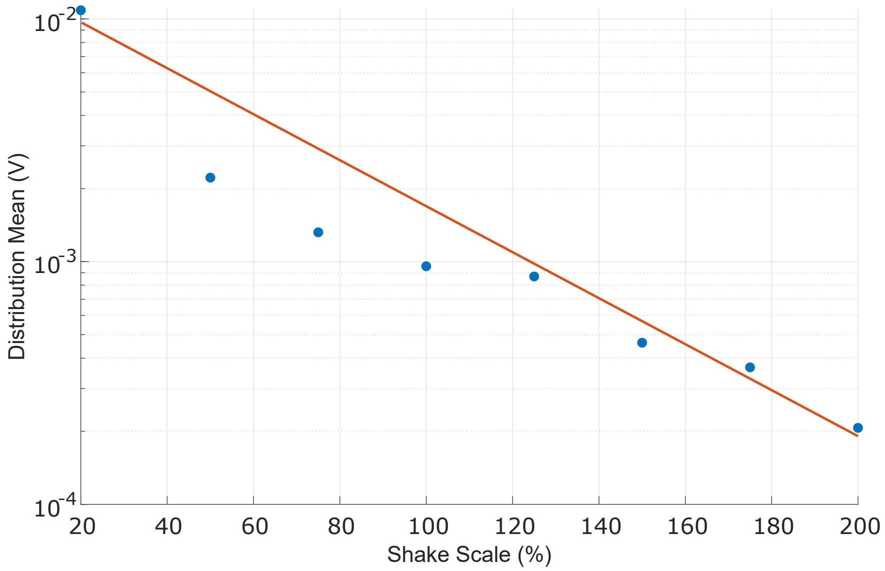

Figure 6.12: Similar to the acceleration case, the trend of the PDF peak shows a shift in the distribution as the structure is damaged.

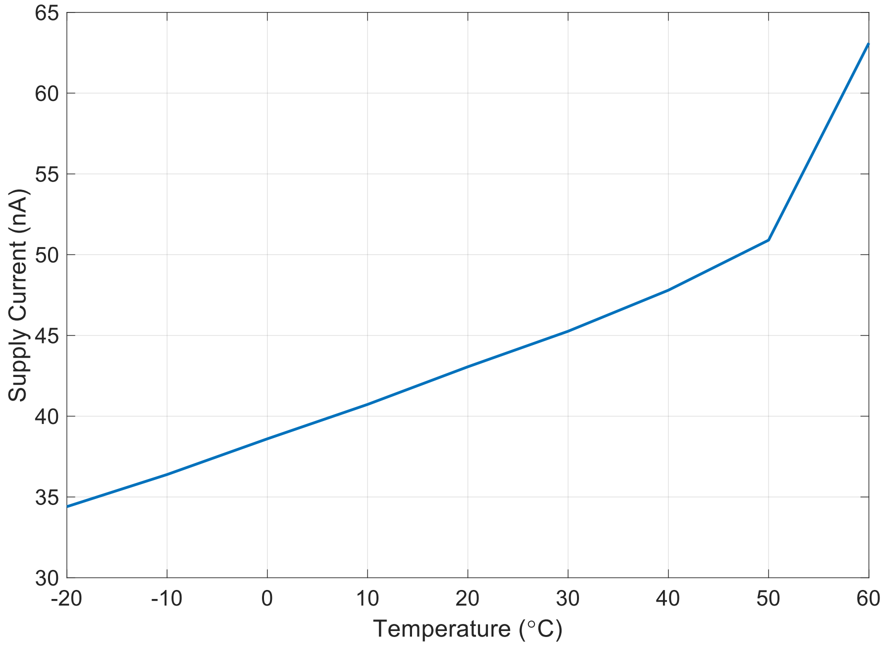

Figure 6.13: The amount of current draw from a piezoelectric excited to 7 V varies with temperature.

6.1.3 Energy Requirements

With respect to the amount of energy that the PFG self-powered sensor requires, the current drawn from a piezoelectric that is mechanical stimulated to generate 7 V was measured from −20 °C to 60 °C in 10 °C increments. The resulting supply current plot is shown in Figure 6.13, and tends to remain below 50 nA. In this configuration, it is expected that one channel of the PFG is injecting, and all supporting references and injection control circuitry is active to use 260 nW at room temperature. In earlier work for initial PFG implementations [75] the power requirement was 200 µW, and versions ranging from 5 nW to 800 nW have been reported [103, 104, 19]. There is still potential for optimizing these self-powered data-logging methods into the pW scale.

6.2 Self-Powered Wireless

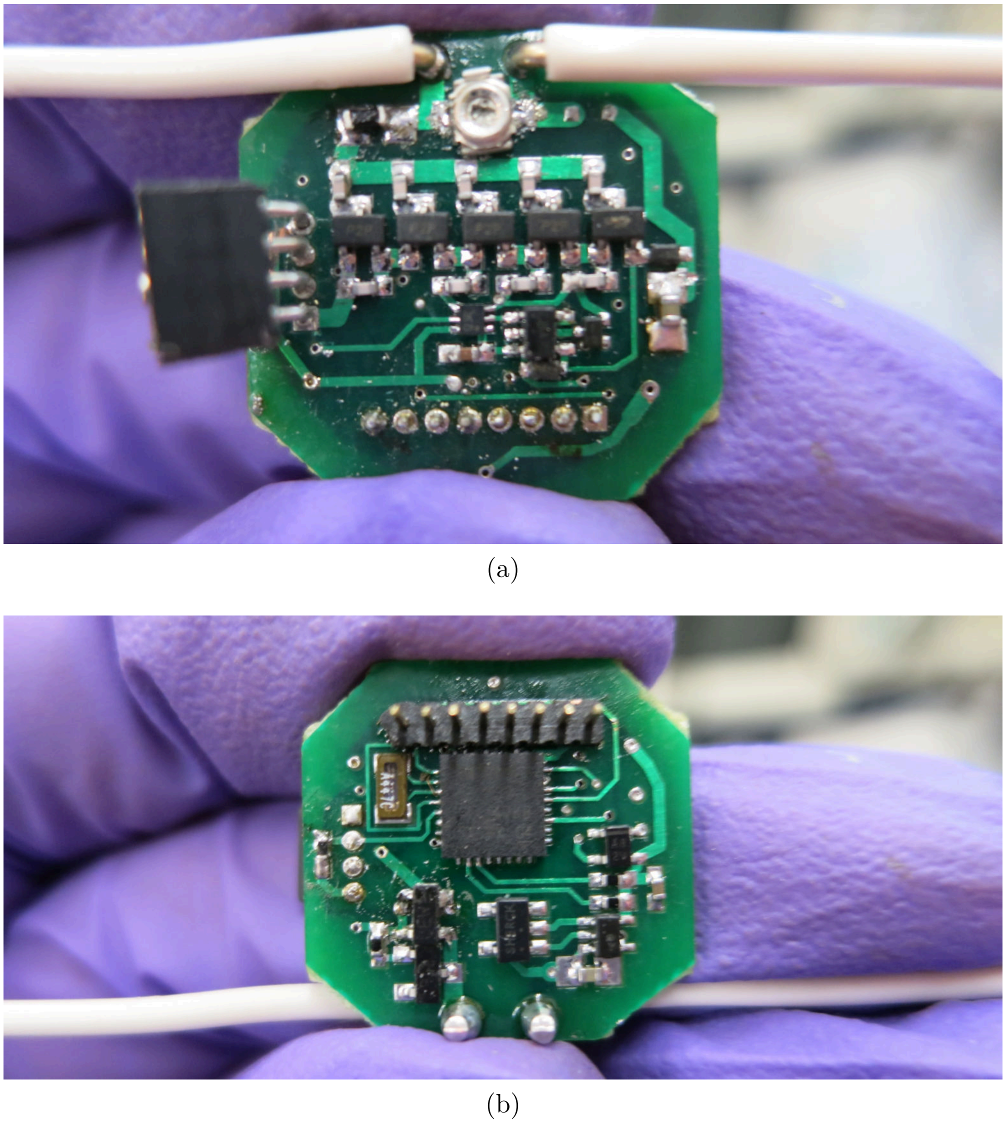

Figure 6.14: A self-powered wireless interface that uses backscatter for communication.

Besides the transducer selection, which was detailed in Section 6.1, the PFG core sensor of Chapter 4 requires a communication interface. In previous testing, that interface had been wired. Beginning in this section, different types of wireless interfaces are explored. Initial exploration of a wireless interface began with building a self-powered system to complement the self-powered PFG sensing core. For this purpose, a backscatter platform derived from the Intel WISP research [105, 106], was designed. Our implementation, which strips out components that were unnecessary for our purposes is shown in Figure 6.14. The PCB was about 1 cm^2 and has a five-stage RF-to-DC rectifier stage connected to a dipole antenna tuned for 915 MHz. The rectified signal undergoes an envelope detection for decoding of incoming commands. The detected command is sent to a Texas Instruments MSP430 microcontroller, which implements the state machine of Figure 6.15a, to decode the five available commands. Four of these commands are shown in Figure 6.15b, and the fifth command is the case where none of the shown commands were detected, in which case the MSP430 simply reads the content of the PFG and transmits it back to a reader. Utilizing a variance-based processor could push the energy requirements of this stage well below the limits of modern digital systems [107, 108]. Although the technologies discussed here are limited to those of RF, there is no technical limitation that would prevent other energy delivery methods, such as ultrasound or self-capacitance [109].

Detailed laboratory testing of this interface is omitted from this report, as access to comprehensive testing facilities for wireless backscattering was not available. The testing that was done showed the system capable of interfacing and reading data from the PFG core (attached on a plug-in module) at open-air, direct line-of-sight distances of approximately 50 cm, as shown in the setup of Figure 6.16. The self-powered backscattering wireless board with a PFG sensor was embedded in an H-gage strain sensor and deployed at the BioRePavation test facility in Nantes, France with the aid of Institut Français des Sciences et Technologies des Transports, de l'Aménagement et des Réseaux (IFSTTAR).

An image of the test facility is shown in Figure 6.17, with a diagram of the sensor placement as in Figure 6.18 and a picture from the installation given in Figure 6.19. The facility hosts

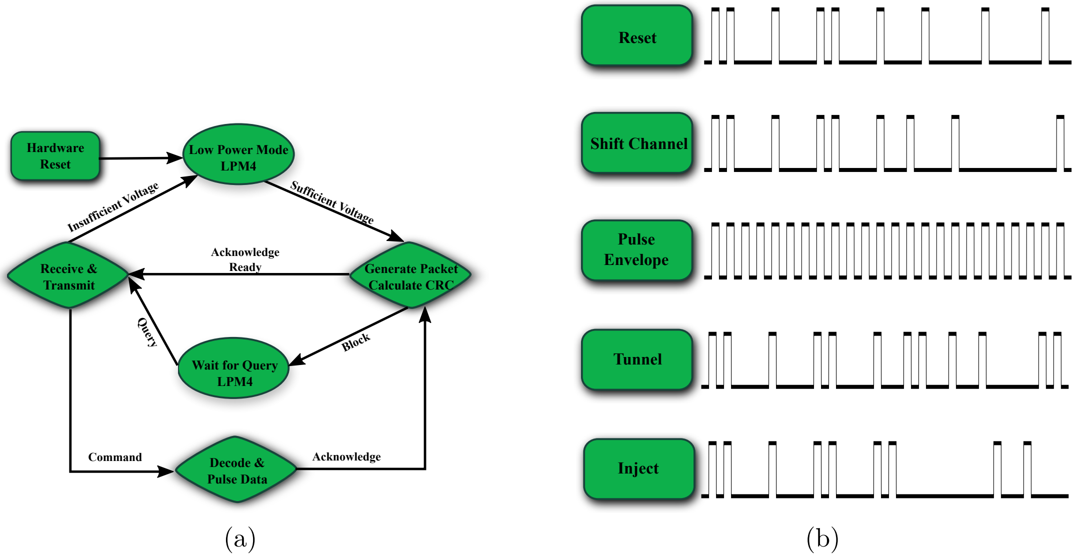

Figure 6.15: Showing (a) the state machine and (b) communication protocol for the self-powered wireless implementation.

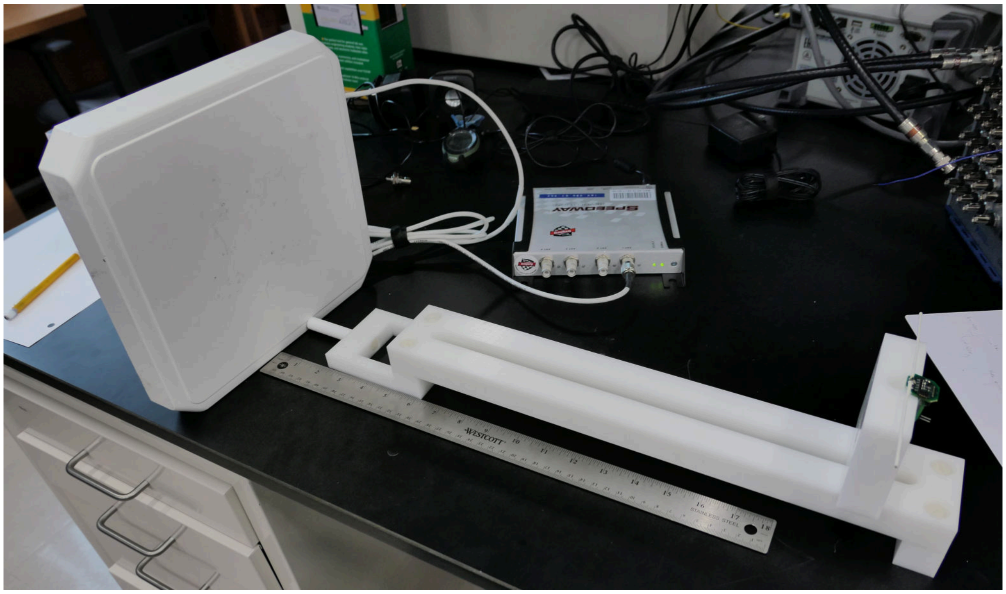

Figure 6.16: Testing the communication distance of the backscatter link, distances were stable at around 50 cm.

a pavement fatigue test track, which contains a heavy traffic simulator. The simulator is equipped with a central motor unit and four arms that are fitted with wheels and variable weights to apply heavy truck loads. The test track allows for testing of upwards of one

Figure 6.17: The BioRePavation test facility, coordinated by IFSTTAR, in Nantes, France.

million loading cycles in a single month.

Unfortunately, once deployed under the asphalt pavement, the self-powered wireless interface failed to establish a communication link. The failure was either due to the change in impedance of the backscattering center frequency (which was not adjustable using equipment available at the time), or the attenuation of the asphalt pavement was too great. Although a more extensive examination of the failure would have been useful, it was not pursued by this author since that topic alone would generate sufficient work for a dissertation. Since last explored in the context of interfacing with the PFG sensor, other researchers have reported improvements that could make this approach viable [110, 111, 112, 113], and the topic of self-powered sensor utilizing backscatter remains an open research topic.

Additional data from the Nantes deployment is not available for public dissemination yet, but laboratory testing [114] of a similar condition is presented here. The objective is to recreate the damage index variation curves using only the cumulative information tracked

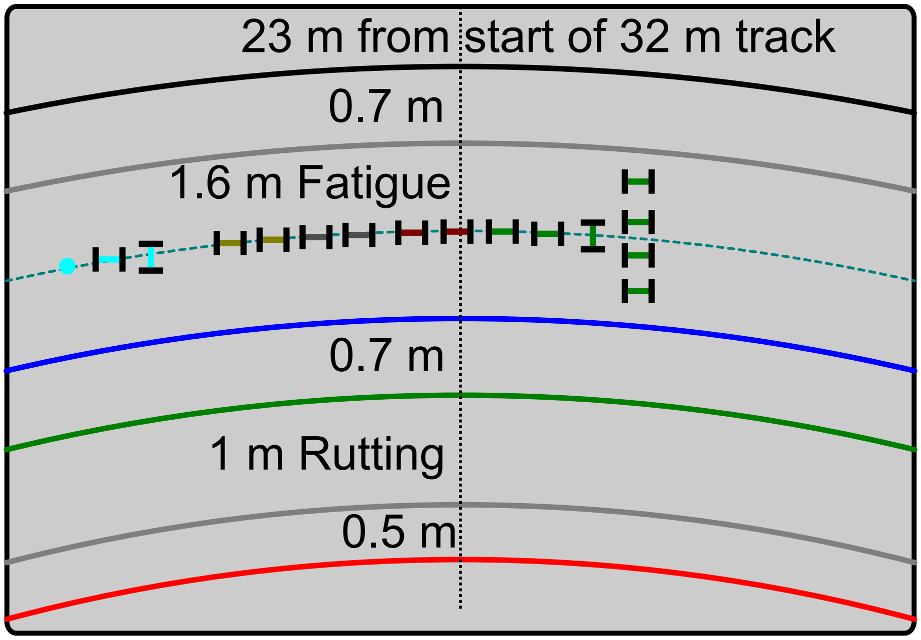

Figure 6.18: Dimensions of the test track in Figure 6.17, with approximate placement of H-gage sensors. Wireless PFG sensors are depicted with reg, wired PFG with green, and other commercial/unaffiliated strain sensors using blue, yellow and grey.

by the sensor, and then predict the remaining useful life. Plain concrete three-point single edge notched beam specimens ($100 \times 100 \times 400\,\mathrm{mm}^3$, with the span being 400 mm) were tested under constant and variable amplitude loading. A crack opening displacement (COD) gage was used to measure the crack mouth opening. Each specimen was subjected to a 2 Hz cyclical load. Ten specimens were subjected to constant amplitude loading using a stress ratio (max load/peak load), R, of 0.85 and 0.95. The other specimens were subjected to variable loading in which both the R ratio and the stress ratio were varied at several stages throughout the test. The logged measurements from the PFG sensor are shown in Figure 6.20.

The measured peak strain distributions monitored by the COD gage over the entire life of the specimens under constant and variable loading can be approximated by Gaussian distributions. The considered hypothesis is that a shift in the distribution toward higher strains over time is indicative of damage accumulation [115]. Fig. 6.21 shows the measured

Figure 6.19: The H-gage sensors being placed for installation before being covered by virgin aggregate and petroleum bitumen asphalt pavement.

strain cumulative distribution function (CDF) from the sensor at different life stages of the beam. The normalized probability distribution function reconstructed from the measured CDF (Fig. 6.22) clearly illustrate the shifts in the mean toward higher values, which can be correlated to damage. Additional analysis is relegated to the realm of civil engineering and though omitted from this dissertation, is available in literature [97, 100, 79].

6.3 Quasi-Self-Powered Wireless

Structural health monitoring (SHM) is the process used to identify potential damage or impending failure in civil infrastructure. While SHM technique include legacy approaches like routine/manual inspection of different structural components, recent developments in the SHM field have investigated the capabilities and advantages of wireless sensor networks

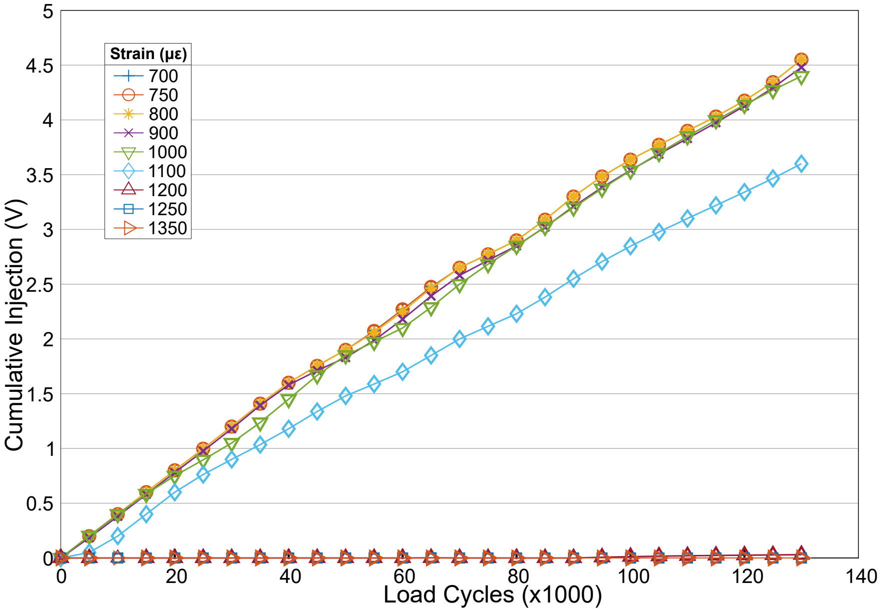

Figure 6.20: The logged data from the PFG sensors (with supply voltage 5 V) is roughly linear with respect to the number of loading cycles.

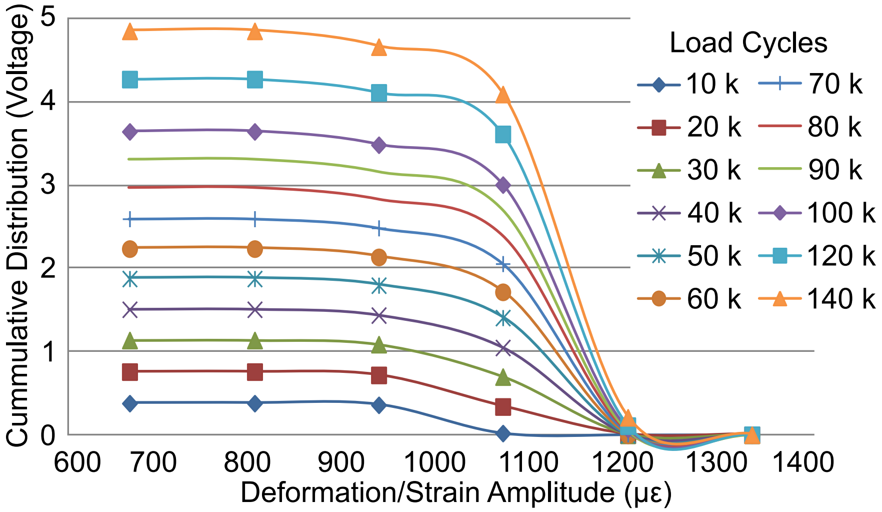

Figure 6.21: Cumulative distribution of voltages from data in Figure 6.20.

(WSNs) for sensing and data collection [116, 117, 118]. However, nearly all of the viable sensing platforms use an external power source, such as: mains power, batteries, or solar [119, 120, 121, 122]. The need for explicit wiring significantly hampers the coverage of the sensors on a large infrastructure like a multi-span bridge. Also, periodic replacement of batteries

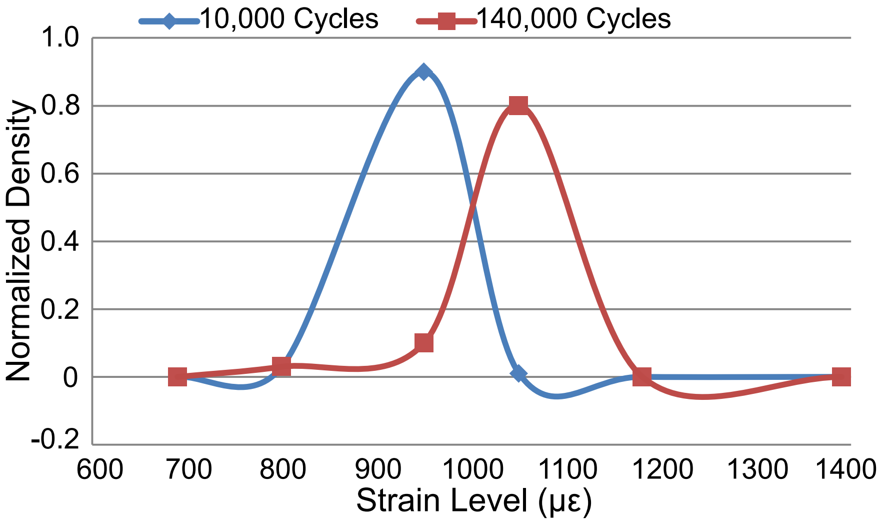

Figure 6.22: Showing the distribution of PFG data, as the sensor logs more loading cycles, the plots shift higher on the x-axis if the test material fatigues.

can restrict the number of deployable sensors if the batteries do not match or exceed the structure's lifespan. While energy-harvesting solutions such as solar can be beneficial, they are not always an option in sensors that require complete encapsulation or placement away from direct sunlight [123, 124, 125, 126, 127]. Also, many of these sensors utilize polling methods and sleep-wake cycles to reduce their energy usage [128, 129, 130] which could lead to data loss when the objective is to accurately record the impact of rare events like earthquakes or localized buckling.

Several researchers have developed concepts for SHM, but only a few have been able to deploy these devices on real life structures under actual loading and environmental conditions. One example or real-world deployment is reported in [131], where a proof of concept wireless sensing unit is shown to acquire data and transmit directly to a single base station with no intermediate hops. However, the proposed method does limit the placement of sensor nodes and has not been shown to scale beyond single devices. A wireless sensor network with multiple hops, "Wisden," has been demonstrated to accurately determine the dominant modal frequencies of a structure, although this also has limitations on the scalability and the type of data that can be collected [132].

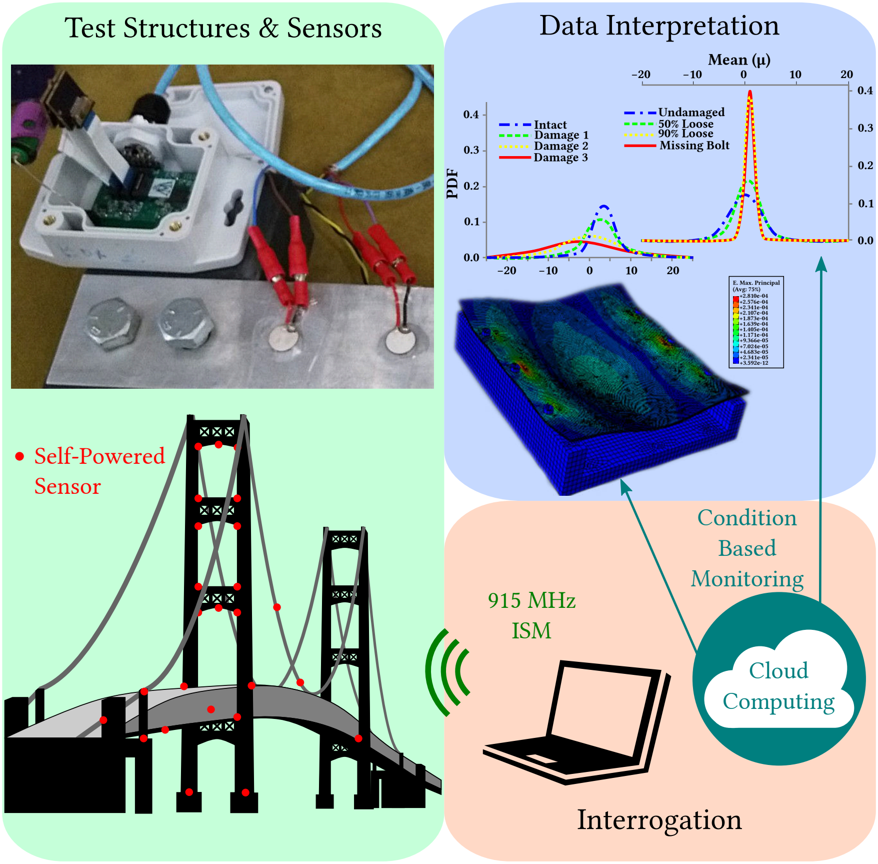

Figure 6.23: Overview of the test deployment at the Mackinac Bridge.

To overcome the inherent limitations that arise from sensors that require an external power source, a Piezo-Floating-Gate (PFG) sensor was proposed [17, 18, 133] and a System on Chip (SoC) was implemented in Chapter 4. By leveraging the self-powered, continuous measurements of the PFG sensor, periodic wireless interrogation will enable a "sense-now-retrieve-later" paradigm [134, 135]. In Section 6.2, the wireless interrogation was attempted using self-powered backscattering. Yet, this method was insufficient for even sub-1 m interrogation through asphalt pavement. With super structures containing more RF-shielding materials such as steel or concrete, it is expected that the backscattering as implemented in Section 6.2 would also fail, thus in this section the wireless interface is replaced with an active transmission. The combination of the self-powered sensor with the active RF interface yields a quasi-self-powered wireless sensor. This platform is tested on a bridge health monitoring application, with a deployment on one of the longest suspension bridges in the world, the Mackinac Bridge in northern Michigan. Testing at this site was conducted for over 18 months and counting. The basic framework of sensing that was used in the application is presented in Figure 6.23, which shows how self-powered sensors could be attached to the Mackinac Bridge on the left. Periodic interrogation would be done using the 915 MHz ISM frequency and data is logged on a general purpose computer for further analysis. Detailed data interpretation that infers the health of the structure is not detailed in this dissertation as it is beyond the scope of research, and readers should not assume that any presented findings are indicative of the current condition of the Mackinac Bridge.

6.3.1 System Design for Deployment

The Mackinac Bridge is the gateway to the north that connects the upper and lower peninsulas of Michigan in the United State of America. At the time of it's construction in the 1950's it was heralded as one of the greatest engineering structures in the world, and claimed the title of longest suspension bridge; decades later it remains the longest suspension bridge in the western hemisphere with a total structure length of 3038 m(26 372 ft) and width of 20.9 m(68.6 ft) and peak tower height of 168 m(552 ft). Its scale provides an excellent venue for testing our bridge sensing platform, especially consider the harsh climate that the sensors will need to endure, with months of sub-zero weather anticipated.

In earlier deployments of the PFG for pavement monitoring applications, the feasibility of using backscatter RF for data retrieval was demonstrated [76, 80, 81]. However, these methods do not work well in the presence of RF attenuating materials, as was the case in

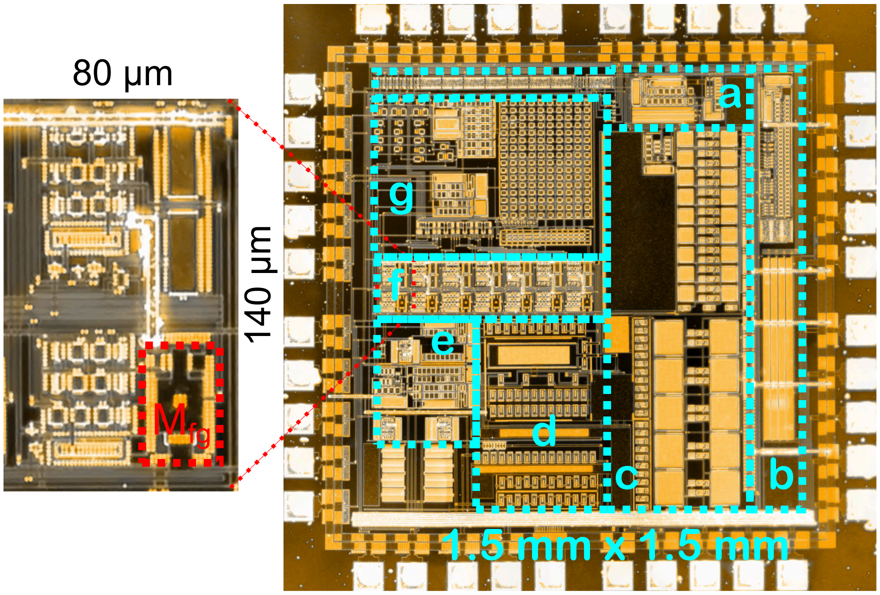

Figure 6.24: (a) Digital Control, (b) Oscillator, (c) Charge Pumps, (d) Protection, Rectifier, and Time Dilation, (e) Pulse ADC, (f) PFG Core, (g) Voltage Reference and Injection Control. Zoomed inset shows a single channel of the PFG, with the floating-gate highlighted in red.

Section 6.2. It is assumed that they would also fail in communicating on the dense steel structure of the bridge, especially considering that the placement of the sensors from the road surface would be greater than the open-air communication distances verified in the laboratory. Therefore, the self-powered PFG sensor is coupled to an active Radio Frequency (RF) communication link leading to a quasi-self-powered platform [134, 135, 136].

Initial Prototypes

Before the 2016–2017 winter season, an initial prototype was deployed on the bridge to get a rough indication of the environmental conditions that a deployed sensor would be subjected to and also used this opportunity to ensure that an appropriate procedure for mounting the piezoelectric transducers to the steel super structure was in place, such that it would survive temperatures below −40 °C [135].

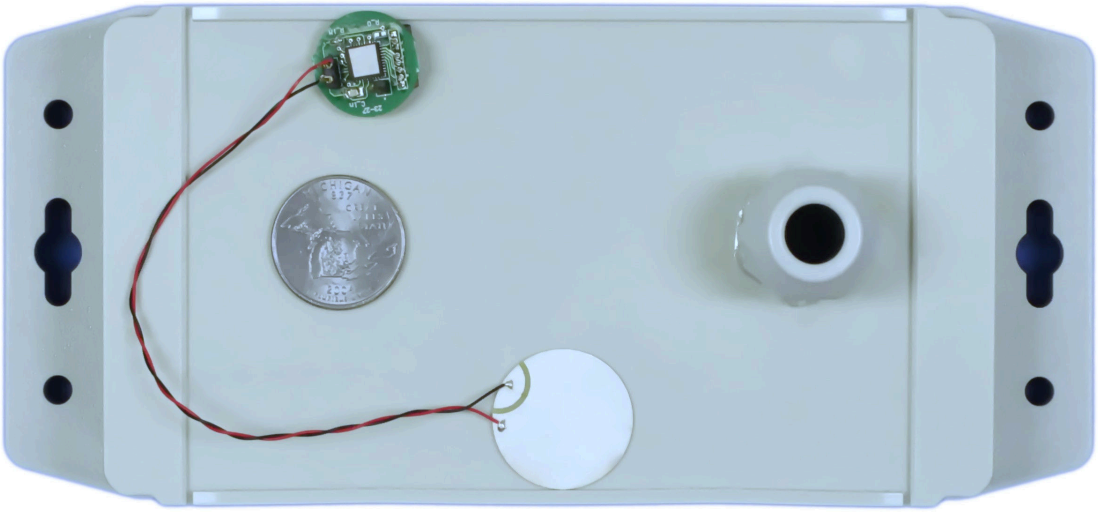

(a)

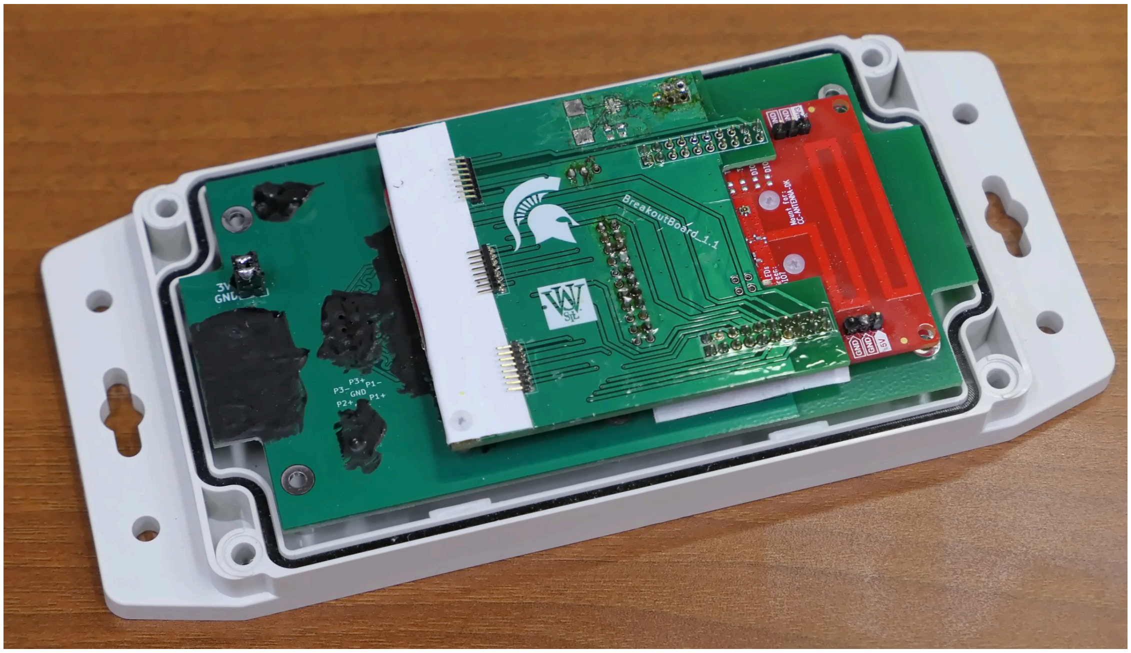

(b)

Figure 6.25: The first prototype (a) with lid on, a U.S. quarter is shown for scale, and the size of the PFG module and PZT transducer are shown, (b) a look inside the first prototype that implements the RF communication.

The initial prototype consisted of a Texas Instruments (TI) CC1310 Launchpad connected to three PFG sensors using a custom PCB as an adaptor. In previous cases, the PCB were designed in Eagle [137], but due to licensing restrictions, further PCB designs were done in

KiCAD. For protection against the elements, the prototype was placed in a plastic enclosure of dimensions 16 cm×9 cm×4 cm. Each PFG sensor was connected to one of PZT1, PZT2, or PZT3 using the C8101.41.03 cable, with the three cables passing through a single cable gland. To power the Launchpad, four AA batteries were used to provide approximately 10 Ah of 3 V supply. The CC1310 from TI is a commercial off-the-shelf RF microcontroller (MCU) that enables wireless communication in the 915 MHz Industrial, Scientific and Medical radio band (ISM band), while simultaneously offering capabilities typical of MCUs, such as programmable general purpose input/output pins (GPIO), clock timing with ms precision, and user-programmable firmware. In this initial prototype, the GPIO are used to give a rising edge to pre-determined pins of the PFG to send commands such as: increment selected channel, reset all channels, program current channel, enable readout, and reset PFG state machine. By using a second TI CC1310 Launchpad that is connected to a PC, one can send specific wireless commands that are encoded per TI's sub-GHz specifications to control individual PFG sensors within each prototype, and to log the output data of the sensors on the PC for further analysis. On the RF side, the CC1310 was configured for an average active supply current draw of 12 mA with wireless communication sensitivity below −110 dB m. Estimates using TI datasheets suggest that this setup could yield wireless ranges in excess of 1 km even with a low efficiency PCB antenna.

Images of the initial prototype are shown in Figure 6.25 with the actual installation cite omitted here, but available in [134]. At the time of installation in September, the three PFG sensors had readings of 5468 Hz, 5335 Hz, and 5202 Hz. After two months of deployment, the collected readings in November were 1661 Hz, <800 Hz, and 1034 Hz for the three PFG sensors, respectively. Although specific infrastructural health based on these data points cannot be commented on, it does demonstrate that the platform was continuously logging data even without external power, and that the chosen active RF solution was sufficient in enabling transmissions that allows interrogation of the sensors while simply driving over the bridge with a laptop and Launchpad at the Mackinac Bridge speed limit of 45 mph ($72\,\mathrm{km\,h^{-1}}$).

Unfortunately, the first prototype did not survive the first winter season. The failure mode was the ingress of moisture from a gap in the single cable gland (which was filled with silicone sealant) that built up inside the enclosure box. The moisture caused a short of the internal electronics and the batteries were found to have died. It is hypothesized that this was not an issue during the two months of deployment between September and November since sub-zero temperatures were less common. Once the snow and ice accumulated in the winter, it would also increase the chance of water making its way into the enclosure. The PFG sensors and PZT transducers were operational during evaluation of the prototype after it was recovered from the bridge and taken back to the laboratory.

Second Prototype

Taking into account the lessons learned from the initial prototype, an improved version was designed. The improved sensor assembly is shown as Figure 6.26a and the weatherproof enclosure is presented in Figure 6.26b. A custom PCB that has a built-in PCB antenna connected to TI's CC1310 RF MCU was designed to minimize cost. As in the initial prototype, this component enables the active wireless communication and interfaces with up to three PFG sensors per box. Each PFG is soldered onto an individual daughterboard module that can be easily swapped in or out on the RF motherboard via flexible flat cables. This capability allows for rapid replacement of PFG sensors if a change in the injection rate, diagnosis of a failure, or resetting the floating gate memory (though possible through the wireless communication, we removed this option to prevent malicious tampering of data at this stage) is required.

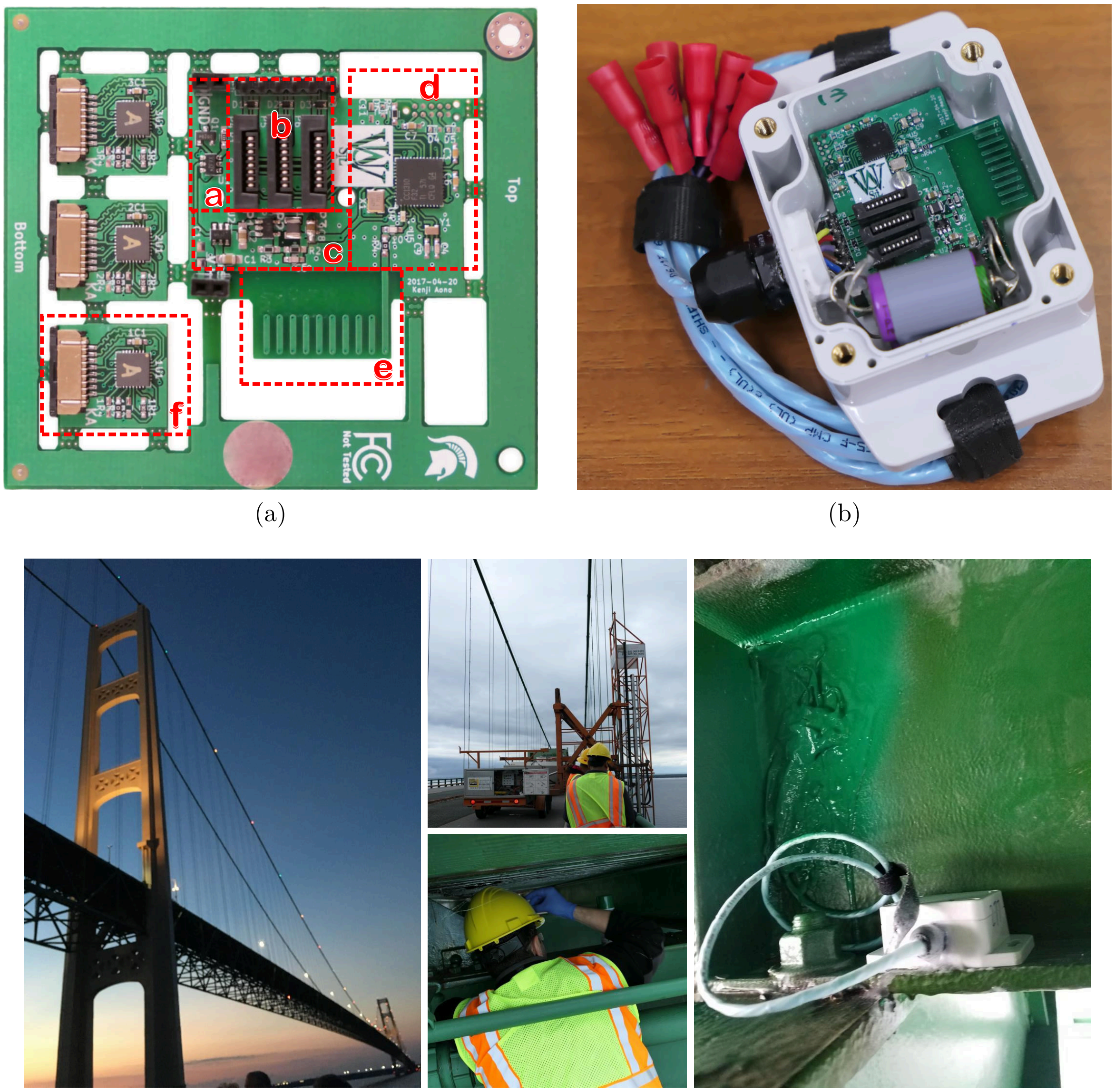

(a) (b)

(c)

Figure 6.26: (a) Custom built PCB that has a. ultra-low-power sleep mode, b. interface to hot-swappable PFG sensors, c. buck converter, d. RF MCU, e. antenna, and f. PFG sensor modules. (b) Shows an assembled box, sans sensor modules and (c) has images of the Mackinac Bridge and the installation on steel support beams.

The three cables were replaced with a single six conductor cable (General Cables, C3029.41.86) which uses 24 AWG wires, a flouropolymer jacket insulation that is rated for operation between −40 °C to 150 °C and has a reduced capacitance of 13 pF/ft between conductors and

23 pF/ft conductor-to-shield capacitance. This allows the cable gland to give a tighter fit, the inside of the gland was filled with a copious amount of sealant.The water-tightness of this setup was verified with a one week submersion test with daily agitation of the water in the submersion tank. The inside of the box did not show any signs of being compromised, and the non-conformal coated electronics still responded after being removed from the water bath. In the final deployed prototype, all electrical components in the box were treated with a silicone conformal coating, which by itself provides protection against water or ice causing electrical shorts. The enclosure was reduced in size to $59 \times 94 \times 35\,\mathrm{mm}^3$ and the material was also upgraded from an economical plastic to a more robust UV-stabilized polycarbonate.

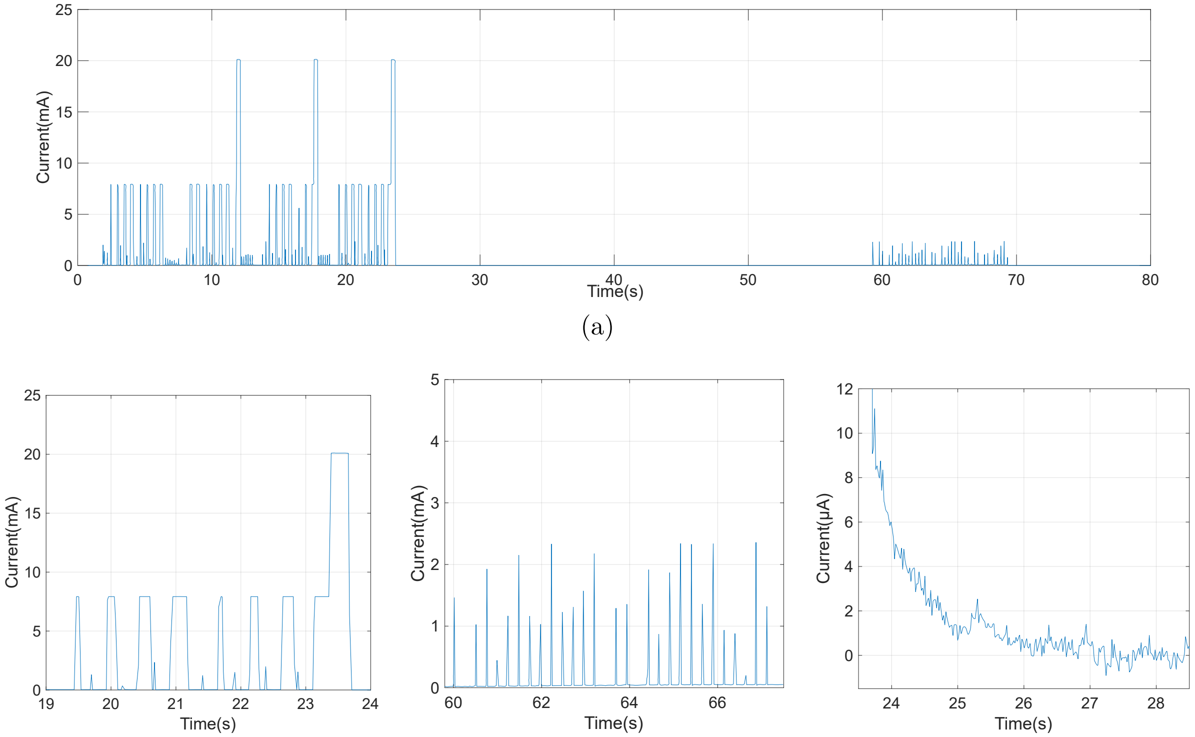

(a)

(b)

(c)

(d)

Figure 6.27: Showing (a) the state machine and (b) communication protocol for the self-powered wireless implementation.

The RF motherboard also includes a buck converter to extract more energy from the batteries before the system stops responding due to low supply voltage. Additionally, a nano-power timer (TI TPL5111) disconnected all electronics from the battery by turning off a load switch. This user-configurable timer was set for 5 minutes, therefore the prototype would be unresponsive for 5 minutes at a time, but would only lose a miniscule amount of supply current to leakage, measured to be less than 50 nA (Figure 6.27d). On the initial startup, the RF MCU is programmed to go into a "search" mode where it will listen for an interrogator (i.e. an operator that has a similar RF board connected to their PC and is asking for data) with supply current measured in Figure 6.27c. Only if an interrogator is detected will the prototype transmit the PFG sensor data. The transmission was repeated three times to ensure delivery and the supply current of a single transmission cycle is shown in Figure 6.27b. The "search" before transmit is done since the energy cost of a transmission is much larger than receiving, in particular the CC1310 was configured to listen for an interrogator for 6 s at a time with an average supply current of 225 µA while a transmission can take as long as 13.5 s with an order of magnitude larger supply current of 2.5 mA. Based on these supply currents, one can estimate typical supply currents of:

$$\begin{aligned}
\text{Request} &= \frac{I_{\text{on}}t_{\text{on}} + I_{\text{search}}t_{\text{search}} + I_{\text{off}}t_{\text{off}}}{t_{\text{on}} + t_{\text{search}} + t_{\text{off}}} \\
&= \frac{2.5\,\text{m}\cdot 13.5 + 225\,\mu\cdot 6 + 50\,\text{n}\cdot 300}{13.5 + 6 + 300} < 110\,\mu\text{A} \\
\text{No request} &= \frac{I_{\text{search}}t_{\text{search}} + I_{\text{off}}t_{\text{off}}}{t_{\text{search}} + t_{\text{off}}} \\
&= \frac{225\,\mu\cdot 6 + 50\,\text{n}\cdot 300}{6 + 300} < 5\,\mu\text{A}
\end{aligned}$$

If data are collected from these sensor boxes twice a day (that is, 1% of the time), and they use a ½ AA battery with 1.2 Ah of capacity, then it would remain operational for:

$$1.2\,\mathrm{Ah} \div (0.99 \cdot 5\,\mu + 0.01 \cdot 110\,\mu)\ \mathrm{A} \cdot \left(\frac{1\,\mathrm{yr}}{8766\,\mathrm{h}}\right) \approx 23.5\,\mathrm{years}.$$

In a more traditional sensing platform, the MCU would need to periodically poll the sensors to collect sufficiently meaningful data, which would prevent them from operating at the nA range that this prototype does. Moreover, in such polling methods, the collected data would necessarily be missing spurious parts of the history since they are not doing continuous data collection [80]. It should be noted that many conventional battery formulations would fail to last decades in an actual deployment, lead-acid might decay 5% per month, and the latest alkaline batteries have 2% self-discharge annually. Lithium-ion tends to do even worse, with 2% lose per month. And these rates are further exacerbated in real-world deployments that endure thermal cycling [138]. In the proposed application, a lithium thionyl chloride battery from Tadiran is utilized, the supplier has over 40 years of experience, and has documented customers that have deployed this battery chemistry successfully for over 25 years [139]. Accelerated testing with thermal cycling was done in-lab to verify the manufacturer's claims and a TL-4902 was modeled to last upwards of 50 years. Using this battery pushes the limitation of the sensing platform's lifespan towards surface mount components such as capacitors, which are only guaranteed for 20 years of operation. Some of these operational limitations can be designed around by inspecting Monte Carlo analysis and defining a safe margin of degradation.

6.3.2 Deployment Data

The improved prototype was deployed in May of 2017, and in this section two particular events that show the data-logging capability of the proposed quasi-self-powered platform are shown. Again, the absolute strain measurements are not recorded, nor are any inferences as to the infrastructural health made with the collected data. What is shown is that the PFG sensors are able to detect an abnormal spike in traffic, namely the large influx of bridge crossings that occurs during the annual Mackinac Bridge Labor Day Walk.

Data from 2017

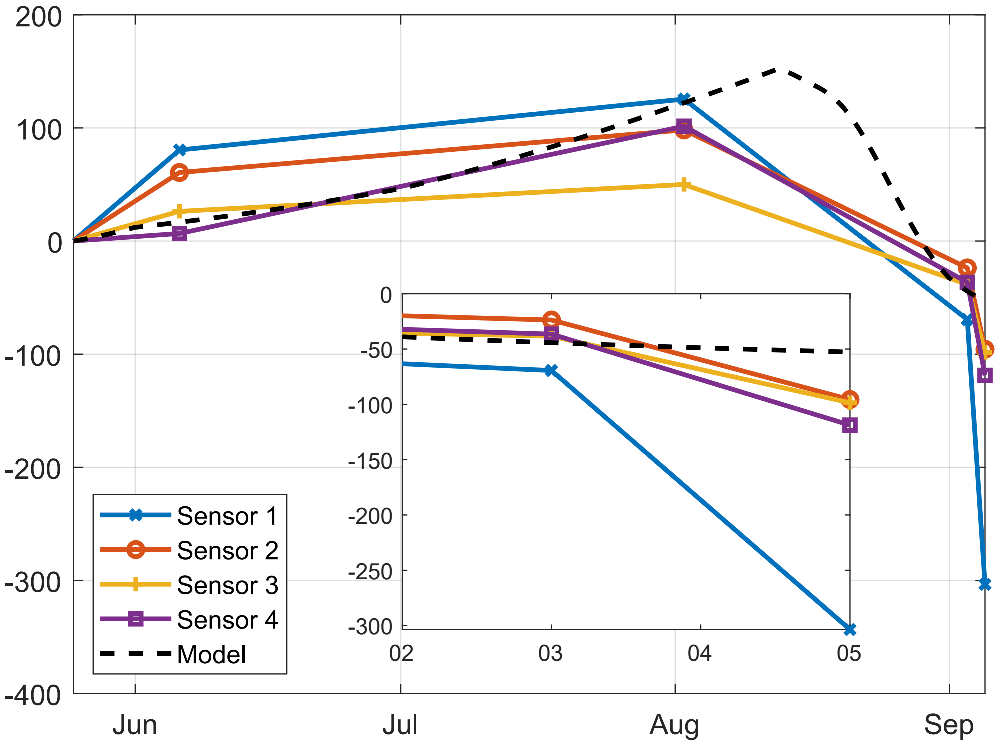

Figure 6.28: Measurements from the summer of 2017, which showed a deviation in expected response based on vehicle traffic, possibly due to the Labor Day Walk.

The data collected between May 25th and September 5th of 2017 are presented in Figure 6.28 after having the corrective factors from Chapter 4 applied [135]. Sensors 1 through 3 are at the same installation site and show the same trend in data logging, with some difference in peak frequency as well as injection rate due to fabrication mismatch. Sensor 4 was on a different installation site, but had a similar configuration in terms of PZT size and PFG tuning parameters. The sparse data collection appears to follow the trend that we expected based on the PFG characterizations from in-lab testing [19, 72, 73, 140, 141] and the traffic statistics of the Mackinac Bridge provided by the Mackinac Bridge Authority. The trend line is shown as the dashed black. The inset of Figure 6.28 shows the data collected before and after the Mackinac Bridge Labor Day Walk (on Sep. 4th), which drew a crowd of over 25,000 people, much greater than usual traffic on the bridge. It shows that during the event the sensors logged a much larger amount of data than it had in the days before. The deviation from the model trace, which is based on monthly traffic statistics, highlights the extra strain that the Labor Day Walk placed on the sensors. Note that measurements are shown in a unitless, corrective-factor-applied frequency output of a single channel from each PFG sensor, from which a layperson may have trouble extracting any meaningful information. It has been previously demonstrated that similar data can infer the structural damage progression in steel frames, girders, and plates [142].

Data from 2018

After leaving the prototypes deployed on the bridge for the 2017–2018 winter season, they were still responding when returning to the bridge in the spring of 2018. Upon opening the boxes for inspection, it was found that none of the four units showed signs of water ingress or other hardware failures. The battery levels were also as expected based on the calculated operational lifespan of 23.5 yrs per ½ AA battery. The sensors remained operational through

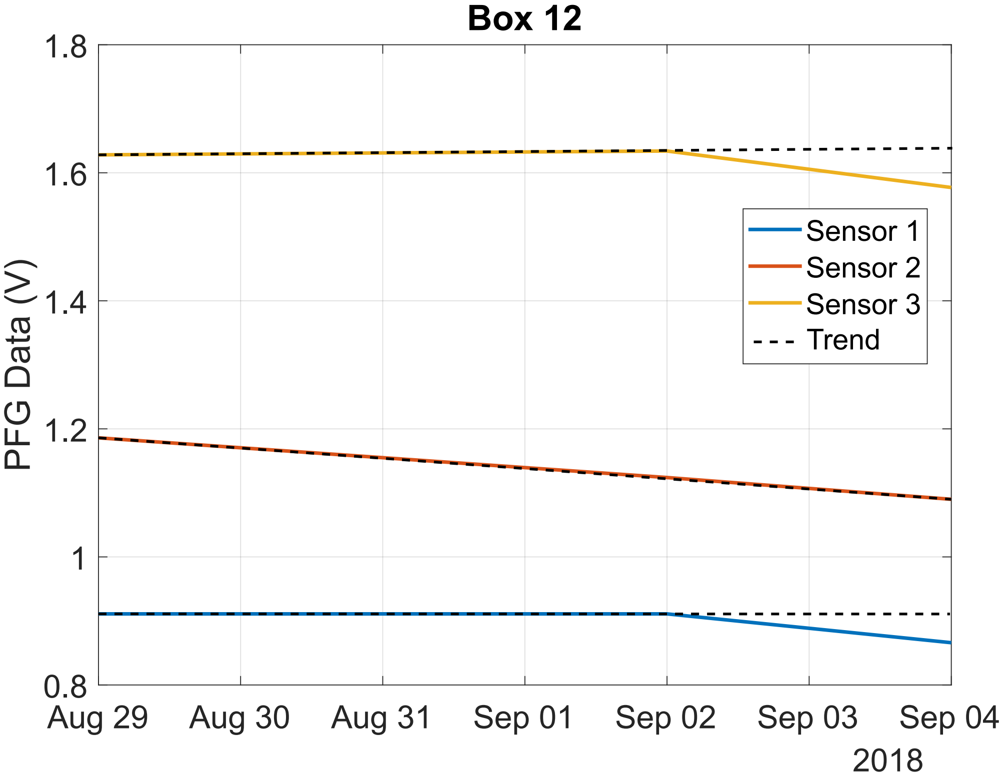

Figure 6.29: PFG with accelerated injection rates were used to focus on the single day event of the Mackinac Labor Day Walk of 2018.

the summer season as well. Before the annual Mackinac Bridge Labor Day Walk for 2018, the PFG sensors in Box 12 were swapped out with ones that would log data more quickly (using a smaller external tuning resistor on the reference voltage generator) to see if the findings from 2017 could be replicated [143]. In this section, the pulse encoder output frequency was translated into an equivalent stored floating gate charge, which is denoted as the PFG Data in volts. The resulting data plots are given in Figure 6.29, and show that the data logging before Labor Day (which was on September 3, 2018) was slower than during the event. Sensor 2 was consistently logging data, regardless of the traffic levels, which might be expected due to the placement of that PZT since it could be tracking the sway of the bridge from winds, or aspects of the bridge health that wouldn't be affected by a change in traffic patterns. According to the Mackinac Bridge Authority, it is typical for winds to cause horizontal sways of 35 ft, and if the placement of the PZT is correct, Sensor 2 could be logging such horizontal strains instead of the vertical strains that would be generated by passing traffic. Sensors 1 and 3 showed a large change cumulative history of strains experienced by their PZTs. More in-depth discussion of the validity of the gathered data with the self-powered sensing platform are reported in literature [144, 75, 145, 146, 140, 97].

6.3.3 Other Deployments

Figure 6.30: Sensor boxes on a wind turbine blade that was tested in collaboration with NREL.

The quasi-self-powered sensor box was also tested on a wind turbine blade [147], as shown in Figure 6.30, in collaboration with the National Renewable Energy Laboratory (NREL) and General Electric. Measurement results are not available for disclosure, but the wireless sensor boxes were able to perform as expected in this deployment as well. Another on-going deployment is with the Federal Aviation Authority (FAA), which is deploying a modified PCB for the quasi-self-powered sensor platform, with a single PFG soldered on the board. The PCB was designed to fit the industry-standard H-shaped strain gage configuration as shown in Figure 6.31. Data from these deployments are not available for discussion in this dissertation, but may be forthcoming in future publications [148, 149, 150, 151].

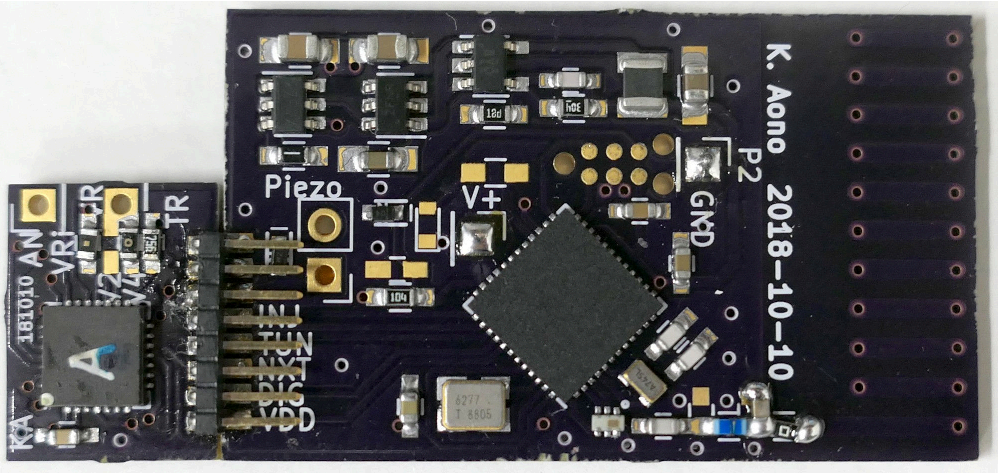

Figure 6.31: Modified PCB for deployment in an embedded H-gage with FAA collaborators.

Chapter 7

Closing Remarks

With this chapter, I conclude a body of work that encompasses the efforts devoted towards a Doctor of Philosophy degree in engineering. The primary interest that drove me to pursue advanced degrees in electrical and computer engineering was: taking inspiration from systems and physical phenomenon that occur in nature and bending them to our will.

Forming the basis of motivation for the jump resonance filter of Chapter 3 was that cochlea exhibit similar nonlinearities [152, 40, 153], yet it was common to use symmetric, linear filters when building filter banks for auditory front-ends [32, 154, 155]. At the time this research was taking place over six years ago, the digital tools available to a single researcher would have been preventative in my search for answering the question of whether or not including such non-ideal features would aid in applications such as speaker recognition. Recent literature continues to investigate similarly using jump resonance features, and with the explosive growth in parallel computing capabilities it can be achieved in the digital domain [156, 157, 158, 159]. Yet, because the reported jump resonance filters exploit physical phenomenon that are inherently preset in analog filters, the energy efficiency remains orders of magnitude greater than their digital brethren.

In another thread of this story, I dove into the world of Piezoelectric-Floating-Gate (PFG) sensors. During the jump resonance investigation, having a means for data-logging of the past experienced input stimuli was something that interested me. My thought was that using the history of past events, I could adaptively program the filter biases to adjust the "hearing" of the silicon cochlea to automatically increase its performance as it "ages". Since the jump resonance filter already used floating-gates to tune the biasing of the transconductance amplifiers within the biquad filter [160, 161] it was only natural for me to extend my field of research to the PFG sensors developed by my advisor.

A note to readers, the work in Chapter 3 and Sections 6.1 & 6.2 mostly took place while I was at Michigan State University. The work in Sections 6.3 & Chapter 5 were conducted primarily at Washington University in St. Louis, with Chapter 4 overlapping between both universities.

7.1 Findings and Conclusion

- **JUMP RESONANCE HYSTERESIS IN SILICON COCHLEA:** An oft unsought artifact that presents in certain current-mode filter configurations when attempting to attain high quality factor filtering, jump resonance, was probed for useful work. The sharp filter edges in the frequency domain, and the non-symmetric nature of the hysteresis was wielded to generate a features set that was more discriminating than standard linear filters. With respect to probability of detection on a test set of 20 speakers, a linear filter implemented in hardware had 90.94%, whereas the jump resonance chip that was fabricated achieved 98.75%.

- **CHARACTERIZATION OF A LINEAR INJECTOR:** A System-on-Chip (SoC) implementation of the linear injector reported by Dr. Huang [20] was tested under various conditions. After considering additional buffering distortions and a lower supply voltage of 1.8 V versus the originally reported 4 V, certain aspects such as the linearity (effective number of bits 12.979) and repeatable nature of the linear injection (less than 1% error) were validated. In the course of a more in-depth testing that leveraged new laboratory assets such as a thermally-controlled environment chamber, several shortcomings were uncovered. For example, the digital readout circuitry may deviate as much as 8% with a 1 °C change in ambient temperature, or the output buffers may not correctly reflect the charge stored on the floating-gate.

- **Transfer to Practice for Cyber-Physical System:** The Piezoelectric-Floating-Gate (PFG) sensor was taken out of the laboratory setting and deployed to real world test cases. This involved fabrication of a SoC with all necessary voltage references and interface circuitry for programming, sensing, and reading. Another major thrust of this effort was investigating wireless interrogation techniques that would enable the PFG sensor to be embedded within structures. Early efforts centered around deployments that could tolerate having wires exposed or those that could allow for backscatter power and communication. The use of cabling limited the sites that could be targeted, and the self-powered backscattering technique proved difficult to master without significant resource investment. To circumvent these limitations, quasi-self-powered and hybrid-powered wireless methods were proposed and implemented in practice. These methods have demonstrated the usefulness of the PFG's self-powered sensing in structural health monitoring applications.

Although not all of the work can be published, I would like to acknowledge the many partners in deployment testing: Mackinac Bridge Authority (MBA), Federal Highway Administration (FHWA), Federal Aviation Administration (FAA), Air Force Research Lab (AFRL) Materials and Manufacturing Directorate, National Wind Technology

Center (NWTC), National Renewable Energy Laboratory (NREL), Michigan Department of Transportation (MDOT), Florida Department of Transportation (FDOT),French Institute of Science and Technology for Transport, Spatial Planning, Development and Networks (IFSTTAR), Michigan State University (MSU), University of Southern California (USC), University of Nevada-Reno (UNR), University of Missouri (MU), University of Nottingham, and University of Palermo.

- **MODIFIED FEEDBACK AND INPUT OF LINEAR INJECTOR:** In the case of structural health monitoring with the PFG sensor, the acceleration of structures causes micro strains across the surface of the material. Via the piezoelectric transducer, these strains become voltages that are interfaced with our PFG SoC. The electric field potential is a function of the input strain level, but not necessarily the frequency of the strains. When data-logging sensor data, there is an apparent desire for having frequency data about input stimuli since it would allow better selectivity for monitoring of specific events. A modification to the core of the linear feedback injector of the PFG was proposed, using similar filter techniques as in the jump resonance chip. Although a low-pass filter response was expected, the measurements from a fabricated chip shows a more bandpass like response. In many deployments, a bandpass filter would be useful, but this modified topology will require additional study before it is ready for deployments. Another modification was done to the input stage, which now allows for a capacitively coupled input directly to the floating-gate node. It was verified that this method offers a means for data-logging of input stimuli smaller than the ≈6 V required for the traditional PFG. Using a differential structure, it would be possible to log and detect stimuli in the milli-volt scale.

7.2 Future Direction

- **Developing a More Robust Cyber-Physical System:** To overcome some of the limitations in the current implementation, several tasks can need to be undertaken. First, the entire design should be migrated away from the ON Semiconductor 0.5 µm process to a more readily available process such as the 180 nm process by TSMC. This transition would enable a more rapid cadence of iterations to test and verify new ideas. Second, in the interest of time, design choices like having a single-slope ADC (has non-monotonic output), using a PTAT current source (more than 5% deviation per 1 °C), and having simple amplifiers (cannot drive rail-to-rail) were made during the prototyping phase. Now that the prototypes have demonstrated the capabilities of the PFG concept, the circuit implementations of certain blocks should be reevaluated. A move to 180 nm could also enable the placement of RF components onto the SoC, which would vastly decrease the cost of deployment and allow greater flexibility in applications such as backscattering.

  Aside from the straightforward changes to the PFG implementation, there were many topology variations proposed in the course of this dissertation work that did not get fully fleshed out and explored. These include variants that can: log the time of events, have programmable level thresholds, greater injection sensitivity using diodes, daisy-chainable SoC data banks, non-overlapping data-logging (i.e. channel 1 stops recording if channel 2 is activated), higher effective number of bits, etc.

- **Exploring Domains for the PFG Beyond Structural Health Monitoring:** In Chapter 6, the PFG was deployed and testing on several civil engineering applications, primarily with respect to structural health monitoring. This technology can also be used in biomedical applications, as reported in Appendix A. Further exploration of non-civil applications has been limited due to a lack of time, and because the traditional PFG required large excitations to trigger the data-logging process, thereby limiting applications to the legs which absorb large impact forces [162]. With the more sensitive variant of the PFG that utilizes capacitive coupling, topics such as spinal cord fusion, organ growth, and cranial trauma could be avenues of research.

References

[1] A. Hande, R. Bridgelall, and B. Zoghi, "Vibration energy harvesting for disaster asset monitoring using active RFID tags," *Proceedings of the IEEE*, vol. 98, no. 9, pp. 1620–1628, 2010.

[2] A. M. Zungeru, L.-M. Ang, S. Prabaharan, and K. P. Seng, "Radio frequency energy harvesting and management for wireless sensor networks," *Green mobile devices and networks: Energy optimization and scavenging techniques*, pp. 341–368, 2012.

[3] H.-U. Kim, W.-H. Lee, H. R. Dias, and S. Priya, "Piezoelectric microgenerators-current status and challenges," *IEEE transactions on ultrasonics, ferroelectrics, and frequency control*, vol. 56, no. 8, 2009.

[4] S. Roundy, P. K. Wright, and J. Rabaey, "A study of low level vibrations as a power source for wireless sensor nodes," *Computer Communications*, vol. 26, no. 11, pp. 1131–1144, 2003, ubiquitous Computing.

[5] S. Dalola, M. Ferrari, V. Ferrari, M. Guizzetti, D. Marioli, and A. Taroni, "Characterization of thermoelectric modules for powering autonomous sensors," *IEEE Transactions on Instrumentation and Measurement*, vol. 58, no. 1, pp. 99–107, 2009.

[6] R. A. Bullen, T. Arnot, J. Lakeman, and F. Walsh, "Biofuel cells and their development," *Biosensors and Bioelectronics*, vol. 21, no. 11, pp. 2015–2045, 2006.

[7] S. H. Kondapalli, Y. Alazzawi, M. Malinowski, T. Timek, and S. Chakrabartty, "Multiaccess In Vivo Biotelemetry Using Sonomicrometry and M-Scan Ultrasound Imaging," *IEEE Transactions on Biomedical Engineering*, vol. 65, no. 1, pp. 149–158, Jan. 2018.

[8] G. E. Moore, "Progress in digital integrated electronics," in *Proc. IEEE Int. Electron Devices Meet. Dig. Tech Papers*, 1975, pp. 11–13.

[9] L. Bolotnyy and G. Robins, "The case of multi-tag RFID systems," in *IEEE International Conference on Wireless Algorithms, System and Applications (WASA)*, Chicago, U.S.A., Aug. 2007, pp. 174–186.

[10] M. Lallart, L. Garbuio, L. Petit, C. Richard, and D. Guyomar, "Double synchronized switch harvesting (DSSH): A new energy harvesting scheme for efficient energy extraction," *Ultrasonics, Ferroelectrics and Frequency Control, IEEE Transactions on*, vol. 55, no. 10, pp. 2119–2130, 2008.

[11] L. Garbuio, M. Lallart, D. Guyomar, C. Richard, and D. Audigier, “Mechanical energy harvester with ultralow threshold rectification based on SSHI nonlinear technique,” *Industrial Electronics, IEEE Transactions on*, vol. 56, no. 4, pp. 1048–1056, 2009.

[12] Y. K. Ramadass and A. P. Chandrakasan, “An efficient piezoelectric energy harvesting interface circuit using a bias-flip rectifier and shared inductor,” *Solid-State Circuits, IEEE Journal of*, vol. 45, no. 1, pp. 189–204, 2010.

[13] S. Xu, K. D. Ngo, T. Nishida, G.-B. Chung, and A. Sharma, “Low frequency pulsed resonant converter for energy harvesting,” *Power Electronics, IEEE Transactions on*, vol. 22, no. 1, pp. 63–68, 2007.

[14] R. D’hulst, T. Sterken, R. Puers, G. Deconinck, and J. Driesen, “Power processing circuits for piezoelectric vibration-based energy harvesters,” *Industrial Electronics, IEEE Transactions on*, vol. 57, no. 12, pp. 4170–4177, 2010.

[15] D. Kwon and G. A. Rincón-Mora, “A 2-m BiCMOS Rectifier-Free AC–DC Piezoelectric Energy Harvester-Charger IC,” *Biomedical Circuits and Systems, IEEE Transactions on*, vol. 4, no. 6, pp. 400–409, 2010.

[16] A. Tabesh and L. G. Fréchette, “A low-power stand-alone adaptive circuit for harvesting energy from a piezoelectric micropower generator,” *Industrial Electronics, IEEE Transactions on*, vol. 57, no. 3, pp. 840–849, 2010.

[17] S. Chakrabartty, “Self-powered Strain-rate Sensor,” 2010, patent No. 7757565, Issued 2010.

[18] S. Chakrabartty, N. Lajnef, N. Elvin, and A. Gore, “Self-powered Sensor,” 2011, patent No. 8056420, Issued 2011.

[19] C. Huang, N. Lajnef, and S. Chakrabartty, “Calibration and characterization of self-powered floating-gate usage monitor with single electron per second operational limit,” *Circuits and Systems I: Regular Papers, IEEE Transactions on*, vol. 57, no. 3, pp. 556–567, 2010.

[20] C. Huang, P. Sarkar, and S. Chakrabartty, “Rail-to-Rail, Linear Hot-Electron Injection Programming of Floating-Gate Voltage Bias Generators at 13-Bit Resolution,” *IEEE Journal of Solid-State Circuits*, vol. 46, no. 11, pp. 2685–2692, 2011. [Online]. Available: https://doi.org/10.1109/JSSC.2011.2167390

[21] J. L. Douce, “A note on the evaluation of the response of a non-linear element to sinusoidal and random signals,” *Proceedings of the IEE - Part C: Monographs*, vol. 105, no. 7, pp. 88–92, Mar. 1958.

[22] S. H. Kyong, “Jump Criteria of Nonlinear Control Systems and the Validity of Statistical Linearization Approximation,” *The Bell System Technical Journal*, vol. 48, no. 8, pp. 2529–2543, Sep. 1969.

[23] A. Fukuma and M. Matsubara, “Jump resonance in nonlinear feedback systems–Part I: Approximate analysis by the describing-function method,” *IEEE Trans. Autom. Control*, vol. 23, no. 5, pp. 891–896, Oct. 1978.

[24] L. T. Lewis, “Harmonic Analysis for Non-Linear Characteristices,” *Transactions of the American IEE*, vol. 73, no. 1, pp. 693–700, 1954.

[25] A. R. Bergen and R. L. Franks, “Justification of the Describing Function Method,” *SIAM J. on Control and Optimization*, vol. 9, no. 4, pp. 568–589, 1971.

[26] C. F. Ho, “An extension to fukuma and matsubara jump resonance criterion by the use of describing functions,” *Radio and Electronic Engineer*, vol. 442, no. 15, pp. 562–568, 1972.

[27] A. Fukuma and M. Matsubara, “Jump Resonance Criteria of Nonlinear Control Systems,” *IEEE Trans. Autom. Control*, vol. 11, no. 4, pp. 699–706, Oct. 1966.

[28] H. Hatanaka, “The Frequency Responses and Jump-Resonance Phenomena of Nonlinear Feedback Control Systems,” *J. Basic Eng.*, vol. 85, no. 2, pp. 236–242, Jun. 1969.

[29] K. Hirai and N. Sawai, “A general criterion for Jump Resonance of Nonlinear Control Systems,” *IEEE Trans. Autom. Control*, vol. 23, no. 5, pp. 896–901, Oct. 1978.

[30] A. M. Hopkin and K. Ogata, “An analytic Frequency-Response Solution for a higher order Servomechanism with a nonlinear control element,” *J. Basic Eng.*, vol. 81, no. 1, pp. 41–45, Mar. 1959.

[31] C. D. Salthouse and R. Sarpeshkar, “Jump Resonance: A Feedback Viewpoint and Adaptive Circuit Solution for Low-Power Active Analog Filters,” *IEEE Trans. Circuits Syst.*, vol. 53, no. 8, pp. 1712–1725, Aug. 2006.

[32] E. A. Freeman and M. L. Devine, “Calculation and avoidance of jump resonance in feedback amplifier circuits,” *Proc. IEE*, vol. 115, no. 1, pp. 229–235, Jan. 1968.

[33] R. S. Moni and K. R. Rao, “Jump-Phenomenon in Active-*RC* Filters,” *IEEE Trans. Circuits Syst.*, vol. 29, no. 1, pp. 54–55, Jan. 1982.

[34] J. Glass, “Acoustic Properties of Speech Sounds,” Jun. 1999, presented at WS’99, hosted by The Center for Language and Speech Processing at The John Hopkins University.

[35] A. Fazel and S. Chakrabartty, “An Overview of Statistical Pattern Recognition Techniques for Speaker Verification,” *IEEE Circuits Syst. Mag.*, vol. 11, no. 2, pp. 62–81, 2011.

[36] K. Aono, S. Chakrabartty, and T. Yamasaki, "Infrasonic Scene Fingerprinting for Authenticating Speaker Location," in *2017 IEEE International Conference on Acoustics, Speech and Signal Processing (ICASSP)*, Mar. 2017, pp. 361–365.

[37] V. Chan, S.-C. Liu, and A. van Schaik, "AER EAR: A Matched Silicon Cochlea Pair with Address Event Representation Interface," *IEEE Trans. Circuits Syst. I*, vol. 54, no. 1, pp. 48–59, Jan. 2007.

[38] R. Sarpeshkar, "Energy-efficient adaptive signal decomposition: The silicon and biological cochlea," in *Circuits and Systems, 1999. ISCAS '99. Proceedings of the 1999 IEEE International Symposium On*, 1999, pp. 70–73.

[39] H. N. Teodorescu, "AI Tools for Speech Analysis Applied to the Romanian Language," in *Proceedings of The 4th European Computing Conference*, 2010, pp. 272–279.

[40] L. Bian, E. E. Linhardt, and M. E. Chertoff, "Cochlear hysteresis: Observation with low-frequency modulateddistortion product otoacoustic emissions," *J. Acoust. Soc. Am.*, vol. 115, no. 5, pp. 2159–2172, May 2004.

[41] L. Bian and N. M. Scherrer, "Low-frequency modulation of distortion product otoacousticemissions in humans," *J. Acoust. Soc. Am.*, vol. 122, no. 3, pp. 1681–1692, Sep. 2007.

[42] S. S. Lamba and R. J. Kavanagh, "Phenomenon of isolated jump resonance and its applications," *Proc. IEE*, vol. 118, no. 8, pp. 1047–1050, Aug. 1971.

[43] R. J. Kavanagh and D. M. Sinclair, "A Novel Frequency Meter Using Jump Resonance," *IEEE Trans. Instrum. Meas.*, vol. 23, pp. 178–179, Jun. 1974.

[44] A. Tustin, "A method of analysing the effect of certain kinds of non-linearity in closed-cycle control systems," *Electrical Engineers - Part IIA: Automatic Regulators and Servo Mechanisms, Journal of the Institution of*, vol. 94, no. 1, pp. 152–160, May 1947.

[45] J. P. Campbell, "Testing with the YOHO CD-ROM voice verification corpus," in *Acoustics, Speech, and Signal Processing, 1995. ICASSP-95., 1995 International Conference On*, vol. 1, May 1995, pp. 341–344.

[46] W. M. Campbell, K. T. Assaleh, and C. C. Broun, "Speaker recognition with polynomial classifiers," *IEEE Trans. Speech Audio Process.*, vol. 10, no. 4, pp. 205–212, May 2002.

[47] A. Gore and S. Chakrabartty, "Min-Max Optimization Framework for Designing SigmaDelta Learners: Theory and Hardware," *IEEE Trans. Circuits Syst. I*, no. 3, pp. 604–617, 2010.

[48] Ahana Gangopadhyay, Kenji Aono, Darshit Mehta, and Shantanu Chakrabartty, "A Coupled Network of Growth Transform Neurons for Spike-Encoded Auditory Feature Extraction," *bioRxiv*, Apr. 2018.

[49] B. Gold and N. Morgan, *Speech and Audio Signal Processing.* New York, New York: John Wiley and Sons, 2000.

[50] R. Auckenthaler, M. Carey, and H. Lloyd-Thomas, "Score normalization for text-independent speaker verification system," *Digital Signal Processing*, vol. 10, no. 1, 2000.

[51] Y. Gu and T. Thomas, "A text-independent speaker verification system using support vector machines classifier," in *Proc. Eur. Conf. Speaker Communication and Technology (Eurospeech'01)*, Aalborg, Denmark, Sep. 2001, pp. 1765–1769.

[52] S. Chakrabartty and G. Cauwenberghs, "Gini-Support Vector Machine: Quadratic Entropy Based Multi-class Probability Regression," *Journal of Machine Learning Research*, pp. 813–839, Apr. 2007.

[53] K. Aono, R. K. Shaga, and S. Chakrabartty, "Exploiting jump-resonance hysteresis in silicon cochlea for formant trajectory encoding," in *2012 IEEE 55th International Midwest Symposium on Circuits and Systems (MWSCAS)*, Aug. 2012, pp. 85–88.

[54] K. Aono, "Extracting Speaker Features from Sub-Vocal Speech Using Jump Resonance Filtering," Nov. 2013.

[55] Kenji Aono, "Extracting Speaker Features from Sub-Vocal Speech Using Jump Resonance Filtering," in *Michigan Space Grant Consortium, Annual Fall Conference*, University of Michigan, Ann Arbor, MI, Nov. 2013, pp. 1–30.

[56] ——, "Jump Resonance Filtering for Biometrics via Electromyography in Sub-Vocal Speech," in *Michigan Space Grant Consortium*, Aug. 2013, pp. 1–5.

[57] ——, "EMG-based Speech Filtering & Classifier," in *MSGC Annual Conference.* Michigan Space Grant Consortium, Aug. 2014, pp. 1–4.

[58] D. C. Guterman, I. H. Rimawi, T.-L. Chiu, R. D. Halvorson, and D. J. McElroy, "An Electrically Alterable Nonvolatile Memory Cell Using a Floating-Gate Structure," *IEEE Transactions on Electron Devices*, vol. ED-26, no. 4, pp. 576–586, 1979.

[59] L. R. Carley, "Trimming Analog Circuits Using Floating-Gate Analog MOS Memory," *IEEE Journal of Solid-State Circuits*, vol. 24, no. 6, pp. 1569–1575, Dec. 1989.

[60] K. Yang and A. G. Andreou, "A Multiple Input Differential Amplifier Based on Charge Sharing on a Floating-Gate MOSFET," *Analog Integrated Circuits and Signal Processing*, vol. 6, pp. 197–208, 1994.

[61] S. L. Miller, “Ionization Rates for Holes and Electrons in Silicon,” *Physical Review*, vol. 105, no. 4, pp. 1246–1249, Feb. 1957.

[62] M. Lenzilinger and E. H. Snow, “Fowler-Nordheim Tunneling into Thermally Grown SiO_2,” *J. Applied Physics*, vol. 40, no. 1, pp. 278–283, Jan. 1969.

[63] L. Zhou, K. Aono, and S. Chakrabartty, “Gaussian Process Regression for Improving the Performance of Self-powered Time-of-Occurrence Sensors,” in *2018 IEEE 61st International Midwest Symposium on Circuits and Systems (MWSCAS)*, Aug. 2018.

[64] D. Mehta, L. Zhou, K. Aono, and S. Chakrabartty, “Self-powered Sensing and Time-Stamping of Tampering Events,” in *2018 IEEE 61st International Midwest Symposium on Circuits and Systems (MWSCAS)*, Aug. 2018.

[65] L. Zhou and S. Chakrabartty, “Linearization of CMOS Hot-Electron Injectors for Self-Powered Monitoring of Biomechanical Strain Variations,” *IEEE Transactions on Biomedical Circuits and Systems*, 2016.

[66] ——, “Self-powered sensing and time-stamping of rare events using CMOS fowler-nordheim tunneling timers,” in *Circuits and Systems (ISCAS), 2016 IEEE International Symposium On*. IEEE, 2016, pp. 2839–2842.

[67] ——, “Self-Powered Timekeeping and Synchronization Using Fowler–Nordheim Tunneling-Based Floating-Gate Integrators,” *IEEE Transactions on Electron Devices*, vol. 64, no. 3, pp. 1254–1260, 2017.

[68] Liang Zhou, Kenji Aono, and Shantanu Chakrabartty, “Tamper Sensitive Authentication of Passive IoT Devices Using Self-Powered CMOS Timers,” in *TECHCON*. Austin, TX: SRC, 2018. [Online]. Available: https://www.src.org/library/publication/p093901/p093901.pdf

[69] L. Zhou and S. Chakrabartty, “Modeling of CMOS Zero-power Timers for Dynamic Authentication of Passive Assets,” in *SRC TECHCON*, 2016.

[70] L. Zhou, “Self-powered Time-Keeping and Time-of-Occurrence Sensing,” Ph.D. dissertation, Washington University in St. Louis, 2018.

[71] P. Sarkar and S. Chakrabartty, “Compressive Self-Powering of Piezo-Floating-Gate Mechanical Impact Detectors,” *Circuits and Systems I: Regular Papers, IEEE Transactions on*, vol. 60, no. 9, pp. 2311–2320, 2013.

[72] K. Aono, T. Covassin, and S. Chakrabartty, “Monitoring of repeated head impacts using time-dilation based self-powered sensing,” in *IEEE International Symposium on Circuits and Systems, ISCAS 2014, Melbourne, Victoria, Australia, June 1-5, 2014*, 2014, Peer-reviewed Conference, pp. 1620–1623. [Online]. Available: https://doi.org/10.1109/ISCAS.2014.6865461

[73] T. Feng, K. Aono, T. Covassin, and S. Chakrabartty, “Self-Powered Monitoring of Repeated Head Impacts Using Time-Dilation Energy Measurement Circuit,” *IEEE Trans. Biomed. Circuits and Systems*, vol. 9, no. 2, pp. 217–226, 2015. [Online]. Available: https://doi.org/10.1109/TBCAS.2015.2403864

[74] T. Feng, “Design and Implementation of Efficient Energy Harvesting Circuits for Ultra Low Power and Impact Energy Applications,” Ph.D. dissertation, Michigan State University, 2016.

[75] C. Huang and S. Chakrabartty, “Compact self-powered CMOS strain-rate monitoring circuit for piezoelectric energy scavengers,” *Electronics Letters*, vol. 47, no. 4, pp. 277–278(1), 2011.

[76] ——, “An Asynchronous Analog Self-Powered CMOS Sensor-Data-Logger With a 13.56 MHz RF Programming Interface,” *IEEE Journal of Solid-State Circuits*, vol. 47, no. 2, pp. 476–489, 2012. [Online]. Available: https://doi.org/10.1109/JSSC.2011.2172159

[77] P. Sarkar, C. Huang, and S. Chakrabartty, “An Ultra-Linear Piezo-Floating-Gate Strain-Gauge for Self-Powered Measurement of Quasi-Static-Strain,” *Biomedical Circuits and Systems, IEEE Transactions on*, vol. 7, no. 4, pp. 437–450, 2013.

[78] ——, “An ultra-linear piezo-floating-gate strain-guage for self-powered measurement of quasi-static-strain,” *IEEE Trans. Biomed. Circuits Syst.*, vol. 7, no. 4, pp. 437–450, 2013.

[79] N. Lajnef, K. Chatti, S. Chakrabartty, M. Rhimi, and P. Sarkar, “Smart Pavement Monitoring System,” Michigan State Univ. & Federal Highway Administration, Washington, DC, FHWA-HRT-12-072 Final Rep. DTFH61-08-C-00015, 2013.

[80] S. Chakrabartty, T. Feng, and K. Aono, “Gen-2 RFID Compatible, Zero Down-time, Programmable Mechanical Strain-monitors and Mechanical Impact Detectors,” in *Proceedings Volume 8692, Sensors and Smart Structures Technologies for Civil, Mechanical, and Aerospace Systems, San Diego, CA, USA, Apr 19, 2013*, 2012, Peer-reviewed Conference, p. 86921A. [Online]. Available: https://doi.org/10.1117/12.2011956

[81] K. Aono, N. Lajnef, F. Faridazar, and S. Chakrabartty, “Infrastructural health monitoring using self-powered Internet-of-Things,” in *IEEE International Symposium on Circuits and Systems, ISCAS 2016, Montréal, QC, Canada, May 22-25, 2016*, 2016, Peer-reviewed Conference, pp. 2058–2061. [Online]. Available: https://doi.org/10.1109/ISCAS.2016.7538983

[82] P. E. Hasler, “Foundations of learning in analog VLSI,” Ph.D. dissertation, California Institute of Technology, 1997.

[83] N. Lajnef, R. Burgueno, W. Borchani, and S. Chakrabartty, "Sub-Hz self-powered sensing based on mechanical-buckling driven hot-electron injection," in *2014 IEEE International Symposium on Circuits and Systems (ISCAS)*, Jun. 2014, pp. 670–673.

[84] L. M. Miller, E. Halvorsen, T. Dong, and P. K. Wright, "Modeling and experimental verification of low-frequency MEMS energy harvesting from ambient vibrations," *Journal of Micromechanics and Microengineering*, vol. 21, no. 4, p. 045029, 2011.

[85] K. Najafi, T. Galchev, E. E. Aktakka, R. L. Peterson, and J. McCullagh, "Microsystems for energy harvesting," in *2011 16th International Solid-State Sensors, Actuators and Microsystems Conference*, Jun. 2011, pp. 1845–1850.

[86] W. Jaikla and M. Siripruchyanan, "An electronically controllable capacitance multiplier with temperature compensation," in *2006 International Symposium on Communications and Information Technologies*, Oct. 2006, pp. 356–359.

[87] Y. Tsividis, "Signal-to-Noise Ration, Dynamic Range, and Power Dissipation," *IEEE Solid-State Circuits Magazine*, vol. 10, no. 4, Nov. 2018.

[88] Kenji Aono, Darshit Mehta, and Shantanu Chakrabartty, "Analog Non-volatile Memory with In-built Filtering," 2019, (In Preparation).

[89] N. G. Elvin, N. Lajnef, and A. A. Elvin, "Feasibility of structural monitoring with vibration powered sensors," *Smart Materials and Structures*, vol. 15, no. 4, pp. 1422–1429, 2006.

[90] Hassene Hasni, Kenji Aono, Owen Pochettino, Nizar Lajnef, and Shantanu Chakrabartty, "Long-term Structural Health Monitoring of Steel Bridges Using Quasi-self-powered Sensors: The Mackinac Bridge Case Study," *Structural Health Monitoring*, 2019, (In Preparation).

[91] P. Jiao, W. Borchani, A. H. Alavi, H. Hasni, and N. Lajnef, "An energy harvesting and damage sensing solution based on postbuckling response of nonuniform cross-section beams," *Structural Control and Health Monitoring*, vol. 25, no. 1, p. e2052, 2018.

[92] P. Jiao, W. Borchani, H. Hasni, and N. Lajnef, "A new solution of measuring thermal response of prestressed concrete bridge girders for structural health monitoring," *Measurement Science and Technology*, vol. 28, no. 8, p. 085005, 2017.

[93] A. H. Alavi, H. Hasni, N. Lajnef, K. Chatti, and F. Faridazar, "An Intelligent Structural Damage Detection Approach Based on Self-powered Wireless Sensor Data," *Automation in Construction*, vol. 62, pp. 24–44, 2016.

[94] H. Hasni, N. Lajnef, A. H. Alavi, K. Aono, and S. Chakrabartty, "Local-global Damage Identification Approach Using Hybrid Network of Self-powered Sensors," in *The 7th World Conference on Structural Control and Monitoring (7WCSCM)*, Jul. 2018, pp. 1–8.

[95] H. Hasni, K. Chatti, N. Lajnef, S. Chakrabartty, and K. Aono, “Damage Progression Identification in Asphalt Concrete Pavements: A Smart Self-powered Sensing Approach,” in *Advances in Materials and Pavement Prediction*, ser. International Conference on Advances in Materials and Pavement Performance Prediction (AM3P 2018), Apr. 2017, pp. 1–10.

[96] H. Hasni, P. Jiao, A. H. Alavi, N. Lajnef, and S. F. Masri, “Structural health monitoring of steel frames using a network of self-powered strain and acceleration sensors: A numerical study,” *Automation in Construction*, vol. 85, pp. 344–357, 2018.

[97] H. Hasni, A. Alavi, P. Jiao, N. Lajnef, K. Chatti, K. Aono, and S. Chakrabartty, “A New Approach for Damage Detection in Asphalt Concrete Pavements Using Battery-Free Wireless Sensors with Non-Constant Injection Rates,” *Measurement*, vol. 110, pp. 217–229, 2017. [Online]. Available: https://doi.org/10.1016/j.measurement.2017.06.035

[98] H. Hasni, A. H. Alavi, P. Jiao, and N. Lajnef, “Detection of fatigue cracking in steel bridge girders: A support vector machine approach,” *Archives of Civil and Mechanical Engineering*, vol. 17, no. 3, pp. 609–622, 2017.

[99] H. Hasni, A. H. Alavi, N. Lajnef, M. Abdelbarr, S. F. Masri, and S. Chakrabartty, “Self-powered piezo-floating-gate sensors for health monitoring of steel plates,” *Engineering Structures*, vol. 148, pp. 584–601, 2017.

[100] H. Hasni, A. H. Alavi, K. Chatti, and N. Lajnef, “A self-powered surface sensing approach for detection of bottom-up cracking in asphalt concrete pavements: Theoretical/numerical modeling,” *Construction and Building Materials*, vol. 144, pp. 728–746, 2017.

[101] “Accelerated Bridge Construction.” [Online]. Available: https://wolfweb.unr.edu/homepage/saiidi/USDOT/documents.html

[102] “California Department of Transportation.” [Online]. Available: http://wolfweb.unr.edu/homepage/saiidi/caltrans/abc-systems.html

[103] L. Zhou, A. C. Abraham, S. Y. Tang, and S. Chakrabartty, “A 5 nW Quasi-Linear CMOS Hot-Electron Injector for Self-Powered Monitoring of Biomechanical Strain Variations,” *IEEE Transactions on Biomedical Circuits and Systems*, vol. 10, no. 6, pp. 1143–1151, 2016.

[104] ——, “Approaching the Limits of Piezoelectricity driven Hot-electron Injection for Self-powered in vivo Monitoring of Micro-strain Variations,” in *Circuits and Systems (ISCAS), 2016 IEEE International Symposium On.* IEEE, 2016, pp. 1810–1813.

[105] A. P. Sample, D. J. Yeager, P. S. Powledge, A. V. Mamishev, and J. R. Smith, “Design of an RFID-based Battery-Free Programmable Sensing Platform,” *IEEE Trans. Instrumentation and Measurement*, vol. 57, no. 11, Nov. 2008.

[106] S. Roy, V. Jandhyala, J. R. Smith, D. J. Wetherall, B. P. Otis, R. Chakraborty, M. Buettner, D. J. Yeager, Y.-C. Ko, and A. P. Sample, "RFID: From Supply Chains to Sensor Nets," *Proceedings of the IEEE*, vol. 98, no. 9, Sep. 2010.

[107] S. H. Kondapalli, X. Zhang, and S. Chakrabartty, "Variance-based digital logic for energy harvesting internet-of-things," in *IEEE International Symposium on Circuits and Systems (ISCAS).* IEEE, 2017, pp. 1–4.

[108] ——, "Energy-dissipation limits in variance-based computing," *Fluctuation and Noise Letters*, vol. 17, no. 02, p. 1850013, 2018.

[109] Yarub Alazzawi, Kenji Aono, Erica Scheller, and Shantanu Chakrabartty, "Exploiting Self-capacitances for Wireless Power Transfer," *IEEE Trans. Biomed. Circuits Syst.*, 2019, (Submitted).

[110] V. Talla and J. R. Smith, "Hybrid analog-digital backscatter: A new approach for battery-free sensing," in *2013 IEEE International Conference on RFID (RFID)*, Apr. 2013, pp. 74–81.

[111] P. Zhang, P. Hu, V. Pasikanti, and D. Ganesan, "EkhoNet: High Speed Ultra Low-power Backscatter for Next Generation Sensors," in *Proceedings of the 20th Annual International Conference on Mobile Computing and Networking*, ser. MobiCom '14, Maui, Hawaii, USA, 2014, pp. 557–568.

[112] A. Varshney, C. Pérez-Penichet, C. Rohner, and T. Voigt, "LoRea: A Backscatter Architecture That Achieves a Long Communication Range," in *Proceedings of the 15th ACM Conference on Embedded Network Sensor Systems*, ser. SenSys '17, Delft, Netherlands, 2017, pp. 50:1–50:2.

[113] Y. Peng, L. Shangguan, Y. Hu, Y. Qian, X. Lin, X. Chen, D. Fang, and K. Jamieson, "PLoRa: A Passive Long-range Data Network from Ambient LoRa Transmissions," in *Proceedings of the 2018 Conference of the ACM Special Interest Group on Data Communication*, ser. SIGCOMM '18, Budapest, Hungary, 2018, pp. 147–160.

[114] H. Hasni, N. Lajnef, K. Chatti, K. Aono, and S. Chakrabartty, "Intelligent Pavement Condition Assessment Using Piezo-Floating-Gate Sensors," in *The 7th World Conference on Structural Control and Monitoring (7WCSCM)*, Jul. 2018, pp. 1–10.

[115] A. H. Alavi, H. Hasni, N. Lajnef, K. Chatti, and F. Faridazar, "Damage detection using self-powered wireless sensor data: An evolutionary approach," *Measurement*, vol. 82, pp. 254–283, 2016.

[116] Y. Yu, W.-H. Kang, C. Zhang, J. Wang, and J. Ou, "A stochastic analysis framework for a steel frame structure using wireless sensor system measurements," *Measurement*, vol. 69, pp. 202–209, 2015.

[117] C.-B. Yun and J. Min, "Smart sensing, monitoring, and damage detection for civil infrastructures," *KSCE Journal of Civil Engineering*, vol. 15, no. 1, pp. 1–14, 2011.

[118] J. P. Lynch and K. J. Loh, "A summary review of wireless sensors and sensor networks for structural health monitoring," *Shock and Vibration Digest*, vol. 38, no. 2, pp. 91–130, 2006.

[119] R. Bennett, B. Hayes-Gill, J. A. Crowe, R. Armitage, D. Rodgers, and A. Hendroff, "Wireless monitoring of highways," in *Smart Structures and Materials 1999: Smart Systems for Bridges, Structures, and Highways*, vol. 3671. International Society for Optics and Photonics, 1999, pp. 173–183.

[120] S. Cho, C.-B. Yun, J. P. Lynch, A. T. Zimmerman, B. F. Spencer Jr, and T. Nagayama, "Smart wireless sensor technology for structural health monitoring of civil structures," *Steel Structures*, vol. 8, no. 4, pp. 267–275, 2008.

[121] G. J. Yun, S.-G. Lee, J. Carletta, and T. Nagayama, "Decentralized damage identification using wavelet signal analysis embedded on wireless smart sensors," *Engineering Structures*, vol. 33, no. 7, pp. 2162–2172, 2011.

[122] D. G. Watters, P. Jayaweera, A. J. Bahr, D. L. Huestis, N. Priyantha, R. Meline, R. Reis, and D. Parks, "Smart Pebble: Wireless sensors for structural health monitoring of bridge decks," in *Smart Structures and Materials 2003: Smart Systems and Nondestructive Evaluation for Civil Infrastructures*, vol. 5057. International Society for Optics and Photonics, 2003, pp. 20–29.

[123] P. Pasupath, M. Z. Zhou, D. P. Neikirk, and S. L. Wood, "Unpowered Resonant Wireless Sensor Nets for Structural Health Monitoring," in *2008 IEEE Sensors*, Oct. 2008, pp. 697–700.

[124] D. Sackin, "A Feasibility Study of Embedded Microdevices for Infrastructure Monitoring; Smart Aggregate for Concrete," Ph.D. dissertation, A thesis submitted in partial fulfillment of the requirements for the degree of Master of Science, 1999.

[125] I. Korhonen and R. Lankinen, "Energy harvester for a wireless sensor in a boiler environment," *Measurement*, vol. 58, pp. 241–248, 2014.

[126] B. Spencer Jr, M. E. Ruiz-Sandoval, and N. Kurata, "Smart sensing technology: Opportunities and challenges," *Structural Control and Health Monitoring*, vol. 11, no. 4, pp. 349–368, 2004.

[127] J. Sirohi and I. Chopra, "Fundamental understanding of piezoelectric strain sensors," *Journal of intelligent material systems and structures*, vol. 11, no. 4, pp. 246–257, 2000.

[128] J. Lynch, "Overview of wireless sensors for real-time health monitoring of civil structures," in *Proceedings of the 4th International Workshop on Structural Control*, 2004, pp. 189–194.

[129] J. P. Lynch, "Design of a wireless active sensing unit for localized structural health monitoring," *Structural Control and Health Monitoring: The Official Journal of the International Association for Structural Control and Monitoring and of the European Association for the Control of Structures*, vol. 12, no. 3-4, pp. 405–423, 2005.

[130] M. J. Whelan, M. V. Gangone, K. D. Janoyan, and R. Jha, "Real-time wireless vibration monitoring for operational modal analysis of an integral abutment highway bridge," *Engineering Structures*, vol. 31, no. 10, pp. 2224–2235, 2009.

[131] J. P. Lynch, K. H. Law, A. S. Kiremidjian, T. W. Kenny, E. Carryer, and A. Partridge, "The design of a wireless sensing unit for structural health monitoring," in *Proceedings of the 3rd International Workshop on Structural Health Monitoring.* Stanford University Stanford, CA, 2001, pp. 12–14.

[132] J. Paek, N. Kothari, K. Chintalapudi, S. Rangwala, and R. Govindan, "The performance of a wireless sensor network for structural health monitoring," in *UCLA: Center for Embedded Network Sensing.* UCLA, 2004, pp. 1–12.

[133] S. Chakrabartty, "Self-powered Strain-gauge," 2016, patent No. 9331265, Issued 2016.

[134] K. Aono, S. H. Kondapalli, N. Lajnef, G. Pekcan, F. Faridazar, and S. Chakrabartty, "Self-powered Sensors to Facilitate Infrastructural Internet-of-Things for Smart Structures," in *ANCRiSST 13th International Workshop on Advanced Smart Materials and Smart Structures Technology, Tokyo, Japan, July 22-23, 2017*, 2017, Workshop. [Online]. Available: https://www.researchgate.net/publication/323456921

[135] K. Aono, H. Hasni, O. Pochettino, N. Lajnef, and S. Chakrabartty, "Quasi-self-powered Infrastructural Internet of Things: The Mackinac Bridge Case Study," in *Proceedings of the 2018 on Great Lakes Symposium on VLSI*, ser. GLSVLSI '18, May 2018, pp. 335–340.

[136] S. H. Kondapalli, O. Pochettino, K. Aono, and S. Chakrabartty, "Hybrid-powered Internet-of-Things for Infrastructure-to-Vehicle Communication," in *2018 IEEE 61st International Midwest Symposium on Circuits and Systems (MWSCAS)*, Aug. 2018.

[137] Kenji Aono, "Application Note: PCB Design with EAGLE," *Michigan State University*, vol. Department of Electrical & Computer Engineering, pp. 1–33, 2011.

[138] K. Technologies, "Evaluate lithium ion self-discharge of cells in a fraction of the time traditionally required," December 2017.

[139] H. Reuning and M. Joosse, "Investigations into the lifetime of gas meter batteries in the netherlands," *Metering International*, vol. 2, pp. 78–81, 2013.

[140] W. Borchani, K. Aono, N. Lajnef, and S. Chakrabartty, "Monitoring of Postoperative Bone Healing Using Smart Trauma-Fixation Device With Integrated Self-Powered

Piezo-Floating-Gate Sensors," *IEEE Trans. Biomed. Engineering*, vol. 63, no. 7, pp. 1463–1472, 2016. [Online]. Available: https://doi.org/10.1109/TBME.2015.2496237

[141] L. Zhou, K. Aono, and S. Chakrabartty, "A CMOS Timer-Injector Integrated Circuit for Self-Powered Sensing of Time-of-Occurrence," *IEEE J. Solid-State Circuits*, vol. PP, pp. 1–11, 2018. [Online]. Available: https://doi.org/10.1109/JSSC.2018.2793531

[142] H. Hasni, K. Aono, N. Lajnef, S. Chakrabartty, and F. Faridazar, "Toward Autonomous Self-Powered Self-Sensing Civil Infrastructures," in *NDE/NDT for Structural Materials Technology for Highway Bridges (SMT) and the International Symposium on Non-Destructive Testing in Civil Engineering (NDT-CD)*, ser. SMT and NDT-CE, Aug. 2018.

[143] Kenji Aono, Hassene Hasni, Owen Pochettino, Nizar Lajnef, and Shantanu Chakrabartty, "Quasi-self-powered Piezo-Floating-Gate Sensing Technology for Continuous Monitoring of Large-Scale Bridge," *Frontiers in Built Environment*, 2019, (Submitted).

[144] N. Lajnef, N. G. Elvin, and S. Chakrabartty, "A piezo-powered floating-gate sensor array for long-term fatigue monitoring in biomechanical implants," *Biomedical Circuits and Systems, IEEE Transactions on*, vol. 2, no. 3, pp. 164–172, 2008.

[145] P. Sarkar, "Programmable and Reconfigurable Strain-powered Micro-data-loggers Based on Linear Piezo-floating-gate Injectors," Ph.D. dissertation, Michigan State University, 2012.

[146] W. Borchani, "Energy harvesting from localized dynamic transitions in post-buckled elastic beams under quasi-static loading," Ph.D. dissertation, Michigan State University, 2015.

[147] Hassene Hasni, Kenji Aono, Owen Pochettino, Nizar Lajnef, and Shantanu Chakrabartty, "A Robust Fatigue Crack Detection in Wind Turbine Blade: Battery-Free Sensing Approach," 2019, (In Preparation).

[148] Owen Pochettino, Sri Harsha Kondapalli, Kenji Aono, and Shantanu Chakrabartty, "Enabling Long-term Infrastructure to Vehicular Communication with Hybrid Powered Systems," in *IEEE International Symposium on Circuits and Systems, ISCAS 2019, Sapporo, Japan, May 26-29, 2019.* Sapporo, Japan: IEEE, 2019, (Submitted).

[149] Owen Pochettino, Kenji Aono, Hassene Hasni, Nizar Lajnef, and Shantanu Chakrabartty, "Infrasructural Internet-of-Things Using Quasi-self-powered Structural Health Monitoring Sensors," in *9th International Conference on Structural Health Monitoring of Intelligent Infrastructure*, Aug. 2019, (Submitted).

[150] Sri Harsha Kondapalli, Owen Pochettino, Kenji Aono, Hassene Hasni, Nizar Lajnef, and Shantanu Chakrabartty, "Embedded H-gage with Self and Quasi-self-powered Sensors for Pavement Monitoring," in *9th International Conference on Structural Health Monitoring of Intelligent Infrastructure*, St. Louis, MO, U.S.A., Aug. 2019, (Submitted).

[151] Sri Harsha Kondapalli, Liang Zhou, Kenji Aono, and Shantanu Chakrabartty, "Self-Powered CMOS Time Synchronized Temperature Monitoring," in *IEEE International Symposium on Circuits and Systems, ISCAS 2019, Sapporo, Japan, May 26-29, 2019*, 2019, (Submitted).

[152] W. S. Rhode, "Observations of the vibration of the Basilar Membrane in Squirrel Monkeys using the Mőssbauer Technique," *The Journal of the Acoustical Society of America*, vol. 49, no. 4B, p. 1218, 1971.

[153] T. Reichenbach and A. J. Hudspeth, "A ratchet mechanism for amplification in low-frequency mammalian hearing," *Proceedings of the National Academy of Sciences*, vol. 107, no. 11, pp. 4973–4978, 2010.

[154] D. L. Hiser and R. L. Gieger, "Impact of OTA Nonlinearities on the Performance of Continuous-Time OTA-C Bandpass Filters," in *Circuits and Systems, 1990., IEEE International Symposium On*, May 1990, pp. 1167–1170 vol.2.

[155] L.-S. Ma, C.-H. Wu, J.-L. Jaw, B.-F. Wu, and J.-W. Perng, "Jump Resonance Analysis for Systems with Parametric Uncertainties," in *Broadband, Wireless Computing, Communication and Applications (BWCCA), 2010 International Conference On*, Nov. 2010, pp. 654–659.

[156] J. Guerreiro, A. Reid, J. C. Jackson, and J. F. C. Windmill, "Active Hearing Mechanisms Inspire Adaptive Amplification in an Acoustic Sensor System," *IEEE Transactions on Biomedical Circuits and Systems*, vol. 12, no. 3, pp. 655–664, Jun. 2018.

[157] ——, "Bio-inspired active amplification in a MEMS microphone using feedback computation," in *2017 IEEE Biomedical Circuits and Systems Conference (BioCAS)*, Oct. 2017, pp. 1–4.

[158] S. J. van Albada, A. G. Rowley, J. Senk, M. Hopkins, M. Schmidt, A. B. Stokes, D. R. Lester, M. Diesmann, and S. B. Furber, "Performance Comparison of the Digital Neuromorphic Hardware SpiNNaker and the Neural Network Simulation Software NEST for a Full-Scale Cortical Microcircuit Model," *Frontiers in Neuroscience*, vol. 12, p. 291, 2018. [Online]. Available: https://www.frontiersin.org/article/10.3389/fnins.2018.00291

[159] A. L. Nuttall and A. Fridberger, "Instrumentation for Studies of Cochlear Mechanics: From von Békésy forward," *Hearing Research*, vol. 293, no. 1, pp. 3–11, 2012.

[160] S. Chakrabartty, R. K. Shaga, and K. Aono, “Noise-Shaping Gradient Descent-Based Online Adaptation Algorithms for Digital Calibration of Analog Circuits,” *IEEE Transactions on Neural Networks and Learning Systems*, vol. 24, no. 4, pp. 554–565, Apr. 2013.

[161] K. Aono, R. K. Shaga, and S. Chakrabartty, “Exploiting Jump-Resonance Hysteresis in Silicon Auditory Front-Ends for Extracting Speaker Discriminative Formant Trajectories,” *IEEE Transactions on Biomedical Circuits and Systems*, vol. 7, no. 4, pp. 389–400, Aug. 2013.

[162] J.-P. Kulmala, J. Kosonen, J. Nurminen, and J. Avela, “Running in highly cushioned shoes increases leg stiffness and amplifies impact loading,” *Scientific Reports*, vol. 8, no. 17496, 2018.

[163] N. Lajnef, S. Chakrabartty, N. Elvin, and A. Elvin, “Piezo-powered floating gate injector for self-powered fatigue monitoring in biomechanical implants,” in *2007 IEEE International Symposium on Circuits and Systems*, May 2007, pp. 89–92.

[164] M. Albert and L. F. McCaig, “Emergency department visits for motor vehicle traffic injuries: United States, 2010–2011,” National Center for Health Statistics, Hyattsville, MD, NCHS Data Brief, No. 185, 2015.

[165] H. K. Uhthoff, P. Poitras, and D. S. Backman, “Internal plate fixation of fractures: Short history and recent developments,” *Journal of Orthopaedic Science*, vol. 2, no. 11, pp. 118–126, 2006.

[166] S. M. Bhandari, “An economic evaluation of early versus delayed operative treatment in patients with closed tibial shaft fractures,” *Arch. Orthop. Trauma Surg*, vol. 122, no. 6, pp. 315–323, Dec. 2012.

[167] R. Hammer, “Accuracy of radiologic assessment of tibial shaft fracture union in humans,” *Clin. Orthop. Related Res*, vol. vol., pp. 233–238, Oct. 1985.

[168] H. Sano, “Correlation of radiographic measurements with biomechanical test results,” *Clin. Orthop. Related Res*, vol. 368, pp. 271–278, Nov. 1999.

[169] A. Gorecki and W.Glinkowski, “Clinical experiences with ultrasonometric measurement of fracture healing,” *Technol. Health Care*, vol. 14, pp. 321–333, 2006.

[170] K. Malizos, “Transosseous application of low-intensity ultrasound for the enhancement and monitoring of fracture healing process in a sheep osteotomy model,” *Bone*, vol. 38, pp. 530–539, Apr. 2006.

[171] V. C. Protopappas, M. G. Vavva, D. I. Fotiadis, and K. N. Malizos, “Ultrasonic monitoring of bone fracture healing,” *IEEE Trans. Ultrason. Ferroelect. Freq. Control*, vol. 6, no. 55, pp. 1243–1255, Jun. 2008.

[172] L. J. Cunningham, “Monitoring the mechanical properties of healing bone,” *Clin. Orthop. Related Res*, vol. 467, no. 8, pp. 1964–1971, Aug. 2009.

[173] S. Kumaravel and S. Sundaram, “Monitoring of fracture healing by electrical conduction: A new diagnostic procedure,” *Indian J. Orthop*, vol. 46, no. 4, pp. 384–390, Aug. 2012.

[174] J. Richardson, “Measuring stiffness can define healing of tibial fractures,” *J. Bone Joint Surg. Br*, vol. 76, pp. 389–394, May 1994.

[175] L Claes, R Grass, T Schmickal, B Kisse, C Eggers, H Gerngross, W Mutschler, M Arand, T Wintermeyer, and A Wentzensen, “Monitoring and healing analysis of 100 tibial shaft fractures,” *Surg*, vol. 387, pp. 146–152, Jul. 2002.

[176] K. Shah, “Fracture stiffness measurement in tibial shaft fractures: A non-invasive method,” *Clin. Biomech*, vol. 10, pp. 395–400, Dec. 1995.

[177] N. Rydell, “Forces acting on the femoral head-prosthesis. A study on strain gauge supplied prostheses in living persons,” *Acta Orthopaedica Scandinavica*, vol. 37, no. 88, pp. 1–132, 1966.

[178] K. Kaufman, “Instrumented implant for measuring tibiofemoral forces,” *J. Biomech*, vol. 29, pp. 667–671, May 1996.

[179] G. Bergmann, “High-tech hip implant for wireless temperature measurements in vivo,” *PLoS ONE*, vol. 7, no. 8, p. 43489, Aug. 2012.

[180] C. Ruther, “A new approach for diagnostic investigation of total hip replacement loosening,” *Biomed. Eng. Syst. Technol*, vol. 273, pp. 74–79, Jan. 2011.

[181] B. Morris, “E-Knee: Evolution of the electronic knee prosthesis: Telemetry technology development,” *J. Bone Joint Surg. Am*, vol. 83, no. 2, pp. 62–66, 2001.

[182] I. Kutzner, “The influence of footwear on knee joint loading during walking—In vivo load measurements with instrumented knee implants,” *J. Biomech*, vol. 46, no. 4, pp. 796–800, Feb. 2013.

[183] S. Taylor, “Telemetry of forces from proximal femoral replacements and relevance to fixation,” *J. Biomech*, vol. 30, pp. 225–234, Mar. 1997.

[184] E. Schneider, “Loads acting in an intramedullary nail during fracture healing in the human femur,” *J. Biomech*, vol. 34, no. 7, pp. 849–857, Jul. 2001.

[185] B. Heinlein, “Design calibration and pre-clinical testing of an instrumented tibial tray,” *J. Biomech*, vol. 40, pp. 4–10, 2007.

[186] F. Graichen, “Implantable 9-channel telemetry system for in vivo load measurements with orthopedic implants,” *IEEE Trans. Biomed. Eng*, vol. 54, no. 2, pp. 253–261, Feb. 2007.

[187] D. Seo, R. M. Neely, K. Shen, U. Singhal, E. Alon, J. M. Rabaey, J. M. Carmena, and M. M. Maharbiz, “Wireless Recording in the Peripheral Nervous System with Ultrasonic Neural Dust,” *Neuron*, vol. 91, no. 3, pp. 529–539, 2016.

[188] S. H. Kondapalli, Y. Alazzawi, M. Malinowski, T. Timek, and S. Chakrabartty, “Feasibility of Self-powering and Energy Harvesting using Cardiac Valvular Perturbations,” *IEEE Transactions on Biomedical Circuits and Systems*, vol. PP, 2018.

[189] N. Vitković, S. Mladenović, M. Trifunović, M. Zdravković, M. Manić, M. Trajanović, D. Mišić, and J. Mitić, “Software Framework for the Creation and Application of Personalized Bone and Plate Implant Geometrical Models,” *J Healthcare Engineering*, pp. 1–11, 2018.

[190] M. Hannan, “Energy harvesting for the implantable biomedical devices: Issues and challenges,” *BioMed. Eng*, vol. 13, pp. 1–23, Dec. 2014.

[191] S. Platt, “The use of piezoelectric ceramics for electric power generation within orthopedic implants,” *IEEE ASME Trans. Mechatronics*, vol. 10, no. 4, pp. 455–461, Aug. 2005.

[192] G. Cochran, “External ultrasound can generate microampere direct currents in vivo from implanted piezoelectric materials,” *J. Orthopedic Res*, vol. 6, no. 1, pp. 145–147, 1988.

[193] N. Elvin, “Implantable bone strain telemetry sensing system and method,” Mar. 2000, uS6034296A.

[194] N. Lajnef, W. Borchani, R. Burgueño, and S. Chakrabartty, “Self-powered Piezo-floating-gate Smart-gauges based on Quasi-static Mechanical Energy Concentrators and Triggers,” *IEEE Sensors Journal*, vol. 15, no. 2, pp. 676–683, 2015.

[195] B. Geerts, K. L. Verstraete, Brugge/BE, and Ghent/BE, “Nonunion From Head to Toe,” in *ECR 2013.* Electronic Presentation System, 2013, pp. C–1645.

[196] D. Marsh, “Concepts of fracture union delayed union and nonunion,” *Clin. Orthop. Related Res*, vol. 355, pp. 22–30, Oct. 1998.

[197] J. Doornink, “Far cortical locking enables flexible fixation with periarticular locking plates,” *J. Orthop. Trauma*, vol. 25, pp. 29–34, Feb. 2011.

[198] A. Khalafi, “The effect of plate rotation on the stiffness of femoral LISS: A mechanical study,” *J. Orthop. Trauma*, vol. 20, pp. 542–546, Sep. 2006.

[199] B. Fang, T. Feng, M. Zhang, and S. Chakrabartty, “Feasibility of B-mode diagnostic ultrasonic energy transfer and telemetry to a cm lt;sup gt;2 lt;/sup gt; sized deep-tissue implant,” in *2015 IEEE International Symposium on Circuits and Systems (ISCAS)*, May 2015, pp. 782–785.

[200] G. Bergmann, “Hip contact forces and gait patterns from routine activities,” *J. Biomech*, vol. 34, no. 7, pp. 859–871, Jul. 2001.

[201] K. A. Egol, “Biomechanics of locked plates and screws,” *J. Orthop. Trauma*, vol. 18, no. 8, pp. 488–493, Sep. 2004.

Appendix A

Piezo-Floating-Gate Application: Bone Healing Tracking

After a traumatic bone fracture, a typical medical procedure is to implant a metal stabilizer that bears the load while the tissue and bone heals. Achieving better patient outcomes via in-vivo monitoring of the changes in growth and mechanical properties of the affected zone is an existing challenge. Current techniques involve patients coming into a medical facility for imaging; yet this presents an undue burden on the patient in terms of time and money spent, moreover, this will only provide a snapshot of the healing process. If there exists a method for providing a historical view of continuously collected data, at a low-cost and with minimal impact to patient mobility, it could aid in practitioners assessing bone healing progress and ascertaining if removal of the bone fixation device is a proper course of action. This appendix presents a feasibility study of using the Piezo-Floating-Gate (PFG) sensors for self-powered monitoring of the bone-healing process with measurement results from a biomechanical phantom comprising a femur fracture fixation plate, PVDF film, PZT discs, piezo polymer cable, a strain gauge, and the PFG sensor. Bone healing was emulated by inserting materials with varying elastic moduli into a gap between a distal femur fracture that the femur fracture fixation plate was attached to. This work has been reported in [140], with an earlier feasibility study in [163] and a lower-power method that forgoes the linear injection process as demonstrated by [103].

A.1 Introduction

In the year 2011, around a quarter million emergency department visits involved traumatic fractures cause by motor vehicle traffic injuries [164]. Unlike stress fractures, the high energies involved in motor vehicle incidents means that fractures tend to be more traumatic (i.e. a complete break of the bone) and are more likely to require a surgical procedure to implant a fixation device to facilitate proper healing [165]. This invasive procedure of implanting a foreign object on the fracture site remains one of the most effective medical options, yet it is not without failures, as 10 % of all fractures result in non-union and nearly 50 % in the case of a tibia fracture [166]. Since the fixation device is implanted, practitioners cannot optically observe the progression of healing and instead will rely on subjective methods such as radiography, which can result in inaccuracies due to the amount of callus (material bridging the gap in bone fractures) not being directly correlated to the stiffness of the bone [167, 168]. Contemporary observation methods require that patients periodically undergo radiography tests, which can cause delays in the early detection of a failure in the fixation device implant. Due to the infrequent availability of observations, coupled with the mediocre detection rate of said observations, a patient can waste significant time in recovery that has to be reset if the fixation device requires a replacement (and subsequently re-fracturing the bone).

Several researchers have proposed the use of ultrasonic wave propagation in assessing bone healing, by measuring changes in the velocity and attenuation of ultrasound, they attempt to quantify the bone and callus stiffness [169, 170, 171]. Nevertheless, these methods are insufficient for in-vivo measurements due to the surrounding soft tissue interfering with the isolated measurement of the bone fracture site and more critically have not been shown to correlate with bone stiffness [172]. Using external fixators, it has been shown that running electrical current through the bone and measuring changes in electrical characteristics such as conductance or impedance can assess healing progress [173]. The mechanical stiffness of the callus can also be measured directly when removing the fixation devices, but this would occur after removal of all fixation devices and is not practical to have patients undergo a removal surgery just to find that the fracture was not healed and they need to reattach the fixation device [174, 175]. Indirect measurement of the mechanical stiffness can be done if the fracture is treated with external fixators by measuring the deflection of fixation pins or device deformation [176, 172]. From these works, it has been shown that monitoring the orthopedic implant's mechanical load is a valid means of detecting the amount of bone healing that has taken place. This is because post-surgery any load applied to the site is initially supported by the fixation device. During healing, as callus ossifies, the bone will begin to take a portion of the load, and any loads applied will be shared by both the fixation device and the bone. As healing takes place, the callus becomes stiffer and stiffer, thereby further reducing the share of the load that the fixation device needs to carry. The technical challenge then, is how to continuously monitor the mechanical strain levels of the implanted fixation device while it is in use.

One of the earliest examples of a sensing device in an orthopedic implant to measure in-vivo forces and strains comes from a prosthesis with strain-gauges wired to an external data acquisition system [177]. Another example is a total knee implant that could measure the dynamic tibiofemoral forces and the center of applied pressure [178]. This orthopedic implant contained four different load cells and was also wired to an external data acquisition system. Although useful for directly tapping into the implant for collecting information, these methods limit patient mobility and do not allow for continuous monitoring of the implant during typical loading conditions.

With the advent of high bandwidth wireless communication, several researchers have proposed implantable orthopedics with telemetry systems for hip implants [179, 180], knee joints [181, 182], femurs [183, 184], and tibial tray [185] to send in-vivo load, strain, and temperature data wirelessly. The majority of reported telemetry technologies rely on on-board energy storage in the form of batteries or super-capacitors to power the sensing, computation, storage, and wireless communication. The use of batteries is less than ideal as they will limit the usable telemetry lifetime, are more invasive, and can introduce chemical hazards. For use cases that only require periodic monitoring, inductive links or other energy harvesting techniques can be used to remotely deliver energy to or communicate with the implanted fixation device [186, 187, 7, 188]. These approaches will be limited in their range, and require external contraptions that prevent long-term autonomous monitoring. More ideally, a sensor that is seamlessly integrated into a custom fixation device [189] that can harvest its operation energy directly from the mechanical load and continuously log the statistics of loading would be implanted. The use of piezoelectric transducers to harvest energy in orthopedics has been proposed as a viable method [190, 191]. Prototypes of devices that were sized to harvest from in-vivo compressive or tensile loads what was conventionally considered sufficient energy, resulted large form factors that limit their usefulness as implantables [192, 193]. This appears to be an ideal application for the PFG of Section 4, which would allow one to compute and store cumulative statistics of strain-rates and stresses experienced by a patient while operating within power limits not possible with any competing health and usage sensing technology [194]. An illustration of a femur fracture with an implanted fixation device that has been endowed with the PFG sensor is shown in Figure A.1 along with plots of the collected data for a properly healing versus non-healing bone fracture.

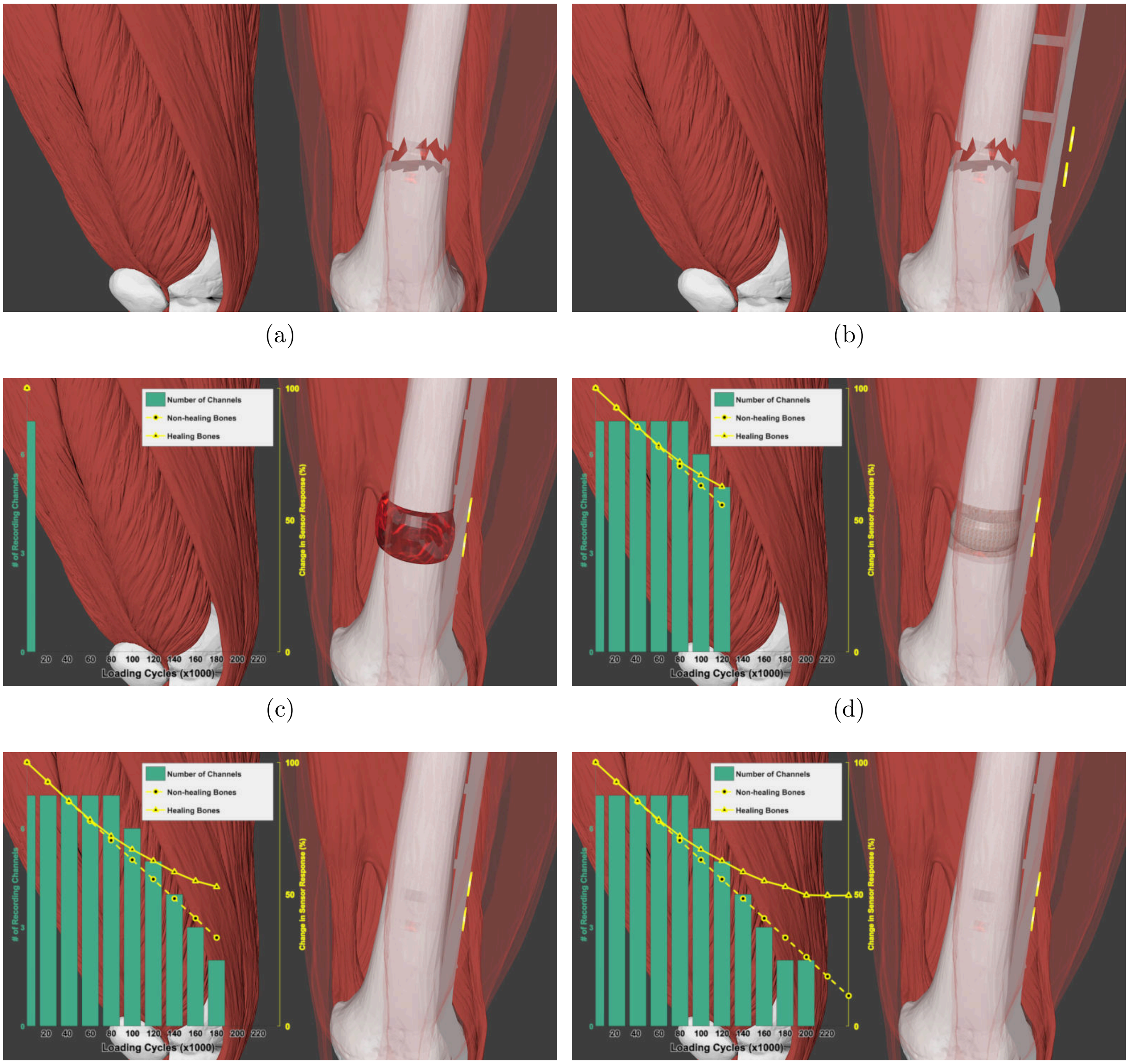

(a) (b)

(c) (d)

(e) (f)

Figure A.1: Illustrations showing (a) bone fracture (b) bone fixation plate and PFG sensors (shown as yellow discs), (c) initially the plate will be taking the entire load and all PFG channels will inject (d) as the new bone forms it supports part of the weight and the number of channels recording will decrease (e) the bone grows stiffer as it heals, further reducing the strain experienced by the plate as its loading is decreased (f) once fully healed, the PFG will not record data. Note that the number of channels shown is only for the healing case.

A.2 Modeling of Strain-Evolution in Fixation Plate During Bone Healing

Before tossing the PFG onto a femur fracture fixation device willy-nilly, an intuition for the magnitude of induced strain on the surface of the fixation device when a patient obambulates is modeled. The modeled parameters are used for sizing of the piezoelectric transducer. In modeling the healing process it is key to consider the three major phases: reactive, reparative, and remodeling [195]. Figure A.1 shows the key phases. In Figure A.1a, the bone has suffered a fracture and the femur comprises two disconnected pieces. Within a few hours after fracture, a blood clot, or hematoma, will form in the reactive phase using the blood released from damaged blood vessels as in most injuries and is shown as a red blob in Figure A.1c. Note that in Figure A.1b the bone fixation device is shown during the installation process and though not shown, a hematoma may have formed. The reparative phase will occur hours after setting the bone and a hyaline cartilage and a spongy bone will develop using periosteal proximal and periosteal distal cells. These tissues will develop across the fracture's divide and unite the disjoint set as shown in Figure A.1d. The new mass of heterogenous tissue is known as fracture callus and forms within the gap of the fracture to restore some of the original bone integrity. During this phase the callus may be slightly larger than the original bone and appear as a collar. In the reparative phase, the internal callus within the gap and the external callus that forms the collar are replaced by woven spongy bone. The hyaline cartilage and woven bone are gradually replaced with lamellar bone in the form of trabecular bone in a process known as callus ossification. This stage is shown in Figure A.1e and by Figure A.1f the trabecular bone develops into compact bone and the medullary cavity is restored by removing parts of the internal callus. Even at the the trabecular bone stage, most of the bone's strength will be restored and the fixation device will be minimally loaded. Depending on many factors such as age, nutrition, fracture severity, etc. the duration of each phase will differ between patients, a successful bone healing process is determined by the level of bone stiffness within a defined period [196]. Delayed or may be caused by a cessation of the priosteal callus production; however, it can eventually heal by endosteal healing, or rapid fracture bridging after cessation of the periosteal healing response. If the bridging does not occur after the cessation of both periosteal and endosteal healing responses, it is diagnosed as non-union [196].

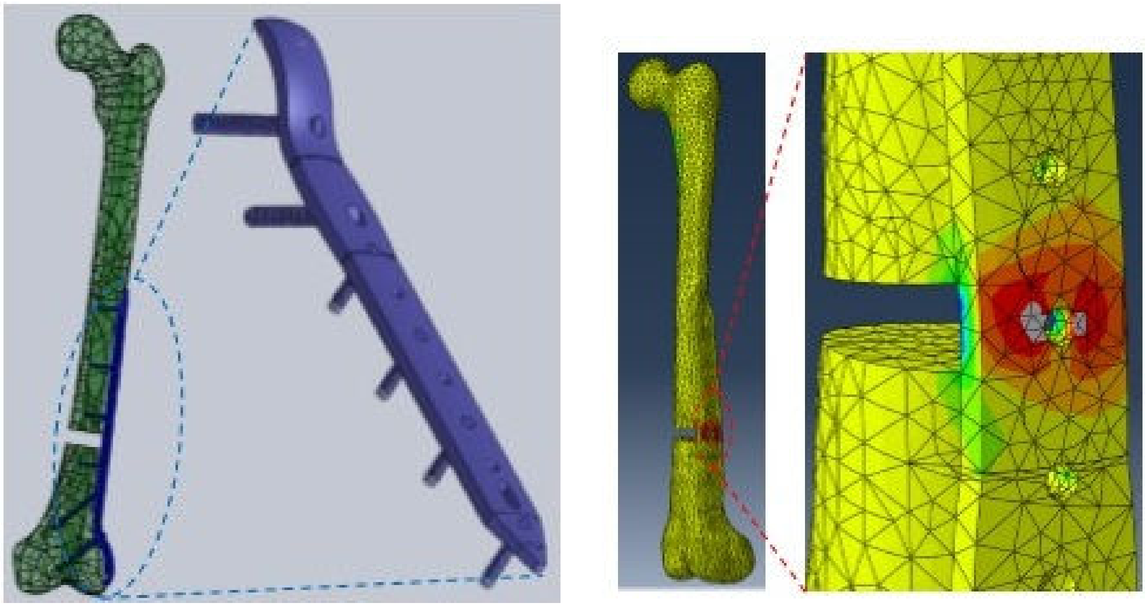

(a) (b)

Figure A.2: Model and simulation of a femur bone fracture and fixation device interaction.

The progression of bone healing is non-linear and dependent on several variables, but we can expect at least two features of bone healing progression to remain consistent across presented cases. Namely during the initial phase the fixation device will carry the load whilst during final phases the fused segments of bone will take the majority of the load. A model of a fractured bone and fixation plate was created in SolidWorks and is shown in Figure A.2a, with femur bone, plate and mounting screws based on model parameters from [197, 198]. A unstable distal femur fracture was modeled using a 12 mm gap osteotomy on the synthetic femur replica. The gap osteotomy was stabilized using a periarticular locking plate of the 10-hole NCB Femoral Plate from Zimmer Inc. variety. A distal plate segment was applied using three 6.5 mm locking head screws to the metaphysics and the proximal plate was applied to the diaphysis with four 5 mm locking head screws.

This model was imported into ABAQUS for finite element model (FEM) analysis to numerically investigate the distribution and variation of in-vivo implant strains over an example healing period. The elastic moduli of the bone was 16 GPa and the fixation plate was 110 GPa. Tetrahedral elements were used for the linear static analysis with rigid, no penetration contact behavior defined for the lateral interaction between the bone and fixation plate. The distal fixture was fixed and a concentrated compression load applied to the femoral head center, Figure A.2b illustrates the strain distribution with low areas shown in blue and high areas as red. It is evident that the maximal strain concentration is adjacent to the hold located at the fracture centerline.

Bone healing was simulated by replacing the fracture gap geometry with materials of varying elastic modulus. For an applied load of static force with 420 N, the experimentally measured strains from a strain gauge and numerically computed strains from FEM are presented as Figure A.3. When changing the elastic modulus of the material filling the osteotomy gap, we observe a decent agreement between experimental and simulation values. For elastic modulus representative of a healed bone, the strain levels were simulated as 50 % of the initial levels, both of which are on the order of 100 $\mu\epsilon$. Previous AIM Lab members have reported that such levels of strain variation, with loading frequencies under 1 Hz, a typical piezoelectric transducer might harvest a couple hundred nanoWatts [20]. These experimental results [140, 146] strongly suggest the applicability of the PFG for this scenario.

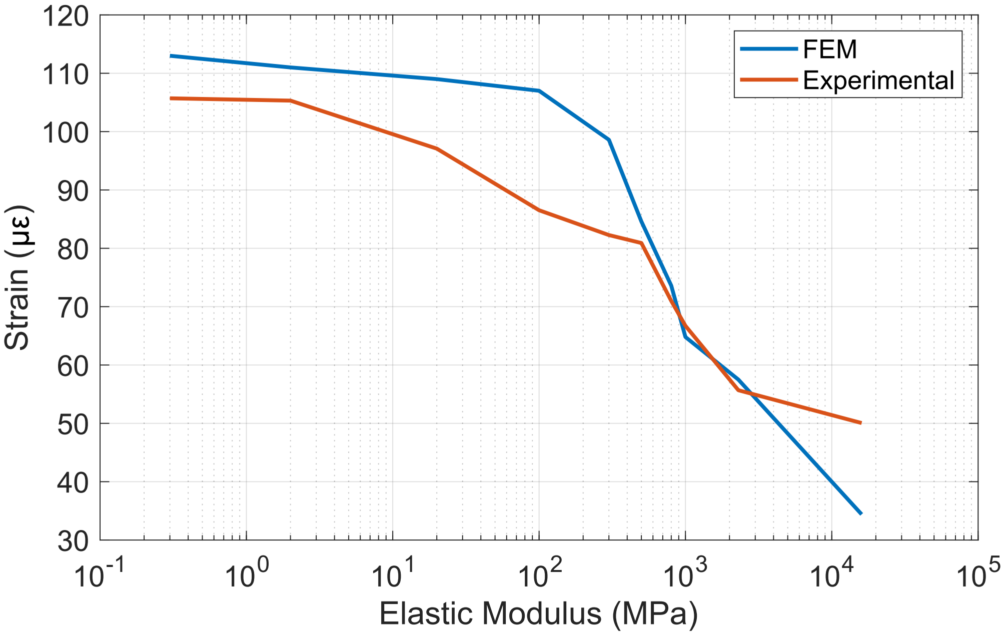

Figure A.3: A comparison between experimentally measured strain and FEM simulations for varying elastic modulus.

A.3 PFG Based Self-powered Sensing and Data Logging

The working principle of the PFG sensor is detailed in the main text of this dissertation, see Section 4. The beauty of this physics-based sensing approach is in the way it eliminates the need for precise voltage regulation, energy storage, analog-to-digital converts, microcontroller units and random-access memories to enable a non-volatile memory that has the potential to operate with just picoWatts. As in all of the applications presented within this dissertation the initial programming of the PFG requires an external power source for setting the floating-gates to a known value and collecting calibration data. The data for the particular chip used during testing is shown in Figure A.4 and shows that all channels are linear across the utilized recording range. We use the parameters of a $ax + b$ linear line fit on each channel when interpreting the results. For example, in Figure A.4, the injection

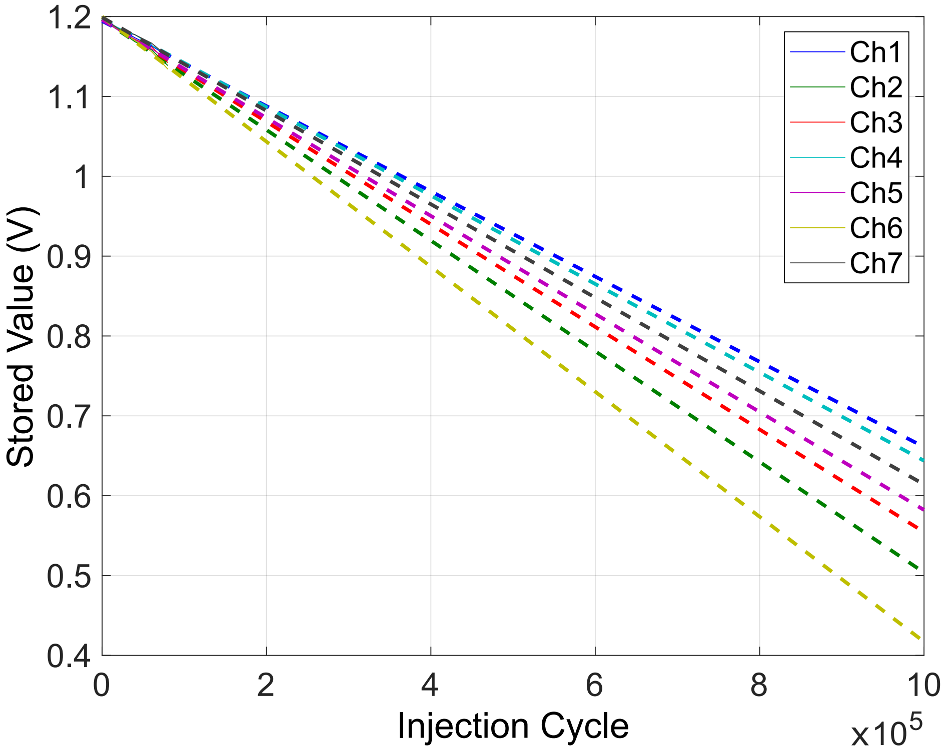

Figure A.4: Showing the actual linearity calibration data for the PFG used in bone healing monitoring.

cycles are large enough for all seven channels of the PFG to inject, the offset parameter b is already applied to show all channels starting from a stored value of 1.2 V. We see that channel six injected much faster than channel one and at the end of a million injections channel six was at 417.1 mV while channel one was at 661 mV. One can arbitrarily scale all channels to channel one, thus the corrective parameter a for channel on is 1, while it would be $\frac{661}{417.1} = 1.585$ for channel six.

The system architecture of the particular PFG sensor utilized for this study is given in Figure A.5. The programming is assumed to take place before implanting, although it is technically possible to reprogram the floating-gate values in-vivo by coupling RF or ultrasound energy sources [199]. A graph showing the sensor's recording capacity as a variable of tuning resistance of it's voltage references is presented in Figure A.6. The value of R_{Tune}

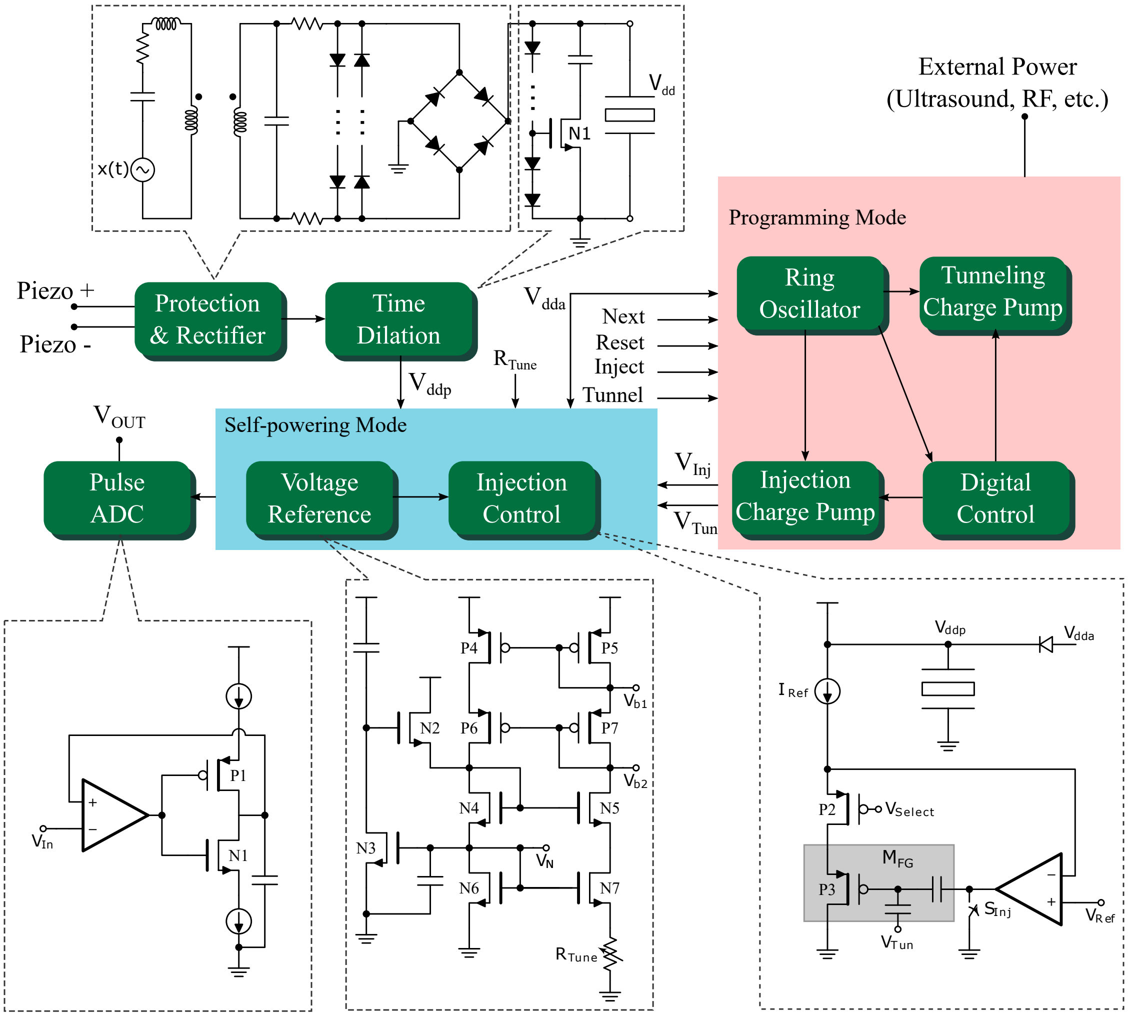

Figure A.5: A system architecture of the PFG sensor chipset with schematics for self-powered blocks.

was selected to allow 200 000 cycles of injection, sourcing a readily-available resistor resulted in the particular value of 3.2 MΩ. The applied force for each loading cycle was 600 N at 2 Hz, as this is the loading used for the longer-term testing (explained in the next subsection). Measured parameters of the PFG are given in Table A.1 and micrograph of the actual variant of the PFG is presented as Figure A.7.

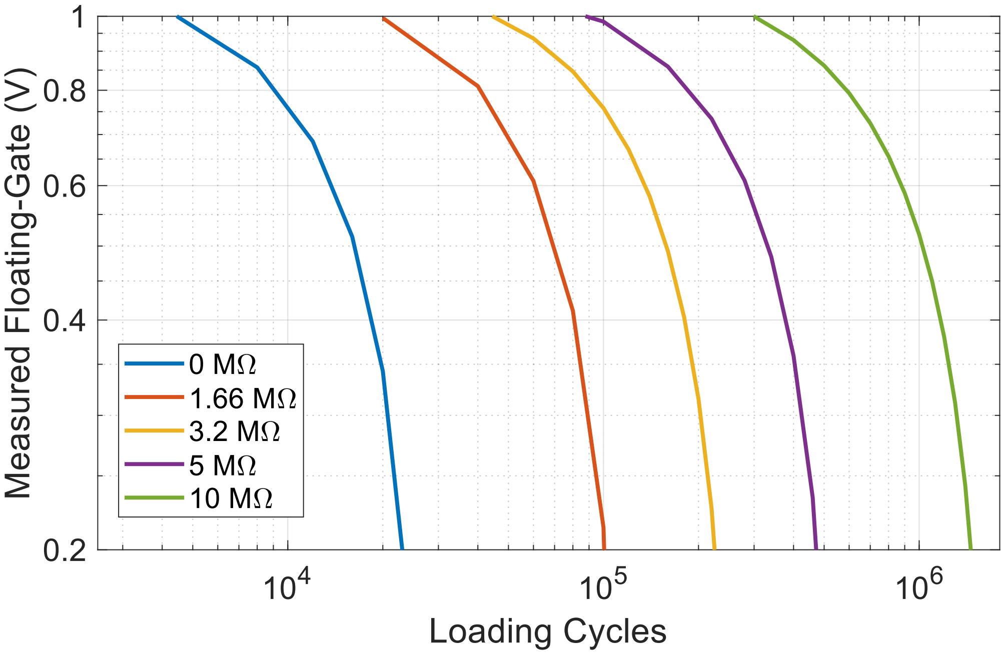

Figure A.6: Change in the number of recorded loading cycles with respect to tuning resistor of the PFG.

A.4 Experimental Setup

The phantom used in the experimental testing follows a setup as presented in [198]. A section of a synthetic femur replica was cut out to mimic a traumatic fracture, and the gap osteotomy was stabilized using the periarticular locking plate of Figure A.8. The distal fixture was rigidly mounted with an epoxy layer to the base of a MTS model Flextest 40 with series 370 load unit to provide a controlled loading cycle. A compression load was applied to the femoral head center via a hinge joint such that the load vector intersected the femoral head and the epicondylar center. Five different piezoelectric transducers were attached to the device for monitoring the strain variation during testing, two PZT-5A piezo ceramic discs (STEMINC-PIEZO, Part number SMD12T06R412WL) were place above and below the fracture. A piezo copolymer cable (Measurement Specialties 20AWG Cable - Copolymer) was attached alongside the plate, and a polyvinylidene flouride (PVDF) film

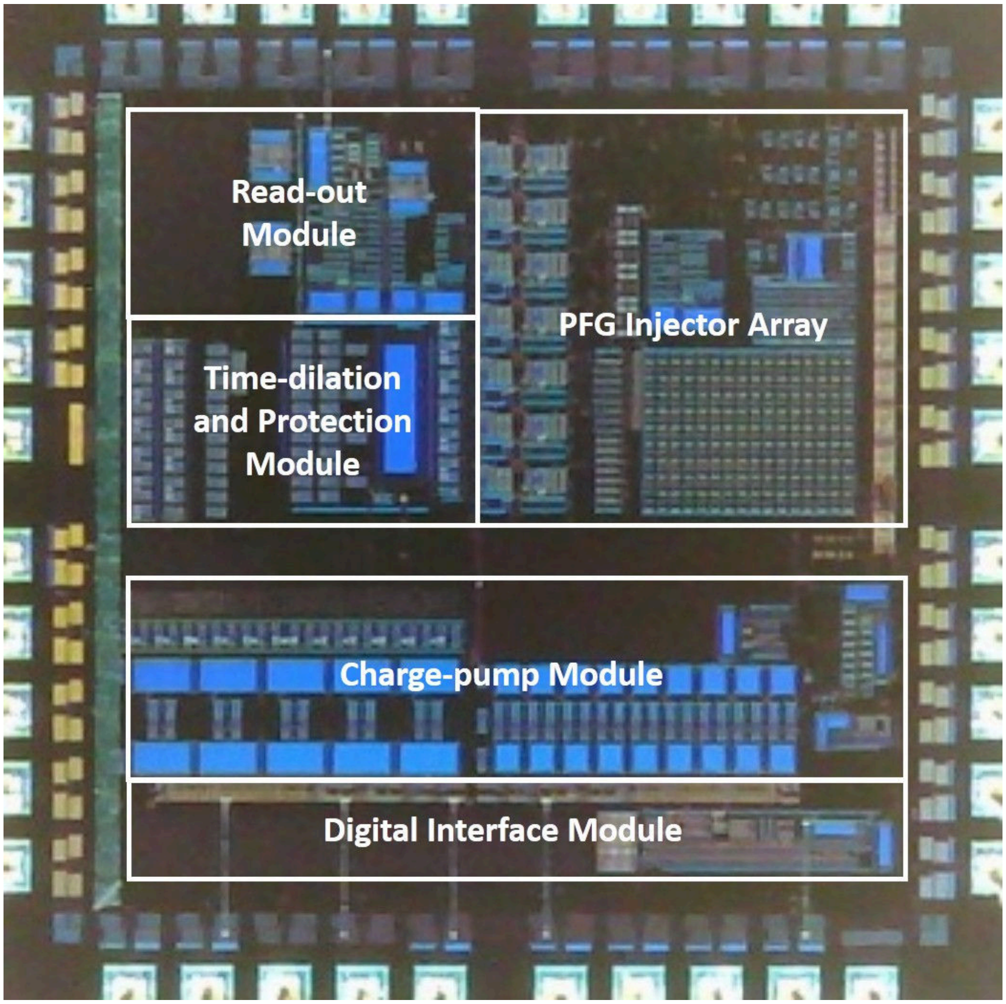

Figure A.7: The micrograph of the actual, fabricated chip used for testing. A 10 nF tuning capacitor and 3.2 MΩ resistor are located off-chip.

(model number DT2-052K/L with rivets) was attached on the inside of the implant. The properties of these piezoelectrics are detailed in Table A.2. Finally, a commercial strain gauge was placed at the fracture centerline. A Crack Opening Displacement (COD) gauge was used to verify the resulting compression of the osteotomy gap at the far cortex. Each piezoelectric was connected to the PFG sensor board (bottom left of Figure A.8 to record the cumulative history of voltage variation.

Table A.1: Specification of Linear Injector Circuit

Parameters	**Value**
Technology	0.5 µm CMOS
Size	$1.5\,\mathrm{mm}^2 \times 1.5\,\mathrm{mm}^2$
Supply Voltage	1.8 V
Floating-Gate Capacitance	100 fF
Minimum Energy (Sensing)	100 nJ
Power Dissipation (Programming)	150 µW
Power Dissipation (Read-out)	75 µW
Read-out resolution	8 bits at 10 kHz
Channel	**Threshold**
1	7.2 V
2	7.7 V
3	7.9 V
4	8.7 V
5	9.2 V
6	9.8 V
7	10.2 V

Table A.2: Properties of Piezoelectric Transducer

Type	**Dimension** (mm)	**Elastic Modulus** (GPa)	**Capacitance** (nF)	**Electrical Permittivity** ($\mathrm{nF\,m^{-1}}$)	**Piezoelectric Constant d31** ($\mathrm{pm\,V^{-1}}$)
PZT-5A Discs	ϕ12 x 0.6	76	2.9	16.38	190
PVDF Film	$12x0.09x62$	2	1.7	0.115	23
Copolymer Cable	ϕ2.72 x 240	2.3	0.35	0.079	11

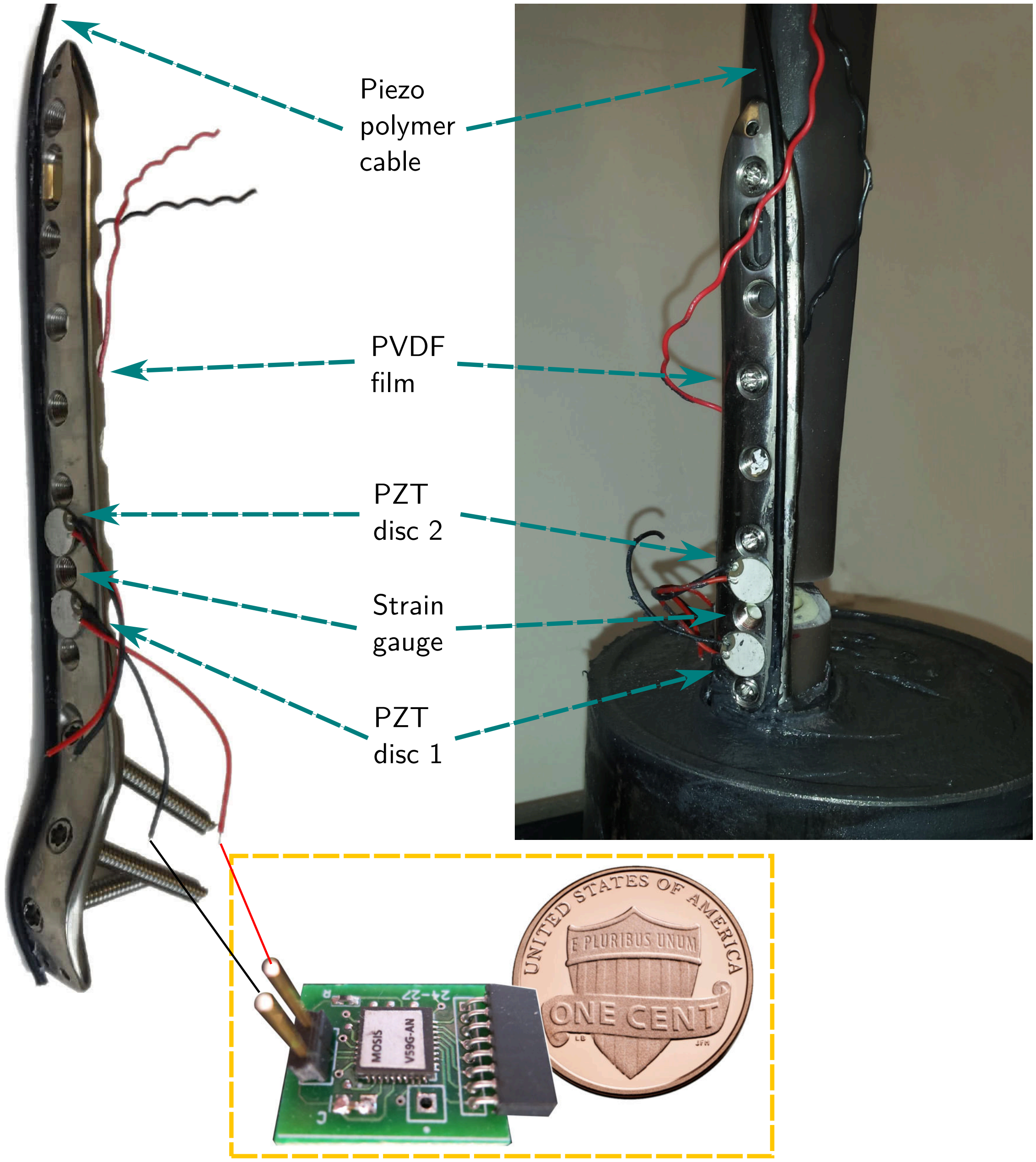

Figure A.8: Experimental setup showing the placement of piezoelectric transducers on the bone fixation device (left) with the PFG sensor board (bottom-left) and the fixation device affixed to a model femur (right).

In the first set of experiments, the healing period was simulated with 2000 cycles of loading of a 420 N cyclic axial load at 2 Hz frequency to the femoral head center. This loading force was selected to be lower than the expected 1870 N levels from walking [200]. Before any simulated healing, these loads were sufficient for causing injection across all seven channels of the PFG. Data were collected for 2000 cycles with the osteotomy left flexible to simulate a non-healing case. In the second test, a quickly-healing case is emulated by swapping out different materials in the osteotomy with increasing elastic modulus every 200 cycles as detailed in Figure A.9. For the composite materials, layers of hard silicone and thin aluminum plates were stacked to achieve the desired elastic modulus (higher ratio of aluminum to silicone results in higher elastic modulus). In a more realistic scenario, a complete fracture might have a healing period of four months and can be simulated with 200 000 cycles of loading [201]. In this testing, the applied force was increased to 600 N while maintaining the 2 Hz cycle rate. The progression of materials used to mimic a more slowly healing bone is given in Figure A.10. In this case, a non-healing condition is modeled by applying the full 200 000 cycles without any materials inside the osteotomy, whereas a healing case swaps out the material to fill the osteotomy every 20 000 cycles.

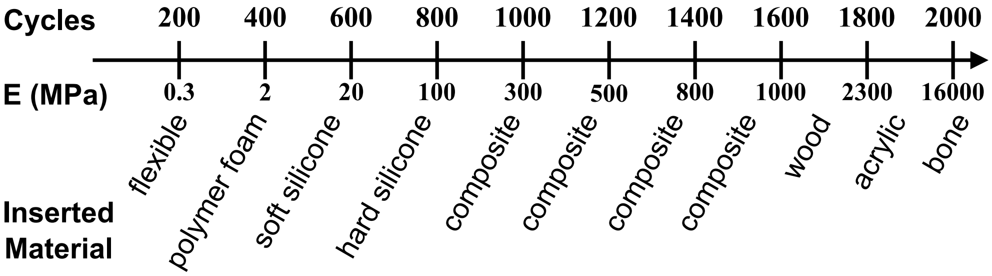

Figure A.9: The materials and their elastic modulus along with when they were used with respect to the number of cycles. This emulates a quickly-healing case.

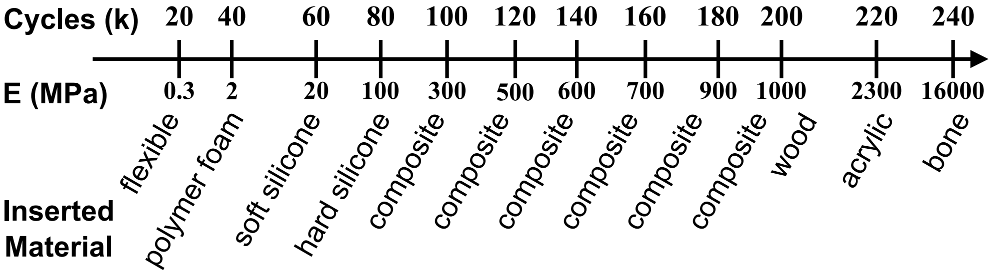

Figure A.10: The materials and their elastic modulus along with when they were used with respect to the number of cycles. This emulates a slowly-healing case.

A.5 Results

A.5.1 PFG Activation for Femur Loading

Due to the placement and low mechanical-to-electrical coupling coefficients, the PVDF film and copolymer cable generated voltages below 1 V, which was insufficient for logging data on this version of the PFG. The maximum observed voltages generated by the different types of piezoelectrics is in Table A.3. PZT Disc 1 is the ceramic disc that was placed above the fracture line. Femur loading caused compression and bending due to load eccentricity that resulted in the ceramic disc placed below the fracture line, PZT Disc 2, being the best option for recording all channels of the PFG. The results in this table were collected during the non-healing test with loads of 420 N.

Table A.3: Maximum Generated Voltage by Piezoelectric

Piezo Transducer	**Generated (V)**
PVDF Film	0.8 V
PZT Disc 1	2.4 V
PZT Disc 2	10.53 V
Copolymer	0.67 V

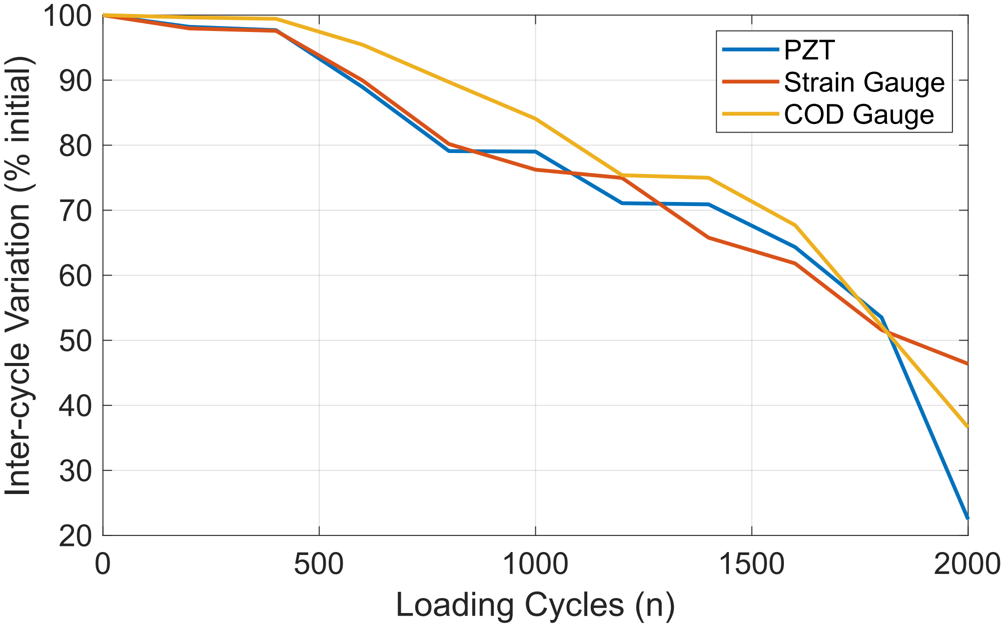

Figure A.11: Variability between the measurement devices of PZT Disc 2 (below fracture), strain gauge, and COD gauge. All three are in close agreement during the entire bone healing process.

Figure A.11 gives the different results observed across three types of piezoelectric transducers, with respect to their initially observed values at the start of osteotomy compression. As the fast bone healing process is simulated, all three modalities show similar rates of decreasing voltage generated with increased gap stiffness (i.e. lower strain levels). These results verify that PZT Disc 2 will enable the PFG to log statistics similar to the ground truth collected using commercial, externally-powered strain sensors.

A.5.2 Logged Data for Healing Periods

As in Figure A.11, a comparison of the PZT Disc 2 against a standard strain gauge is presented in Figure A.12. To reiterate, a measurement of 100 % would be the voltage generated when the osteotomy is non-healed or filled with flexible material. As the material in the gap increases in stiffness, the share of the load on the bone fixation plate decreases, consequently the generated voltage on the piezoelectric transducer will decrease. A complete snapshot showing the relative variation of the memory with respect to non-healing and healing bones is presented as Figure A.13. The number of channels recording is only for the healing case, in the non-healing case all seven channels always inject and the red line shows a completely linear trend as expected from the PFG with linear injection feedback. Table A.4 gives the actual load cycles at which certain PFG channels stopped recording, note that channel one is the most sensitive, and each subsequent channel has approximately one diode drop of additional voltage required to log data as highlighted in Table A.1.

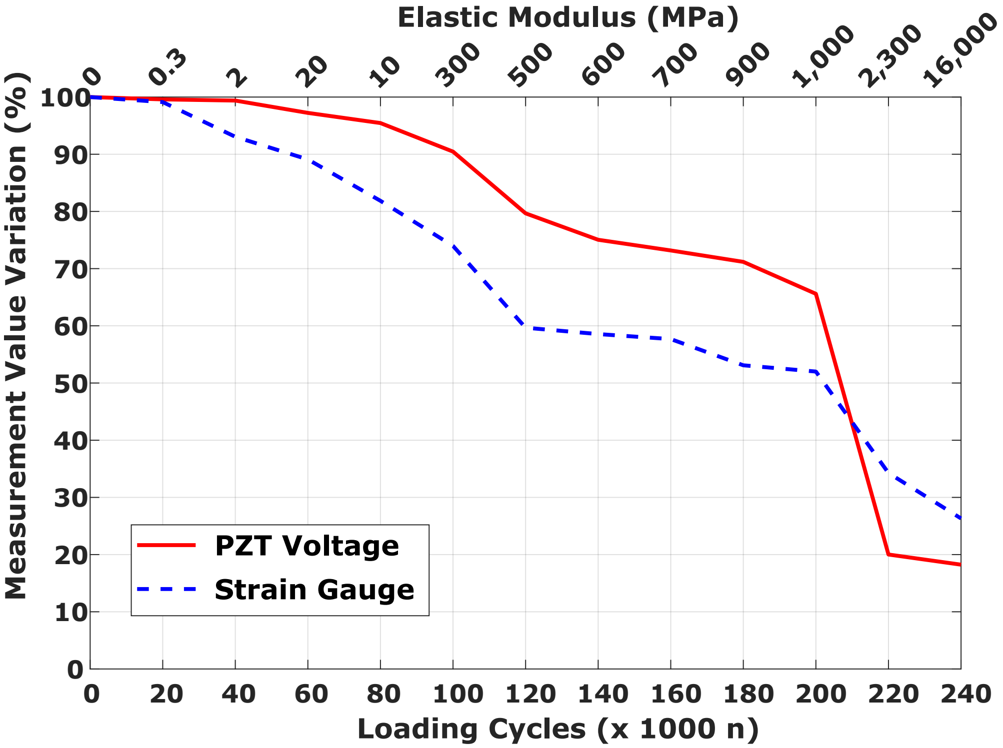

Figure A.12: Variability between the measurement devices of PZT Disc 2 (below fracture) and strain gauge for the slower bone healing simulation.

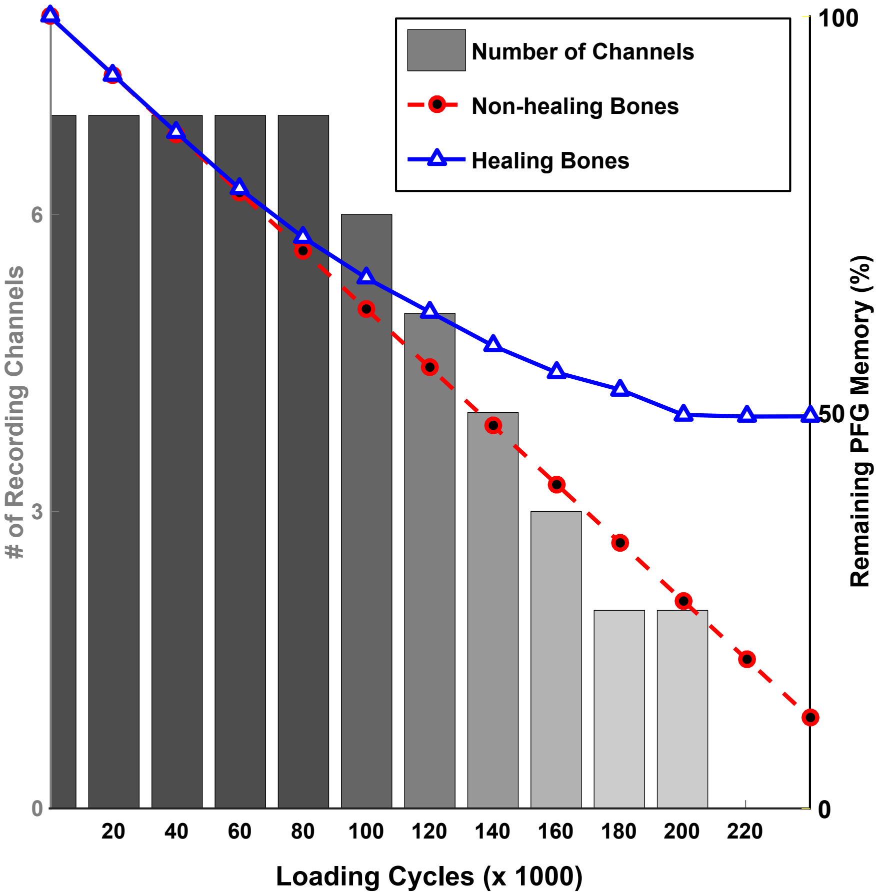

Figure A.13: The bars indicate how many channels are recording data. The blue line is for a properly healing bone, which shows that at some point the strain experienced is sufficiently small enough to prevent any data logging on the PFG. In the red line, a non-healing case is shown.

Table A.4: PFG Recording Cutoff

PFG Channel	**Healing Load Cycle** (x1000)	**Non-Healing Load Cycle** (x1000)
1	100	240
2	120	240
3	140	240
4	160	240
5	180	240
6	200	240
7	200	240

A.6 Discussion and Conclusion

This foray into a biomedical application shows the potential for using the PFG in energy-constrained in-vivo measurement. In particular, bone healing of a femur was demonstrated. Because the sensor is powered directly by the strain variations on the fixation device, it achieves essentially continuous data logging that is not possible with conventional sensors on the market. This experiment did not utilize wireless telemetry since it was to show feasibility, but we have previously demonstrated the potential for RF and other wireless data retrieval systems. The packaging and biocompatibility of the PZT transducers and PFG sensor was not considered.

A major limitation in this approach is that the entire PFG sensor needs to be powered using the piezoelectric transducer. In the presented form, such a sensor would require the transducer to generate at least 7 V to have any meaningful data collection. Such large voltages will require significant loading, thus precluding this method from being applied to bones besides the femur, tibia, knee, or hip. The method also assumes that the sustained injuries are not so significant as to prevent a patient from ambulating or walking about. In the cases of bed-ridden or wheelchair-bound patients the PFG sensors would not record any statistics as the bone fixation device would not be sufficiently loaded. To increase the utility of a PFG-based monitoring of bone healing, the use of a more sensitive architecture, as outlined in Section 5, is suggested. With data logging sensitivities potentially extending down into the mV range, the modified PFG could record bone healing progress in many more situations. With increased sensitivity, a similar method could even be applied for monitoring of stents or sutures. This is a topic for future exploration and not detailed in this dissertation.

Thanks to Dr. Aaron Purdue from University of Michigan and Dr. Hallie P. Brinkerhuff from Zimmer-Biomet for their valuable comments and discussions regarding the progression of bone-healing and the integration of the PFG sensors onto a fixation device. The material in this appendix is based upon work supported in part by the National Science Foundation STTR Phase I grant 1417044 (Sub-contract through Piezonix LLC.) and the Graduate Research Fellowship Program under Grant Nos. DGE-0802267 and DGE-1143954. Any opinions, findings, and conclusions or recommendations expressed in this material are those of the author and do not necessarily reflect the views of the National Science Foundation.